AFRL-AFOSR-JP-TR-2016-0083

Plasma Assisted Ignition and Combustion at Low Initial Gas Temperatures: Development of Kinetic Mechanism

Svetlana Starikovskaya
FX CONSEIL

10/05/2016
Final Report

Air Force Research Laboratory
AF Office Of Scientific Research (AFOSR)/ IOA
Arlington, Virginia 22203
Air Force Materiel Command

REPORT DOCUMENTATION PAGE

Form Approved
OMB No. 0704-0188

1. REPORT DATE *(DD-MM-YYYY)*
17-10-2016

2. REPORT TYPE
Final

3. DATES COVERED *(From - To)*
01 May 2013 to 30 Apr 2016

4. TITLE AND SUBTITLE
Plasma Assisted Ignition and Combustion at Low Initial Gas Temperatures: Development of Kinetic Mechanism

5a. CONTRACT NUMBER

5b. GRANT NUMBER
FA2386-13-1-4064

5c. PROGRAM ELEMENT NUMBER
61102F

6. AUTHOR(S)
Svetlana Starikovskaya

5d. PROJECT NUMBER

5e. TASK NUMBER

5f. WORK UNIT NUMBER

7. PERFORMING ORGANIZATION NAME(S) AND ADDRESS(ES)
FX CONSEIL
7 RUE ST DOMINIQUE
PARIS, 75007 FR

8. PERFORMING ORGANIZATION REPORT NUMBER

9. SPONSORING/MONITORING AGENCY NAME(S) AND ADDRESS(ES)
AOARD
UNIT 45002
APO AP 96338-5002

10. SPONSOR/MONITOR'S ACRONYM(S)
AFRL/AFOSR IOA

11. SPONSOR/MONITOR'S REPORT NUMBER(S)
AFRL-AFOSR-JP-TR-2016-0083

12. DISTRIBUTION/AVAILABILITY STATEMENT
A DISTRIBUTION UNLIMITED: PB Public Release

13. SUPPLEMENTARY NOTES

14. ABSTRACT

The Final Technical Report summarizes the results of work performed with partial financial support of AOARD AFOSR during a period May 1, 2013 April 30, 2016. The three first chapters are devoted to the study of the nanosecond capillary discharge in the form of the fast ionization wave (FIW). The fourth chapter describes physics of a nanosecond surface dielectric barrier discharge (SDBD) at ambient gas temperature and high pressures (1-6 bar) in air. Details about the filamentation and about morphology of the surface streamers are given in the Chapter 5. Chapter 6 presents a preliminary numerical analysis of the ignition by a nanosecond discharge. Chapter 7 presents the high pressure high temperature reactor built recently at Laboratory for Plasma Physics. Chapter 8 describes the results of analysis of role of O(1D) in plasmaassisted combustion including gas mixtures with hydrocarbons. The last, 9th Chapter contains a brief review of state of the art in plasma assisted ignition and combustion.

15. SUBJECT TERMS
AOARD, Combustion, Plasma

16. SECURITY CLASSIFICATION OF: a. REPORT	b. ABSTRACT	c. THIS PAGE	17. LIMITATION OF ABSTRACT	18. NUMBER OF PAGES
Unclassified	Unclassified	Unclassified	SAR	173

19a. NAME OF RESPONSIBLE PERSON
KNOPP, JEREMY

19b. TELEPHONE NUMBER *(Include area code)*
315-227-7006

Standard Form 298 (Rev. 8/98)
Prescribed by ANSI Std. Z39.18

Laboratory for Physics of Plasma, Ecole Polytechnique

Plasma Assisted Ignition and Combustion at Low Initial Gas Temperatures: Development of Kinetic Mechanism

AOARD Project # FA2386-13-1-4064
Final Technical Report, May 1 2013 — April 30, 2016

Date Submitted: *August 30, 2016*

PI: Dr. Svetlana STARIKOVSKAIA,
Laboratory for Plasma Physics (LPP), CNRS UMR 7648
Ecole Polytechnique
Route de Saclay, 91128 Palaiseau, FRANCE
Phone (+33)–1–69–33–59–45
E–mail: svetlana.starikovskaya@lpp.polytechnique.fr
URL: http://www.lpp.fr

Participants

Sergey STEPANYAN,
PhD student in 2011—2014,
Laboratory for Plasma Physics (LPP), CNRS UMR 7648
Ecole Polytechnique
Route de Saclay, 91128 Palaiseau, FRANCE
Andrei KLOCHKO,
PhD student in 2011—2014,
Laboratory for Plasma Physics (LPP), CNRS UMR 7648
Ecole Polytechnique
Route de Saclay, 91128 Palaiseau, FRANCE
Sergey SHCHERBANEV,
PhD student,
Laboratory for Plasma Physics (LPP), CNRS UMR 7648
Ecole Polytechnique
Route de Saclay, 91128 Palaiseau, FRANCE
Nikita LEPIKHIN,
PhD student,
Laboratory for Plasma Physics (LPP), CNRS UMR 7648
Ecole Polytechnique
Route de Saclay, 91128 Palaiseau, FRANCE

Collaborators

Dr. Nikolay POPOV,
Laboratory of microelectronics,
Skobeltsyn Institute of Nuclear Physics,
Moscow State University,
building 1/2, Leninskie gory 119991 Moscow, RUSSIA
Phone (+7)–905–789–12–56
E–mail: NPopov@mics.msu.su

Contents

Abstract

The Final Technical Report summarizes the results of work performed with partial financial support of AOARD AFOSR during a period May 1, 2013 — April 30, 2016.

The three first chapters are devoted to the study of the nanosecond capillary discharge in the form of the fast ionization wave (FIW). Since FIWs at moderate pressures allow comprehensive measurements of the electric field, electron density, electric current, and deposited energy, they are very promising objects for the kinetic study of nanosecond discharges. The aim of the present study was to measure oxygen atoms density at the conditions of high gas heating in the near aftreglow due to energy exchange on the time scale shorter than V–T relaxation (or so–called fast gas heating). O–atom density was measured in the discharge (0 – 30 ns), by actinometry (Chapter 1) and in the afterglow ($t < 2.5$ μs), by TALIF technique (Chapter 2). Measurements were performed at moderate pressure, about 30 mbar, at conditions of very high specific deposited energy (about 1 eV/molecule) and gas heating up to 2000 – 25000 K during 2 μs. Study of $N_2(C^3\Pi_u)$ quenching in nitrogen in early aftreglow demonstrated that, in early afterglow of the nanosecond capillary discharge, additional production of electrons by reaction of associative ionization, can be important (Chapter 3). According to measurements and calculations, the electron density in the afterglow can be as high as 10^{15} cm^{-3} during hundreds of nanoseconds.

The fourth chapter describes physics of a nanosecond surface dielectric barrier discharge (SDBD) at ambient gas temperature and high pressures (1-6 bar) in air. At atmospheric pressure, the discharge develops as a set of streamers starting synchronously from the high-voltage electrode and propagating along the dielectric layer. Streamers cover the dielectric surface creating “quasi–uniform” plasma layer. At high pressures and high voltage amplitudes on the cathode, the filamentation of the discharge is observed a few nanoseconds after the discharge starts. Parameters of the observed “streamers-to-filaments” transition are measured; physics of transition is discussed on the basis of theoretical estimates and numerical modeling. Set of discharge reactions has been suggested and analyzed. More details about the filamentation and about morphology of the surface streamers are given in the Chapter 5. In particular, it was proven that “surface streamers” are flat, with the dimensions much smaller in the direction perpendicular to the surface then in the plane parallel to the surface.

It has been proved, in the framework of French national Project ANR PLASMAFLAME, that nanosecond SDBD decreases significantly the ignition delay time for a set of hydrocarbon–containing mixtures. The experiments have been performed in collaboration with Lille University, PC2A laboratory, in rapid compression machine (RCM) equipped with a specially developed electrode system. Chapter 6 presents a preliminary numerical analysis of the ignition by a nanosecond discharge. Experimentally measured

deposited energy and the ideas of the discharge spatial structure were taken to estimate the volumetric deposited energy in the discharge. Typical electric fields were used to estimate the production of oxygen atoms. Strongly diluted (76% of Ar) stoichiometric n–butane:oxygen mixture has been chosen for numerical analysis. It was shown that significant modification of a cool flame can be achieved under the action of the discharge due to initiation of reactions with atomic oxygen; even small additions of O–atoms, $< 1\%$ shift the ignition delay time by a few order of magnitude. This fact proves that the nanosecond SDBD discharge, studied in Chapters 4–5, can be extremely efficient for a multi–point ignition of combustible mixtures at elevated gas densities.

Chapter 7 presents the high pressure high temperature reactor built recently at Laboratory for Plasma Physics. The HPHT reactor allows work in the pressure range 10 Torr–12 bar at initial gas temperatures 300–700 K. The initiation of combustion of lean H_2:air mixtures, $ER = 0.5 - 0.6$, by nanosecond surface dielectric barrier discharge (nSDBD) was studied experimentally at high initial pressures $P = 3 - 6$ bar. The discharge was studied in different gas mixtures for the pressure range $1 - 12$ bar. The ignition was initiated by two different discharge modes: streamer or filamentary nSDBD. The influence of the discharge structure and energy deposition on the ignition is demonstrated. Three regimes of multi-point ignition were observed: ignition with a few kernels, quasi-uniform ignition along the edge of high voltage electrode and ignition along the plasma channels. The velocities of flame propagation are analyzed. The minimum ignition energy of the discharge and ignition delay time of combustion have been measured and analyzed with the help of kinetic numerical modeling.

Chapter 8 describes the results of analysis of role of $O(^1D)$ in plasma–assisted combustion including gas mixtures with hydrocarbons. At relatively low initial temperatures, the effect of electronically excited $O(^1D)$ atoms on the oxidation and reforming of combustible mixtures can be quite significant due to the high rates of reactions of $O(^1D)$ atoms with hydrogen and hydrocarbon molecules and low rates of the reactions of atomic particles in the ground electronic state. It should be noted the important role of the reactions of $O(^1D)$ atoms in the process of hydrocarbons dissociation in fuel–air mixtures. This conclusion is particularly important because it allows the assumption that the uncertainty of the cross sections of electron impact dissociation of hydrocarbons will not influence significantly production of active particles in hydrocarbon–air plasmas.

The last, 9^{th} Chapter contains a brief review of state of the art in plasma assisted ignition and combustion. The experimental data on modification of ignition and combustion of different gas mixtures be nanosecond discharges, obtained by different authors are summarized on a single “pressure–temperature” plot and in the Table listing the composition of the gas mixtures, allowing comparative analysis of parameters of PAI/PAC experiments in different laboratories. The idea of the development of a special kinetic mechanism of plasma assisted ignition is discussed on the basis of numerical modeling using two standard combustion mechanisms, GRI and Combustion Chemistry Center, C^3. A set of conditions necessary to consider an experiment on combustion triggered by plasma as a kinetic experiment is formulated.

Chapter 1

Capillary nanosecond discharge at high energy release ($> 1eV/mol$): O-atoms density by actinometry at nanosecond time scale.

1.1 Introduction

Nanosecond discharges comprising fast ionization waves (FIW) have been intensively studied over the last few decades. These discharges are initiated by nanosecond high-voltage pulses in long tubes (with the distance between electrodes much greater than the tube diameter) at relatively low gas pressures, typically $1 - 100$ Torr. In most studies [1], the FIW discharges are initiated by $1 - 10$ kV pulses of positive or negative polarity in tubes a few cm in diameter and tens of cm in length. Similar to streamer discharges, the main physical processes responsible for ionization in the FIW front are ionization by electron impact and photoionization. A distinctive feature of FIWs is the presence of high energy electrons in the FIW front [2]. These electrons provide uniform pre-ionization in the FIW front, leading to spatially uniform development of the discharge [3].

It should be noted that the FIW initiates at the high-voltage electrode for both positive and negative polarity high-voltage pulses. Current conservation is assured by the displacement current. The velocity of the FIW front propagation is a few cm/ns, depending upon the pressure and the tube diameter [4]. A kinetic description of FIWs has been developed over the last 15 years [5], focusing on the electron density, electron energy distribution function (EEDF) and the production of chemically active species (radicals and excited molecules).

Nanosecond capillary discharges have been studied for years, mainly for potential laser and X-ray applications [6]. A brief review of the study of FIWs in capillary discharges can be found in [1] or in earlier Russian reviews [7]. These discharges were initiated in capillary tubes $1-3$ mm in diameter, using higher voltage amplitudes (a few tens-hundreds of kV), with pulse durations of a few nanoseconds to hundreds of nanoseconds.

The high energy density in the discharge leads to significant kinetic transformations on the gas media. The typical energy density of an FIW in tubes of a few cm in diameter is of the order of $10^{-3} - 10^{-4}$ J/cm^3 for a voltage amplitude 10 kV [5]. This causes high-energy but low density excitation of atoms and molecules: the typical molecular oxygen dissociation degree reported is about 10^{-3} [8]. Decreasing the tube diameter, at constant voltage parameters, does not change dramatically the current through the tube [9] but results in higher current and energy densities. For a 10 kV, 20 ns pulse in a tube 1.5 mm in diameter and 80 mm in length and at gas pressure about 20 Torr, about 50% of the incident pulse energy is absorbed, giving a volumetric deposited energy of about 10^{-1} J/cm^3, or 1 eV/molecule.

It should be noted that, at conditions of high energy density, a fast temperature increase ($5 \cdot 10^{10}$ Ks^{-1}) is observed in the near afterglow of a nanosecond discharge in atmospheric air preheated to 1000 K in a 4 mm discharge gap [10] due to fast excitation of electronically excited nitrogen, followed by oxygen dissociation and de-excitation. The details of kinetics of fast gas de-excitation (fast gas heating) in air at electric fields of $100 - 1000$ Td are discussed in [11].

Over the last ten years, nanosecond discharges have been widely used for various applications: initiation and sustaining of combustion [12, 13, 14, 15] and air flow control [16]. Changes in electrode configurations, voltage pulse parameters, gas mixtures etc. causes significant changes in the kinetics. This explains the renewed interest in the fundamental study of nanosecond discharges and their early afterglow [10, 17].

Since FIWs at moderate pressures allow comprehensive measurements [1, 5, 17] of the electric field, electron density, electric current, and deposited energy, they are very promising objects for the kinetic study of nanosecond discharges. Oxygen atoms, being the primary active radicals in discharges in O_2-containing mixtures, play a key role in the discharge chemistry. The O-atoms can be produced form O_2 by two major reaction pathways: direct electron impact dissociation or via the reaction with electronically excited nitrogen molecules [10, 11, 18]. The main aim of two following chapters is to analyze the time-resolved absolute density of O-atoms in the early afterglow of a nanosecond discharge in synthetic air, over the time interval 200 ns-2 μs, in a capillary discharge tube at high energy density and high gas temperature.

1.2 Experimental setup

The discharge that was used with respect to these requirements, is a repetitively pulsed capillary nanosecond discharge, initiated in a quartz tube containing flowing synthetic air of 13 to 30 mbar pressure. The tube has a 1.5 mm inner diameter, 3.4 mm outer diameter, and is 80 mm in length. At both ends of the tube are two metal conical electrodes connected to two cables. One 25 m cable - later denoted as the High Voltage (HV) cable - connects the HV electrode to a FID FPG-10MKS20 high voltage generator, while the other 100 m cable has an open termination, and is used to obtain a reflected pulse 1 μs after the discharge, for purpose of emission spectroscopy diagnostics.

Two back current shunts, placed 12.5 m before and after the discharge, are used to measure the current and the voltage of the pulses that propagate in the cables. Additionally, a capacitive probe, located above the discharge tube, and which can be slid along a rail positioned in the grounded screen surrounding the discharge assembly, is used to obtained a measurement of the local electric field in the discharge. These measurements also provide a precise estimation of the energy that is deposited in the discharge.

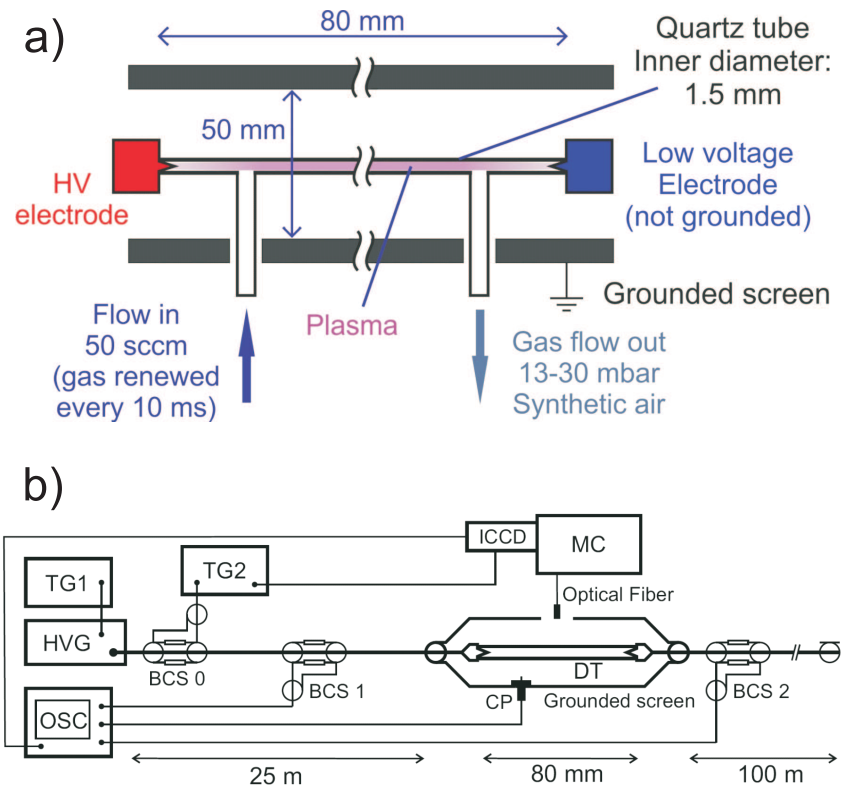

Figure 1.1: Top: scheme of the discharge setup. bottom: complete experimental setup for electrical and spectrometric measurements. DT - Discharge tube; BCS - Back Current Shunt; TG - Triggering generator; HVG - High Voltage Generator; CP - Capacitive Probe; ICCD - Intensified CCD Camera; OSC - Oscilloscope; MC - Monochromator.

A scheme of the discharge setup, and a scheme of the complete experimental setup for actinometry measurements are presented in Fig. 1.1.

1.3 Temperature and role of O atoms in the fast gas heating kinetics

In this experiment, fast gas heating is evidenced by rotational spectroscopy measurements of the gas temperature, based on the $N_2(C^3\Pi_u, v = 0) \rightarrow N_2(B^3\Pi_g, v = 1)$ transition. The results are shown in Fig. 1.2.

Spectra are acquired upon arrival of the subsequent pulses coming to the discharge. The absence of strong emission between the pulses ensures that direct electron impact is the main excitation mechanism during the pulses, and hence the obtained spectra correspond to the rotational temperature of the ground state of nitrogen, which is in equilibrium with the translational temperature of the gas due to the sufficient amount of collisions during the lifetime of the emitting state.

Now, it should be noted that energy deposition measurements show that about 1 eV per molecule are deposited in the discharge after all three pulses. Mainly because of this high energy, model[11] predicts a high degree of O_2 dissociation in the discharge,

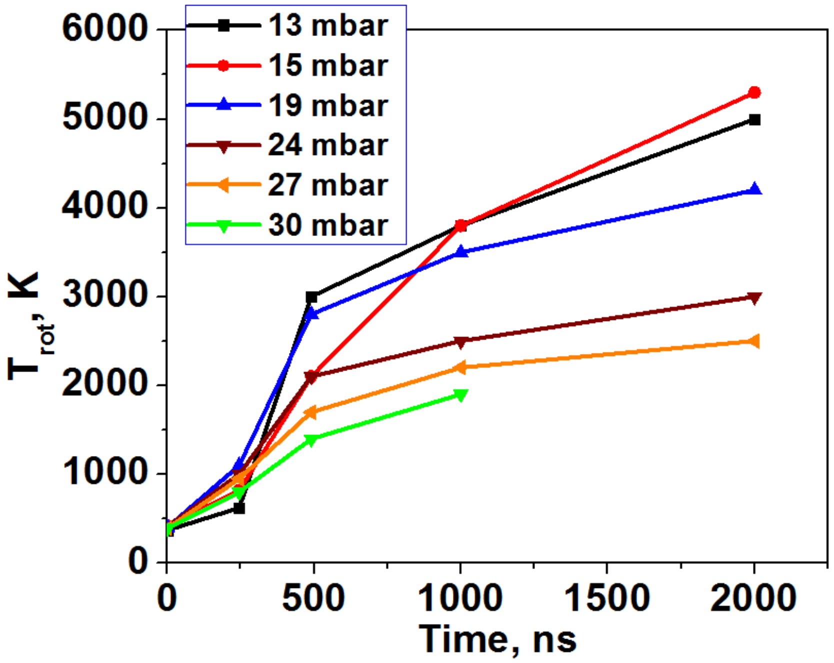

Figure 1.2: Rotational temperature measurements, based on emission spectroscopy of the second positive system of nitrogen.

with up to complete dissociation at the lower pressures, after the three pulses. This high dissociation degree will strongly impact the kinetics of fast gas heating, mainly through reactions such as

$$N_2^* + O \rightarrow NO(v) + N(^2D) \tag{1.1}$$

which have a higher yield to fast gas heating, than reactions involving dissociation of O_2 molecules.

In other words, O atoms play a critical role in the reaction pathways of fast gas heating, and their abundance might drastically change the efficiency of the fast conversion of deposited energy to gas thermal energy. In this respect, O atoms are a key parameter that needs to be measured in order to validate any kinetic model describing fast gas heating in air.

1.4 Actinometric measurement of atomic oxygen concentrations

In order to measure O atoms concentrations, we have developed a diagnostic method based on actinometry of atomic oxygen, with backup from another detailed 0D kinetic model that uses the ZDPlasKin[19] framework.

The actinometric measurement consists in the comparison of the intensity of two emission lines, one being the 844.6 nm line corresponding to the $O(3p^3P) \rightarrow O(3s^3S)$ atomic transition, and the other one corresponding to the 750.4 nm emission of the $Ar(2p_1) \rightarrow Ar(1s_2)$ transition. A scheme of the excitation mechanism is given by Fig. 1.3.

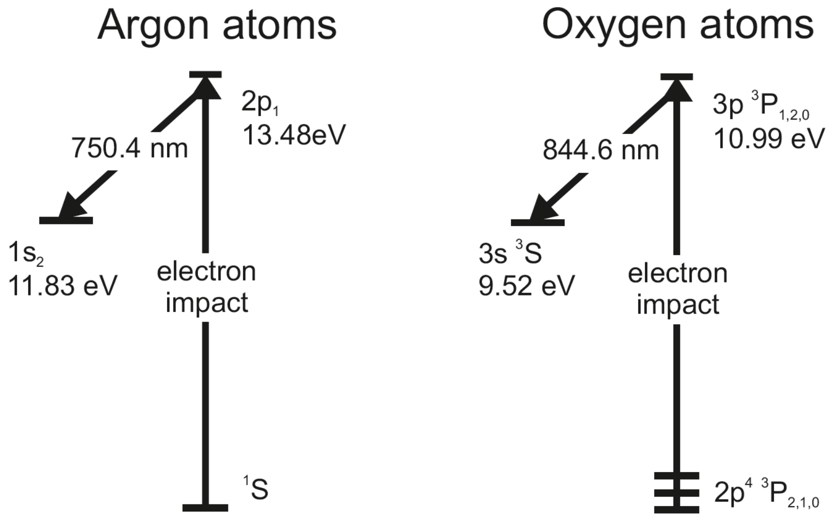

Figure 1.3: excitation scheme of Argon (left) and Oxygen (right) atoms from their respective ground states. The proximity of the fluorescence wavelengths ensures a more precise calibration procedure of the optical system.

The classical actinometry principle supposes:

1. direct electron impact excitation as the only population mechanism of both radiative states under study
2. exact or highly similar excitation threshold for both states
3. similar behavior of the excitation cross sections with respect to electron energy
4. radiative decay as the only depopulation mechanism of the excited states.

However, in the case of our experiment, these requirements are at best partially fulfilled. Indeed, it has been pointed out that great care must be taken of other processes like dissociative or stepwise excitation[20]; excitation thresholds differ by about 2.5 eV, and the shape of the excitation cross sections with respect to electron energy is indeed slightly different. Finally, at the pressures of our experiments, quenching becomes the main depopulation mechanism, and in addition, quenching coefficients are not always known at the temperatures of a few thousand K, that are reached in the afterglow of our discharge.

In order to remedy to these problems, a detailed kinetic model was built on the basis of the ZDPlasKin solver. This model aims to predict the concentrations of all species involved in the population and depopulation processes of the excited states under study, so as to be able to take into account all these processes in the interpretation of the experimental data from actinometry. The scheme of Kossyi [18] was completed with reactions involving the $O(3p^3P)$ state, as well as Argon atoms, ions, and 2 Argon excited states. The necessary cross section data was taken from the literature [21, 22, 23, 24, 25, 26]

The observed emission lines intensity is shown in Fig. 1.4. Now, we can write the following equations for population and depopulation of Argon and oxygen excited states:

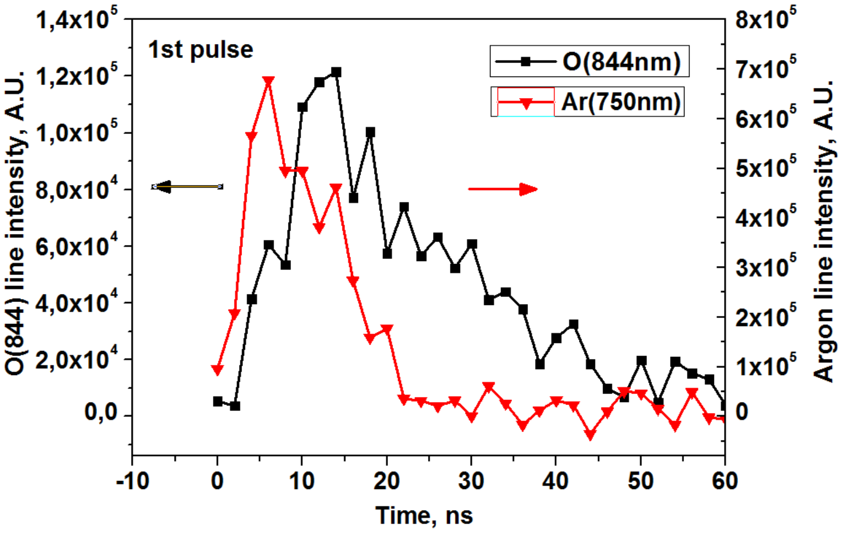

Figure 1.4: intensity of the emission lines of the O(3p^{3}P) and Ar(2p$_1$) states, as a function of time, during the first pulse.

$$\frac{d[O^*]}{dt} = k_e^O n_e[O] + k_{de}^O n_e[O_2] + k_e^{O(^1S)} n_e[O(^1S)] + k_e^{O(^1D)} n_e[O(^1D)] - \frac{[O^*]}{\tau_{O^*}} - [O^*]\Sigma_i k_{Q,i}^{O^*}[Q_i] \quad (1.2)$$

$$\frac{d[Ar^*]}{dt} = k_e^{Ar} n_e[Ar] - \frac{[Ar^*]}{\tau_{Ar^*}} - [Ar^*]\Sigma_i k_{Q,i}^{Ar^*}[Q_i] \quad (1.3)$$

Where k_e^X is the excitation rate constant for species X , k_{de}^O is the dissociative excitation rate constant for molecular oxygen, $k_{Q,i}^{X^*}$ is the quenching rate constant for species X^* by species Q_i, and n_e is the electron density. Reorganizing these equations and dividing (1.2) by (1.3), one gets:

$$\frac{\frac{d[O^*]}{dt} + \frac{[O^*]}{\tau_{O^*}} + [O^*]\Sigma_i k_{Q,i}^{O^*}[Q_i]}{\frac{d[Ar^*]}{dt} + \frac{[Ar^*]}{\tau_{Ar^*}} - [Ar^*]\Sigma_i k_{Q,i}^{Ar^*}[Q_i]} = \frac{k_e^O[O] + k_{de}^O[O_2] + k_e^{O(^1S)}[O(^1S)] + k_e^{O(^1D)}[O(^1D)]}{k_e^{Ar}[Ar]} \quad (1.4)$$

now, the correspondence between excited state densities and collected emission intensity is written as follows:

$$I_{844} = c_{844}\frac{[O^*]}{\tau_{O^*}} \quad (1.5)$$

with a similar equation for Ar atoms. Finally, we have the following equation for O atoms density, as calculated from actinometry:

$$\begin{aligned}[O] = &\frac{k_e^{Ar}[Ar]}{k_e^O}\,\frac{\tau_{O^*}}{\tau_{Ar^*}}\,\frac{c_{750}}{c_{844}}\,\frac{\frac{dI_{844}}{dt} + \frac{I_{844}}{\tau_{O^*}} + I_{844}\Sigma_i k_{Q,i}^{O^*}[Q_i]}{\frac{dI_{750}}{dt} + \frac{I_{750}}{\tau_{Ar^*}} + I_{750}\Sigma_i k_{Q,i}^{Ar^*}[Q_i]} \\ &- \frac{k_{de}^O[O_2]}{k_e^O} - \frac{k_e^{O(^1S)}[O(^1S)]}{k_e^O} - \frac{k_e^{O(^1D)}[O(^1D)]}{k_e^O}\end{aligned} \quad (1.6)$$

with the first term on the right hand side corresponding to the experimental intensity ratio, corrected for quenching, radiative lifetimes, light collection efficiency, derivatives

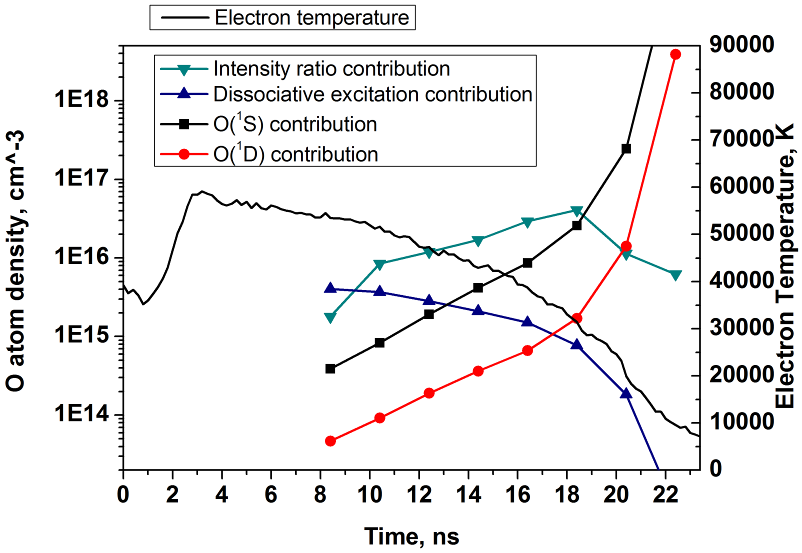

Figure 1.5: experimental data corrected for all needed parameters, and contributions of all secondary processes.

and difference in the excitation cross sections. The second term corresponds to dissociative excitation, and the third and the fourth to excitation through O(^{1}S) and O(^{1}D) metastables, respectively.

All needed rate coefficients are calculated through ZDPlasKin. However, it should be noted that, for excitation through metastables, only a set of data with limited validity was

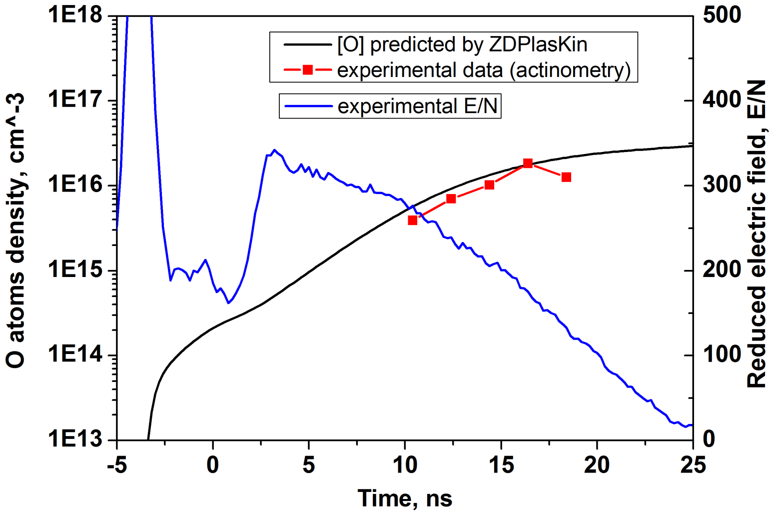

Figure 1.6: O atoms density, as predicted by the ZDPlasKin model, and as measured by actinometry. The reduced electric field is plotted to help localize the data in time.

found in the literature, as, to the best of our knowledge, no experimental measurement of the needed cross sections was made available. Thus, contributions from these processes are subject to caution.

In Fig. 1.5, contributions from all 4 terms discussed above are shown. It can be seen that, after 18 ns, the contribution from metastables jumps to very high values with no physical meaning. This is due to the fact that the excitation cross section for the O(3p^{3}P) state becomes very low; and thus, a small error in the reduced electric field at that point would result in a big difference in the values of all contributions, because the rate constant for excitation of O(3p^{3}P) from the ground state appears in all four contributions. For similar reasons, the point at 8 ns is rejected. This leaves four usable points, and the final O atoms concentration, as a function of time, is compared to the prediction of the ZDPlasKin model in Fig. 1.6. It can be seen that reasonably good agreement is attained between experiments and calculations, giving good confidence in the model.

1.5 Conclusions

A reasonable agreement between the experimental data and results of numerical modeling validates th main statement concerning the capillary discharge at moderate pressures: a capillary nanosecond discharge developing at high electric fields is a very efficient source of atomic species. Additional production of atomic oxygen should be efficient in gas mixtures where excited species can be quenched by oxygen molecules with the following dissociation. This is true about air and in general about N_2:O_2 mixtures, where nitrogen triplets are able to store enough energy for oxygen dissociation. The next chapter is devoted to TALIF measurements of O-atoms density in the afterglow of the capillary discharge, on sub-microsecond and microsecond time scale.

Bibliography

[1] Vasilyak L M, Kostyuchenko S V, Kudryavtsev N N and Filyugin I V 1994 Fast ionisation waves under electrical breakdown conditions Phys. Usp. 37 247-68

[2] Babich L P, Loiko T V and Tsykerman V A 1990 High-voltage nanosecond discharge in a dense gas at a high overvoltage with runaway electrons Sov. Phys. Usp. 33 521-40

[3] Anikin N B, Zavialova N A, Starikovskaia S M, and Starikovskii A Yu 2008 Nanosecond-Discharge Development in Long Tubes IEEE Trans. on Plasma Science 36 902-3

[4] Asinovsky E I, Lagarkov A N, Markovets V V and I. M. Rutkevich I M 1994 On the similarity of electric breakdown waves propagating in shielded discharge tubes Plasma Sources Sci. Technol. 3 556-63

[5] Starikovskaia S M, Anikin N B, Pancheshnyi S V, Zatsepin D V and Starikovskii A Yu 2001 Pulsed breakdown at high overvoltage: development, propagation and energy branching Plasma Sources Sci. Technol. 10 344-55

[6] Zoran V I, Ganciu M, Pointu A M, Collins C B and Popescu I Iovitz 1997 X-ray generation in inverse capillary discharges for pumping Hyperfine Interactions 107 415-30

[7] Asinovskii E I, Vasilyak L M and Markovets V V 1983 Wave breakdown of gas filled gaps. I. Fast stage of the breakdown High Temperatures 21 371-81 (In Russian); Asinovskii E I, Vasilyak L M and Markovets V V 1983 Wave breakdown of gas filled gaps. II. Breakdown in distributed systems High Temperatures 22 577-90 (In Russian)

[8] Starikovskaia S M 1995 On the energy branching in the high voltage nanosecond discharge. Dissociation of O2 Fizika Plazmy 21 541-548 (In Russian)

[9] Mintoussov E I, Pendleton S J, Gerbault F G, Popov N A and Starikovskaia S M 2011 Fast gas heating in nitrogen-oxygen discharge plasma: II. Energy exchange in the afterglow of a volume nanosecond discharge at moderate pressures J. Phys. D: Appl. Phys. 44 285202

[10] Rusterholtz D L, Lacoste D A, Stancu G D, Pai D Z and Laux C O 2013 Ultrafast heating and oxygen dissociation in atmospheric pressure air by nanosecond repetitively pulsed discharges J. Phys. D: Appl. Phys. 46 464010

[11] Popov N A 2011 Fast gas heating in a nitrogen-oxygen discharge plasma: I. Kinetic mechanism J. Phys. D: Appl. Phys. 44 285201

[12] Starikovskiy A Yu and Aleksandrov N L 2013 Plasma-assisted ignition and combustion Progress in Energy and Combustion Science 39 61-110

[13] Adamovich I V, Choi I, Jiang N, Kim J-H, Keshav S, Lempert W R, Mintusov E I, Nishihara M, Samimy M and Uddi M 2009 Plasma assisted ignition and high-speed flow control: non-thermal and thermal effects Plasma Sources Sci. Technol. 18 034018

[14] Sun W, Won S H and Ju Y 2014 In situ plasma activated low temperature chemistry and the S-curve transition in DME/oxygen/helium mixture Combustion and Flame (available online, http://dx.doi.org/10.1016/j.combustflame.2014.01.028)

[15] Bak M and Cappelli M A 2012 A Simulation of the Effects of Varying Repetition Rate and Pulse Width of Nanosecond Discharges on Premixed Lean Methane-Air Combustion Journal of Combustion 2012 137653

[16] Rethmel C, Little J, Takashima K, Sinha A, Adamovich I V and Samimy M 2011 Flow Separation Control Using Nanosecond Pulse Driven DBD Plasma Actuators International Journal of Flow Control 3 213-32

[17] Takashima K, Adamovich I V, Xiong Zh, Kushner M J, Starikovskaia S M, Czarnetzki U and Luggenhoelscher Dirk 2011 Experimental and modeling analysis of fast ionization wave propagation in a rectangular geometry Physics of Plasmas 18 083505

[18] Kossyi I A, Kostinsky A Y, Matveev A A and Silakov V P 1992 Kinetic scheme of the non-equilibrium discharge in nitrogen-oxygen mixtures Plasma Sources Sci. Technol. 1 207-20

[19] S. Pancheshnyi, B. Eismann, G.J.M. Hagelaar, L.C. Pitchford, computer code ZDPlasKin (University of Toulouse, LAPLACE, CNRS-UPS-INP, Toulouse, France, 2008)

[20] Fuller N C M, Malyshev M V, Donnelly V M, and Herman I P. Characterization of transformer coupled oxygen plasmas by trace rare gases optical emission spectroscopy and langmuir probe analysis. *Plasma Sources Sci. Technol.*, 9:116127, 2000

[21] Laher R R and Gilmore F R. Updated excitation and ionization cross sections for electron impact on atomic oxygen. *J. Phys. Chem. Ref. Data*, 19:277, 1990

[22] Puech V and Torchin L. Collision cross sections and electron swarm parameters in argon. *J. Phys. D: Appl. Phys.*, 19:2309, 1986

[23] Schulman M B, Sharpton F A, Chung S, Lin C C, and Anderson L W. Emission from oxygen atoms produced by electron-impact dissociative excitation of oxygen molecules. *Phys. Rev. A*, 32(4):2100, 1985

[24] Gordillo-Vazquez F J and Kunc J A. Diagnostics of plasmas with substantial concentrations of atomic oxygen. *Phys. Rev. E*, 51:6010, 1995

[25] Bittner J, Kohse-Höinghaus K, Meier U, and Just T. Quenching of two-photon-excited H(3s, 3d) and O(3p $^3P_{2,1,0}$)atoms by rare gases and small molecules. *Chem. Phys. Lett.*, 143:6, 1988.

[26] Sadeghi N, Setser D W, Francis A, Czarnetzki U and Döbele H F. Quenching rate constants for reaction of Ar(4p'$[1/2]_0$, 4p$[1/2]_0$ and 4p$[3/2]_2$ and 4p$[5/2]_2$) atoms with 22 reagent gases. *J. Chem. Phys.*, 115:3144, 2001

Chapter 2

O-atoms density by TALIF at sub-microsecond time scale in the capillary discharge.

2.1 Details of the TALIF measurement of O atom density

In the two–photon absorption laser induced fluorescence (TALIF) technique atoms are excited to a state A by absorption of two photons from probing laser beam at wavelength λ_L, and then de–excite to a state B by emitting a third photon at wavelength λ_F. The probability to absorb two photons is relatively low; however, for species such as O atoms, all dipole–permitted excitations from the ground state are in the vacuum ultra violet (VUV) range [1], thus making any one–photon LIF diagnostic of these species experimentally challenging. In these cases, TALIF is a good alternative.

The energy levels used in this study are shown in Fig. 2.1. Let us consider the population and de–excitation mechanisms for O atoms in the excited $3p^3P$ state in the presence of intense 225.58 nm laser radiation (all wavelengths are given in atmospheric pressure air). The fluorescence to the $3s^3S$ state at 844.6 nm is observed [2]. If the energy of the incident UV laser radiation is sufficiently low, secondary "unwanted" processes can be neglected. The three main secondary processes are photo–ionization, depletion of the ground state by optical pumping and amplified stimulated emission (ASE).

Photo–ionization corresponds to the absorption of one more photon from the probing laser radiation by the 3p 3P excited state [3], resulting in the ionization of the excited O atom. This loss mechanism has a linear dependence on the laser energy, and the $O(3p^3P)$ atom density. Depletion of the O atom ground state by optical pumping is an artificial modification of the naturally present ground state O atom density, which results in a decrease of the TALIF excitation rate. Finally, ASE is the stimulated emission of fluorescence in the direction of the laser beam. Indeed, as the atoms are excited along the laser beam path, the fluorescence light emitted in the direction of the laser beam can produce stimulated emission from the $O(3p^3P)$ atoms because of the significant length of the highly populated excitation volume [4].

In addition to these three main processes, it should be noted that although the ab-

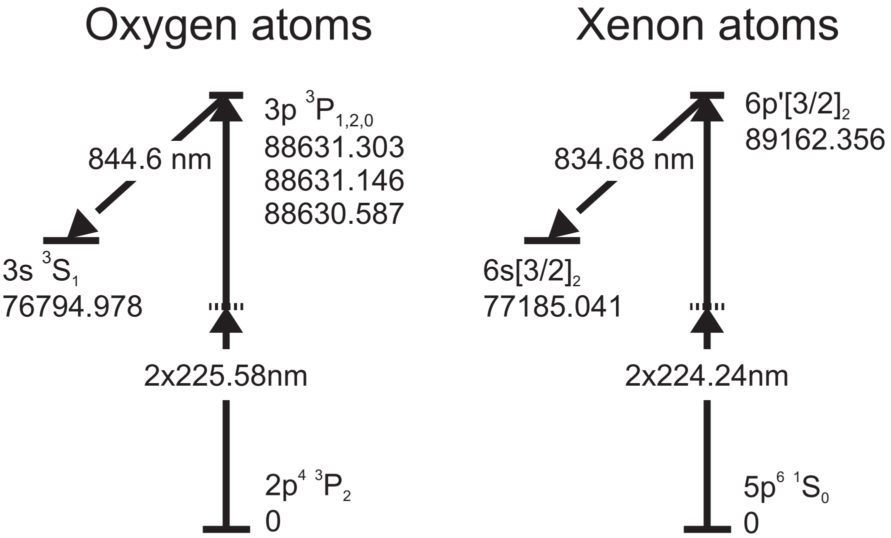

Figure 2.1: Energy diagram of the chosen TALIF excitation and fluorescence levels for O and Xe atoms, allowing absolute calibration of the O atom measurement [2]. The transition energies are given in vacuum wavenumbers taken from [1, 9]; the transition wavelengths are given in atmospheric pressure air.

sorption of 226 nm radiation by ground state O_2 is only possible through the very weak Herzberg continuum [5, 6], highly vibrationally excited O_2 can absorb light at this wavelength through the Schumann–Runge bands, leading to photo–dissociation [7]. The rate of this process increases linearly with the laser energy, and with the density of the relevant absorbing vibrationally excited O_2 states.

In the absence of the four mentioned processes (at low laser intensity), the dependence of the collected TALIF signal on laser energy will be quadratic [2, 8]. At higher laser intensity these secondary processes will cause deviations from quadratic behaviour. However, each of the four processes mentioned will become significant above a different specific laser intensity, which may also depend on the discharge parameters. Therefore it is important to establish that, for each TALIF measurement, we are working below the laser intensity threshold where deviation from quadratic behaviour occurs. All TALIF measurements in this work were made below that threshold, in the so–called "linearity regime".

In this work, the TALIF calibration scheme proposed by Niemi et al.[2] was used, in which the signal from the TALIF excitation of O atoms is compared to a similar experiment with Xenon atoms, in the same vacuum vessel. See the excitation scheme in Fig. 2.1.

In the linearity regime, the time variation of the density of excited O atoms is described by the following rate equation:

$$\frac{d[\mathrm{O}^*](t,\vec{r})}{dt} = R_L(t,\vec{r},\nu_L) \cdot \left[\mathrm{O}(2\mathrm{p}^4\ {}^3\mathrm{P}_2)\right](t,\vec{r}) - K(\mathrm{O}) \cdot [\mathrm{O}^*]\,(t,\vec{r}) \qquad (2.1)$$

where $[\mathrm{O}^*](t,\vec{r})$ is the $\mathrm{O}(3\mathrm{p}^3\mathrm{P})$ density, $[\mathrm{O}(2\mathrm{p}^4\ {}^3\mathrm{P}_2)](t,\vec{r})$ is the $J = 2$ state of the ground

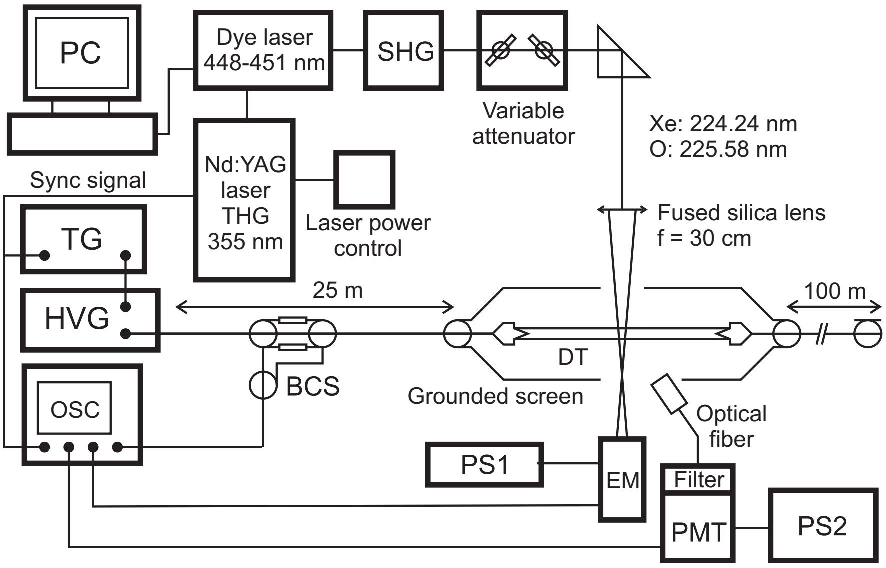

Figure 2.2: Experimental setup for the TALIF measurement. SHG/THG: Second/Third harmonic generation; TG: Triggering generator; HVG: High voltage generator; OSC: Oscilloscope; BCS: Back current shunt; DT: Discharge tube; EM: Energy meter; PS: Power supply; PMT: Photomultiplier; PC: Computer.

state O atom density which is probed by TALIF radiation, $R_L(t, \vec{r}, \nu_L)$ is the TALIF excitation rate, ν_L is the laser centre wavelength, $K(\mathrm{O}) = A(\mathrm{O}) + \sum_i k_i^{\mathrm{O}}[\mathrm{Q_i}]$ is the total removal rate of O^*, with $A(\mathrm{O})$ the total optical de–excitation rate of the $\mathrm{O(3p^3P)}$ state, $[\mathrm{Q_i}]$ the density of quenching partner i and k_i^{O} the corresponding quenching rate constant. The considered quenching partners are $\mathrm{N_2}$, $\mathrm{O_2}$ and O atoms. $K(\mathrm{O})$ is assumed to be constant across the TALIF excitation volume.

The excited O atom density after the laser pulse, assuming that the O atom density varies slowly in time compared to the TALIF excitation rate, and does not vary in space across the TALIF excitation volume, is expressed as follows:

$$[\mathrm{O}^*](t, \vec{r}) = s \cdot [\mathrm{O}](t_0) \cdot \int_{t_0}^{t} R_L(t', \vec{r}, \nu_L) \cdot e^{K(\mathrm{O})(t'-t)} dt' \tag{2.2}$$

$$s = \frac{5}{\sum_J (2J+1) \cdot exp(-E_J/k_B T_g)}, \tag{2.3}$$

where s is the statistical factor taking into account that the $\mathrm{O(2p^4\ ^3P_2)}$ state represents only a fraction of the total O atom density, assuming a Boltzmann distribution with a gas temperature T_g of the three involved fine structure states $\mathrm{O(2p^4\ ^3P_{2,1,0})}$, E_J being the energy of each component. The time t_0 corresponds to the instant when the laser pulse arrives in the plasma, and defines the origin for the five delays, at which TALIF measurements were made.

The fluorescence signal from O^* is collected by an optical fibre and detected by a photomultiplier tube (PMT) with a narrow bandpass filter. The time- and laser wavelength–integrated PMT signal, SPMT, is equal to

$$S_{PMT}(t_0) = G \cdot \eta \cdot \chi \cdot e \cdot \frac{S_\Omega}{4\Pi} \frac{A_{jk}}{K(\mathrm{O})} \cdot s \cdot [\mathrm{O}](t_0) \cdot G^{(2)} \cdot \sigma^{(2)} \cdot I_L^2 \cdot \int_V \int_{t_0}^{t_0+T_d} \left(\frac{f_0(t, \vec{r})}{h\nu_{\mathrm{O}}} \right) dt dV \quad (2.4)$$

Here G is the PMT gain, η is the quantum efficiency at the fluorescence wavelength, χ is the transmission efficiency of the fibre and bandpass filter, e is the elementary charge, S is the collection solid angle, A_{jk} is the $3p^3P \rightarrow 3s^3S$ optical de–excitation rate, V is the TALIF excitation volume, $G^{(2)}$ is the photon statistical factor (equal to two) for the absorption of two photons from a chaotic radiation field [10], $\sigma^{(2)}$ the two-photon excitation cross section, I_L is the laser energy, T_d corresponds to the time needed for the TALIF signal to decay below the detection threshold, O is the central frequency of the O atom TALIF absorption, and $f_0(t, \vec{r}) = W(t, \vec{r})/I_L$ is the local, instantaneous laser power flux divided by the laser energy. $S_{PMT}(t_0)$ will thereafter be referred to as a relative TALIF data point.

The calibration scheme depicted in Fig. 2.1 works as follows. First, the air plasma is probed with laser light at 225.58 nm, resulting in TALIF radiation from $O(3p^3P)$ atoms at 844.6 nm, which is recorded by the detection system. Then, the plasma is switched off and the air in the discharge cell is replaced by xenon. When excited by 224.24 nm radiation to the Xe(6p'[3/2]$_2$) state, xenon emits light at 834.68 nm, that is, with excitation and fluorescence wavelengths very similar to those for O atoms. Finally, the relative TALIF data points S_{PMT} from O and Xe atoms are compared, and, as the xenon density is easily known from a pressure measurement, an absolute O atom density can be derived:

$$[\mathrm{O}](t_0) = [\mathrm{Xe}] \cdot \frac{\gamma(\mathrm{Xe})}{\gamma(\mathrm{O})} \cdot \frac{a(\mathrm{Xe})}{a(\mathrm{O})} \cdot \frac{1}{s} \cdot \frac{S_0(\mathrm{O}, t_0)}{S_0(\mathrm{Xe})}. \quad (2.5)$$

Here $\gamma(\mathrm{X}) = \eta_{\mathrm{X}} \cdot \chi_{rmX} \cdot \sigma^{(2)}(\mathrm{X})$, $a(\mathrm{X}) = A_{jk}(\mathrm{X})/K(\mathrm{X})$, and $S_0(\mathrm{X}, t_0) = S_{PMT}(\mathrm{X}, t_0) \cdot (\nu_X/I_L(\mathrm{X}))^2$. In (2.5), $a(\mathrm{O})$ depends on $[\mathrm{O}](t_0)$ through quenching on O atoms and on a decreasing concentration of O_2 molecules. We can write the following, assuming that dissociation of N_2 molecules is negligible:

$$K(\mathrm{O})(t) = A(\mathrm{O}) + k^{\mathrm{O}}_{\mathrm{O}_2}[\mathrm{O}_2](0) + k^{\mathrm{O}}_{\mathrm{N}_2}[\mathrm{N}_2] + \left(k^{\mathrm{O}}_{\mathrm{O}} - \frac{k^{\mathrm{O}}_{\mathrm{O}_2}}{2} \right) \cdot [\mathrm{O}](t) \quad (2.6)$$

$$K(\mathrm{O})(t) = K(\mathrm{O})_0 - \left(\frac{k^{\mathrm{O}}_{\mathrm{O}_2}}{2} - k^{\mathrm{O}}_{\mathrm{O}} \right) \cdot [\mathrm{O}](t) \quad (2.7)$$

$$\frac{1}{a(\mathrm{O})(t)} = \frac{K(\mathrm{O})(t)}{A_{jk}(\mathrm{O})} = \frac{1 - \beta \cdot [\mathrm{O}](t)}{a(\mathrm{O})_0} \quad (2.8)$$

$$[\mathrm{O}](t_0) = \frac{[\mathrm{O}](t_0)_0}{1 + \beta \cdot [\mathrm{O}](t_0)_0}, \quad (2.9)$$

where $\beta = (k^{\mathrm{O}}_{\mathrm{O}_2} - 2k^{\mathrm{O}}_{\mathrm{O}})/(2K(\mathrm{O})_0)$, $a(\mathrm{O})_0 = A_{jk}(\mathrm{O})/K(\mathrm{O})_0$, and $[\mathrm{O}](t_0)_0$ is obtained by replacing $a(\mathrm{O})$ by $a(\mathrm{O})_0$ in (2.5).

The room temperature quenching rate constants used in this work, as well as the natural lifetimes, are given in Table 2.1.

Constant	Value (10^{-10} cm^{3}s^{-1})	Reference
$k^{O}_{O_2}$	9.3	[11]
$k^{O}_{N_2}$	5.9	[11]
k^{O}_{O}	1.0	[12]
k^{Xe}_{Xe}	3.6	[2]
Coefficient	**Value (10^{-7} s^{-1})**	**Reference**
$A_{jk}(O)$	2.88	[2]
$A_{jk}(Xe)$	2.45	[2]

Table 2.1: Quenching rate constants for collision partners of interest, and Einstein coefficients for spontaneous emission for the O and Xe excited states.

It is important to note that, in (2.3) and (2.5), both the s and $a(O)$ factors depend on the gas temperature, because the quenching rate constants present in K may have a noticeable temperature dependence. Very few data exist in the literature about quenching of the $O(3p^3P)$ state at temperatures other than room temperature. Measurements of decay rates in flames have been made in the burnt gases of an $H_2/O_2/Ar$ flame at 27 mbar and 1350 K [13], a $CH_4/O_2/Ar$ flame at 53 mbar and 1750 K [14] and an H_2/O_2 flame at atmospheric pressure and 2500 K, with the help of 35 ps laser pulses [15]. In all these cases, the quenching was attributed mainly to H_2O, because of the high value ($4.9 \cdot 10^{-9}$ cm^{3}s^{-1}) of its quenching rate constant at room temperature [16], the very slow quenching by Ar atoms ($0.14 \cdot 10^{-10}$ cm^{3}s^{-1} [2]), and the fact that water and in some cases argon are the two major quenching partners in the burnt gases of the three flames that were studied. From these measurements, it can be concluded that $k^{O}_{H_2O}$ first decreases with temperature up to 1350 K to a value of about $2 \cdot 10^{-9}$ cm^{3}s^{-1}, and then stays approximately constant up to 2500 K.

The quenching rate of $O(3p^3P)$ by N_2 has also been measured in [14] at 1750 K to be $4.6 \cdot 10^{-10}$ cm^{3}s^{-1}, that is, only slightly lower than the room temperature value of $5.9 \cdot 10^{-10}$ cm^{3}s^{-1}. It should however be noted that the decay rate measurements leading to this value were close to the minimum decay rate that could be distinguished with the apparatus in [14].

In this Chapter, two different limiting assumptions will be compared for the behaviour of quenching rate coefficients with gas temperature. The first assumption corresponds to constant quenching rate coefficients with gas temperature. The second assumption corresponds to constant quenching cross sections with gas temperature; in this case, because of the increase in the gas mean particle velocity the quenching rate constants will rise, and we have:

$$k^{X}_{X}(T) = k^{X}_{X}(T_0) \cdot \sqrt{T/T_0} \tag{2.10}$$

where T_0 is the room temperature (300 K).

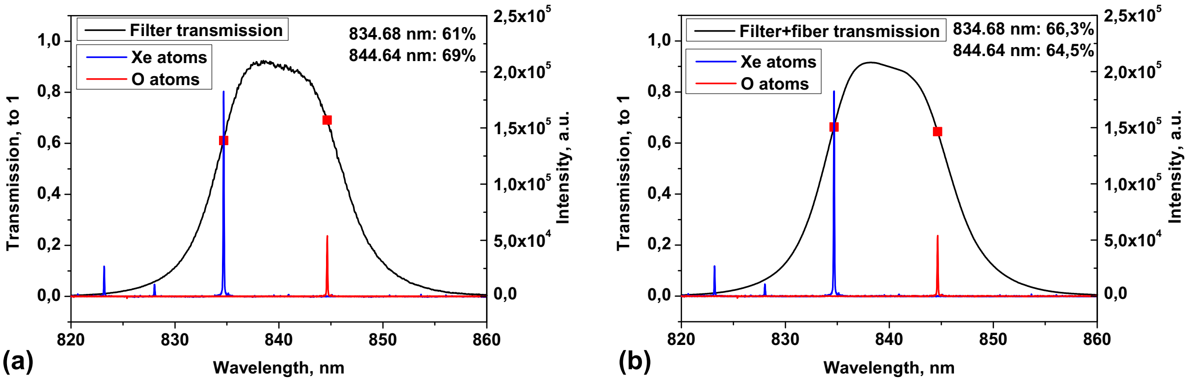

Figure 2.3: Transmission factor of (a) the filter illuminated by a distant point source; (b) the filter when illuminated by an optical fibre with fibre exit head close to the filter. The TALIF emission spectra of Xe and O atoms have been provided for reference.

2.2 Experimental setup

The details of the TALIF setup are given by Fig. 2.2. A 10 Hz pulsed frequency–tripled Nd:YAG laser (355 nm, Spectra Physics Quanta–Ray PRO Series LAB–170) was used to pump a dye laser (Sirah Cobra-Stretch CSTR–DA–24). Coumarin 2 (peak efficiency at 450 nm) in ethanol was used as the dye laser working medium. The dye laser radiation was frequency–doubled by a BBO crystal to obtain wavelengths around 225.58 nm (for O atoms) and 224.24 nm (for Xe atoms). The resulting beam was approximately 5 mm in diameter, with FWHM about 10 ns. The beam energy was measured by an amplified pyroelectric energy meter with sensitivity 1100 V/J, installed after the discharge tube. Energy measurements before the tube were also made on a regular basis during the experiments to monitor the power losses caused by the capillary walls. The laser energy inside the capillary was varied between 1 and 200 μJ by means of a variable attenuator that does not change the beam spatial profile.

The fluorescence light was collected by an optical fibre placed above the discharge, and then fed to one of two different detection systems, depending on the measurement that was performed. In the system used for quantitative measurements, the light was passed through a bandpass filter (840 nm centre wavelength, 13 nm FWHM) installed after the fibre. It was the recorded by a Hamamatsu R3896 red-sensitive photomultiplier tube (PMT) connected to a Lecroy WR64–Xi oscilloscope (600 MHz, 5 GS/s). In the system used for spectroscopy measurements, the light was fed directly through the entrance slit of an Andor Shamrock SR303i monochromator equipped with an Andor iStar DH734–18U–03 ICCD camera.

The transmission of the optical fibre and bandpass filter were measured using an absorption bench (comprising an Energetiq EQ–99 LDLS lamp and an Acton SP2500 spectrometer equipped with a Princeton PI–MAX 4 ICCD camera). The transmission of the bandpass filter is shown in Fig. 2.3. Fig. 2.3 a represents the transmission of the filter illuminated by a normally incident parallel beam of light, and figure Fig. 2.3 b shows a calculation of the estimated transmission of the filter illuminated by light coming from a fibre head situated a few cm before the filter. The shift of the transmission function to the

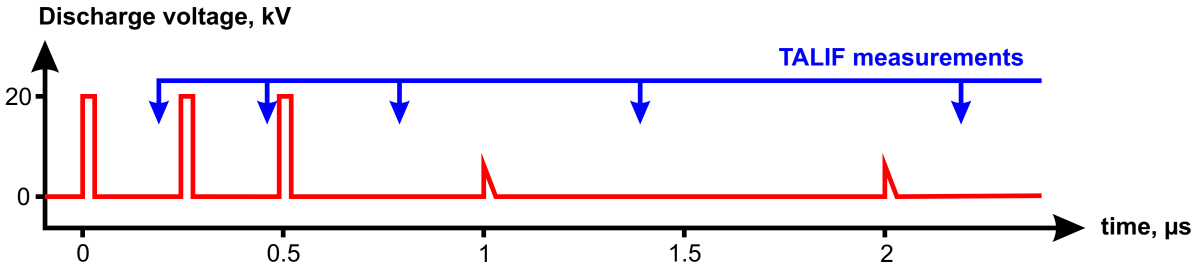

Figure 2.4: Voltage applied to the discharge electrodes in time, and temporal location of the TALIF measurements.

left in wavelength in Fig. 2.3 b is due to light arriving at the interference filter with a non-normal angle because of the proximity of the fibre exit head. This non–normal incidence reduces the optical path difference between any two reflections between the filter thin layers, and hence, the centre wavelength of the filter decreases. The angular distribution of light rays at the fibre exit head was measured by substituting the PI–MAX ICCD camera to the PMT and filter assembly, and used to calculate the curve on Fig. 2.3 b. The background-corrected TALIF fluorescence spectra of O and Xe atoms (measured using the Andor spectroscopy system described above) are provided for reference.

It can be seen that the secondary fluorescence lines of Xenon at 828.01 nm (corresponding to collisional transfer to the $6p[1/2]_0$ state and then de-excitation to the $6s[3/2]^0_1$ state) and 823.16 nm (corresponding to de–excitation $6p'[3/2]_2 \rightarrow 6s[3/2]^0_2$) [4] are suppressed by the interference filter to 0.66% of the signal from the 834.68 nm line. A unique O line at 844 nm occurs between 820 and 860 nm, ensuring that no other transition is observed by the PMT during all TALIF measurements. We used the calculated transmission efficiencies in Fig. 2.3 b to analyze our experimental results : 66.3% for the Xe line and 64.5% for the O line.

The synchronization scheme of the experiment is the following: the laser control unit fires the laser flashlamps at a 10 Hz repetition rate, and the flash lamp synchronization signal is used to trigger the FID high voltage pulse generator, with a delay adjusted by a BNC 575–4C pulse/delay generator. The discharge initiates with a given delay before the laser pulse (defined by the triggering of the Q-switch). This delay is varied from 190 to 2190 ns, with a jitter of 20 ns, with rare events at 200 ns due to occasional jitter in the HV nanosecond generator. The overall jitter in the delay is caused both by the HV generator, and the delay between the flash lamp and the laser Q–switch which has a 5 ns variability. A simplified timeline of the voltage applied to the discharge tube, obtained from back current shunt measurements, as well as the temporal location of the TALIF data sets, is shown in Fig. 2.4. Five measurements are made, at 190, 460, 790, 1390 and 2190 ns. All measurements are made as long as possible after each discharge pulse, while still having one point between each pair of subsequent pulses, in order to reduce the background signal from plasma-induced emission at wavelengths transmitted by the filter. The measurements at 190 and 460 ns are distinguished from the discharge emission because the variation in time of the latter is slow enough, so that the quickly decaying TALIF signal can be singled out easily above that slowly varying background.

Finally, a gas temperature measurement was performed by analysing the emission

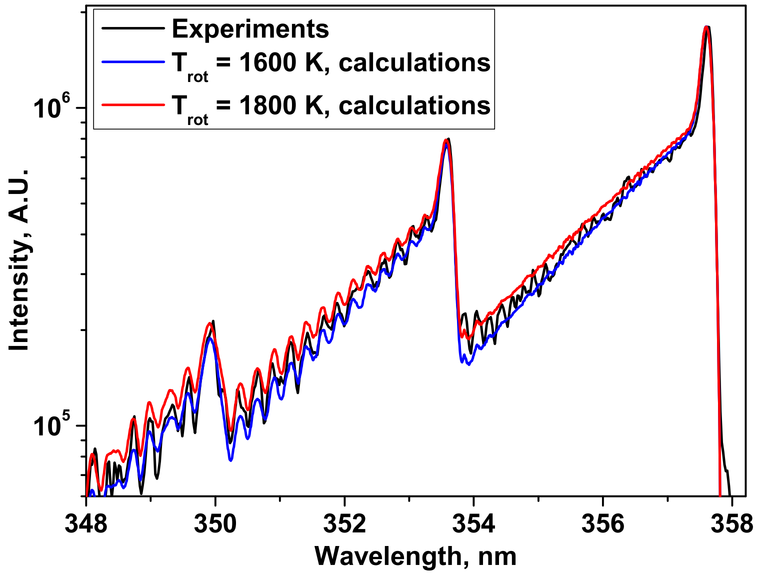

Figure 2.5: Experimental and calculated spectra of the $N_2(C^3\Pi_u$, v=0,1,2)→ $N_2(B^3\Pi_g$, v=1,2,3) transitions in an N_2:O_2= 4:1 mixture at 27 mbar, corresponding to the third discharge pulse (t = 490 ns).

spectrum of the $N_2(C^3\Pi_u$, v=0,1,2)→ $N_2(B^3\Pi_g$, v=1,2,3) transitions. The spectra were recorded, by means of an Andor Shamrock SR303i monochromator and an Andor DH734–18U–03 ICCD camera. The emission was measured for each of the five discharge pulses seen in Fig. 2.4, with 30 ns exposure time. Each time a discharge occurs, the $N_2(C^3\Pi_u)$ state is populated from the ground state by direct electron impact, and hence its rotational distribution is directly linked to that of the fundamental state [17]. To be sure that the emission resulting from indirect population mechanisms like collisional de–exitation of $N_2(A^3\Sigma_g^+)$, is at least one order of magnitude less intense than the emission caused by direct excitation by electron impact, the spectra were checked in between and during each discharge pulse. Electron impact excitation is active during the discharge, while indirect processes involving long–living species like $N_2(A^3\Sigma_g^+)$, happen both before and during the discharge with similar reaction rate.

The obtained spectra were fitted by the SPECAIR code [18] to get the gas temperature. Typical experimental and numerical spectra are shown in Fig. 2.5. The two proposed numerical spectra give an maximum limits of possible uncertainty of the temperature measurement of ±100 K in the case of the third pulse (t=490 ns). A gas temperature of 1700 ± 50 K is obtained from the spectra.

2.3 Results and discussion

The temporal variation of the gas temperature, measured by rotational spectroscopy of the second positive system of nitrogen, is plotted in Fig. 2.6. A sharp increase in temperature

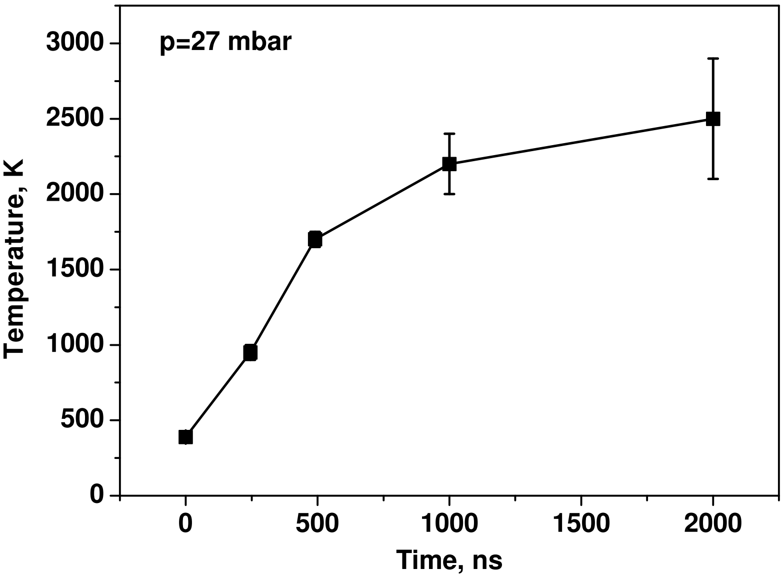

Figure 2.6: Gas temperature measured by rotational spectroscopy of nitrogen in capillary FIW discharge in synthetic air at 27 mbar.

after the first two pulses at 0 and 245 ns is clearly seen at 245 and 490 ns, with a subsequent temperature increase at $1 - 2$ μs caused by a slow energy release in the afterglow of the discharge. The increase in error with time is caused by the decrease in signal to noise ratio due to the small amplitude of the last reflected pulse. It should be noted that the characteristic gas dynamic expansion time, 60 μs, determined by the capillary tube geometry, is much longer than the 2 μs time scale of the experiments. Consequently, the gas density can be considered constant over the entire time interval under study, apart from the increase in the total number of particles caused by O_2 dissociation.

The high gas temperature in the discharge afterglow is taken into account in the TALIF measurement, through the s statistical factor, the quenching coefficients, and the Doppler broadening coefficients used to model the emission and excitation line widths for O atoms at 844.6 and 225.58 nm, respectively. The details are presented below.

Time-resolved fluorescence signals taken by the PMT are shown in Figs. 2.7 a and 2.7 b, for O and Xe atoms. The characteristic decay time of the O-atom emission, dominated by quenching, is expected to be as low as 1 ns in the case of constant cross sections with temperature. Consequently, the fluorescence time profile of O atoms closely reproduces the laser excitation time profile $\int_V R_L(t', \vec{r}, \nu_L) dV$, convoluted with the PMT response function. In Fig. 2.7 a, the observed exponential decay corresponds to a lifetime of 3.7 ns, which in turn yields quenching rate constants significantly (40%) lower at high temperature than at room temperature. This estimation is consistent with significant O_2 dissociation (O having a very weak self-quenching [12]) and the slight decrease in the N_2 quenching rate constant observed by Gasnot et al. [14]. This decay rate will be used as a lower bound, the actual total O(3p^{3}P) quenching rate being necessarily higher than this

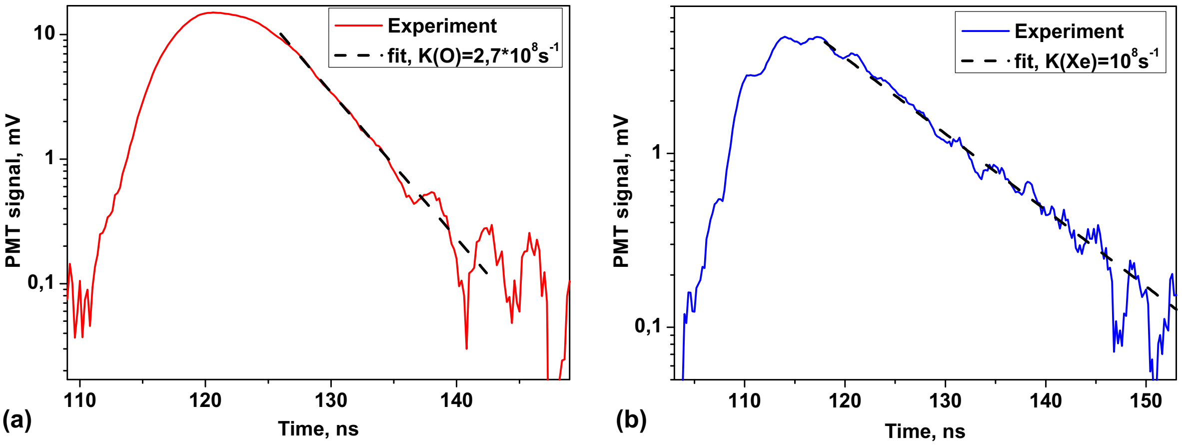

Figure 2.7: TALIF signal on photomultiplier tube in time, background subtracted. (a) Oxygen line, 27 mbar synthetic air, 2500 K, 2.2 μs after discharge; (b) xenon line, 8.5 mbar pure xenon, 293 K, no discharge.

value.

The laser pulse duration and the PMT response time are not short enough to allow the decay rates $K(O)$ to be extracted from the experimental O atom decay curves, therefore the quenching rates must be estimated from the coefficients in the literature. For Xe atoms, on the other hand, the decay rate is slow enough to be measured due to the lower pressure range (0.8 – 8.5 mbar). Unfortunately in this case the laser energy had to be kept very low (< 10 μJ for pressures up to 8 mbar) to avoid the presence of stimulated emission that would otherwise artificially increase the decay rate at the beginning of the emission curve, where the effect of noise was the smallest. Going below the threshold for ASE resulted in the usable part of the decay curve becoming too noisy for a precise, independent measurement of the xenon decay rates, especially at low pressures where there was less signal. It can nonetheless be noted that the chosen quenching rate from [2], $3.6 \cdot 10^{-10}$ cm^{3}s^{-1}, agrees well with the measured decay curves at relatively high Xe pressure (see Fig. 2.7 b).

It should also be noted that the PMT signal recorded when the laser is detuned from the TALIF resonance still exhibits a constant background level. This signal is due to the broadband (as checked with the monochromator) fluorescence of the quartz capillary. The intensity of the background signal depends only on the laser energy, and on the position of the laser beam relative to the capillary (location of the laser spot on the quartz walls). This fact was checked by pumping the capillary tube down to $2.5 \cdot 10^{-2}$ mbar, and firing the laser on and off TALIF resonance. The signal kept a constant value throughout that process. The time integrated intensity of the background fluorescence, as collected by the PMT through the narrow bandpass filter, was found to be proportional to $I_L^{0.66}$. This background fluorescence, taken with the laser detuned from the resonance, was subtracted from the TALIF signal taken when scanning the O atom absorption line.

The integrated in time fluorescence profiles are plotted against laser wavelength in Figs. 2.8 a and 2.8 b for O and Xe atoms. The background level was set to zero manually, thus eliminating the contribution from the capillary wall fluorescence. The data in both of

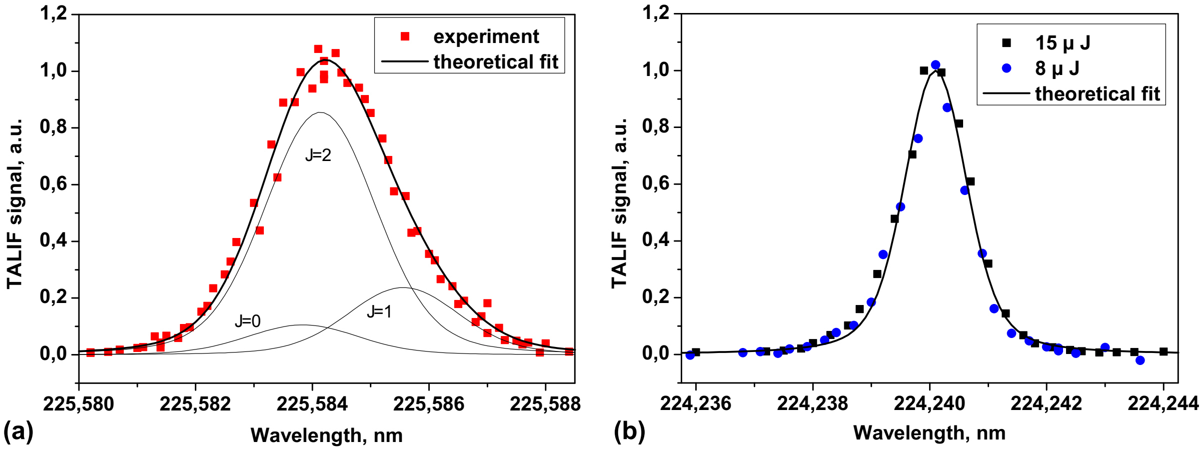

Figure 2.8: TALIF PMT signal integrated in time, plotted as a function of laser wavelength. (a) O atoms, 27 mbar synthetic air, 2500 K, 2.2 μs after breakdown, laser energy 108 μJ; (b) Xe atoms, 8.6 mbar pure xenon, 293 K, no breakdown, laser energy 15 and 8 μJ. The same scale in laser wavelength was used. Note the broad linewidth of the O line, due to the three fine–structure levels of O(3p^{3}P), and the broadening due both to the high temperature of the gas 2 μs after breakdown, and the lighter nature of O atoms compared to xenon atoms.

these graphs are taken below the saturation threshold, as will be shown later. The xenon absorption line was fitted with a Voigt profile, of Gaussian width 1 pm and Lorentzian width 0.46 pm (all widths are FWHM). In comparison, the xenon Doppler broadening is expected to be 0.24 pm. The rest of the broadening is caused by the laser linewidth, and the effective TALIF line profile. In the case of O atoms, a Gaussian width of 2.0 pm was used, with the same Lorentzian FWHM. The weighing of the three fine-structure components, plotted in thin lines in Fig. 2.8 a, was taken from [19], and the relative position of each component is from [9]. The good agreement of the fit suggests that the 2.0 pm Gaussian width is composed of 1 pm caused by the laser linewidth, and 1.73 pm corresponding to Doppler broadening for O atoms at 1900 K. If the actual laser linewidth was much smaller, the 2 pm could be entirely attributed to Doppler broadening and a temperature of 2500 K would be found, like in the temperature measurements.

The experimental dispersed fluorescence spectra of laser-excited O and Xe atoms are shown in Figs. 2.9 a and 2.9 b, respectively. The xenon line with extremely narrow Doppler width (about 1 pm at 300 K for emission at 834 nm) was used to obtain the instrumental transmission function of the spectrometer around 840 nm, which was determined to be a Voigt profile of 66 pm Gaussian and 33 pm Lorentzian widths, which resulted in a total 87 pm FWHM.

These parameters were used to fit the O line, and determine the relative contributions of each fine structure state 3p ^{3}P$_{2,1,0}$, which are labelled with their respective J quantum number in Fig. 2.9 a. Indeed, the expected Doppler broadening for O atoms, 8 pm, is completely obscured by the 66 pm of the instrumental function. The weighing from [19], observed in the excitation spectra, is used here to determine the contributions of the three fine structure states. It can be seen that the resulting fit is slightly too broad in the

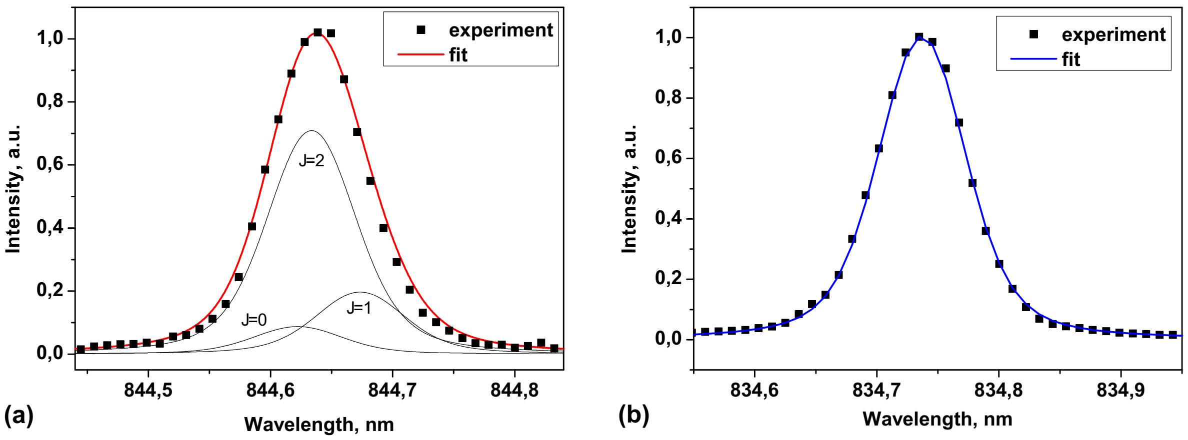

Figure 2.9: TALIF dispersed fluorescence signal taken with a spectrograph and ICCD camera. (a) oxygen atoms, laser wavelength 225.583 nm, 27 mbar synthetic air, 2500 K, 2.2 μs delay after first discharge; (b) xenon atoms, laser wavelength 224.238 nm, 8.6 mbar pure xenon, 293 K, no discharge.

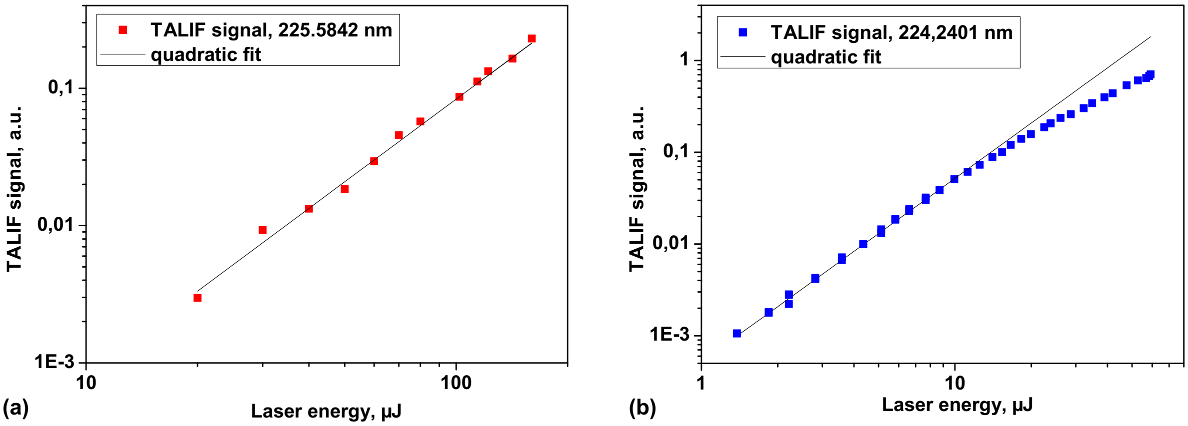

Figure 2.10: Calibration curves for (a) oxygen atoms, 27 mbar synthetic air, 2500 K, 2.2 μs after breakdown and (b) xenon atoms, 8.6 mbar pure xenon, 293 K, no discharge.

wings. A better fit is obtained with relative intensities for the J = 2, 1 and 0 components of respectively 0.8072, 0.0560 and 0.1368, a weighing that differs from [19] by up to three times, especially for the $J = 1$ component.

The time–integrated TALIF signals taken at 225.5842 nm (for O atoms) and 224.2401 nm (for Xe atoms) recorded over a large interval of laser energy, are shown in Figs. 2.10 a and 2.10 b, respectively, in a logarithmic scale. The solid line indicates quadratic (i.e. unsaturated) behaviour. The fluorescence from the capillary walls was modelled as a contribution to the signal that scales with laser energy to the power two thirds (as discussed above), and subtracted.

It can be seen that quadratic behaviour is observed from 0 to 150 μJ in oxygen, and from 0 to 10 μJ in xenon. It should be pointed out, that, in the case of xenon, the quadratic regime extends as far as 25 μJ when the pressure was lowered to 2 mbar. This latter value agrees with the measurement by Niemi et al. [2] at 10 Pa. As the only non–quadratic contribution that could change with pressure is amplified stimulated emission (ASE), this decrease in threshold energy was attributed to the fact that increasing the pressure increases the excited state density, and hence, the efficiency of ASE at a given laser energy. Finally, on the basis of the discussed laser energy dependency curves, the measurement energies were chosen to be 100 μJ for O atoms and 8 μJ for Xe atoms.

In order to obtain the absolute values of the O atom concentrations for the five chosen delay times, equation (2.5) was used. The s statistical factor varied from 1.60 to 1.72 with temperature. The quenching rates as well as the natural lifetimes are given in Table 2.1. The pure optical branching ratios $A_{jk}(\mathrm{X})/A(\mathrm{X})$ are 1 for O atoms [2] and 0.733 for Xe atoms [20].

The resulting O–atom densities are plotted against time in Fig. 2.11, for the two different assumptions concerning the behaviour of quenching coefficients with temperature, considered earlier in the text: curve "no $Q(T)$" corresponds to quenching coefficients constant with gas temperature, whereas curve "with $Q(T)$" corresponds to quenching coefficients following (2.10). The limit of 100% O_2 dissociation is plotted for reference, based on the O_2 density that exists in the capillary before the first discharge. The statistical error in the measurement procedure is estimated to be 15%, based on reproducibility of the measurements.

It can be seen that, first, the difference between the curves derived using the two different assumptions about the quenching rate temperature dependence is greater than a factor of 2. Only a temperature–resolved measurement of the fluorescence lifetimes could alleviate this uncertainty. It can nonetheless be noted that the constant cross section assumption does not seem to be valid up to 2500 K, because the dissociation degree would then exceed 100%. In both cases, a large dissociation degree is achieved at the end of the three discharge pulses. The three first points indicate conversion of discharge energy to O_2 dissociation, probably quenching of $N_2(B,C)$ on O_2.

It is possible to give a rough estimate of the O atom density expected after all three pulses: the energy needed to produce an O atom in air in the discharge under study, based on the value of the reduced electric field, was calculated in [21]. This so–called G–factor is comprised between 4.9 and 5.7 eV/atom over a broad range of reduced electric fields ($150 - 400$ Td), which is the typical reduced electric field observed in this discharge [22]. If an average value of 5.4 eV/atom is taken, with 25 mJ deposited by the first two pulses [22, 23], and a capillary volume of 141 mm^3, the resulting O atom density is $2.04 \cdot 10^{17}$ cm^{-3}, which is exactly in between of the curves corresponding to the two assumptions (with $k(T)$ following equation (2.10) or being constant with temperature). This value, estimated based on the G-factor, is marked by a green half–filled circle in Fig. 2.11.

Also, an absolute lower bound on the quenching rate, and hence, the absolute O atom density, can be established based on the observed O atom signal decay rate (see Fig. 2.8 a). If a total removal rate corresponding to the observed decay time of 3.7 ns is taken, without any de-convolution of the PMT response time and the squared laser pulse power waveform, the total quenching rate would be 58% of that observed at room temperature. The corresponding value is marked by an orange triangle in Fig. 2.11.

Finally, it can be concluded that although the uncertainty on the quenching rate

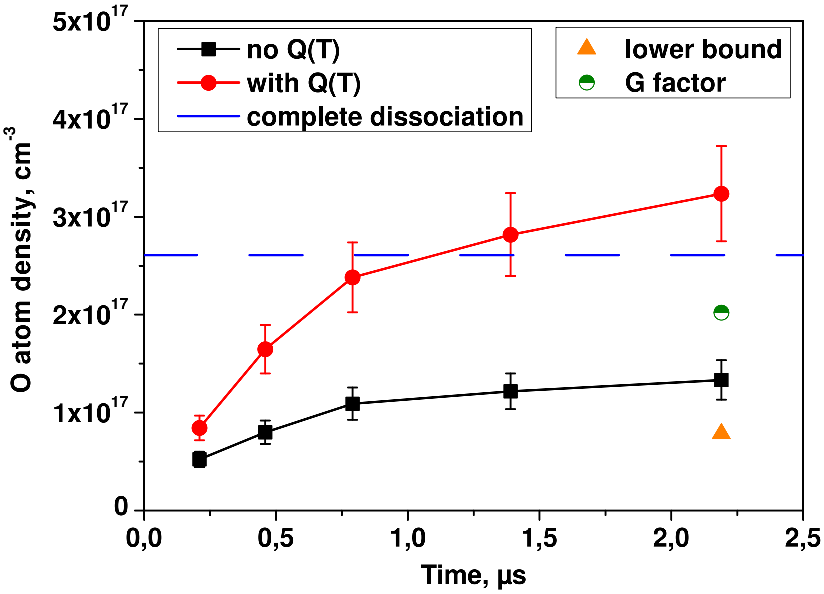

Figure 2.11: TALIF O atom data for 27 mbar synthetic air, and complete dissociation limit (total O atom density available from the gas initial O_2 density).

produces a large uncertainty in the measured O atom value, simple energy branching considerations indicate a dissociation fraction of atomic oxygen of about 70% after 2 μs, which falls in-between the two quenching models. As such, the measurements and theoretical estimations are coherent, and the TALIF technique is promising for the study of discharge parameters, radical densities and fundamental rate constants at high gas temperature and high O_2 dissociation degree.

2.4 Conclusions

The two–photon absorption laser–induced fluorescence technique was applied to measure the O atom density on a sub–microsecond time scale, in a capillary nanosecond discharge initiated in air at about 30 mbar. A high dissociation degree, up to complete dissociation, is observed 2 microseconds after the initial breakdown. The high gas temperature, measured by rotational spectroscopy of the second positive system of molecular nitrogen, raised the question of the temperature dependence of the quenching rate constants of the excited state which is observed by TALIF. At the discharge temperatures observed in this work, the assumptions of either a constant quenching rate, or a constant quenching cross section, results in a difference in the measured O atom concentration of more than a factor of two. Measurement of quenching coefficients would enable a more precise analysis of the key role played by O atoms in air discharge chemistry in the case of high dissociation degree and high gas temperature, which will benefit theoretical studies of fast gas heating.

Bibliography

[1] Moore C E 1993 Tables of Spectra of Hydrogen, Carbon, Nitrogen, and Oxygen Atoms and Ions CRC Series in Evaluated Data in Atomic Physics ed J W Gallagher (Boca Raton, FL: CRC Press) (339 pp)

[2] Niemi K, Schulz-von der Gathen V and Doebele H F 2005 Absolute atomic oxygen density measurements by two-photon absorption laser-induced fluorescence spectroscopy in an RF-excited atmospheric pressure plasma jet Plasma Sources Sci. Technol. 14 375-86

[3] Dixit S N, Levin D A and McKoy B V 1988 Resonant enhanced multiphoton ionization studies in atomic oxygen Phys. Rev. A 37 4220-8

[4] Miller J C 1989 Two-photon resonant multiphoton ionization and stimulated emission in krypton and xenon Phys. Rev. A 40 6969-76

[5] Buijsse B, van der Zande W J, Eppink A T J B, Parker D H, Lewis B R and Gibson S T 1998 Angular distributions for photodissociation of O 2 in the Herzberg continuum J. Chem. Phys. 108 7229-43

[6] Tonokura K, Shafer N and Matsumi Y 1991 Photodissociation of oxygen molecules at 226 nm in the Herzberg I system J. Chem. Phys. 95 3394-8

[7] Wysong I J, Jeffries J B and Crosley D R 1989 Laser-induced fluorescence of O(3p 3P), O2, and NO near 226 nm: photolytic interferences and simultaneous excitation in flames Opt. Lett. 14 767-9

[8] Pindzola M S 1978 Two-photon excitation of atomic oxygen Phys. Rev. A 17 1021-7

[9] Saloman E B Energy 2004 Levels and Observed Spectral Lines of Xenon, Xe I through Xe LIV J. Phys. Chem. Ref. Data 33 765-921

[10] Loudon R 1983 The Quantum Theory of Light 2nd edition (Oxford: Clarendon)

[11] Niemi K, Schulz-von der Gathen V and Döbele H F 2001 Absolute calibration of atomic density measurements by laser-induced fluorescence spectroscopy with two-photon excitation J. Phys. D: Appl. Phys. 34 2330-5

[12] Dilecce G, Vigliotti M and De Benedictis S 2000 A TALIF calibration method for quantitative oxygen atom density measurement in plasma jets J. Phys. D: Appl. Phys. 33 L53-6

[13] Meier U, Bittner J, Kohse-Höinghaus K and Just T 1989 Discussion of two-photon laser-excited fluorescence as a method for quantitative detection of oxygen atoms in flames Proceedings of the Combustion Institute 22 1887-96

[14] Gasnot L, Desgroux P, Pauwels J F and Sochet L R 1997 Improvement of two-photon laser induced fluorescence measurements of H- and O-atoms in premixed methane/air flames Appl. Phys. B 65 639-46

[15] Ossler F, Larsson J and Alden M 1996 Measurements of the effective lifetime of O atoms in atmospheric premixed flames Chem. Phys. Lett. 250 287-92

[16] Bittner J, Kohse–Höinghaus K, Meier U and Just T 1988 Quenching of two-photon excited H(3s,3d) and O(3p $^3P_{2,1,0}$) atoms by rare gases and small molecules Chem. Phys. Lett. 143 571-6

[17] Ochkin V N 2009 Spectroscopy of Low Temperature Plasma (Weinheim: Wiley) pp

[18] Laux C O 2002 Radiation and nonequilibrium collisional-radiative models Physico-Chemical Modeling of High Enthalpy and Plasma Flows (von Karman Institute Lecture Series 2002-07) ed D Fletcher et al (Rhode-Saint-Genese, Belgium: Von Karman Institute)

[19] Saxon R P and Eichler J 1986 Theoretical calculation of two-photon absorption cross sections in atomic oxygen Phys. Rev. A 34 199-206

[20] Horiguchi H, Chang R S F and Setser D W 1981 Radiative lifetimes and twobody collisional deactivation rate constants in Ar for Xe(5p 56p),Xe(5p 56p), and Xe(5p 57p) states J. Chem. Phys. 75 1207-18

[21] Klochko A V, Popov N A and Starikovskaia S M 2012 Study of a fast gas heating in a capillary nanosecond discharge. Discharge parameters and temperature increase in the afterglow Proc. of the 50th AIAA Aerospace Sciences Meeting, Nashville, TN, AIAA paper 2012-1162

[22] Klochko A V, Salmon A, Lemainque J, Popov N A, Booth J-P., Xiong Z, Kushner M J and Starikovskaia S M 2014 Experimental and numerical study of fast gas heating and O atom production in a capillary nanosecond discharge Proc. of the 52nd AIAA Aerospace Sciences Meeting, National Harbor, MD, AIAA paper 2014-1030

[23] Klochko A V, Popov N A, Booth J-P and Starikovskaia S M 2013 Study of fast gas heating in a capillary nanosecond discharge in air. TALIF O atoms measurements and kinetic modeling Proc. of the 51st AIAA Aerospace Sciences Meeting, Grapevine, TX, AIAA paper 2013-0574

Chapter 3

Extra–density of electrons in the afterglow of a capillary nanosecond discharges: influence of electron density on quenching of electronically excited species

3.1 Introduction

As it was mentioned in two previous chapters, concentration in space and time of energy transmitted from external electrical circuit to gas, causes significant influence on parameters of resulting plasma. Extremely high power density is typical for so-called "pinch capillary discharges" [1, 2]. High temperature completely ionized plasma is produced in a pumped of gas-filled capillary under the action of sub-microsecond high-voltage pulses and electric currents of tens of kA.

Plasma, obtained in a capillary tube about 1 mm in diameter under the action of a pulse of the electric current tens of A in amplitude and tens of nanosecond in duration, is a low-temperature plasma. Still, the specific energy in the discharge is high. For 30 kV voltage amplitude on the discharge gap, $I = 70$ A and 30 ns pulse duration, at the conditions of 15% of pulse energy absorbed uniformly in a capillary tube 1 mm in diameter and 10 cm in length at atmospheric pressure, a specific energy can be estimated as 0.2 eV/molecule. This specific energy, at electric fields of 200-300 Td, can significantly change gas kinetics in the discharge and in the afterglow [3].

During last decades, nanosecond capillary discharges were suggested for various applications. Capillary discharge in N_2:O_2 mixtures was studied as active media for non–cavity lasers working on the second positive system of molecular nitrogen. The amplitudes of the nanosecond pulses varied from 30 kV [4, 5] to 300 kV [6, 7], and the pressures were between 2 and 35 Torr. Electrical current reached tens–hundreds of amperes.

Another example of using capillary discharge at high energy release can be found in [8], where the electrode, 13 cm in diameter consisted of a set of hundreds of capillary tubes. The system was efficiently used to trigger the detonation in C_3H_8/C_4H_{10}:$5O_2$:xN_2, $0 < x < 10$ mixtures; Chapman–Jouguet (CJ) velocity was reached at a distance equal to only one diameter of the electrode.

A lot of publications recently is devoted to study of a capillary discharge in the form of so-called "plasma jet"[9]. Plasma jets are used for plasma medicine [10, 11] or for surface modification [12, 13]. They are capillary discharges with dielectric barrier or with open electrodes, with sinusoidal or pulsed power supply, in a noble gas flowing through the capillary. Plasma treatment of living cells or of the surface takes place on the exit of the capillary, in the region of mixing if the noble gas and atmospheric air. Although overall deposited energy in the flowing afterglow is small, a specific energy in the discharge region can be high enough to change conventional plasma chemical kinetic so that reactions between the active species created in the discharge become important.

As far as production of excited species and radicals is extremely important for mentioned applications, different optical methods, such as time-resolved actinometry and optical emission spectroscopy, LIF, TALIF are widely used to study plasma of discharges with high specific deposited energies. At relatively high deposited energies and high reduced electric fields, a significant density of excited species and high dissociation degree are achieved [14]. At pressures higher than a few tens of Torrs, detailed analysis of collisional quenching becomes important [15].

Ambiguity of diagnostics based on optical emission in plasma at high collisional frequency is a very important topic. This problem is common for plasma confined into small volume in artificial way, for example, for capillary discharges at moderate pressures, for microplasmas, for transient plasmas when microdischarges or filaments naturally contain zones of high specific deposited energy. In recent review [**?**] devoted to physics, chemistry and diagnostics of microplasmas and atmospheric pressure discharges, it is underlined that any advanced optical diagnostics requires a detailed understanding of plasma kinetics, in particular understanding of population and depopulation mechanism of main excited states.

Up to now, in majority of studies, including laser–related papers [4, 5, 6, 7], common knowledge about gas discharges at relatively low specific deposited energy is used to treat the obtained data. In particular, "conventional" quenching rates for $N_2(C^3\Pi_u)$ are taken to derive a population of electronically excited states. At the same time, it has been recently demonstrated [17] that quenching of $N_2(C^3\Pi_u)$ in a capillary tube in air at energy release about 1 eV/molecule is not described by well-known quenching rates on N_2 and O_2 molecules [18], and that significant O_2 dissociation [14] can not be a reason of observed strong quenching. The experiments [17] were made for 5—60 mbar for different N_2:O_2 mixture composition; it was found that the quenching rate increases with specific deposited energy. As far as in pure nitrogen the deviation from the quenching rate predicted by [18] was the strongest, it was decided to perform a detailed analysis of quenching in the afterglow of nanosecond capillary discharge in nitrogen. It should be noted that molecular nitrogen is a very specific "kinetic" medium: significant energy is stored in metastable electronically excited molecules $N_2(A^3\Sigma_u^+)$, $N_2(a'^1\Sigma_u^-)$ and atoms $N(^2D)$, $N(^2P)$. The excited molecules and atoms, participating in the reactions of associative ionization, significantly influence the electric field in the discharge [19] and provide relatively high electron density in the discharge afterglow [20].

This chapter is aimed at understanding the kinetic peculiarities of fast $N_2(C^3\Pi_u)$ quenching in pure nitrogen at moderate pressures at high specific deposited energy in the near afterglow of a nanosecond capillary discharge.

3.2 Experimental setup

The nanosecond discharge was initiated in the capillary tube 1.5 mm of internal diameter, 3.4 mm of external diameter and 70 mm inter-electrode distance, presented schematically in figure 3.1 a. Two gold–covered pin–shape high (HV) and low (LV) voltage electrodes were mounted at the ends of the tube. Grounded metallic screen of a rectangular shape 48 mm x 60 mm surrounded the capillary. The gas was changed flowing trough the side tubes placed 4 mm apart from the electrodes.

A general scheme of the experimental setup is given by figure 3.1 b. The capillary tube is inserted into a break of the central wire of a long coaxial cable. A metal screen around the tube is connected to the cable ground shield. The length of the cable between the high voltage generator (HVG) and the capillary tube is equal to 25 m, the cable connected to the low voltage electrode is 100 m in length. For a few additional experiments, discharge tubes with different lengths/diameters and different loads at the low voltage electrode were used.

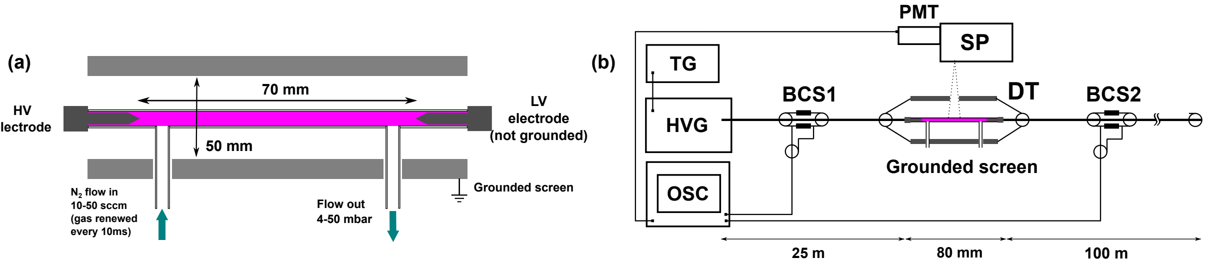

Figure 3.1: (a) The discharge cell configuration with 1.5 mm inner diameter tube and 70 mm inter-electrode distance; (b) General scheme of the experimental setup. TG: triggering generator; HVG: high voltage generator; OSC: oscilloscope; BCS: back current shunt; PMT: photomultiplier tube; SP: spectrometer; DT: discharge tube. The delay cable can be disconnected from the LV electrode.

High–voltage pulses 9.3 kV in amplitude, 4 ns rise time and 29 ns FWHM were produced by a commercial solid state high–voltage generator FID FPG 10–MKS20 HV (FID GmbH) with a 10 Hz frequency. Within a few nanoseconds after the voltage applied to the high–voltage electrode, a fast ionization wave (FIW) started from the electrode and propagated along the capillary tube with a high velocity (for example, for 80 A transmitted current, the velocity of the FIW propagation was equal to 1.4 cm/ns [21]).

For the present study, the experiments with different energy deposited to the discharge at the condition that all other parameters are fixed were a crucial issue. To get different deposited energies with the same incident pulses, the high–voltage electrode was partially screened to provide a stochastic discharge start. The statistic analysis of the transmitted current has been made, and the data were averaged over preliminary selected data corresponding to a given value of transmitted electric current with a standard deviation not exceeding 5%.

Pure nitrogen (Air Liquide, <100 ppm of impurities) was flowing trough the tube with 50 sccm rate; the high flow rate, at low discharge repetitive frequency, provided complete change of gas between the subsequent pulses. The pressure was measured upstream and downstream of the capillary by a Pirani-type TPR-010 (for pressures below 5 mbar) and a capacitive-type CMR 261 (for pressures above 5 mbar) pressure gauges from Pfeiffer Vacuum. The pressure and density distribution inside the capillary were calculated by COMSOL package using a weakly compressible Navier-Stokes simulation based on the capillary geometry including the gas inlets, the measured pressures and the flow rate. Finally, the pressure in the center of the capillary tube was kept constant during each experiment and was in the range $P = 5 - 60$ mbar.

The current and voltage in the cable were measured by two custom–made calibrated back current shunts (BCSs) soldered into the cable shield break 12.5 m before and after the discharge tube. The signals from the BCSs were registered by a LeCroy WaveRunner 600 MHz oscilloscope. The principles of back current shunt measurements can be found elsewhere [22]. Energy deposited to the discharge tube in each pulse was calculated from the signals obtained by back current shunts as a difference between the energy stored in the incident pulse, and the sum of energy of charging of the capacitance of the discharge cell and the energies of the reflected and transmitted pulses:

$$W_{BCS} = \frac{1}{Z}\int_{t_0}^{t_{pulse}} (U^2_{refl.vac.}(t) - U^2_{refl.}(t) - U^2_{trans.}(t))dt, \tag{3.1}$$

where t_0 and t_{pulse} are the beginning and the end of the pulse respectively, $U_{refl.vac.}(t)$ is a voltage waveform for the reflected pulse in vacuum without discharge, $U_{refl.}(t)$ for the reflected pulse with discharge, and $U_{trans.}(t)$ for the transmitted pulse. $Z = 50$ Ohm is a wave impedance of the high–voltage cable.

It should be noted that in this paper two successive pulses coming from the high voltage generator will be considered. The first pulse is the initial high–voltage pulse coming from the HVG to the discharge tube, and the second pulse is the high–voltage pulse reflected from the generator because of mismatching of the cable impedance and of the input impedance of HVG, and coming to the discharge tube 250 ns later. These main high voltage pulses will be designated as the “first pulse” and the “second pulse” in the text below. They will be considered as incident pulses; and for each of them a pulse reflected from the discharge cell, and a pulse transmitted through the discharge cell to the cable connected to the low voltage electrode, will be analyzed.

The longitudinal electric field was measured with the help of a custom–made calibrated capacitive probe. The capacitive probe, inserted in a slit of the upper part of the screen, provided measurements of electric potential along the discharge tube with sampling interval of 1 mm. The metal tip of the probe, protruded from the grounded screen to 12 mm from the tube axis, was at floating potential and was connected through a 330 pF coaxial capacitor to a 50 Ohm oscilloscope input. The electric potential measured at the detector was related to the potential inside the capillary tube using the procedure described in [21]. Optical emission from the discharge was collected by ANDOR SR–500i monochromator with 1200 l/mm grating. Both slits were 100 μm wide; as a result, the optical resolution of the system was 0.4 nm FWHM, as checked with a mercury lamp. The light was detected by a Hamamatsu H6610 photomultiplier tube (PMT), with a typical rise time of 0.7 ns and transit time spread of 0.16 ns, connected to the oscilloscope with a 1 m–length coaxial cable with double shielding. The light was collected from the orifice in the grounded screen, 1 cm in length, providing a temporal resolution of 0.7 ns at velocity of the FIW propagation of 1.4 cm/ns. The data were taken in the mode of accumulation of the signal, selected by the transmitted current as described above.

3.3 Numerical modeling

The numerical modeling focuses on the detailed kinetics in the discharge in nitrogen after closing of the discharge gap, and in the near afterglow. Experimentally obtained electric current as a function of time was taken as initial data for the calculations. The main part of energy is deposited to the system when the gap between two electrodes is closed, that is when the current is high enough and the electric field has not yet decreased. It was assumed that, after closing the discharge gap, the radial distribution of the electron density corresponds to the calculated in 2D–geometry [21]. The kinetic calculations were carried out in 1D–approximation describing the values as functions of radius r over the cross–section of measurements at axial symmetry. The validity of suggested approximation is proved by the fact that radial gradients of the discharge parameters are much higher than the axial gradients in the direction between the electrodes [21]. The longitudinal electric field E in the cross–section was calculated as

$$E = \frac{I}{2\pi e \int_0^R N_e(r)\mu_e(r) r dr}, \tag{3.2}$$

where $N_e(r)$ is the radial electron density, μ_e is the electron mobility (considered as a function of reduced electric field E/N, with gas density N), R is internal radius of the discharge tube. The gas density assumed to be constant, since the time scale of considered processes (< 1 μs) is much less than a characteristic time of gas extension ($\approx 20-30$ μs for characteristic dimensions of the discharge cell). To verify the results of the calculation, the experimentally measured reduced electric field was compared with $E(t)/N$ dependence calculated from the equation (3.2).

The following equation was solved for the electron density:

$$\frac{\partial N_e}{\partial t} = \frac{1}{r}\frac{\partial}{\partial r}(r D_a \frac{\partial N_e}{\partial r}) + N_e \nu_{ion} - Q_{rec} + Q_{as}. \tag{3.3}$$

Here D_a is the ambipolar diffusion coefficient, ν_{ion} is the frequency of ionization by electron impact (a function of $E(t)/N$), Q_{rec} is the rate of electron–ion recombination, and Q_{as} describes additional production of electrons due to associative ionization. Similar balance equations have been written for N_2^+, N_3^+ and N_4^+ ions. As far as the impurities in the system did not exceed 100 ppm, no other ions have been taken into account and kinetics was restricted by chemistry of pure nitrogen. The following neutral species were considered by the model: $N_2(X^1\Sigma_g^+)$, $N_2(A^3\Sigma_u^+)$, $N_2(B^3\Pi_g)$, $N_2(W^3\Delta_u)$, $N_2(B'^3\Sigma_u^-)$, $N_2(C^3\Pi_u)$, $N_2(a'^1\Sigma_u^-)$, $N(^4S)$, $N(^2D)$, $N(^2P)$. Three levels $N_2(B^3\Pi_g)$, $N_2(W^3\Delta_u)$ and $N_2(B'^3\Sigma_u^-)$ were considered and designated as a single $N_2(B)$ level.

Ionization and excitation rates were calculated for each time instant as a function of reduced electric field on the basis of the solution of the Boltzmann equation in a two–term approximation using BOLSIG+ code [23] with the imported [24] cross–sections. It should be noted that the two–term approximation is valid [24, 25, 26] for the considered experimental conditions because the reduced electric field in the region of significant energy input does not exceed a few hundreds of Td. The reactions and rate constants are reviewed in [20, 25, 27, 28].

At the given conditions the density of atomic nitrogen does not exceed $1-2\%$ [29]. So, the influence of the electron–atom collisions on the electron energy distribution function (EEDF) were not taken into account.

As far as at relatively high electron densities, $N_e/N \geq 2 \cdot 10^{-3}$ and low electric fields, $E/N < 100$ Td, electron–electron collisions become important for EEDF formation, electron drift velocity and rates of excitation for considered electronically excited states, the $e - e$ processes were taken into account in the calculations.

3.4 Experimental results

3.4.1 Electrical measurements and FIW structure.

Typical voltage waveforms corresponding to the the first incident from the high–voltage generator, reflected from HV electrode and transmitted through the discharge cell pulses measured by the back current shunts are presented in figure 3.2 a. The electric current can be derived from the voltage waveform dividing the voltage in the cable by the cable impedance, $Z = 50$ Ohm.

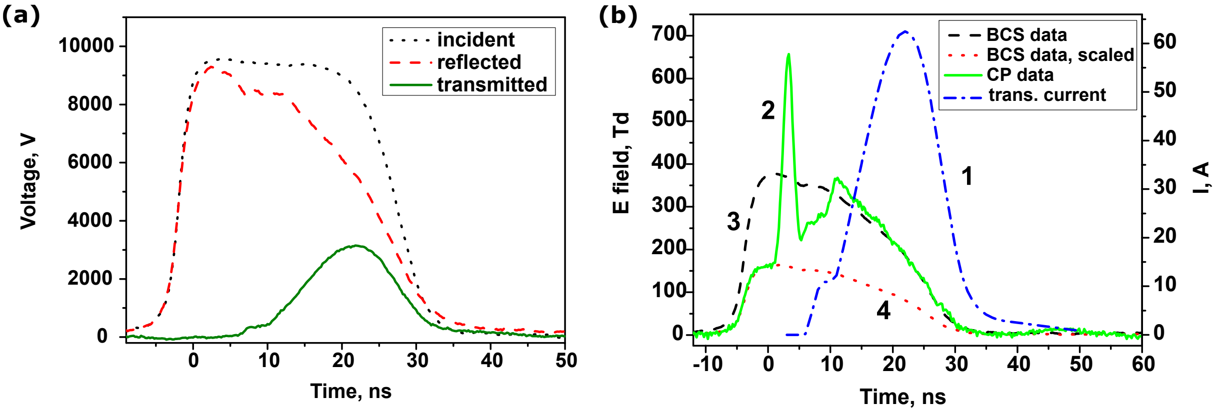

Figure 3.2: Measured electric parameters of the nanosecond capillary discharge. (a) First pulse: typical incident, reflected and transmitted voltage pulses in the cable; (b) Synthetic electric current (curve 1) and measured electric field (curve 2) in the cross–section of measurements together with waveforms used for their synchronization (curves 3 and 4), see explanation in the text.

At the early stage of the discharge, during the FIW propagation from the high–voltage to low–voltage electrode, current flowing through plasma can not be registered by BCS2 installed in the low-voltage cable, since this current closes to the metal screen by displacement current. To take this fact into account in the numerical calculations, the synthetic electric current for the first 10 ns was used. It was obtained as $U_{refl.vac.}(t) - U_{refl.}(t)$ taking into account the finite velocity of the FIW propagation. The final current waveform is given by figure 3.2 b (curve 1). The displacement current, about 10 A in amplitude, is clearly seen at $t < 10$ ns at the curve 1. The electric field in the center of the capillary measured by the capacitive detector is presented in the same figure (curve 2).

Synchronization of the current measured by BCS technique and of the electric filed measured by a capacitive detector is a very important issue for validation of the calculations. Figure 3.2 b illustrates the technique suggested in [21] providing a synchronization with the accuracy of data sampling, 0.2 ns in our case. The electric field measured by the capacitive probe is superimposed with two plots obtained from the back current shunt data. Curve 3 represents the electric field calculated from the difference of potentials between the high–voltage and low–voltage electrodes:

$$E_{BCS}(t) = (U_{inc}(t) + U_{refl}(t) - U_{trans}(t))/l_0, \tag{3.4}$$

where l_0 is the interelectrode distance, $U_{inc}(t) + U_{refl}(t)$ and $U_{trans}(t)$ represent the instantaneous potentials on the high–voltage electrode and on the low–voltage electrode respectively. This curve coincides with $E(t)/N$ measured by capacitive probe at the end of the pulse, when the electric gap is closed. Finally, curve 4 represents the curve 3 scaled down to fit the electric field in the beginning of the pulse, before the fast ionization wave comes to the cross–section of measurements.

Synchronized electric field and current in the cross-section of measurements clearly illustrate the development of the fast ionization wave in the capillary tube. The maximum of $E(t)$ waveform corresponds to the FIW front passing through the cross–section of measurements. In the FIW front, there are two factors leading to a noticeable underestimate in the field measurements. First, the electric current in the FIW front is closed by the displacement current to the metallic screen surrounding the capillary. The direction of the electric field in the front is mainly radial, while the capacitive probe gives the longitudinal electric field. Second, the duration of a sharp peak of the electric field in the FIW front does not exceed $2-3$ nanoseconds (FWHM). For the conditions of the present experiments, a typical length of the FIW front, $2-4$ cm, is only two times higher than a typical half–width of the sensitivity function of the capacitive detector, approximately equal to the distance between the detector and capillary tube axis [22]. So the value of 650 Td is not an exact value although can be used for the estimates and clearly demonstrates that the electric field in the FIW front is extremely high. At this stage, the current is low, a few amperes, and no significant energy is deposited to the gas. The role of the FIW front is to produce relatively high preliminary ionization; this stage is absent in the second pulse coming to the discharge cell 250 ns after the first pulse.

After the FIW front passing the cross-section of observation, there is a stage when FIW reaches the low-voltage electrode and the potential of a low–voltage electrode established, the current is still being low. And finally, at $t > 10$ ns, high current (up to 100 A) flows through the discharge tube to the loading cable, and the reduced electric field stays on the level of $200 - 300$ Td. This stage, if present, is the most important for any chemical application of the nanosecond discharges, providing major energy input and efficient excitation of high energy electronic states of atoms and molecules.

Although development of the fast ionization wave in capillary tube is rather similar to FIW development in long tubes a few centimeters in diameter [30, 31], the resulting parameters of plasma in discharge and near afterglow are very different. When discharge tube diameter decreases, the electric current does not change substantially. Changes of the electric field behind the FIW front are also minor. So the changes in the delivered energy to the whole discharge cell are not significant, while the discharge volume drops. Specific deposited energy changes dramatically, as it is reversely proportional to the volume taken by plasma. At gas density corresponding to pressure of 27 mbar at ambient gas temperature, energy density of 0.1 J/cm^3 corresponds to 1 eV/molecule. Under these conditions, significant changes in kinetics comparing to weakly excited gas can be expected.

3.4.2 Measured decay of optical emission of the second positive system in the discharge and in near afterglow

In the wavelength range of 200 − 400 nm the main optical emission from the capillary nanosecond discharge is due to the emission of the second positive system of molecular nitrogen, $N_2(C^3\Pi_u, v' = 0) \rightarrow N_2(B^3\Pi_g, v'' = 0)$. Emission at $\lambda = 337.1$ nm was studied at different pressures and different values of deposited energy.

In the simplest case of high electric field, low specific deposited energy and low densities of both electrons and excited species, the population/depopulation process of the upper, $N_2(C^3\Pi_u, v' = 0)$ state, is described by three processes [18]. They are population by direct electron impact from the ground state of molecular nitrogen,

$$N_2(X^1\Sigma_g^+) + e \rightarrow N_2(C^3\Pi_u, v' = 0) + e, \tag{3.5}$$

spontaneous emission,

$$N_2(C^3\Pi_u, v' = 0) \rightarrow N_2(B^3\Pi_g, v'') + h\nu, \tag{3.6}$$

and collisional deactivation by background gas,

$$N_2(C^3\Pi_u, v' = 0) + N_2 \rightarrow \textit{products}. \tag{3.7}$$

The rate constants for $N_2(C^3\Pi_u, v' = 0)$ quenching by molecular nitrogen are well–known [18, 32, 33, 34] and in a good correlation in the papers of different authors[35].

The emission decays measured at the conditions of the present work are different from the decay predicted theoretically using the rate constant measured in [18] and taking into account processes (3.6) and (3.7) for $N_2(C^3\Pi_u, v' = 0)$ deactivation. This fact is illustrated by figure 3.3 a, where a typical experimentally obtained semi–logarithmic decay plot for $N_2(C^3\Pi_u, v' = 0) \rightarrow N_2(B^3\Pi_g, v'' = 0)$ is presented together with a theoretically predicted dependence for $T = 295$ K. It is clearly seen that the experimental curves (i) have much faster decays; (ii) demonstrate two exponential slopes, τ_1 and τ_2. It is important to note that both decays, τ_1 and τ_2, correspond to a zone free from electric current, where the excitation by direct electron impact (3.5) is not significant anymore. Another important remark is that the observed sharp decrease of the emission decay can not be caused by small non–controlled additions of molecular oxygen. Indeed, to get the presented in figure 3.3 a decay $\tau_1 = 10.4$ ns for 27 mbar it would be necessary to have 33.3% of molecular oxygen in the gas mixture.

Additional plots presented in figure 3.3 a, taken at different values of electric current, clearly demonstrate the dependence of the decay upon the transmitted current, and so, upon the energy deposited to the discharge. Figure 3.3 b presents the dependence of the observed decay, τ_1^{-1} on the gas pressure. Dashed line shows the theoretical value of τ_0^{-1} decay calculated from the processes (3.6) and (3.7) with quenching rate constant taken from [18]. To check the limit case of significantly decreasing specific deposited energy, a few experiments in a capillary tube 4 mm in diameter with different end loads have been done. A specific deposited energy decreases sequentially in the three series of experiments (see figure 3.3 b), namely: (i) curves (1)–(3) for a 1.5 mm diameter capillary, cable load; (ii) curves (4), (5) for a 4 mm diameter capillary, cable load; (iii) curve (6), (7) for a 4 mm diameter capillary, end load equal to infinity ($R = \infty$), that is disconnected low

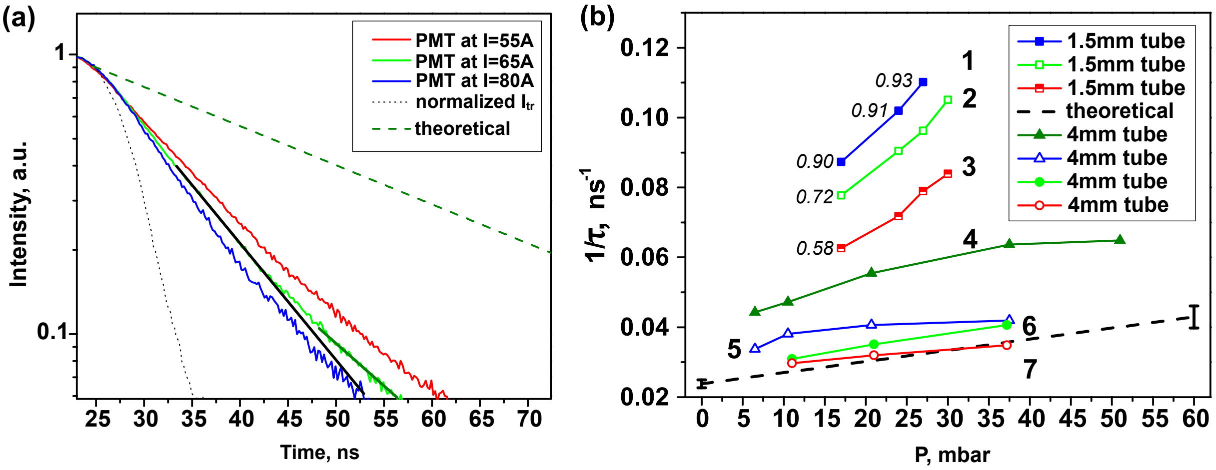

Figure 3.3: Experimental results for $N_2(C^3\Pi_u, v' = 0)$ quenching in a capillary tube in pure nitrogen: (a) experimentally measured emission at 27 mbar for different discharge current; dashed line represents nitrogen emission calculated on the basis of quenching by N_2 with rate constant from [18]; dot line shows a normalized waveform for electric current; (b) reverse decay time τ_1 as a function of pressure for different specific deposited energies. Specific deposited energy decreases with the number of curve, see detailed explanations in the text. Dashed curve is for theoretical prediction.

voltage electrode and the grounded screen. The values of the specific deposited energies corresponding to some of the observed decay rates are presented in the figure 3.3 b in the units of eV/molecule. With decrease of the specific deposited energy in the discharge, the τ_1^{-1} approaches to the theoretically predicted value, and the emission waveform changes to a single-exponential decay.

3.5 Discussion

3.5.1 Analysis of possible factors influencing the quenching decay rate

So, the experimental measurements demonstrate that (i) decay rate for $N_2(C^3\Pi_u)$ quenching in nanosecond capillary discharge in nitrogen increases with specific deposited energy; (ii) the decay is not single–exponential at high deposited energies; (iii) initial quenching rate is 2 to 10 times higher than predicted by reactions (3.6) and (3.7).

A few possible reasons of extra–high quenching rate for $N_2(C^3\Pi_u)$ were analyzed, namely: (i) stimulated emission in the case if conditions for laser transition are fulfilled for $N_2(C^3\Pi_u) \rightarrow N_2(B^3\Pi_g)$ emission; (ii) variation of quenching rate with gas temperature; (iii) quenching by nitrogen atoms; (iv) quenching by other excited species; (v) quenching by electrons.

It is known [36, 37] that laser radiation can be produced by nanosecond discharge under certain conditions in a long capillary tube in molecular nitrogen. Although the discharge power and the length of the capillary tube in experiments [36, 37] were much higher than in the present work, it was experimentally checked that emission observed in the present work is not a laser emission. To do this, time–resolved emission has been measured for a set of wavelengths in the rotational structure, namely 337.0, 336.8, 336.4, 336.0 and 335.6 nm. In spite of the fact that absolute emission values decreases by a factor of 25 through this manifold, the shape of the emission curve remains identical (see figure 3.4). As far as stimulated emission strongly increases with light intensity, it was concluded that no stimulation emission is observed within the rotational band.

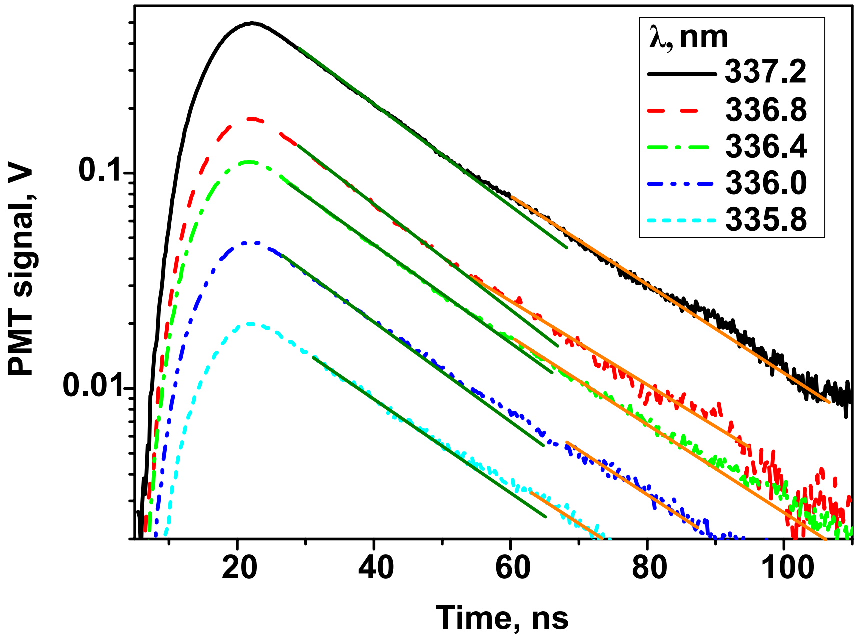

Figure 3.4: Time–resolved $N_2(C^3\Pi_u, v = 0) \rightarrow N_2(B^3\Pi_g, v' = 0)$ emission for the different wavelengths: 337.0, 336.8, 336.4, 336.0 and 335.6 nm at 20.5 mbar pure nitrogen in 4 mm inner diameter tube.

Gas temperature in a near afterglow of a nanosecond discharge can rise significantly because of energy relaxation from electronically excited molecules. This is so–called effect of a fast gas heating described in details for N_2:O_2 mixtures in [25, 38, 39]. In nanosecond discharge in nitrogen, gas heating in near afterglow is mostly caused by reaction between two excited nitrogen molecules [25, 40]:

$$N_2(A^3\Sigma_u^+, v) + N_2(A^3\Sigma_u^+, v') \rightarrow N_2(B^3\Pi_g, v'') + N_2 + Q \tag{3.8}$$

The rate constant for process (3.8) is $k_{3.8} \le 3 \cdot 10^{-10}$ cm^{3}s^{-1} [41]. At typical $N_2(A^3\Sigma_u^+)$ densities about $(3 - 10) \cdot 10^{15}$ cm^{-3} (see figure 3.6), the characteristic time of fast gas heating is about $\tau_h \approx 1$ μs. So, the increase of gas temperature can not be considered as a reason of a strong decay of $N_2(C^3\Pi_u)$ radiation.

After elimination of laser and temperature effect, the most probable scenario for the observed fast decay of N_2 emission is a collisional quenching.

Observed bi–exponential decay of the emission (decay time, τ_1, is changed by a slower decay time, τ_2, both are much faster than the theoretically predicted one, τ_0) in the times of the order of 30 ns means that potential collisional partner is short-lived. Thus it can not be metastable state or vibrationally excited ground states of molecular nitrogen.

The calculations show that the densities of other excited species and atomic nitrogen in the discharge do not exceed 10% of the total gas density (see figure 3.6). To obtain a typical decay time about 10^{-8} s in collisions with such a partner, it is necessary to take a rate constant higher than $2\cdot10^{-9}$ cm^{3}s^{-1} which seems to be not reasonable. Moreover, the characteristic times of quenching of excited states $N_2(B^3\Pi_g)$ and $N_2(a'^1\Sigma_u^-)$ under given conditions is greater than 100 ns, so these states are not short-lived. Thus, we believe that heavy particles are unlikely to be collisional partner responsible for observed abnormally high decay rates.

In [18] a slight effect of increase, less than 10%, of the reverse decay time, has been already observed in nitrogen at low pressures in discharge tube 2 cm in diameter. Quenching of $N_2(C^3\Pi_u)$ by electrons has been suggested there as an explanation. Drawin's semiempirical model [42] on the basis of Bethe–Born approximation with corrections [43] and the principle of detailed balance were used to estimate the cross–section and finally, to calculate the rate constant k_e. The estimate resulted in 10^{-7} cm^{-3}. Below, the idea of quenching of $N_2(C^3\Pi_u)$ by electrons in the reaction

$$N_2(C^3\Pi_u) + e \rightarrow N_2(X^1\Sigma_g^+, A^3\Sigma_u^+, B^3\Pi_g) + e \tag{3.9}$$

for the conditions of the present paper will be developed.

3.5.2 Numerical calculations: long-lived plasma due to associative ionization and quenching of electronically excited states by electrons in the afterglow

Typically in the discharges, quenching by electrons is not important because of high rate of electron–ion recombination. However, at conditions of high specific deposited energy the electron density can be sustained by reactions of associative ionization [19]:

$$N_2(A^3\Sigma_u^+) + N_2(a'^1\Sigma_u^-) \rightarrow N_4^+ + e \tag{3.10}$$

and

$$N_2(a'^1\Sigma_u^-) + N_2(a'^1\Sigma_u^-) \rightarrow N_4^+ + e, \tag{3.11}$$

which are extremely effective at high excitation degree specific for considered capillary discharge. To check the possibility of the long-lived plasma and, as a result, effective quenching of $N_2(C^3\Pi_u)$ state by electrons, the numerical calculations based on the waveform of electric current were performed for the first incident pulse.

To adequately describe quenching of electronically excited molecules by electrons, the radial distribution of electrons and exited species must be taken into account. Indeed, the highest frequency of quenching will take place in the areas with highest density of electrons. In the most of the gas discharges, the electron density profile in the near afterglow is flatter than in the considered discharge due to efficient recombinations in the areas with high charge density. However, at the considered conditions additional ionization in the afterglow is extremely important and the radial electron density distribution can significantly depends on the distribution of excited molecules involved in the reactions of associative ionization (3.10) and (3.11). So, all the calculations were performed in the framework of one-dimensional axisymmetric approximation with initial electron density taken from [21].

Calculated longitudinal reduced electric field is in a good coincidence with the measured $E(t)/N$ (see figure 3.5).

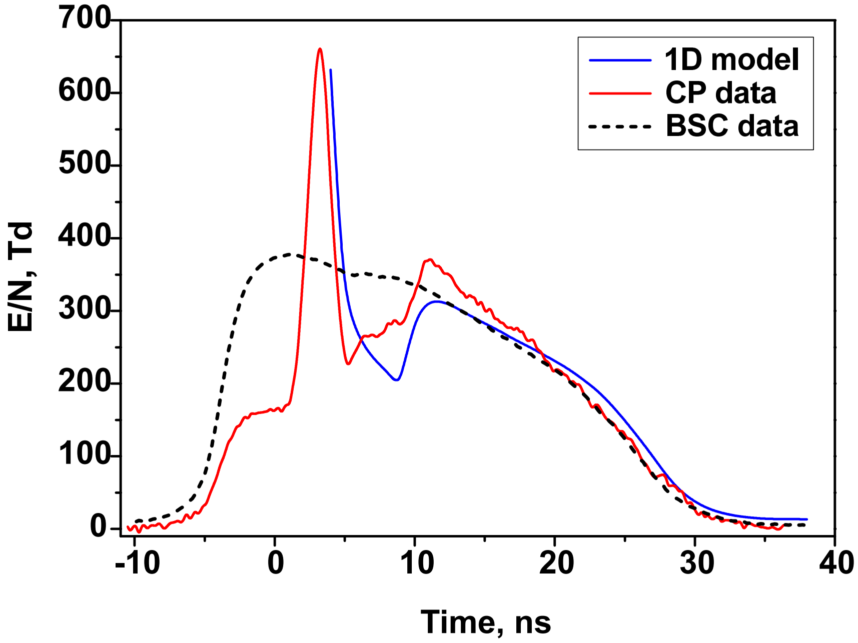

Figure 3.5: Calculated electric field as a function of time. Pure nitrogen, capillary discharge at 27 mbar pressure. Measured profile of the longitudinal electric field and BSC data from Fig.3.2 (b) are given for comparison.

It is clear that the main energy is spent to the gas at the reduced electric fields $E/N = 150 - 300$ Td. Deposited energy at the end of the considered pulse is about 0.8 eV/molecule. Such high specific deposited energy causes a high excitation degree of the molecular nitrogen, which is demonstrated by numerical calculations. Figure 3.6 represents calculated kinetic curves for main excited species at the axis of the discharge. Densities of all electronically excited nitrogen states increase gradually and reach their maxima at the end of the pulse, 25 ns after the transmitted electric current starts. The maximum total density of the excited states is of the order of 10% of the initial nitrogen density. The peak electron density in the discharge reaches $n_e \approx 1.5 \cdot 10^{15}$ cm^{-3}. The recombination at this initial electron density is fast, however it is clearly seen in figure 3.6 that the electron density is kept on the high level in the afterglow due to the reactions of associative ionization (3.10) and (3.11) included in the kinetic model.

The temporal evolution of radial profiles of the electron density and density of $N_2(C^3\Pi_u)$ state are presented in figure 3.7. The spatial distribution of the electron density changes slowly in the afterglow. As far as electrons are produced due to associative ionization, the radial profile of the electron density repeats the radial distribution of the concentration of electronically exited states $N_2(A^3\Sigma_u^+)$ and $N_2(a'^1\Sigma_u^-)$. In contrast to the electron density, the radial distribution of $N_2(C^3\Pi_u)$ state changes in time significantly. In the discharge radial profile of $N_2(C^3\Pi_u)$ state repeats the radial profile of the electron density. At the end of the discharge pulse and in near afterglow the maximum of $N_2(C^3\Pi_u)$ density shifts to the periphery of the capillary cross-section, at $r \approx 0.55$ *mm* (see curves 3 and 4 in figure 3.7 b). This is a result of intensive quenching by electrons at the center of the tube.

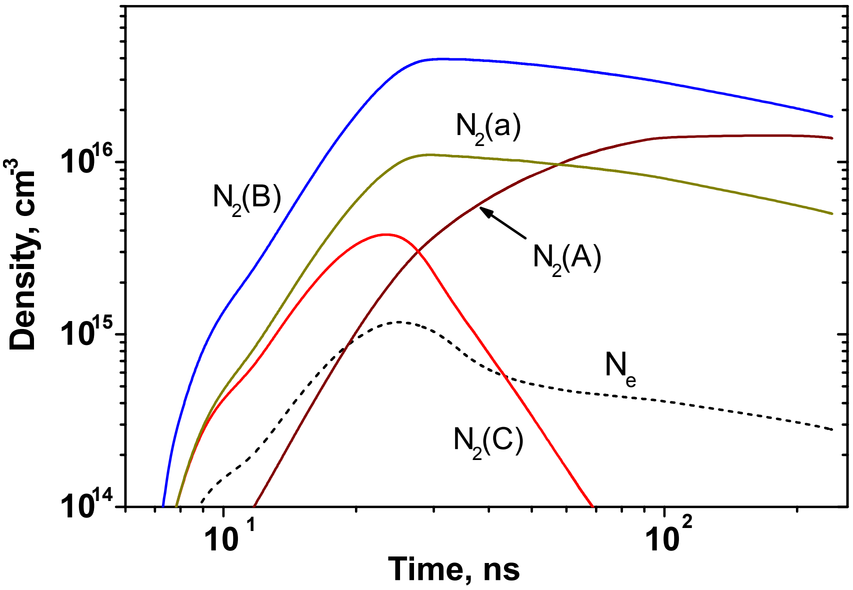

Figure 3.6: Kinetic curves of the main exited species of the molecular nitrogen at the axis of the discharge tube calculated for the first pulse coming to the capillary tube at the same conditions as for figure 3.5.

At time scale higher than 100 ns, the addition production of $N_2(C^3\Pi_u)$ state in the pooling reaction [41]

$$N_2(A) + N_2(A) \rightarrow N_2(C^3\Pi_u, v) + N_2 \tag{3.12}$$

influences the radial distribution of $N_2(C^3\Pi_u)$ state. The effect of the pooling reaction is largest in the region with high $N_2(A^3\Sigma_u^+)$ density (between the tube axis and the walls). As a result, a new $N_2(C^3\Pi_u)$ profile, with a maximum at $r = 0.3$ mm, is formed in long–lived afterglow (curve 5 in figure 3.7 b).

To verify if the high electron density can be a reason of observed abnormally high non–exponential decay of $N_2(C^3\Pi_u)$ emission, the temporal behavior of emission of the second positive system of N_2 was compared with the density of $N_2(C^3\Pi_u)$ calculated under different assumptions about the quenching rate constant k_e. The results are presented in figure 3.8. It is clearly seen that the calculations assuming the rate constant close to $k_e = 10^{-7}$ cm^{3}s^{-1}, fit the experimental curve.

3.5.3 Experimental evidence of long-lived plasma due to associative ionization in the discharge afterglow

Typical time of $N_2(A^3\Sigma_u^+)$ and $N_2(a'^1\Sigma_u^-)$ decay at 27 mbar is comparable with the time between the first and the second pulses, $\Delta t = 250$ ns (see figure 3.6). This gives a unique possibility of the additional experimental check of the effect of associative ionization.

The first method is to measure the electron density in the afterglow. The measurements were performed based on the profiles of the electric field $E(t)$ and current $I(t)$. The average value of the electron density in the cross-section of the tube was calculated as

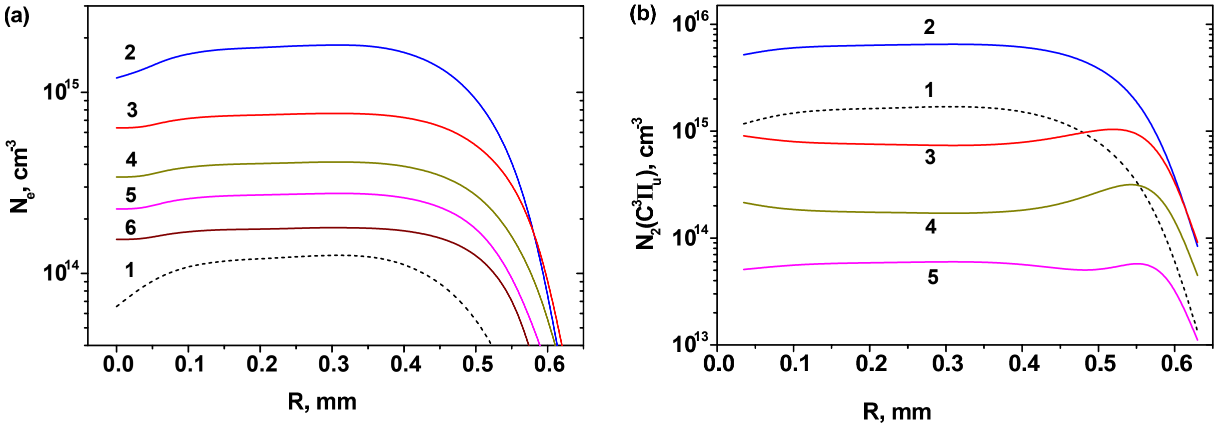

Figure 3.7: (a) The temporal evolution of the radial profiles of the electron density. Curve (1) corresponds to time 1 ns (for this curve N_e was multiplied by factor 30), 2 - 20 ns, 3 - 40 ns, 4 - 60 ns, 5 - 100 ns, 6 - 200 ns; (b) the temporal evolution of the radial profiles of the density of $N_2(C^3\Pi_u)$ state. Curve (1) - 10 ns, 2 - 20 ns, 3 - 40 ns, 4 - 60 ns, 5 - 100 ns. Calculations were performed at the same conditions as for figure 3.5, $k_e = 10^{-7}$ cm^{3}s^{-1}.

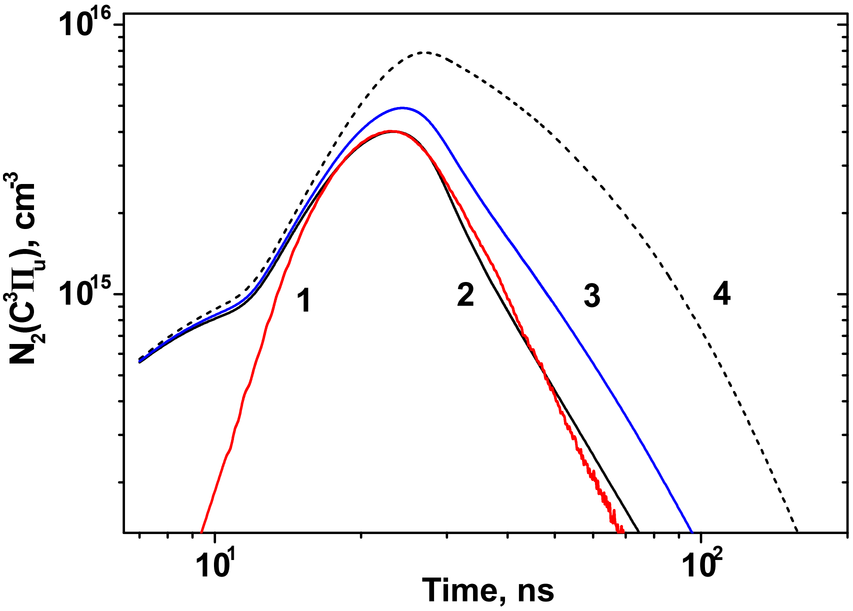

Figure 3.8: Calculated density of $N_2(C^3\Pi_u)$ state averaged over the cross-section of the capillary tube compared to measured emission profile for the first pulse coming to the capillary tube at the same conditions as for figure 3.5. Curve (1) corresponds to PMT signal in arbitrary units, curves (2) – (4) correspond to numerical calculations with the quenching rate constant equal to 10^{-7} cm^{3}s^{-1}, $5 \cdot 10^{-8}$ cm^{3}s^{-1} and 0, respectively.

$$N_e = \frac{I}{e\mu_e SE}. \tag{3.13}$$

Measurements in the main pulse can be done directly from electric current and electric field waveforms similar to presented in figure 3.2 b. To obtain electron density in the afterglow, the additional procedure is required.

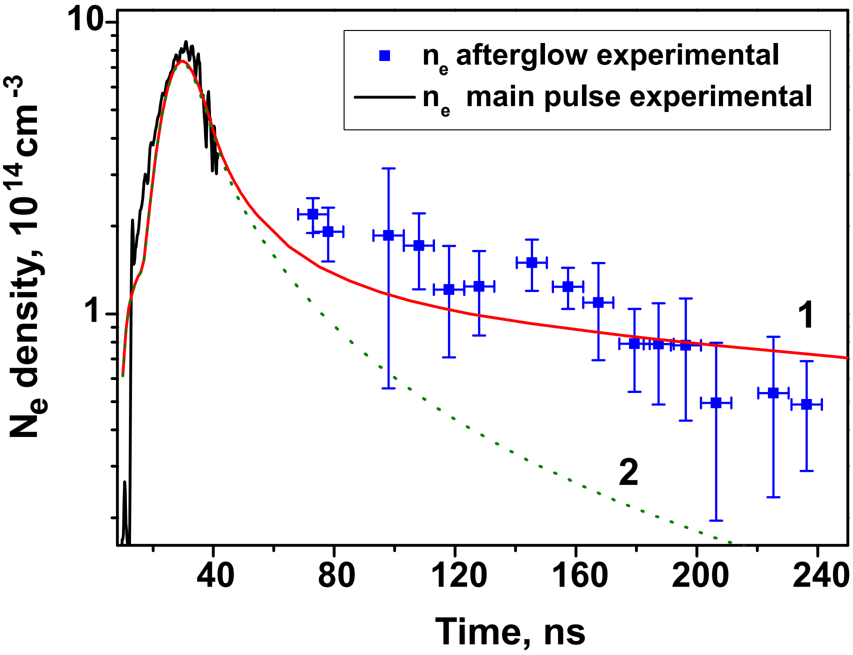

Figure 3.9: Calculated and measured electron density averaged over cross-section of the capillary tube in the afterglow for 27 mbar pure nitrogen and transmitted current 40 A. Calculations are performed with (curve (1)) and without (curve (2)) taking into account the associative ionization.

To measure the electron density profile in the afterglow, the diagnostic pulse with low amplitude was applied with different delays after the main discharge pulse. The reflection of the signal transmitted through the plasma from the end of the delay cable with zero resistance was used as the diagnostic pulse. The length of the diagnostic pulse was about 15 ns FWHM. To maximize the signal-to-noise ratio the central part of the pulse with maximal current was treated. To provide measurements at different time instance, the length of the low-voltage cable was varied.

The amplitude of the reduced electric field in the diagnostic pulse was 60 Td, which is low enough to avoid production of electrons due to ionization by electron impact [?]. The waveform of current in plasma caused by applied diagnostic pulse was obtained by comparison of the signals from BCS1 for two cases: with and without the diagnostic pulse. The last one was measured at matched end-load, equal to the impedance of the used high-voltage cable (50 Ohm). Subtracting this reference signal from the measured one at presence of the diagnostic pulse directly gives the value of the current induced by this pulse. The amplitude of the current is a few amperes, much lower than the amplitude of current in the main pulse used in the measurements, 40 A.

The average electron density in the cross-section of the tube in the afterglow, experimentally obtained with the procedure described above, and results of 1D numerical calculations are presented in figure 3.9.

The good agreement between the calculated value of the electron density and the

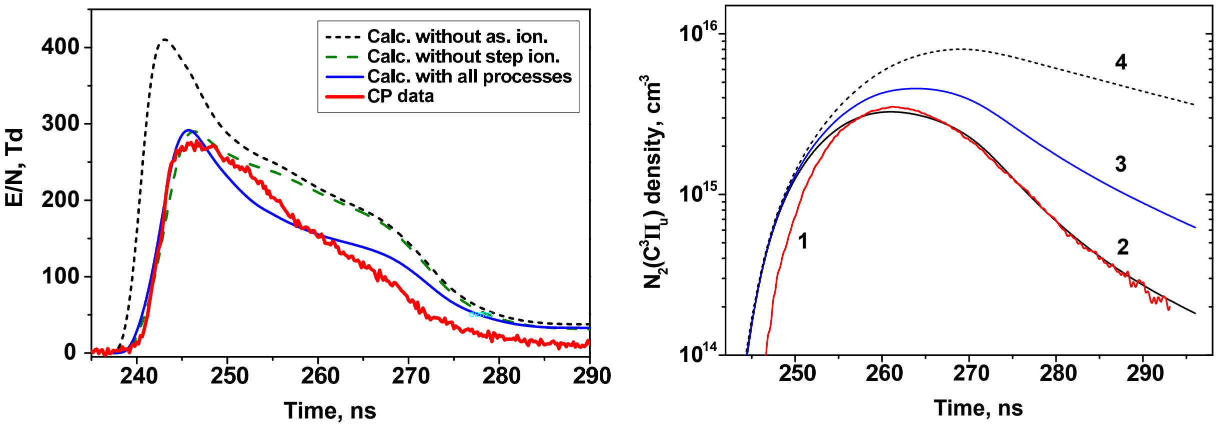

Figure 3.10: Calculation of kinetics for the second pulse at 250 ns after the first pulse. Nitrogen, 27 mbar. (a) Measured current and measured electric field compared with calculated electric field in two assumptions concerning the associative ionization; (b) calculated density of N_2 state compared to measured emission profile. Curve (1) corresponds to PMT signal in arbitrary units, curves (2) – (4) correspond to numerical calculations with the quenching rate constant equal to 10^{-7} cm^{3}s^{-1}, $5 \cdot 10^{-8}$ cm^{3}s^{-1} and 0, respectively.

experimentally obtained one is achieved only if the reactions of associative ionization (3.10) and (3.11) are included in the model (curve 1 in the figure 3.9). Without these reactions plasma decay is much faster (curve 2 in the figure 3.9) that experimentally observed one. Measured and calculated electron density clearly demonstrate that, at conditions of the high specific deposited energy, long-lived plasma can be obtained.

It is also clearly seen from figure 3.6 and figure 3.9 that decreasing of the current causes decreasing of the electron density in the afterglow due to lower excitation degree of nitrogen and, as a consequence, lower efficiency of the reaction of associative ionization. The lower electron density in the main pulse with lower current is in good agreement with figure 3.3 a, where decay of $N_2(C^3\Pi_u, v' = 0)$ decreases with decreasing current value.

The reactions of associative ionization (3.10) and (3.11) determine the residual electron density N_e in the afterglow, in particular, in the beginning of the second pulse at 250 ns after the first main pulse. The calculations of the electric field in the second pulse are sensitive to this value. This can be used as another method to check the effect of associative ionization. The calculations for the second pulse were carried out in two different assumptions: with and without the reactions of associative ionization. The results, presented in figure 3.10, prove the importance of the associative ionization in the afterglow of nanosecond discharge with high specific deposited energy in molecular nitrogen. When reactions (3.10) and (3.11) are taken into account, the waveform for the electric field calculated from the experimentally measured waveform for electric current at initial electron density determined by kinetics between pulses, coincide with $E(t)$ dependence measured experimentally by capacitive probe (see figure 3.10 a). No coincidence is observed if associative ionization is neglected. Finally, quenching of $N_2(C^3\Pi_u)$ in the second pulse is described pretty well within the suggested theory (see figure 3.10 b).

3.6 Conclusions

Study of high–voltage nanosecond capillary discharge in pure nitrogen at high specific deposited energy has been performed. It is shown that, started from deposited energies about 0.1 eV/molecule, quenching of $N_2(C^3\Pi_u)$ state is faster that the quenching caused by collisions with N_2 molecules, and depends upon the energy deposited in the discharge. At specific deposited energies about 0.9 eV/molecule and pressure range $20 - 25$ mbar, a typical time of the emission decay is equal to $\tau_1 \approx 10$ ns instead of theoretically predicted $\tau_0 \approx 30$ ns. The decay is bi-exponential, fast decay corresponding to τ_1 is changed by slower decay τ_2 (also faster than τ_0) in near afterglow, a few tens of nanoseconds after the discharge pulse. Suggested mechanism is based on quenching of $N_2(C^3\Pi_u)$ by electrons.

Numerical 1D–modeling of nanosecond capillary discharge in nitrogen has been performed for the cross-section of measurements. It was based on experimentally measured current $I(t)$, initial radial distribution of the electron density was taken from [21]. The measured reduced electric field $E(t)/N$ in the main pulse was used to validate the calculations.

The numerical calculations show that experimentally measured $N_2(C^3\Pi_u)$ emission profile is in good agreement with calculated one only if the quenching by electrons is included in the model. It is demonstrated that the high electron density in the afterglow is sustained by the reactions of associative ionization from electronically excited $N_2(A^3\Sigma_u^+)$ and $N_2(a'^1\Sigma_u^-)$ states. The presents of a long-lived plasma was proved by electron density measurements in the afterglow.

For additional validation of the suggested quenching mechanism and of the role of the reactions of associative ionization, measurements of $I(t)$, $E(t)/N$) and of $N_2(C^3\Pi_u)$ emission were made for the second high–voltage pulse 250 ns after the main pulse, and compared with results of numerical modeling.

Thus, it has been proved that high quenching rate of $N_2(C^3\Pi_u)$ in capillary discharge in nitrogen at high specific deposited energy is provided by quenching in collisions with electrons. The high electron density in the afterglow is sustained by associative ionization *via* $N_2(A^3\Sigma_u^+)$ and $N_2(a'^1\Sigma_u^-)$ electronically excited molecules.

Bibliography

[1] Vrba P, Vrbova M, Bobrova N A and Sasorov P V 2009 *Eur. Phys. J. D* A study of Z-pinch in capillary filled by boron vapours **54** 481—486

[2] Kameshima T, Kotaki H, Kando M, Daito I, Kawase K, Fukuda Y, Chen L M, Homma T, Kondo S, Esirkepov T Z, Bobrova N A, Sasorov P V and Bulanov S V 2009 Laser pulse guiding and electron acceleration in the ablative capillary discharge plasma *Physics of Plasmas* **16** 093101

[3] Popov N A 2015 Active particles production by pulsed nanosecond discharge in ambient air. quenching of electronically excited states of nitrogen by O_2 molecules and $O(^3P)$ atoms *Proc. of 53rd AIAA Aerospace Sciences Meeting* (5-9 January, 2015, Kissimmee, Florida)

[4] Andersson H E B 1971 An integrated nanosecond pulse generator and laser *Physica Scripta* **4** 215

[5] Andersson H E B and Tobin R C 1974 Electrical breakdown and pumping in an axial-field nitrogen laser *Physica Scripta* **9** 7

[6] Asinovskii E I, Vasilyak L M and Tokunov Y M 1981 Influence of oxygen on generation of nitrogen laser *Teplofiz. Vys. Temp.* **19** 873—875

[7] Abramov A G, Asinovskii E I and Vasilyak L M 1985 Pumping of coaxial nitrogen laser by means of electric breakdown waves *Teplofiz. Vys. Temp* **23** 177—179

[8] Starikovskiy A, Aleksandrov N and Rakitin A 2012 Plasmaassisted ignition and deflagration-to-detonation transition *Philosophical Transactions of the Royal Society of London A: Mathematical, Physical and Engineering Sciences* **370** 740—773

[9] Lu X, Naidis G, Laroussi M and Ostrikov K 2014 Guided ionization waves: theory and experiments *Physics Reports* **540** 123—166 ISSN 0370-1573

[10] Robert E, Barbosa E, Dozias S, Vandamme M, Cachoncinlle C, Viladrosa R and Pouvesle J M 2009 Experimental study of a compact nanosecond plasma gun *Plasma Processes and Polymers* **6** 795—802

[11] Heinlin J, Morfill G, Landthaler M, Stolz W, Isbary G, Zimmermann J L, Shimizu T and Karrer S 2010 Plasma medicine: possible applications in dermatology *JDDG: Journal der Deutschen Dermatologischen Gesellschaft* **8** 968—976

[12] Trizio I, Intranuovo F, Gristina R, Dilecce G and Favia P 2015 *Plasma Processes and Polymers* **12** 1451—1458 He/O_2 atmospheric pressure plasma jet treatments of PCL scaffolds for tissue engineering and regenerative medicine

[13] Colombo V, Fabiani D, Focarete M L, Gherardi M, Gualandi C, Laurita R and Zaccaria M 2014 Atmospheric pressure non-equilibrium plasma treatment to improve the electrospinnability of poly(L-lactic acid) polymeric solution *Plasma Processes and Polymers* **11** 247—255

[14] Klochko A V, Lemainque J, Booth J P and Starikovskaia S M 2015 TALIF measurements of oxygen atom density in the afterglow of a capillary nanosecond discharge*Plasma Sources Science and Technology* **24** 025010

[15] Zhang S, van Gessel A F H, van Grootel S C and Bruggeman P J 2014 The effect of collisional quenching of the $O(3p^3P_j)$ state on the determination of the spatial distribution of the atomic oxygen density in an APPJ operating in ambient air by TALIF*Plasma Sources Science and Technology* **23** 025012

[16] Bruggeman P and Brandenburg R 2013 Atmospheric pressure discharge filaments and microplasmas: physics, chemistry and diagnostics *Journal of Physics D: Applied Physics* **46** 464001

[17] Lepikhin N, Klochko A, Edwards M, Popov N and Starikovskaia S 2015 Capillary nanosecond discharges as a tool for the measurement of quenching coefficients at high specific energy deposition Proc. *53rd AIAA Aerospace Sciences Meeting (5-9 January, 2015, Kissimmee, Florida)* AIAA 2015-0937

[18] Pancheshnyi S, Starikovskaia S and Starikovskii A 2000 Collisional deactivation of $N_2(C^3\Pi_u\ , v = 0, 1, 2, 3)$ states by N_2, O_2, H_2 and H_2O molecules *Chemical Physics* **262** 349—357

[19] Guerra V and Loureiro J 1997 Electron and heavy particle kinetics in a low-pressure nitrogen glow discharge *Plasma Sources Science and Technology* **6** 361

[20] Popov N 2009 Associative ionization reactions involving excited atoms in nitrogen plasma *Plasma Physics Reports* **35** 436—449

[21] Klochko A V, Starikovskaia S M, Xiong Z and Kushner M J 2014 Investigation of capillary nanosecond discharges in air at moderate pressure: comparison of experiments and 2D numerical modelling *J. Phys. D: Appl. Phys.* **47** 365202

[22] Anikin N, Starikovskaia S and Starikovskii A 2004 Study of the oxidation of alkanes in their mixtures with oxygen and air under the action of a pulsed volume nanosecond discharge *Plasma Phys. Rep.* **30** 10281042

[23] Hagelaar G J M and Pitchford L C 2005 Solving the Boltzmann equation to obtain electron transport coefficients and rate coefficients for fluid models *Plasma Sources Sci. Technol.* **14** 722

[24] Phelps A V and Pitchford L C 1985 Anisotropic scattering of electrons by N2 and its effect on electron transport *Phys. Rev. A* **31** 2932–2949

[25] Popov N A 2011 Fast gas heating in a nitrogenoxygen discharge plasma: I. Kinetic mechanism *J. Phys. D: Appl. Phys.* **44** 285201

[26] Mintoussov E I, Pendleton S J, Gerbault F G, Popov N A and Starikovskaia S M 2011 Fast gas heating in nitrogenoxygen discharge plasma: II. Energy exchange in the afterglow of a volume nanosecond discharge at moderate pressures *J. Phys. D: Appl. Phys.* **44** 285202

[27] Kossyi I A, Kostinsky A Y, Matveyev A A and Silakov V P 1992 Kinetic scheme of the non-equilibrium discharge in nitrogenoxygen mixtures *Plasma Sources Sci. Technol.* **1** 207

[28] Herron J T 1999 Evaluated chemical kinetics data for reactions of N(^{2}D), N(^{2}P), and $N_2(A^3\Sigma_u^+)$ in the gas phase *J. Phys. Chem. Ref. Data* **28** 14531483

[29] Popov N A 2013 Dissociation of nitrogen in a pulse-periodic dielectric barrier discharge at atmospheric pressure *Plasma Phys. Rep.* **39** 420424

[30] Vasilyak L M, Kostyuchenko S V, Kudryavtsev N N and Filyugin I V 1994 Fast ionisation waves under electrical breakdown conditions *Phys.Usp.* **37** 247

[31] Starikovskaia S M, Anikin N B, Pancheshnyi S V, Zatsepin D V and Starikovskii A Y 2001 Pulsed breakdown at high overvoltage: development, propagation and energy branching *Plasma Sources Sci. Technol.* **10** 344

[32] Chen C H, Payne M G, Hurst G S and Judish J P 1976 Kinetic studies of N_2 and N_2-SF_6 following proton excitation J. Chem. Phys. 65 38633868

[33] Millet P, Salamero Y, Brunet H, Galy J, Blanc D and Teyssier J L 1973 De-excitation of $N_2(C^3\Pi_u, v' = 0$ and 1) levels in mixtures of oxygen and nitrogen *J. Chem. Phys.* **58** 58395841

[34] Albugues F, Birot A, Blanc D, Brunet H, Galy J, Millet P and Teyssier J L 1974 Destruction of the levels $C^3\Pi_u$, ($v' = 0$, $v' = 1$) of nitrogen by O_2,CO_2, CH_4, and H_2O *J. Chem. Phys.* **61** 26952699

[35] Valk F, Aints M, Paris P, Plank T, Maksimov J and Tamm A 2010 Measurement of collisional quenching rate of nitrogen states $N_2(C^3\Pi_u, v = 0)$ and $N_2^+(B^2\Sigma_g^+, v = 0)$ *J. Phys. D: Appl. Phys.* **43** 385202

[36] Wladimiroff W W and Andersson H E B 1977 The construction and operational analysis of an interference-free, coaxial N_2 laser system *J. Phys. E: Sci. Instrum.* **10** 361

[37] Tokunov Yu M, Asinovskii E I and Vasilyak L M 1981 Lasing and the dynamics of a nanosecond discharge in nitrogen *High Temp.* **19** 347–351

[38] Aleksandrov N L, Kindysheva S V, Nudnova M M and Starikovskiy A Y 2010 Mechanism of ultra-fast heating in a non-equilibrium weakly ionized air discharge plasma in high electric fields *J. Phys. D: Appl. Phys.* **43** 255201

[39] Rusterholtz D L, Lacoste D A, Stancu G D, Pai D Z and Laux C O 2013 Ultrafast heating and oxygen dissociation in atmospheric pressure air by nanosecond repetitively pulsed discharges *J. Phys. D: Appl. Phys.* **46** 464010

[40] Shkurenkov I and Adamovich I V 2016 Energy balance in nanosecond pulse discharges in nitrogen and air Plasma Sources Sci. Technol. 25 015021

[41] Piper L G 1988 State-to-state $N_2(A^3\Sigma_u^+)$ energy-pooling reactions. I. The formation of $N_2(C^3\Pi_u)$ and the Herman infrared system *J. Chem. Phys.* **88** 231–239

[42] Drawin H and Emard F 1976 Instantaneous population densities of the excited levels of hydrogen atoms and hydrogen-like ions in plasmas *Physica B+C* **85** 333–356

[43] Chernyi G G et al 2004 Physical and chemical processes in gas dynamics: physical and chemical kinetics and thermodynamics of gases and plasmas II *Progress in Astronautics and Aeronautics* **vol 197** (Virginia: AIAA Reston)

Chapter 4

Development of DBD discharge at high pressures; filamentation of the discharge

Nanosecond surface dielectric barrier discharge is intensively studied recent 10 years due to increased interest to plasma applications in flow control and combustion [1, 2, 3]. The pioneering experiments [4] based on the known [5] influence of the sinusoidal power DBD discharge on the flow, demonstrated extremely high efficiency of the nanosecond DBD in control of laminar–to–turbulent transition in subsonic flows. The peculiarity of a nanosecond power supply is that the streamers start from the high voltage electrode and propagate synchronously (within 0.2 ns at atmospheric pressure [6]) in the direction perpendicular to the electron edge. Synchronous start of the streamers leads to the initiation of a cylindrical shock wave on the electrode edge [6, 7, 8]. The shock wave, even at low energy input to the discharge, causes a laminar-turbulent transition and subsequent flow reattachment to the surface.

For plasma assisted ignition of combustible mixtures at high pressures, the surface nanosecond DBD in cylindrical geometry has been suggested [9] as an initiator of combustion. This geometry (i) provides maximal possible uniformity of the discharge at high pressures; (ii) leads to multipoint ignition at elevated pressures [10] at minimal possibly hydrodynamic perturbations; (ii) corresponds to cylindrical geometry of a combustion chamber of a rapid compression machine, allowing the experiments at controlled pressure and temperature conditions [11, 12].

For flow control applications, the discharge initiates in the flow, sub–sonic or even transonic flows, with a typical repetitive frequency of a few kHz. For plasma assisted ignition/combustion, a single–short regime of the discharge is used for the experiments in the rapid compression machines [11, 12] and burst modes with tens of pulses separates by microseconds [3, 13] are used for ignition of the combustible mixture flows.

Nanosecond surface discharges at elevated pressures have been studied for a particular case of excimer mixtures in laser physics [14], were the spatial uniformity of the discharge is a very important issue.

To authors knowledge, no systematic study of the nanosecond surface dielectric barrier discharge (SDBD) structure at elevated pressures is reported for air. The aim of the presented chapter is to study the discharge morphology in air within $1-6$ bar pressure

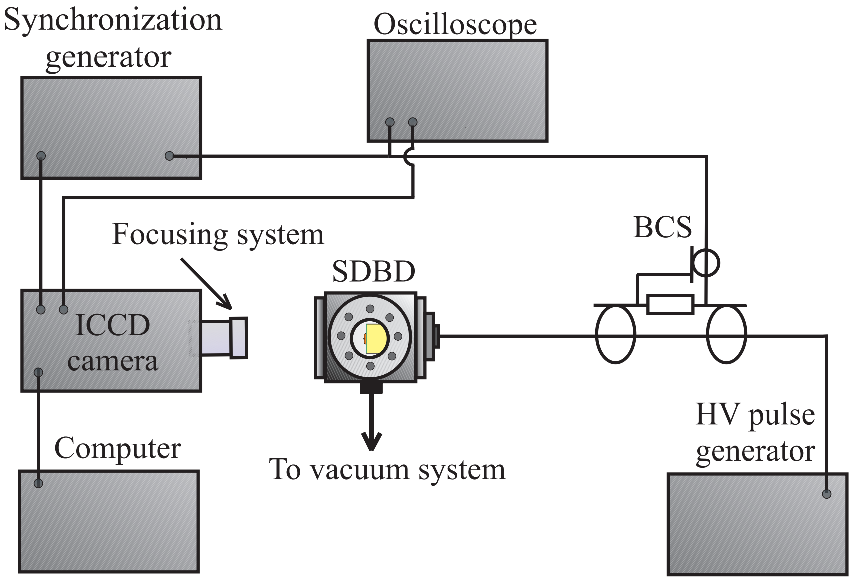

Figure 4.1: Scheme of the experimental setup. BCS–back current shunt.

range at ambient gas temperature.

4.1 Experimental setup

A general scheme of the experimental setup is presented in figure 4.1. The high pressure discharge cell is made of stainless steel and has three optical quartz windows, with a thickness of 15 mm and a diameter of 50 mm. The discharge chamber allows pumping down to 10^{-2} Torr before it is filled by the investigated gas mixture. Two pressure gauges are used to measure the pressure: Pfeiffer capacitive vacuum gauge for the pressures lower than 10 Torr and SCM capacitive gauge for the pressures higher than 1 bar. The chamber was tested up to the pressure P=8 bar, and the experiments have been carried out for a pressure range of 1–6 bar. Synthetic air (80% N_2, 20% O_2, Air Liquide, impurities do not exceed 3 ppm) has been used for the experiments.

A coaxial electrode system [10], schematically represented by figure 4.2, has been developed to obtain a "quasi–uniform" 2D discharge that propagates along the surface in a radially symmetrical geometry. The thickness of the plasma layer in the direction perpendicular to the dielectric plane is about 1 mm. The central coaxial high voltage (HV) electrode is ended by a beveled–edged copper disk, 2 mm in thickness and 20 mm in diameter. The low voltage electrode is made of aluminum. The inner diameter of the low voltage electrode is equal to the outer diameter of the HV electrode, and the outer diameter of the low–voltage electrode is equal to 46 mm. A dielectric layer of PVC 0.3 mm in thickness is located between the electrodes. The discharge starts from the edge of the high voltage electrode and propagates radially along the surface of the PVC layer.

The SDBD electrode system was installed into the port of the high pressure discharge cell, so that one optical window was situated opposite to the electrode system and two others allowed to observe the discharge from the side. The high voltage electrode was connected to the high-voltage generator via a 30 m coaxial 50 Ω cable. The high–voltage

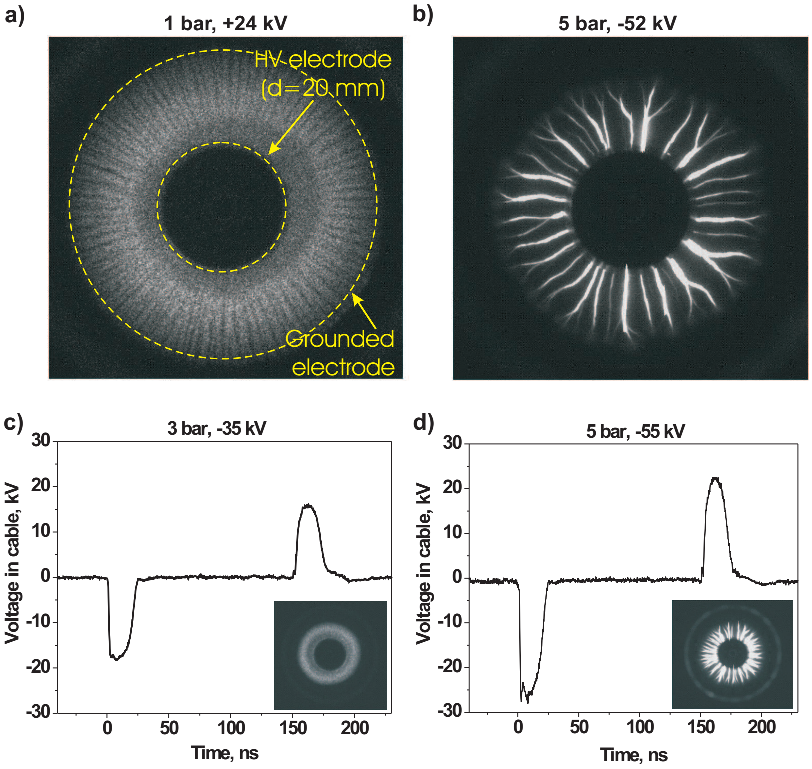

Figure 4.2: Electrode system (left) and typical high-voltage pulse in the cable (right).

(HV) pulse generator (FID Technology, FPG20–03NM) used in experiments provided the following parameters: 0.5 ns pulse front rise time, 20 ns pulse duration on the half–height and ± (12–30) kV voltage range in the cable (see figure 4.2). All discharge SDBD experiments presented in this Report were performed in single shot regime without a gas flow.

Two calibrated back current shunts (BCS) were installed into the cable: one, BCS1, in the middle of the cable and another one, BCS2, 1 m apart from the HV generator. BCS1 was used to measure the voltage on the electrodes, the current through the electrodes and the deposited energy, and the BSC2 was used to synchronize the ICCD camera with the discharge. The signals from the BCSs were registered by a LeCroy WaveRunner 600 MHz oscilloscope.

To study the spatial structure and the development of the surface discharge, a 2D map of emission integrated over the wavelength range 300—800 nm was recorded by ANDOR iStar DH734 ICCD camera. The camera gate was equal to 2 ns. The camera was triggered at different time delays from the beginning of the applied pulse to get the images of the discharge evolution.

In the case of a nanosecond SDBD, the main input to the emission in the considered spectral range is due to transitions of the second positive system of molecular nitrogen. For air, the quenching time of excited levels is determined by the collision of excited nitrogen molecules with molecular oxygen, the rate constant being equal to k=2.7 · 10^{-10} cm^3s^{-1} [15]. The efficient life time of $N_2(C^3\Pi_u)$ is 0.7 ns at the atmospheric pressure and

0.12 ns at $P = 6$ bar, thus ICCD imaging adequately reflects the spatial structure of the discharge, and the resolution is limited by the camera gate.

The monochromator ANDOR 500i combined with ANDOR iStar DH734 ICCD camera was used to study the rotational structure of the second positive systems of nitrogen. The resolution reached in experiments with the grating 2400 l/mm and 100μm input slit width was 0.11 nm. To select the emission from different zones of the discharge, two concentric plastic ring diaphragms of different diameters were installed 3 mm above the dielectric layer coaxially to the electrode system. The diameters of the diaphragms were 20 mm and 26 mm, they selected rings $0-1$ mm and $2-4$ mm from the high voltage electrode respectively. To measure time–resolved emission, monochromator ANDOR 500i and Hamamatsu H6610 photomultiplier tube were used.

To prove that observed peculiarities do not depend upon the geometry of the electrodes, part of the experiments was carried out at atmospheric pressure in linear geometry of the electrodes.

4.2 Experimental results

Two different modes of the discharge can be distinguished at the given experimental conditions, and this is illustrated by Figure 4.3 representing the ICCD images of the discharge taken with a 2 ns camera gate. A discharge, similar to observed in a classical plane–to–plane geometry at atmospheric pressure air, is obtained at relatively low voltages on the high–voltage electrode (see figure 4.3 a). This mode will be further referred as "quasi–uniform" although the discharge consists of a lot of radially propagated emitting channels (streamers) with an optical diameter equal to $0.3-0.5$ mm. A typical observed number of streamers is 120–200. Depending upon the conditions, they are more or less pronounced or even merged together giving the impression of the uniform plasma layer propagating from the high-voltage electrode.

The velocity of the discharge front propagation depends upon voltage, changing from 3.5 to 5 mm/ns for the discharge of positive polarity at 1 bar pressure with the voltage increase from +24 kV to +46 kV on the high-voltage electrode. At these conditions, the velocity is approximately constant along the discharge gap. The discharge slows down with pressure. At negative polarity at the very initial stage of propagation, first $1-2$ ns, the velocity of the emission front is equal to the velocity of the positive polarity discharge. Then the negative polarity SDBD slows down to the velocities $4-6$ times slower than the velocity of the positive polarity discharge. Typically, the emission front of the negative polarity discharge stops at a certain distance without getting the end of the electrode.

The second, filamentary mode of the discharge is observed at high pressures or high voltage amplitude of negative polarity of the voltage pulse. A typical ICCD image of this mode is given by figure 4.3 b. The number of filaments is at least $4-6$ times lower than the number of streamers in the uniform mode, the optical diameter of the filaments is $1-3$ mm. It is worth noting that both modes are low current modes, and that there is no spark formation in the filamentary mode. This fact is confirmed by the signals from the back current shunt BCS1 in the center of the cable, taken for quasi–uniform (figure 4.3 c) and filamentary (figure 4.3 d) regimes. It is clearly seen that, for both modes, a reflected current pulse has an opposite polarity relative to the incident pulse. This means that the reflection takes place from the open edge, no closing of the discharge gap is observed.

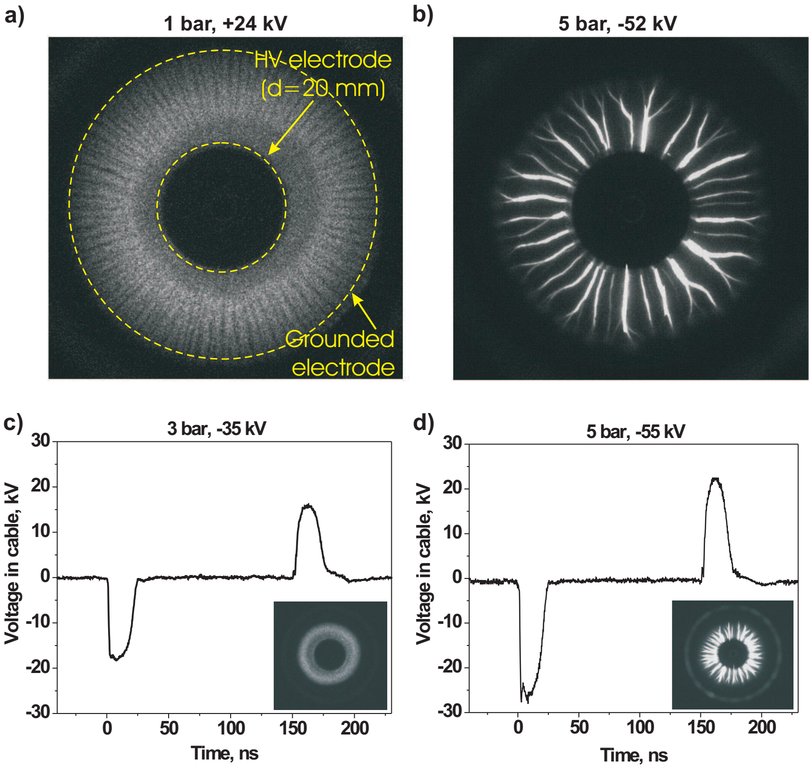

Figure 4.3: ICCD images (a, b) and corresponding signals from the back current shunts (c,d). ICCD gate is 2 ns.

The detailed picture of evolution of the discharge for different pressures and voltages is given by figure 4.4. At positive polarity, the lowest voltage, $U = +24$ kV on the electrode, and the lowest pressure, $P = 1$ bar (figure4.4 a), the discharge develops in the quasi–uniform mode. During a few nanoseconds, the discharge front reaches the low–voltage electrode boundary. The stage of the discharge development corresponds to the most intensive emission. The negative polarity discharge at the same voltage amplitude and pressure (figure4.4 b) develops slowly. The emission is visible mainly on the front of the discharge, in a zone of a few mm in width. Secondary ionization wave starts from the cathode at the decreasing front of the high voltage pulse, at time instants $t > 20$ ns.

For maximal voltage, $U = +47$ kV, and maximal pressure, $P = 6$ bar, a positive polarity discharge is still uniform (figure 4.4 c). The velocity of the propagation slows down. At the back front of the high voltage pulse, only at the highest voltage, some weak filamentation is observed. For the negative polarity discharge, strongly pronounced filamentation is clearly seen (figure 4.4 d). A few nanosecond after the start of the discharge, that is on the plateau of the voltage pulse, initially uniform discharge transforms to filamentary one. The emission intensity increases. The filaments propagate with a velocity comparable with the velocity of a positive polarity discharge at atmospheric pressure, a few mm/ns. They get the end of the low-voltage electrode but the electric circuit remains open, no spark is observed in the system. The emission distribution between filaments is rather uniform. At the back front of the voltage pulse, at $t > 20$ ns,

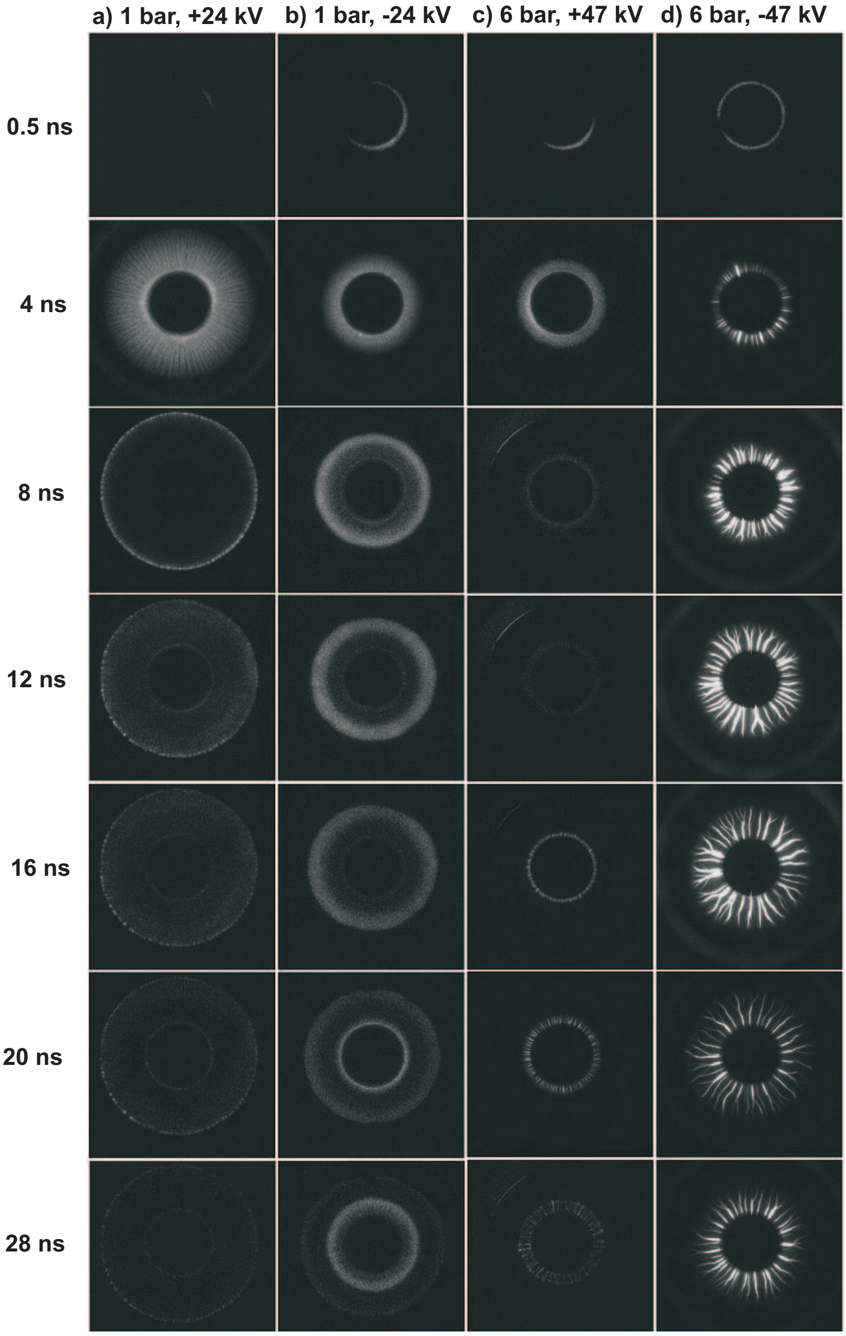

Figure 4.4: Evolution of SDBD in synthetic air for different pressures and voltages. Camera sensitivity is the same for all the images, camera gate is equal to 2 ns. Pulse duration is 20 ns on the half-height.

a secondary discharge, initially filamentary, develops from the edge of the high–voltage electrode.

To find the field of the parameters, corresponding to uniform–to–filamentary mode transition, an additional set of experiments was carried out. The discharge chamber was filled by a synthetic air at a given pressure. The emission from the discharge was controlled by ICCD with 2 ns camera gate, synchronized to the beginning of the high

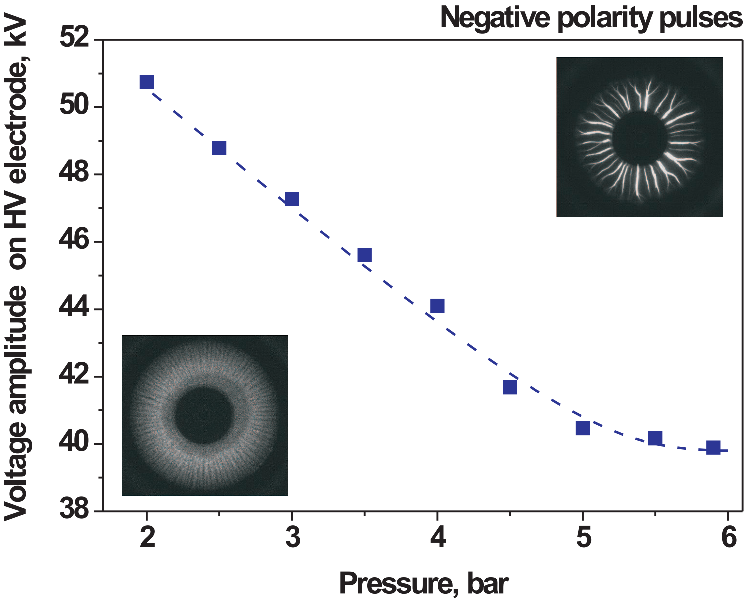

Figure 4.5: Curve separating regions of quasi–uniform diffusive (under the curve) and filamentary (above the curve) discharge as a function of pressure and applied voltage. Negative polarity of the applied pulses. Synthetic air.

voltage pulse with an adjustable delay. The voltage increased until the first filaments were observed. The experiments were performed in a single-shot regime without changing the gas between the experiments. To check the absence of the hysteresis, the experiments were repeated at increasing and then at decreasing voltage. The results are given by figure 4.5. The curve corresponds to the combinations of pressure and voltage when the quasi–uniform discharge transforms into the filamentary. The higher the pressure, the lower is the transition voltage, although it is always in the range of $\sim 40 - 50$ kV on the electrode for the pressure range $1 - 6$ bar.

The details of the transition to filamentary mode at P=3 bar and U=-47 kV are given

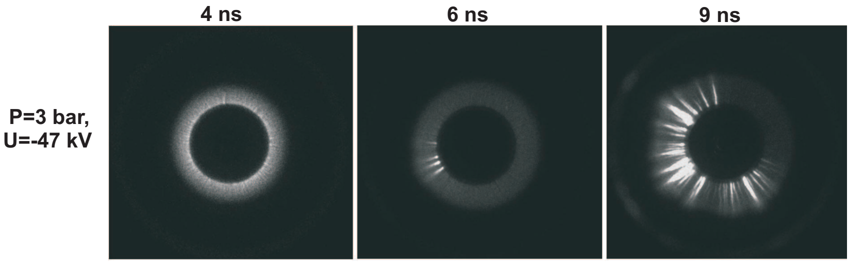

Figure 4.6: Process of transition from quasi-uniform mode to filamentous at P=3 bar, U=-47 kV. Synthetic air. Camera sensitivity is the same for all the images, camera gate is equal to 2 ns.

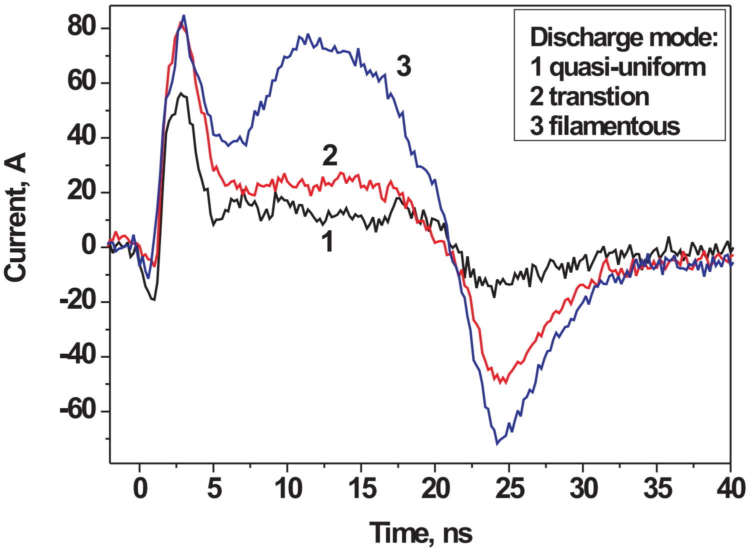

Figure 4.7: Electrical current for $P = 3$ bar: (1) quasi–uniform mode, $U_1 = -36$ kV; (2) transition mode, $U_2 = -47$ kV; and (3) filamentous mode, $U_3 = -55$ kV.

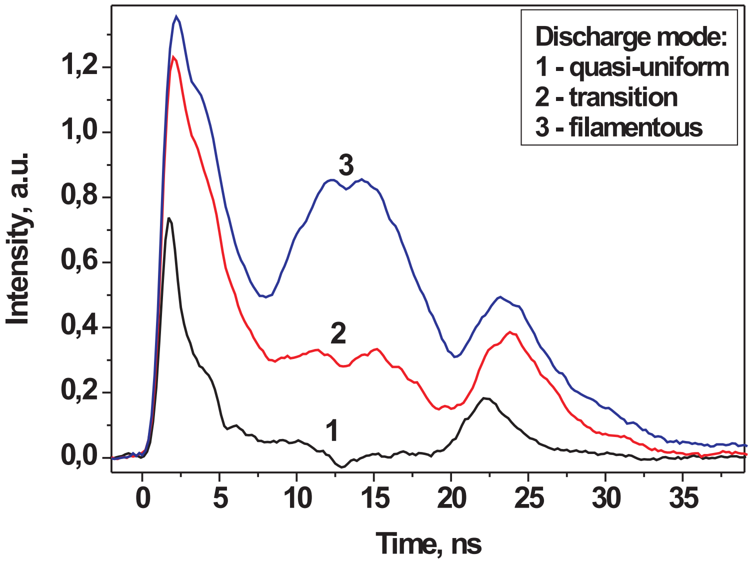

Figure 4.8: Emission oscillograms, $\lambda = 337$ nm, for $P = 3$ bar: (1) quasi–uniform mode, $U_1 = -36$ kV; (2) transition mode, $U_2 = -47$ kV; and (3) filamentous mode, $U_3 = -55$ kV. Emission collected from all the discharge zone.

by a set of ICCD images in figure 4.6. First, the discharge starts from the high–voltage electrode and propagates as the quasi-uniform discharge, that is as a set of streamers with

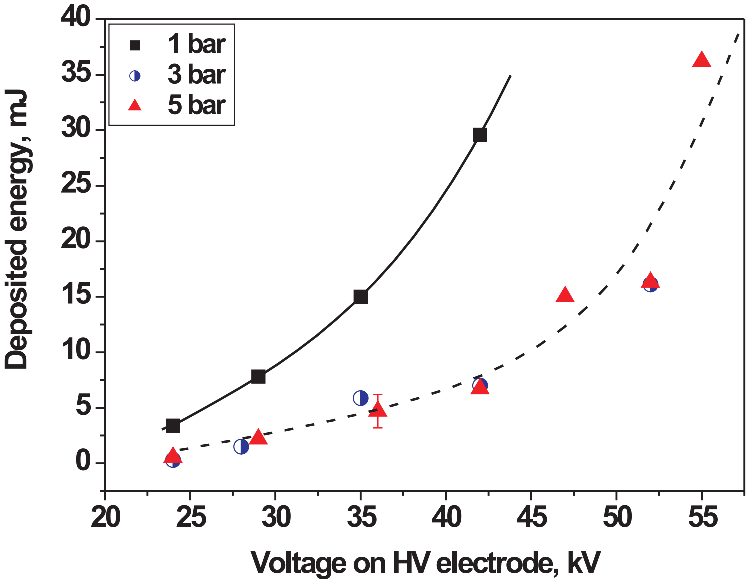

Figure 4.9: Deposited energy in uniform and filamentary modes as a function of voltage on the electrode. $P = 1$ bar, quasi–uniform mode; $P = 3$ bar, transition from quasi–uniform to filamentary mode at $U_2 = -47$ kV; $P = 5$ bar, filamentary mode.

a relatively low emission intensity. Streamers start from the electrode with a velocity a few mm/ns and slow down practically to zero velocity during a few nanoseconds (about $5-7$ ns for the given experimental conditions, this time instant corresponds to the plateau of the high-voltage pulse). At this moment, the emission intensity drops down, and on the week background of the "streamer" emission, a few bright channels develop from the high–voltage electrode with a typical velocity of about 5 mm/ns. The number of bright filaments increases rapidly, and at the end of the pulse they represent already a regular structure. If the voltage is higher than a transition voltage, a regular structure appears within $2 - 4$ ns, as it is shown in figure 4.4 for the pulse of the voltage $U = -47$ kV at pressure $P = 6$ bar.

To get quantitative characteristics of the transition from quasi–uniform to filamentary mode, the electrical current through the discharge, the emission intensity as a function of time and the rotational spectra of emission of molecular nitrogen were measured.

Current through the discharge is presented in figure 4.7. The waveforms were obtained in the following way: first, the losses, namely the signal decay in the cable and charging of the coaxial electrode system in the absence of the discharge were checked experimentally. Second, the current through the discharge was obtained as a difference between the incident and the reflected current pulses from BCS1 taking into account the signal losses. The current obtained in this way corresponds to the sum of the conductivity current and the current of charging of the dielectric surface during the discharge development. The waveforms presented in figure 4.7 correspond to $P = 3$ bar, and to the voltage amplitudes $U_1 = -36$ kV (quasi–uniform mode), $U_2 = -47$ kV (transition mode) and $U_3 = -55$ kV

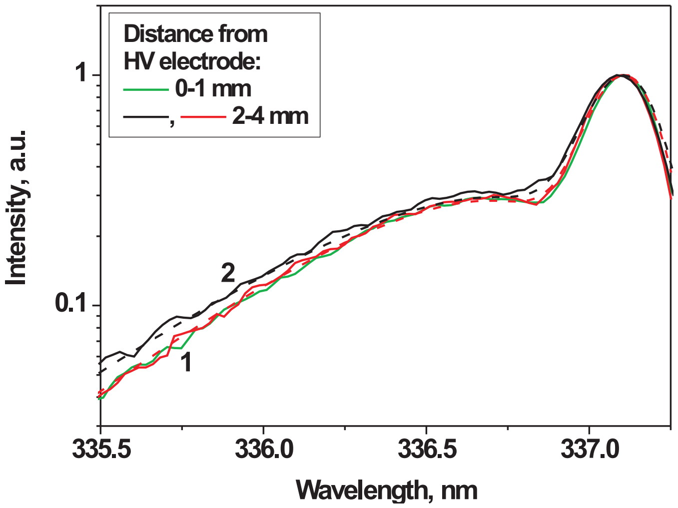

Figure 4.10: Rotational structure of second positive system of nitrogen in synthetic air. The spectra are taken for $P = 3$ bar: (1) quasi–uniform mode, $U_1 = -36$ kV; (2) filamentous mode, $U_3 = -55$ kV. For the quasi–uniform mode, the emission is collected from different distances from the edge of HV electrode, as indicated in the figure. Dashed lines correspond to theoretical approximations at the given temperature (see text).

(filamentous mode). It is seen that the first peak of the current, $0-5$ ns, changes slightly with voltage. This stage corresponds to the very beginning of the discharge, when the discharge pattern is quasi–uniform for all the voltages. At the moment of the transition ($5-7$ ns), a minimum of the current is observed. For quasi–uniform and for transition modes, the currents after this point practically coincide, while for developed filamentary mode (similar to presented in figure 4.4 d), a strong increase of current is observed. If to estimate a number of streamers (for quasi–uniform mode) and filaments (for filamentary mode) in the assumption that, starting from the transition moment, all current is transferred by the filaments only, then the current per channel will be equal 0.1 A/ch for quasi–uniform, 1.6 A/ch for transition and 1.8 A/ch for filamentary modes respectively.

Temporal behavior of emission of the second positive system of molecular nitrogen, transition $N_2(C^3\Pi_u$, v'=0) $\rightarrow N_2(B^3\Pi_g$, v"=0), was measured (figure 4.8) and compared with the behavior of the current. The radiation was collected from the circular diaphragm, selecting the region between 2 and 4 mm from the edge of the high–voltage electrode. As far as an average velocity of negative polarity discharge is about 1 mm/ns (at 3 bar) or lower, the time resolution of the picture, about 2 ns, is limited by crossing the diaphragm (PMT time resolution is equal to 0.7 ns). The intensity of emission increases with voltage, and the shape of the emission changes when a transition to filamentary mode is observed: the peak of emission on the interval $5-20$ ns corresponds to the peak of current (see figure 4.7).

Deposited energy for different pressures is presented in (figure 4.9). The energy was measured as the difference between the energies of incident and reflected pulses taking into account the losses in the cable and charging of the capacitance of the electrode system. The deposited energy decreases rapidly with pressure, by a factor of 4 with pressure increase from 1 to 3 bar, and then practically does not change. Deposited energy increases practically exponentially with the voltage on the electrodes. No sharp change of the energy is seen at the moment of uniform–to–filamentary transition ($P = 3$ bar, $U = -47$ kV).v

The rotational emission spectra of the second positive system of nitrogen for quasi–uniform and for filamentary modes are given by figure 4.10. The radiation was collected from the ring diaphragms selecting the regions $0 - 1$ mm and $2 - 4$ mm from the edge of the high–voltage electrode. It is clearly seen that the spectra for both distances from the high voltage are identic and correspond to the same rotational temperature. The black curve represents theoretical fit for the spectra. For uniform discharge mode, the rotational temperature is equal to $T_{rot} = 300$ K, and for filamentary mode, it is equal to $T_{rot} = 317$ K.

4.3 Discussion

Development of a surface dielectric barrier discharge (SDBD) is a propagation of an ionization wave charging the dielectric surface. Streamers start from the high-voltage electrode and propagate along the surface of the low-voltage electrode covered by a dielectric layer. For negative polarity SDBD, when the high-voltage electrode is a cathode, electrons move from bulk of plasma to the anode. This leads to partial equalizing of electric potential along the vertical axis, and so, to absence of high values of electric fields perpendicular to the dielectric layer, in the bulk of plasma.

It should be noted that the charge distribution on the surface must be relatively uniform [16], because any disturbance in charge distribution induces high electric field and increase of electron flux in this zone, shrinking the non-uniformity.

When the dielectric surface is charged, the influence of processes on the surface and in the bulk of plasma is low. Indeed, plasma decay in the channels can as fast as a few nanoseconds, and space charge can stay on the surface much longer, up to milliseconds.

Comparison of shape of electrical current (taken from figure 4.7) and emission of 2^+ system of molecular nitrogen (taken from figure 4.8) for the regime corresponding to quasi-uniform–to–filamentary transition, is given by figure 4.11. In the streamer channel the conduction current is higher than the displacement current, and so,

$$I_d \sim N_e \cdot \mu_e \cdot E/N, \tag{4.1}$$

where N_e is electron density and μ_e is electron mobility.

The density of the emitting state, $N_2(C^3\Pi_u)$, can be expressed as follows:

$$\frac{dN_C}{dt} = k_C \cdot N_e \cdot [N_2] - N_C \cdot \nu_q. \tag{4.2}$$

Here ν_q is quenching frequency. As far as ([15]) at $P = 3$ bar and $T = 300$ K a typical time of quenching of $N_2(C^3\Pi_u)$ by nitrogen and oxygen molecules is equal to $\nu_q^{-1} \approx 0.2$ ns, that is much lower typical time of changes of emission (see figure 4.11), that is

$$\nu_q \gg \frac{1}{N_C}\frac{dN_C}{dt}. \tag{4.3}$$

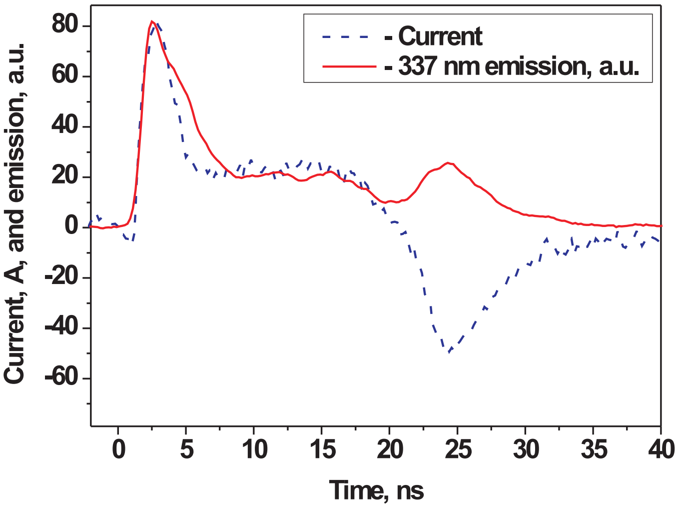

Figure 4.11: Discharge in synthetic air. Comparison of experimental data for electrical current through the high-voltage electrode (blue dashed curve) and for emission of the second positive system of molecular nitrogen at the distance 2-4 mm from the high voltage electrode (red solid curve) at $P = 3$ bar and $U = -47$ kV. Parameters correspond to transition mode.

In this case, using the equation (4.2) it can be obtained for the density of $N_2(C^3\Pi_u)$ molecules:

$$N_C = \frac{k_C(E/N) \cdot N_e \cdot [N_2]}{\nu_q}. \tag{4.4}$$

Thus, the intensity of the emission of the 2^+ system is proportional to

$$Int \propto N_e \cdot (E/N)^\alpha, \tag{4.5}$$

where $\alpha = d\ln(k_C)/d\ln(E/N)$ is an exponential quantity of the rate of excitation of $N_2(C^3\Pi_u)$ by an electron impact as a function of E/N.

For electric fields in the range $E/N = 30 - 130$ Td, $\alpha \geq 5$. So, the ratio of emission intensity Int and discharge current I_d is

$$\frac{Int}{I_d} \propto (E/N)^{\alpha-1}, \tag{4.6}$$

where $(\alpha - 1) \geq 4$. It follows from figure 4.11, that for diffusive (quasi-uniform) mode of the discharge ($t = 2 - 6$ ns, see figure 4.6) and during the transition to filamentary mode, up to the trailing edge of the high-voltage pulse, the ratio $Int/I_d \approx cont.$ As far as α is a large value, this means (see equation (4.6)) that at 2 ns $< t <$ 20 ns the reduced electric field E/N is approximately constant.

The electric field remains constant even under the transition from quasi–uniform to filamentary mode at 6 ns. The fact that electric current value is constant within the

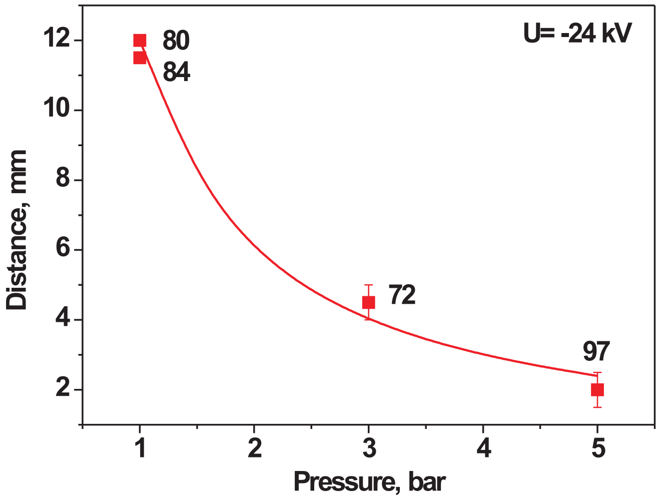

Figure 4.12: Distance of the maximal length of the discharge propagation as a function of gas pressure. Numbers near the curves correspond to longitudinal electric field estimated as described in the text. Solid curve corresponds to $E/N = 80$ Td.

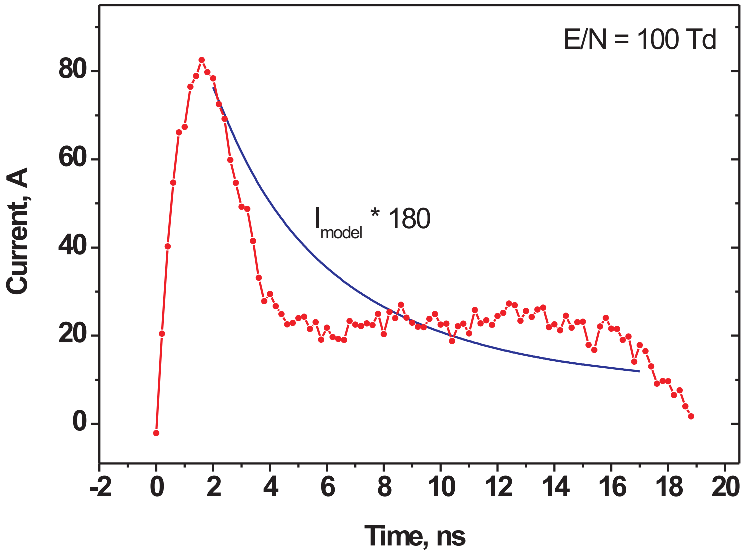

Figure 4.13: Discharge current as a function of time. Curve with points correspond to experimental curve, solid curve corresponds to calculations at $E/N = 100$ Td, $N_e^0 = 2.5 \cdot 10^{15}$ cm^{-3}, $R_0 = 0.08$ mm. Air, $P = 3$ bar, $T = 300$ K. The number of streamers was taken equal to $Z = 180$.

interval at 6 ns $< t <$ 20 ns, means that, at least at the transition mode, new filaments collect "elementary' currents of streamers of the quasi–uniform mode: increase of number of filaments from $Z = 1 - 2$ at 6 ns to $Z = 10 - 20$ at $t = 20$ ns does not change the total

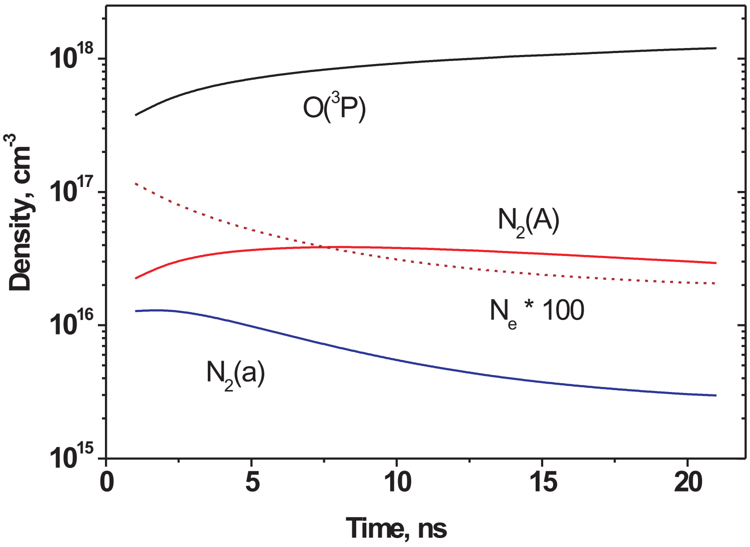

Figure 4.14: Kinetic curves for the main species on the channel axis for the conditions of figure 4.13: $N_e^0 = 2.5 \cdot 10^{15}$ cm^{-3}, $P = 3$ bar, $T = 300$ K.

current.

Let us also note that changing the structure of the whole picture can be also considered as an instability, when a regular structure of streamers separated by less than parts of mm, changes to another regular structure with a distance between filaments of a few mm. If the filaments "collect" the charge of the surrounding streamers, then during this instability development time ($t_{inst} \sim 10$ ns) the charge could be collected through the electrons drift distance. Typical electric field in the head of the ionization front corresponds to the drift velocity $v_{dr} \sim 0.3$ mm/ns, which together with the instability development time gives a spatial scale of inter-channel distance ($L \sim t_{inst} \cdot v_{dr} \sim 3$ mm).

The electric field in the SDBD streamer channel can be estimated on the basis of modeling [17]. According to [17], at $P = 1$ bar and $U = -10$ kV the length of the maximal streamer propagation is $Z = 4$ mm. Under assumption that $U_h \ll U$, where U_h is a potential drop in the streamer head and that the main potential drop takes place along the channel, it is obtained for the average longitudinal electric field in the streamer channel

$$(E/N)_{ch} \approx (U - U_{cath})/(Z \cdot N) \approx 100 \text{ Td}. \qquad (4.7)$$

Here $U_{cath} \approx 0.2$ kV [18] is the voltage on the cathode layer, N is gas number density at $P = 1$ bar and $T = 300$ K, $Z = 0.4$ cm.

Estimation on the basis of the experimental data gives somewhat lower values, about 80 Td. Figure 4.12 represents the maximal length of the streamer propagation, Z in the coaxial electrode system for the voltage $U = -24$ kV on the high–voltage electrode. It is clearly seen that, for all the considered pressure range, the average reduced electric field, calculated in a similar way, is about $E/N \approx 80$ Td.

The obtained values are in a good correlation with the results of the calculations of reduced electric field in the surface streamers [19, 20], where the calculation give a typical value of about 80–110 Td.

Two independent approached were used to estimate the streamer channel radius at conditions of our experiments. It is known [21, 22, 23] that the streamer radius decreases with pressure, $R_{ch} \propto N_0/N$. At atmospheric pressure, the radius of the streamer channel [22, 23, 24] determined from the electron density distribution is equal to $R_{ch} = 0.25 - 0.3$ mm. So, for $P = 3$ bar the streamer radius will be equal to $R_{ch} = 0.08 - 0.1$ mm.

At the current value $I_{sum} = 80$ A, corresponding to the maximum current value of transition mode, and at the number of channels $Z = 150 - 200$, the current per streamer is equal to $j = 0.4 - 0.54$ A. To get the normal current density in the cathode layer, $j_n \approx 1.7$ kA/cm^2 at $P = 3$ bar [18], it is necessary that the streamer radius near the cathode is equal $R_{ch} = 0.09 - 0.1$ mm. This value is in a good correlation with the estimate above made on the basis of measurements and numerical modeling for atmospheric pressure discharges.

The estimated values of the electric field E/N_{ch} and of the streamer channel radius R_{ch} were used as initial parameters for numerical modeling of electron density and electrical current in a single streamer in air at $P = 3$ bar pressure. The calculations were made for $E/N = 100$ Td using 1D axisymmetric model. Processes of production and decomposition of the following ions were taken into account: O_2^+, O_4^+, $O_2^+ \cdot N_2$, N_2^+, N_4^+, NO^+, O^-, O_2^-, O_3^-, O_4^-.Gaussian shape was taken for initial density distribution of the charged particles:

$$N_e(r) = N_e^0 \exp\left[-\left(\frac{r}{R_0}\right)^2\right]. \tag{4.8}$$

The initial channel radius was estimated as $R_0 = 0.08$ mm, the initial electron density was taken equal to $N_e^0 = 2.5 \cdot 10^{15}$ cm^{-3}.

At given value of the electric field along the dielectric surface, E_x/N, a streamer current for every time instant was calculated from the following equation:

$$I = 2\pi e \upsilon_{dr}(E_x/N) \int_0^\infty N_e(r) r dr, \tag{4.9}$$

where $N_e(r)$ is a radial distribution of the electron density, $\upsilon_{dr}(E_x/N)$ is electron drift velocity, depending upon E_x/N. It was assumed that, for considered region, electric field perpendicular to the electrode surface, E_y, is close to zero.

To compare the results of the numerical modeling with the experimental data, the data for a single channel were multiplied by a number of channels, $Z = 180$. The results of comparison of electrical current through the high-voltage electrode are given by figure 4.13.

Table 4.1: Reactions involving negative ions in air

No	Reaction	Rate constant*
R1	$e + O_2 \rightarrow O(^3P) + O^-$	$k = k(E/N)$
R2	$O^- + O(^3P) \rightarrow O_2 + e$	$5.0 \cdot 10^{-10}$
R3	$O^- + O_2(a) \rightarrow O_3 + e$	$3.0 \cdot 10^{-10}$
R4	$O^- + O(^3P) \rightarrow O_2^- + O(^3P)$	$1.0 \cdot 10^{-10}$
R5	$O^- + O_2 + M \rightarrow O_3^- + M$	$1.1 \cdot 10^{-30}$ (300/T)
R6	$O_3^- + O(^3P) \rightarrow O_2 + O_2 + e$	$3.0 \cdot 10^{-11}$
R7	$O_3^- + O(^3P) \rightarrow O_2^- + O_2$	$3.2 \cdot 10^{-11}$

Table 4.1: Reactions involving negative ions in air

No	Reaction	Rate constant*
R8	$O_3^- + CO_2 \rightarrow CO_3^- + O_2$	$5.5 \cdot 10^{-10}$
R9	$e + O_2 + O_2 \rightarrow O_2^- + O_2$	$k(T, T_e)$
R10	$O_2^- + O(^3P) \rightarrow O_3 + e$	$1.5 \cdot 10^{-10}$
R11	$O_2^- + O_2(a) \rightarrow O_2 + O_2 + e$	$2.0 \cdot 10^{-10}$
R12	$O_2^- + O(^3P) \rightarrow O_2 + O^-$	$3.3 \cdot 10^{-10}$
R13	$O_2^- + O_2 + M \rightarrow O_4^- + M$	$3.5 \cdot 10^{-31}$ (300/T)
R14	$O_4^- + M \rightarrow O_2^- + O_2 + M$	$10^{-10} \cdot$ exp(-1044/T)
R15	$O_4^- + O(^3P) \rightarrow O_3^- + O_2$	$4.0 \cdot 10^{-10}$
R16	$O_4^- + O(^3P) \rightarrow O^- + O_2 + O_2$	$3.0 \cdot 10^{-10}$
R17	$O_4^- + H_2O \rightarrow O_2^-(H_2O) + O_2$	$1.5 \cdot 10^{-10}$
R18	$O_x^- + M^+ \rightarrow O_x + M$	$1.0 \cdot 10^{-6}$

* Dimensions for two-body reactions is cm^3/s; dimensions for tree-body reactions is cm^6/s.

Densities for electrons, atomic oxygen and electronically excited nitrogen molecules on the axis of a single streamer for the conditions of figure 4.13 ($N_e^0 = 2.5 \cdot 10^{15}$ cm^{-3}, $P = 3$ bar, $T = 300$ K) are plotted in figure 4.14. During a short time interval, $t < 5$ ns, the electron density decays by a factor of 5 in the processes of electron-ion recombination and electron attachment to oxygen molecules. Then electron density decay slows down, as far as the additional processes of ionization become important. They are the detachment of electrons form the negative ions in collisions with atomic oxygen:

$$\begin{aligned} O_2^- + O(^3P) &\rightarrow O_3 + e, \\ O^- + O(^3P) &\rightarrow O_2 + e, \\ O_3^- + O(^3P) &\rightarrow O_2 + O_2 + e, \end{aligned} \tag{4.10}$$

and associative ionization in collisions with electronically excited nitrogen molecules [26]. Thus, performed calculations confirm that electric current in the discharge during the uniform phase can be explained by kinetics under the given conditions, namely by the fast decay of electron density due to recombination and attachment, and then by relatively slow change of N_e due to additional sources of electrons, namely detachment in collisions with accumulated in the discharge atomic oxygen (see Table 4.1 for details) and associative ionization in collisions with electronically excited nitrogen molecules. Atomic density in the discharge reaches high values, [O(^{3}P)]= 10^{18} cm^{-3}, and electron density at time interval $t = 10 - 20$ ns exceeds $2 \cdot 10^{14}$ cm^{-3}. It should be mentioned that electron density decay on the axis of the discharge is higher than the decrease of current density. Indeed, characteristic frequencies of electron-electron and electron-ion recombination increase with the density of the charged particles, so, plasma decay on the discharge axis is faster than at the periphery. As far as discharge current is calculated using average electron density (see equation (4.9)), the low electron density at the discharge periphery influences the current value. Let us also note that, at $t > 6$ ns, discharge current depends significantly from the E/N value. This is explained by decrease of dissociation of molecular oxygen with E/N and, consequently, by more intensive production of electrons in reactions (4.10).

4.3.1 Ionization–overheating instability as a mechanism of filamentation

Voltage increase on the high-voltage electrode leads to increase of the electric field and, consequently, to the production of charged species near the electrode. The created plasma is polarized forming a charged cathode layer. Typical length of the cathode layer in air is equal $P \cdot d = 0.25$ Torr $\cdot$ cm, that is $d \approx 1.1 \cdot 10^{-4}$ cm cm at $P = 3$ bar and $T = 300$, and normal current density is $j_n/P^2 = 330$ μA/(cm^2$\cdot$ Torr^2) [18], that is $j_n \approx 1.7$ kA/cm^2 at $P = 3$ bar. Typical time of pressure equalization in the cathode layer is about $\tau_g = 3$ ns at $d = 1\mu$m and $T = 300$ K, that is the development of the ionization-overheating instability is possible at our conditions starting from $t = 4 - 6$ ns if the gas heating is high enough. Electric field in the cathode layer is higher than 10^3 Td and decreases with distance from the high-voltage electrode. Electric field in the channels of streamers is about $E/N \approx 100$ Td [16][2]. On the boundary of the cathode layer the electron density is already high and the electric fields are higher than in the channel. Let us estimate a possible gas heating on the boundary. At electron density $N_e^0 = (1 - 2) \cdot 10^{15}$ cm^{-3} and field at the boundary of the cathode layer $E/N \approx 120$ Td [25] the specific deposited energy during first 5 ns is equal to $W = 0.1 - 0.2$ eV/molec, and so gas heating can be as high as $\Delta T = 50 - 100$ K. The main input to fast gas heating under these conditions is due to dissociation of O_2 by an electron impact, due to quenching of electronically excited nitrogen molecules by oxygen molecules and due to quenching of O(^{1}D) excited atoms by molecular nitrogen [28, 29]. Characteristic times of these reactions under given conditions do not exceed 0.3 ns.

Development of an ionization-overheating instability causes the increase of the electron density and the elongation of the plasmoid along the electric field because of the amplification of the field in the head of the plasmoid, a probability of development of the ionization-overheating instability increases with pressure. Indeed, a typical length of the cathode layer decreases with pressure and so, typical hydrodynamic time decreases, allowing gas expansion on a characteristic length scale. In addition, a probability of development of the instability increases with applied voltage. Increase of the applied voltage leads to increase of the ionization degree N_e/N and to increase of a specific deposited energy in the cathode layer. So, gas temperature and velocity of sound in this region increase. An increase of the probability of development of the ionization–overheating instability with pressure and voltage amplitude correlates with the obtained experimental data (see figure 4.5).

4.4 Conclusions

Development and propagation of a pulsed nanosecond surface dielectric barrier discharge has been studied in synthetic air for radially symmetric and for planar geometries for a range of pressures 1-5 bar at ambient temperature. It was shown that, at low voltages, discharge consists of a few hundreds of thin streamers, filling in a "quasi–uniform" manner the dielectric surface. Starting form a certain values of voltage and pressure, in the negative polarity discharge the streamers slow down and stop; and the discharge transforms into a regular filamentary structure. The parameters of the structure (number of filaments, distance between them) practically do not change in the considered range of parameters. No significant changes of the deposited energy, current and electric field are observed at transition point.

Theoretical estimates and numerical modeling show that ionization–overheating instability on the boundary of the cathode layer can be suggested as a mechanism of filamentation. Calculations of kinetics in air at the parameters similar to the parameters of experiments demonstrate that fast, a few nanosecond, decay of the electrical current in the discharge during the uniform phase can be explained by fast decay of electron density due to recombination and attachment. Following detachment in collisions with accumulated in the discharge atomic oxygen and associative ionization in collisions with electronically excited nitrogen molecules keep the electron density at relatively high value, supporting development of the second phase of the discharge.

Bibliography

[1] Starikovskaia S M, Starikovskii A Yu 2010 Plasma assisted ignition and combustion*In: Handbook of Combustion* by Lackner M (Ed.), Winter F (Ed.), Agarwal A K (Ed.), Wiley-VCH, ISBN; 978-3527324491

[2] Starikovskiy A Yu, Aleksandrov N L 2011 Plasma–assisted ignition and combustion *In: Aeronautics and Astronautics* Ed by: Max Mulder. ISBN, 978-953-307-473-3

[3] Adamovich I V, Choi I, Jiang N, Kim J–H, Keshav S, Lempert W R, Mintusov E I, Nishihara M, Samimy M, Uddi M, 2009 Plasma assisted ignition and high-speed flow control: non-thermal and thermal effects *Plasma Sources Sci. Technol.* **18** 034018 (13pp)

[4] Roupassov D V, Zavyalov I N, Starikovskii A Yu, Saddoughi S G 2006 Boundary layer separation control using low–temperature non–equilibrium plasma of gas discharge". *44th AIAA Aerospace Sciences Meeting and Exhibit, 9-12 January 2006, Reno, Nevada. AIAA 2006-373* // Roupassov D V, Zavyalov I N, Starikovskii A Yu, Saddoughi S G 2007 Boundary layer separation control by nanosecond plasma actuators. *Joint Prorulsion Conference, 2007, Miami, Florida, AIAA 2007-4530.*

[5] Roth J R, Sherman D M and Wilkinson S P 1998 Boundary layer flow control with a one atmosphere uniform glow discharge surface plasma *Proc. of AIAA Meeting* Reno, USA, January 1998, paper N98-0328

[6] Starikovskii A Yu, Nikipelov A A, Nudnova M M and Roupassov D V 2009 SDBD plasma actuator with nanosecond pulse–periodic discharge *Plasma Sources Sci. Technol* **18** 034015(17 pp)

[7] Miles R B, Opaits D F, Shneider M N, Zaidi S H, and Macheret S O, 2009 Non–thermal atmospheric pressure plasmas for aeronautic applications *Eur. Phys. J. Appl. Phys.* **47** 22802

[8] Nishihara M, Takashima K, Rich J W, and Adamovich I V, 2011 Mach 5 bow shock control by a nanosecond pulse surface dielectric barrier discharge *Physics of Fluids* **23** 066101

[9] Starikovskaia S M, Allegraud K, Guaitella O, et al 2009 Surface discharges: possible applications for plasma-assisted ignition and electric field measurements. AIAA-2010-1587, 48th AIAA Aerospace Sciences Meeting Including The New Horizons Forum and Aerospace Exposition, 4— 7 Jan 2010, Orlando, Florida, USA.

[10] Kosarev I N, Khorunzhenko V I, Mintoussov E I, Sagulenko P N, Popov N A and Starikovskaia S M, Starikovskii A Yu, 2012 A nanosecond surface dielectric barrier discharge at elevated pressures: time-resolved electric field and efficiency of initiation of combustion *Plasma Sources Sci. Technol.* **21** 045012 (15pp)

[11] Starikovskiy A, Rakitin A, Correale G, Nikipelov A, Urushihara T, Shiraishi T, 2012 Ignition of hydrocarbon–air mixtures by nonequilibrium plasma at elevated pressures up to 40 bar. *Proc. of 50th AIAA Aerospace Sciences Meeting Including the New Horizons Forum and Aerospace Exposition* 9—12 Jan 2012, Nashville, USA.

[12] Stepanyan S A, Boumehdi M A, Vanhove G, Desgroux P, Starikovskaia S M 2013 Time-resolved electric field measurements in nanosecond surfacedielectric discharge. Comparison of different polarities. Ignition of combustible mixtures by surface discharge in rapid compression machine *Proc. of 51st AIAA Aerospace Sciences Meeting, 7-10 January 2013, Grapevine, Texas* AIAA 2013-1053

[13] Sun W, Won S H, Ombrello T, Carter C, Ju Y 2013 Direct ignition and S–curve transition by in situ nanosecond pulsed discharge in methane/oxygen/helium counterflow flame, *Proc. of the Comb. Inst.* **34(1)** 847—855

[14] Boichenko A M, Lomaev M I, Panchenko A N, Sosnin E A and Tarasenko V F 2011 Ultraviolet and VUV excilamps: physics, technique and applications *Tomsk, STT, in Russian*

[15] Pancheshnyi S V, Starikovskaia S M and Starikovskii A Yu 1998 Measurements of rate constants of the N_2 ($C^3\Pi_u$, $v' = 0$), and N_2^+ ($B^2\Sigma_u^+$, $v' = 0$) deactivation by N_2, O_2, H_2, CO and H_2O molecules in afterglow of the nanosecond discharge *Chemical Physics Letters* **29** 523–527

[16] Tanaka D, Matsuoka S, Kumada A and Hidaka K 2009 Two–dimensional potential and charge distributions of positive surface streamer *J. Phys. D: Appl. Phys.* **42** 075204 (6pp)

[17] Gibalov V I, Pietsch G J 2000 The development of dielectric barrier discharges in gas gaps and on surfaces *J. Phys. D: Appl. Phys.* **33** 2618—2636

[18] Raizer Yu P 1991 Gas Discharge Physics *New York: Springer*

[19] Gibalov V I, Pietsch G J 2012 Dynamics of dielectric barrier discharges in different arrangements *Plasma Sources Sci. Technol.* **21** 024010 (35pp)

[20] Likhanskii A, 2009 Study of plasma phenomena at high electric fields in applications for active flow control and ultra–short pulse laser drilling, PhD Thesis, The Pensylvania State University.

[21] Naidis G V 1999 Simulation of streamer-to-spark transition in short non-uniform air gaps *J. Phys. D: Appl. Phys.* **32** 2649-2654

[22] Tardiveau P, Marode E, Agneray A and Cheaib M 2001 Pressure effects on the development of an electric discharge in non-uniform fields *J. Phys. D: Appl. Phys.* **34** 1690-1696

[23] Pancheshnyi S, Nudnova M, Starikovskii A 2005 Development of a cathode-directed streamer discharge in air at different pressures: Experiment and comparison with direct numerical simulation *Phys. Rev.* **71** 016407

[24] Pancheshnyi S V, Starikovskii A Yu 2003 Two-dimensional numerical modelling of the cathode-directed streamer development in a long gap at high voltage *J. Phys. D: Appl. Phys.* **36** 2683

[25] Soloviev V, Krivtsov V 2009 SDBD discharge modelling for aerodynamic applications *J. Phys. D: Appl. Phys.* **42** 125208

[26] Kossyi I A, Kostinsky A Y, Matveev A A, Silakov V P 1992 Kinetic scheme of the non-equilibrium discharge in nitrogen-oxygen mixtures *Plasma Sources Sci. Technol.* **1** 207-220

[27] Popov N A 2010 Evolution of the negative ion composition in the afterglow of a streamer discharge in air *Plasma Physics Reports.* **36** 812-818

[28] Aleksandrov N L, Kindysheva S V, Nudnova M M, Starikovskiy A Yu 2010 Mechanism of ultra-fast heating in a nonequilibrium weakly-ionized air discharge plasma on high electric fields *J. Phys. D: Appl. Phys.* **43** 255201

[29] Popov N A 2011 Fast gas heating in a nitrogen-oxygen discharge plasma: I. Kinetic mechanism *J. Phys. D: Appl. Phys.* **44** 285201

Chapter 5

Morphology of the dielectric barrier discharge for multipoint plasma–assisted ignition at high pressures

5.1 Introduction

Transient plasma of nanosecond discharges is widely used for studying of the kinetic effects connected to plasma assisted ignition (PAI) and plasma assisted combustion (PAC) in hydrocarbon–containing mixtures. In spite of the fact that the PAI/PAC topic is developing for more than 15 years [1, 2, 3], a limited number of experiments is available for high pressures, typical for combustion environment. Three main discharge configurations are used for plasma assisted ignition at high pressures: nanosecond spark in a few mm gap between two point–to–point electrodes; transient plasma ignition (TPI) where current is limited by interelectrode distance and/or pulse duration; and nanosecond surface dielectric barrier discharge (nSDBD) where current is limited by the presence of a thin dielectric layer between the electrodes. The difference between a nanosecond spark, in a single or repetitive mode, and the two last configurations, is that in the spark the high current is flowing through the single discharge channel. In TPI and SDBD configurations, the current is limited, so the energy is low comparing to spark discharge, but multi–channel configuration of the discharge is possible.

The first configuration in repetitive mode is called nanosecond repetitive pulsed discharge (NRPD) and widely studied for sustaining of combustion [4]. The highest pressures in PAI experiments were obtained in [5] and [6]. The experiments [5] were carried out in C_3H_8:air stoichiometric and lean (ER=0.4) mixtures in the pressure range $17 - 40$ atm and temperatures $700 - 1000$ K; localized nanosecond spark, surface dielectric barrier discharge with a pin–like electrode, and a streamer corona (TPI) were used to ignite the mixture. Ignition of methane–air mixture in static high pressure chamber at initial pressure 30 atm and ambient initial temperature by the means of transient plasma ignition has been demonstrated in [6].

Nanosecond surface dielectric barrier discharge (nSDBD) with extended electrodes was proved to ignite efficiently a wide set of combustible mixtures (C_2H_6:O_2 [7], CH_4:O_2:N_2(Ar) [8, 9], C_4H_{10}:O_2:N_2(Ar) [8, 9], C_7H_{16}:O_2:N_2 [10]). This type of discharge was suggested in 2003 for air flow control [11] and since that has been extensively studied experimentally [12, 13] and theoretically [14, 15] at atmospheric pressure. The aim of this paper is to generalize, using atmospheric pressure discharge as a basis, the available knowledge on nSDBD development at high pressures.

5.2 Description of experiments

Two configurations of electrode systems for nanosecond SDBD initiation are considered in the paper. The classical flat electrodes "sandwich–like" airflow configuration was used to study the discharge parameters and the morphology of SDBD in ambient air at atmospheric pressure. Coaxial nSDBD was developed to adapt the surface discharge to the geometry of a rapid compression machine (RCM) [9], where the ignition of combustible mixture at high pressures was initiated near the end plate of the combustion chamber. The coaxial electrode system was used to study the discharge in synthetic air, argon and argon:oxygen mixtures in a constant volume chamber within a pressure range $P = 1 - 6$ atm.

The electrode system was connected to the generator via a 30 m coaxial 50 Ω cable. The high voltage (HV) pulse generator (FID Technology, FPG20–03NM) used in the experiments provided the following parameters: 2 ns front rise time, 20 ns pulse duration on the half–height and ± (12–30) kV voltage range in the cable. All the experiments were performed in a single shot regime without a gas flow.

The calibrated custom made back current shunt (BCS) was soldered in the shield of the coaxial cable 15 m apart from the discharge cell. BCS was used to measure the voltage on the electrodes, the current through the electrodes and the deposited energy. The signals from the BCS were registered by a LeCroy WaveRunner 600 MHz oscilloscope.

The images of the discharge were recorded by PI-MAX4 Princeton Instruments ICCD camera (0.5 ns gate) for the flat airflow configuration and by ANDOR iStar DH-734 ICCD camera (2 ns gate) for the coaxial electrode system. Emission was collected on the photocathode by Cosmicar Pentax YK5028 lens. The camera was triggered at different time delays from the beginning of the applied pulse to obtain the images of the discharge evolution. The images were integrated over the wavelength range $300 - 800$ nm, corresponding mainly to the emission of the second positive system of molecular nitrogen.

5.3 Results and discussion

5.3.1 Positive and negative polarity discharge at atmospheric pressure

The electrode system for a classical airflow geometry is schematically presented in Figure 8.1 a,b. The high–voltage (HV) electrode contacts with a dielectric (0.3 mm PVC layer). The width of the HV electrode is equal to 25 mm, and the length of the grounded electrode under the PVC layer is equal to 70 mm to avoid the boundary effects. The SDBD starts as a set of synchronous streamers propagating along the dielectric in the direction perpendicular to the HV electrode. The images of the discharge with 0.5 ns gate are given by Figure 8.1 c,d.

Two fronts of emission propagating from the high voltage electrode and corresponding to the rise front and to the trailing edge of the high–voltage pulse are observed for both polarities. The first front of emission is clearly seen in Figure 8.1 d. The emission from the

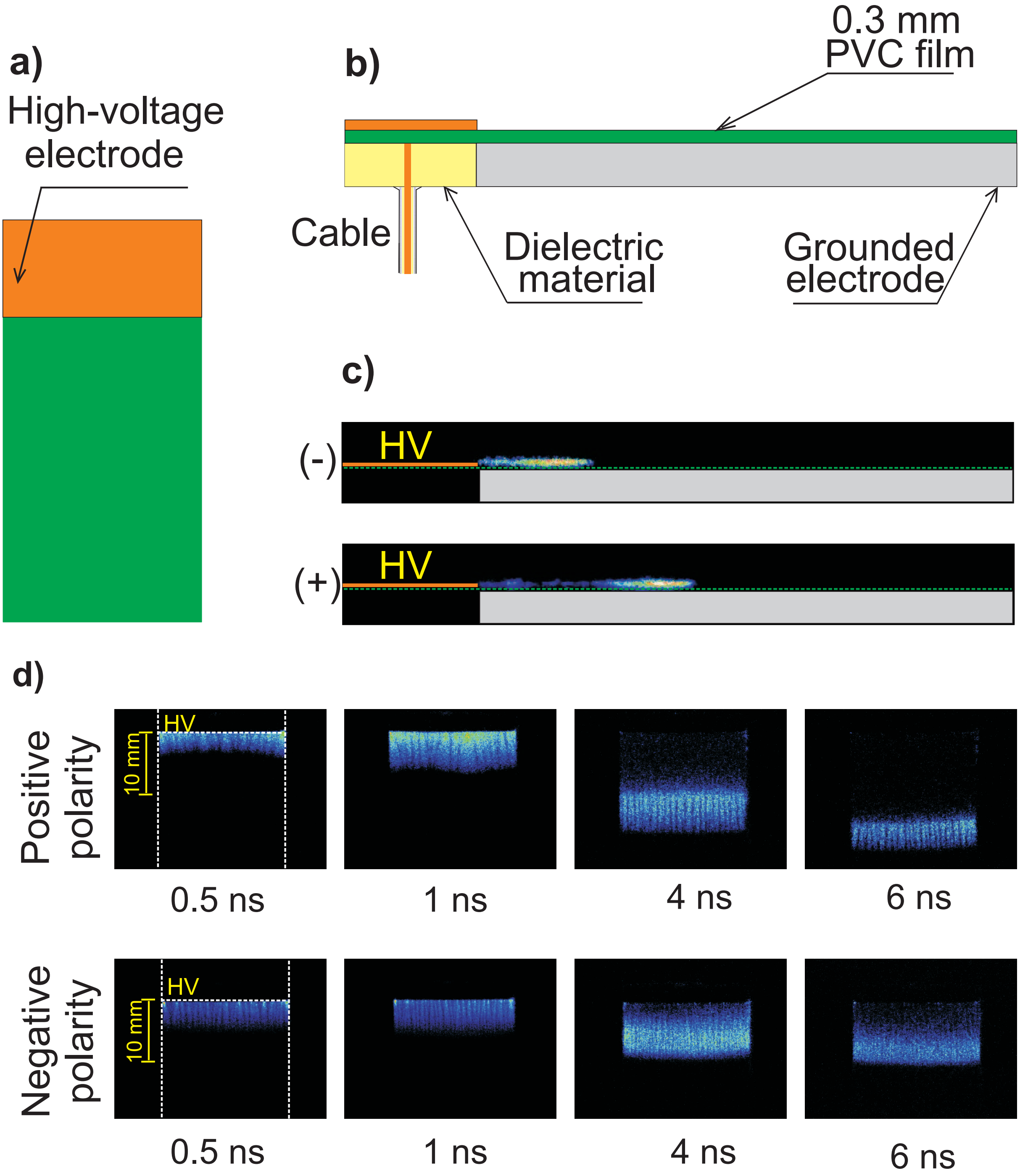

Figure 5.1: Scheme of the electrode system in ”sandwich–like” geometry: (a) frontal view; (b) side view; corresponding ICCD images for the discharges of positive and negative polarities: (c) side view; (d) frontal view. Discharge in ambient air, voltage amplitude on the electrode is $U = 35$ kV, $P = 1$ atm, ICCD camera gate is 0.5 ns.

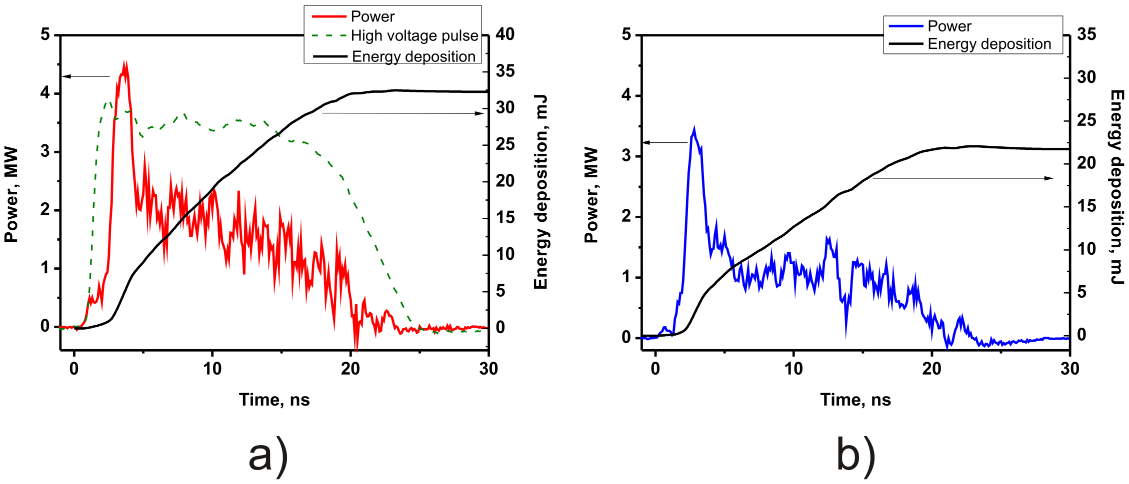

Figure 5.2: Power and energy deposited into the discharges for (a) positive and (b) negative polarities.

negative polarity discharge lasts a few nanoseconds longer. The thickness of the discharge measured from optical emission (see the side view in Figure 8.1 c) is about $0.2 - 0.3$ mm for both negative and positive polarity discharges. The dimensions of the streamers are slightly different in the case of positive and negative polarity. For positive polarity, the optical diameter of the streamers changes is between $0.7 - 1.2$ mm, whereas for negative polarity it is in the range $0.3 - 0.8$ mm. For both polarities, SDBD discharge is rather a "flat" structure, where the optical diameter of the streamers determined form the frontal view is significantly higher than the thickness of the plasma layer.

The synchronous start of the streamers from the high–voltage electrode causes a cylindrical compression wave starting from the electrode [11, 13] and representing a superposition of individual waves generated by each of the streamers. The appearance of a compression wave is a complex interaction of a few physical processes, namely concentrated and synchronous discharge energy release in the roots of the streamers, fast energy relaxation and hydrodynamics on a sub–millimeter scale.

According to numerical modeling [14], a nanosecond SDBD discharge in atmospheric pressure air represents a complex structure with a typical scale of non–uniformities near the dielectric surface equal to units–tens of micron. During the streamer formation, the excessive change of electrons (for negative polarity discharge) or positive ions (for positive polarity discharge) on the surface causes a sharp drop of the electric field in the vicinity of the dielectric surface in direction perpendicular to the surface. The profile of the electron density also changes significantly in the vicinity of the dielectric. For this reason, the optical emission diagnostics gives only the most general presentation of the surface discharge. In particular, the measurements of ratio of two emission bands with different excitation threshold does not give the electric field value, as in uniform plasma [16, 17], but allows to conclude that in the surface streamer head, the ratio of emission of $N_2^+(B^2\Sigma_g^+)$, with the excitation threshold of ε_B=18.4 eV, and $N_2(C^3\Pi_u)$, ε_C=11.03 eV, is a few times higher for the positive polarity SDBD [12, 18] than for the negative polarity.

An important integral characteristics of the discharge is a deposited energy. In the experiments, the deposited energy was measured as a difference between incident and

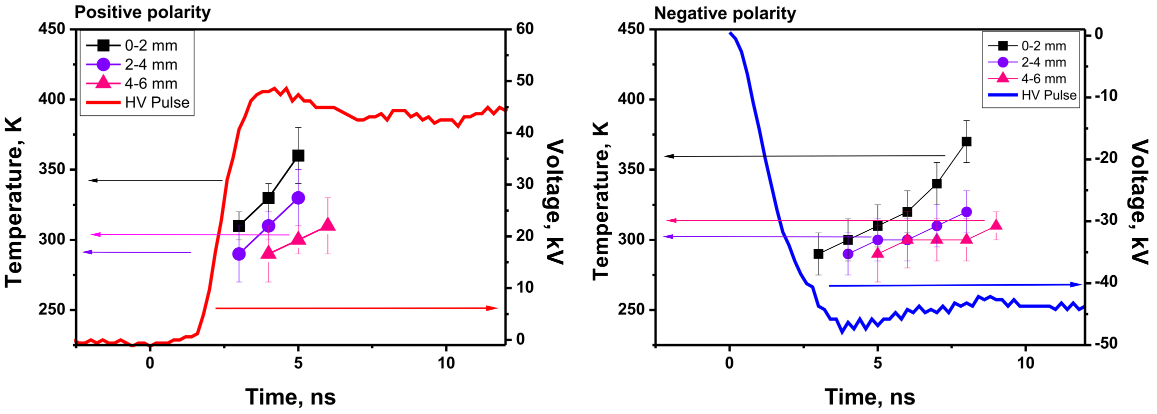

a) b)

Figure 5.3: Time resolved rotational temperature for (a) positive and (b) negative polarity of applied pulses, taken at different distances from the high voltage electrode.

reflected pulses of electrical current. Current for charging of the capacity of the discharge system was extracted experimentally. The total power deposited into the discharge in ambient air for $U = \pm 35$ kV and 20 ns FWHM pulses is shown in Figure 8.2. During the discharge, 32 mJ is deposited into gas for positive and 22 mJ — for negative polarity. If to calculate the energy by the units of length of a streamer, this gives 1 mJ/mm for a positive polarity streamer and 1.5 mJ/mm for a negative polarity streamer. The most considerable power dissipates in the gas during first $5-7$ ns of the pulse, corresponding to a fast propagation of the streamers along the dielectric and charging of a dielectric surface. Significant energy release should be expected in the near–electrode area. In general, a question about volumetric deposited energy and on the influence of energy distribution on the efficiency of combustion initiated by nSDBD still remains open.

The rotational temperature T_{rot} for the same HV pulse parameters was measured from the emission spectra of (0–0) line of 2^+ system of molecular nitrogen superimposing a plot calculated by Specair code [19] with experimentally obtained rotational spectra. The spectra were obtained over the regions 0–2, 2–4 and 4–6 mm counting from the HV electrode with the ICCD camera gate equal to 1 ns. The evolution of rotational temperature at different distances from the electrode and synchronized HV pulses are shown in Figure 8.3. For both positive and negative polarities of the high voltage pulse the temperature increase does not exceed 100 K respectively to the initial temperature that was equal to 290 K. It should be noted that the temperature decreases with the distance from the electrode, that is the energy release near the electrode is higher.

The simple estimate demonstrates that this result is reasonable. It was recently shown [20], on the basis of optical emission and electrical current behavior, that the longitudinal electric field in the surface streamer channel of negative polarity does not change with time and is equal to $E/N \approx 80 - 100$ Td. In assumption that the distance between the streamer channels is comparable with streamer diameters, for the experimental values of current (80 A) and for the thickness of a plasma layer of 250 μm, the current density can be estimated as $j \approx 3$ kA/cm^2. At $E/N = 100$ Td the corresponding electron density is equal to $n_e \approx 2 \cdot 10^{15}$ cm^{-3}, and the energy deposited during first $5-6$ ns can be estimated as

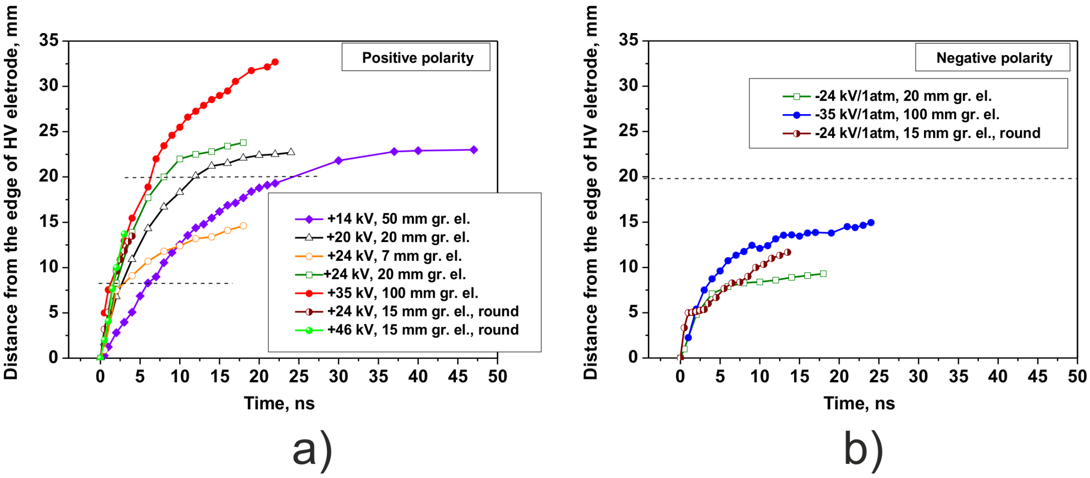

Figure 5.4: Velocity of nSDBD front propagation in air for (a) positive and (b) negative polarity of the high voltage electrode. The voltage amplitude and the length of the grounded electrode are indicated by numbers. The lengths of the electrode is also indicated with a dashed line.

0.1 eV/mol. At $E/N = 100$ Td about 15% of the discharge energy goes to the gas heating *via* fast exchange processes [21], and so, the gas heating in isochoric approximation can be estimated as $\Delta T = 70$ K, what is in reasonable agreement with the measured values. It should be noted that similar values of fast gas heating in the discharge were obtained for nSDBD in air at atmospheric pressure in [12], where, moreover, the additional gas heating due to relaxation of vibrational energy has been recorded in a microsecond time scale.

Measurements of nSDBD front velocity were made for different polarities, voltages, and lengths of the grounded electrode. The results are summarized by Figure 8.4. The figure presents mainly the results obtained for different flat electrode systems but a few plots for the coaxial system prove that there are no strong changes in the velocity between a flat and a radial geometry (see the next section for the details).

For the flat "sandwich–like" electrode system, the velocity of the SDBD front starting from the high voltage electrode, typically equal for positive and negative polarity discharge during 1–2 first nanoseconds of the propagation, typical values are about a few mm per nanosecond. Positive polarity discharge easily covers a few tens of mm of the dielectric length, depending upon the voltage amplitude, and then slows down and stop. At voltage amplitudes higher than 25 kV on the electrode, the velocity slightly depends upon voltage amplitude. For negative polarity discharge, the discharge velocity after 1-2 ns is a few times lower than for positive polarity discharge, and the discharge stops at a certain distance from the high–voltage electrode, 5-15 mm at atmospheric pressure and 15-35 kV voltage amplitude. It should be noted that the velocities presented at the Figure 8.4, are typical for a set of parallel streamers developing synchronously. It is possible to obtain higher velocities of propagation changing the geometry of the system and, consequently, the electric field. Maximal velocity, observed in our experiments with a special pin SDBD electrode, reached 15 mm/ns at 30 kV on the high–voltage electrode.

5.3.2 Positive and negative polarity discharge at elevated pressures

Discharge in coaxial geometry has been developed for plasma assisted ignition at high initial pressures in order to adapt the surface nanosecond barrier discharge for the combustion chamber of the rapid compression machine (RCM). In this case, the discharge develops radially from the edge of the metal disk (20 mm in diameter) served as a high–voltage electrode. The ground electrode is covered by the dielectric layer (PVC) of thickness 0.3 mm (see Figure 7.6 a,b).

This modification of the SDBD discharge was successfully used to ignite stoichiometric C_2H_6:O_2 mixture at ambient initial pressure and temperature in a constant volume chamber [7]. Fast ICCD imaging proved that multiple combustion waves develop, merging, from the high–voltage electrode. It should be noted that no acceleration of the combustion wave along the plasma channels has been recorded [7]. Presumably, the energy release in each of the streamers is small to get a significant gradient of gas temperature and of density of active species along the streamer. At the same time, stable non–detonative combustion initiation is achieved with the distributed nanosecond SDBD system.

A few sets of RCM experiments with ignition of combustible mixtures by nanosecond surface dielectric barrier discharge are recently presented in the literature [8, 9]. The experiments were carried out in methane–oxygen mixture (ER=0.3, 0.5 and 1) diluted by Ar (71-77%) for initial temperatures $T = 900 - 1000$ K and pressures $P = 14 - 16$ atm; and in n–butane–oxygen stoichiometric mixture diluted by 77% of N_2 or Ar ($T = 600 - 900$ K and $P = 6 - 10$ atm). For all the experiments, at voltage amplitude exceeding a certain threshold, a stable multi–point ignition with a following flame propagation has been observed. At these conditions, a typical energy per one streamer/filament, that is for one combustion kernel was estimated as 520 μJ for stoichiometric mixtures [9]. It should be noted that deposited energy measured for methane–containing mixtures with different stoichiometries is visibly (more than one order of magnitude) different, although theoretically calculated energy branching in the discharge is practically the same. This fact confirms, that the experimental study of the discharges in combustible mixtures at elevated pressures is a very important issue for understanding of physics and chemistry of plasma–assisted combustion.

At the same time, the current knowledge about the nSDBD development in non–combustible mixtures is scarce. This section summarizes the information about the nanosecond surface DBD discharge in air at $P = 1 - 6$ atm at voltage amplitude $20 - 60$ kV on the electrode. All the presented data were obtained in coaxial geometry electrodes in a single–shot regime.

The ICCD images of three typical cases are given in Figure 7.6 c. The first (1 atm, +20 kV) case corresponds to "traditional" morphology of nanosecond surface discharge with the only difference that the geometry is coaxial. The velocity of the streamer propagation is in a good correlation with the velocities for the flat electrode system presented in Figure 8.4 b. It should be noted that no visible changes were detected for different edges of the high–voltage electrode, so its sharpness does not seem to be an important parameter. The thickness of the discharge in any of the considered experimental conditions did not exceed 0.5 mm.

The third case (6 atm, -47 kV) was described for the first time in [20]. It was observed in air for negative polarity of the discharge with increase of pressure or of the high voltage

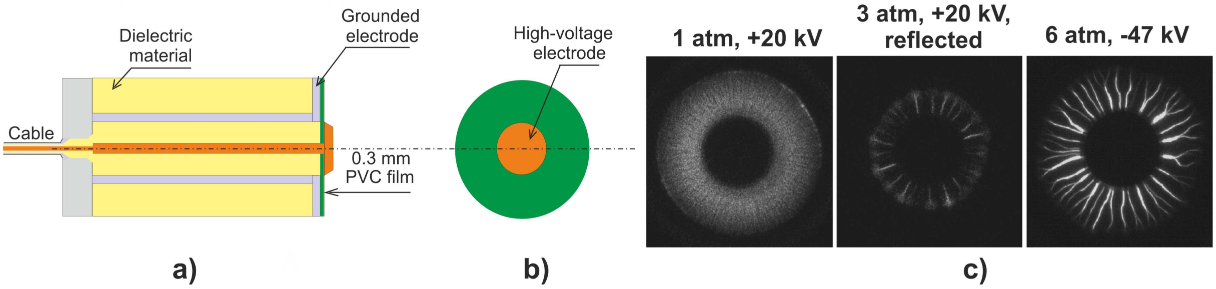

Figure 5.5: Scheme of the electrode system in coaxial geometry: (a) side view; (b) frontal view; and (c) corresponding ICCD images for the discharges of positive and negative polarities. Discharge in synthetic air, ICCD camera gate is 2 ns.

pulse amplitude. The fast transition from the streamer (or "quasi–uniform" [20]) form to filamentary discharge occurs at the conditions of a single–shot regime. The wave of the radially propagated streamers stops at certain distance (this distance was $2-7$ mm, depending upon pressure and amplitude) from the high voltage electrode, similar to negative polarity streamers at atmospheric pressure (see Figure 8.4 b), the emission from the streamers abruptly decreases, and a few bright filaments start from the electrode and propagate in the radial direction. The filaments are the most bright near the electrode; emission intensity decreases radially; a weak streamer "bush" can be identified at the head of each filament. They travel through the charged region on the surface of the dielectric and continue to move with relatively high velocity up to the end of the pulse. The number of the filaments increases during the pulse duration. At long (about 10 mm) distances from the electrode the filaments can branch into $2-3$ smaller filaments. During the falling edge, a bright emission propagates from the electrode along the developed filament channels. Weak emission of the second positive system on N_2 "in the traces" of the filaments is observed during hundreds of nanoseconds after the discharge. In the developed filamentation mode, one filament is created instead of $4-6$ streamers, and the filamentation structure is very regular, as it is represented in Figure 7.6 c. No temperature increase, neither significant increase of electrical current or deposited energy is detected at streamer–to–filament transition [20]. It was suggested that a physical reason for this "single–shot" filamentation is the ionization–heating instability on the boundary of the cathode layer [20].

The second case represented in Figure 7.6 c (3 atm, +20 kV) is the only case corresponding to a "double pulse". "Reflected" in the caption of the figure means that the ICCD image is recorded during the reflected pulse of negative polarity coming, because of mismatching of the cable and the generator, to the discharge system 250 ns after the first pulse of positive polarity. In this case, a stratified structure, similar to observed at atmospheric pressure in pulse–periodic regime [22], appears step–by–step during a few nanoseconds from initially stratified streamers, no abrupt transition is observed. The channels never branch; the emission is uniform along the channel with a well-pronounced streamer "brush" at the head of each channel. No increase of emission is observed at the falling edge of the pulse; no emission is detected after the pulse. It is possible to assume that the mechanism responsible for the filamentation can be different from the mechanism responsible for the filamentation a few nanoseconds after the start of the pulse.

Figure 5.6 gives a review of the images of a nanosecond SDBD at elevated pressures.

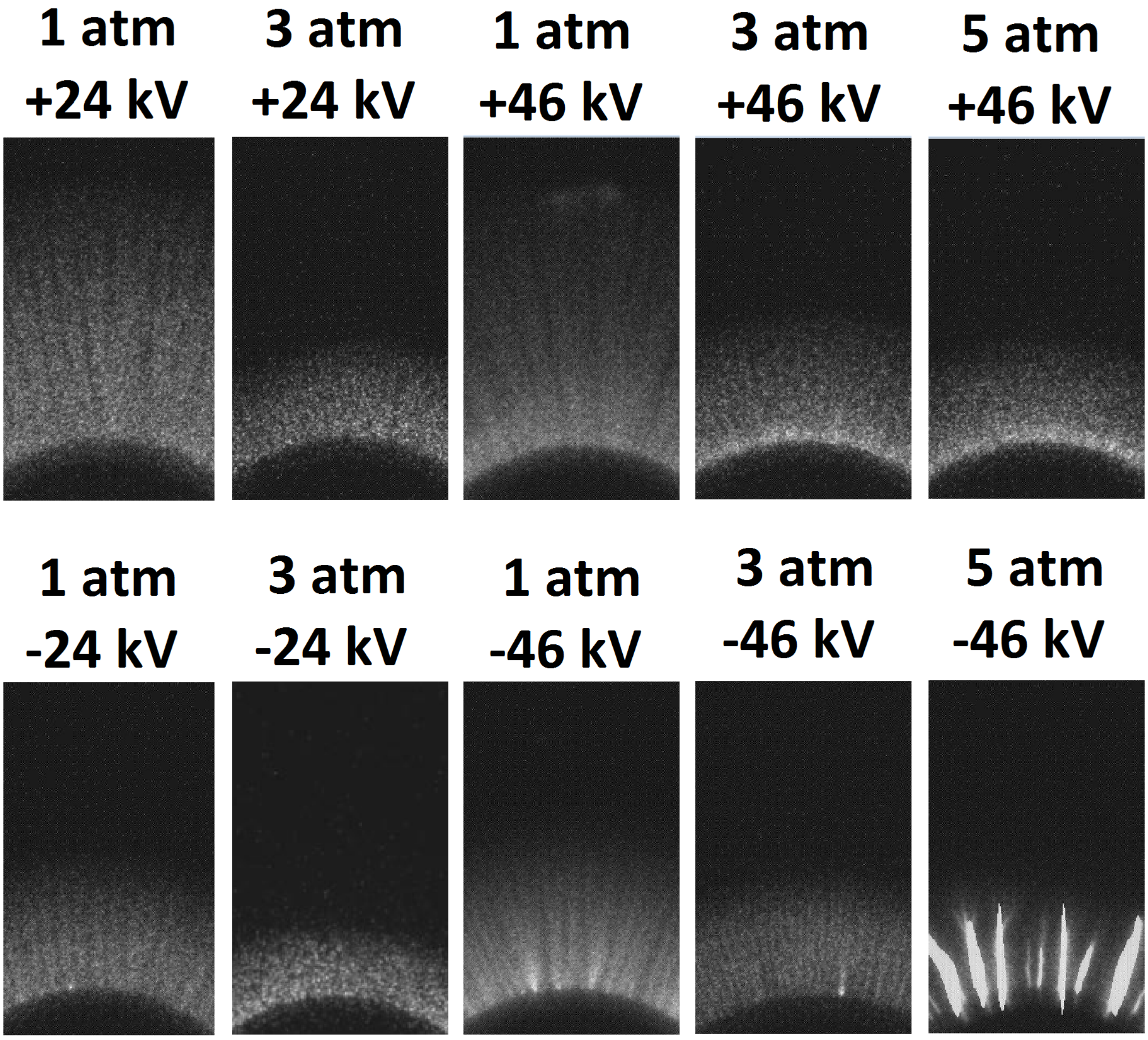

Figure 5.6: Review of ICCD images of nanosecond surface dielectric barrier discharge in synthetic air. Pressures and voltages are indicated near each frame. Camera gate is equal to 2 ns. Segment of the high voltage electrode (20 mm in diameter) is seen at the lower part of each frame.

For all considered pressures, in the absence of filamentation, a typical "optical radius" R of the streamer when images is taken in the direction perpendicular to the dielectric surface, is always higher for a positive polarity discharge. Indeed, at voltage amplitude $U = \pm 46$ kV for $P = 1$, 3 and 5 atm, $R_+ = (1.4 \pm 0.2)$, 0.9 and 0.8 mm respectively for positive polarity, and $R_- = 1$, 0.5 and 1.2 mm for negative polarity. The R_- at 5 atm is a distance between the filaments (see Figure 5.6 for 5 atm and -46 kV), the distance between the initial streamers being approximately 4 times smaller. Let us note that this fact does not correlate with a streamer in the air gap, where the diameter of a streamer of negative polarity is always higher [23], but does correlate with the smaller "near–surface" gap between the streamer of the negative polarity and the surface in numerical modeling [14].

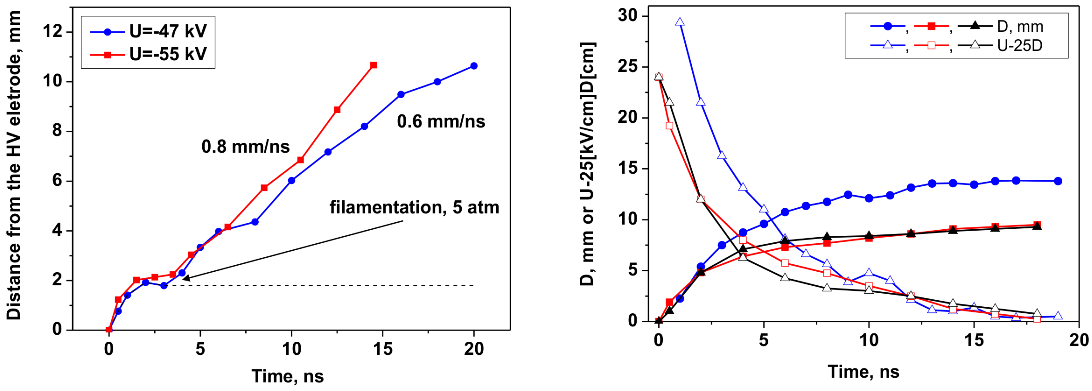

a) b)

Figure 5.7: (a) Position of a streamer/filament head in time. Synthetic air, 5 atm, -47 kV and -55 kV; (b) Distance between a streamer head and the HV electrode, D, and $(U - 25 \cdot D)$ value for different voltages U and different lengths of the ground electrode for ambient air, $P = 1$ atm. Blue curves correspond to $U = -35$ kV, length of the ground electrode 70 mm; black and red curves – to $U = -24$ kV and length of the electrode 20 and 7 mm respectively.

Transition to filamentary regime, if exists in the combustible mixtures, can be extremely important for re–distribution of energy in the discharge. At the same time, a physics of this transition is not yet clear enough. Figure 5.7 a presents so–called $x - t$ diagram (position of a streamer head as a function of time) for the regimes where streamer–to–filament transition in a single pulse has been observed. After the transition, filaments propagate with a constant velocity, below 1 mm/ns, for a distance of tens of mm. The transition point, where streamers slow down and stop, is indicated in the Figure as "filamentation".

It was assumed [20] that the streamers stop when the potential drop on the channel is equal to the voltage on the electrode. At transition point, 3 atm and -47 kV, the longitudinal E/N value was estimated to be approximately equal to 100 Td (which corresponds to electric field value of 25 kV/cm at $P = 1$ atm). Figure 5.7 b gives a few plots for velocity of the negative polarity nSDBD fronts at atmospheric pressure together with calculated $(U - 25 \cdot D)$ value (here $25[\mathrm{kV/cm}] \cdot D$ represents the rest of potential on the streamer channel under the assumption that the cathode fall is negligible comparing to the voltage amplitude). It is seen that the streamers stop when the voltage drop on the channel is equal to the potential on the high voltage electrode. Similar consideration leads to the conclusion that in filaments and in positive polarity streamers the longitudinal electric field in the channel must be, in any case, significantly lower than in the negative polarity streamers.

5.3.3 Modification of discharge in different mixtures

Summarizing current experimental knowledge of a nanosecond discharge at high pressures at different mixtures, it is possible to conclude the following: two waves of emission propagating from the high voltage electrode are always observed without dependence on

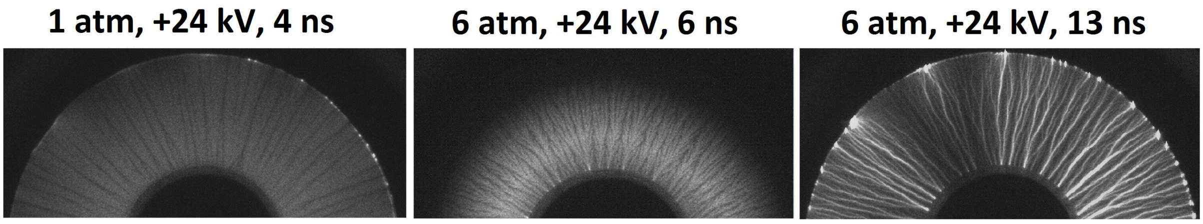
1 atm, +24 kV, 4 ns

6 atm, +24 kV, 6 ns

6 atm, +24 kV, 13 ns

Figure 5.8: ICCD images of nanosecond surface dielectric barrier discharge in argon at $P = 1$ atm and $P = 6$ atm.

high voltage polarity or gas nature; with pressure increase, the velocity and the maximal distance of the discharge propagation decreases. With voltage increase at constant pressure, the velocity of the discharge and the maximal length of propagation increase, but no scaling on PU parameter is observed: pressure increase typically causes significant morphological changes of the discharge.

The morphology of the discharge depends significantly on a gas mixture composition. Figure 5.8 represents an example of nSDBD development in pure argon. Maximal length of discharge propagation is always much higher than in air under similar conditions. Practically no difference at the scale of 15 mm electrode length is observed between the propagation of the positive and the negative polarity discharge. Peculiar multi–branched streamer patterns are observed at pressure increase (6 atm, +24 kV, 6 ns). During a single pulse, positive or negative polarity, they collapse into thin elongated channels (6 atm, +24 kV, 13 ns).

Special attention must be given to the changes in the discharge structure with addition of hydrocarbons. Typically, addition of hydrocarbons or other molecules with a large cross-section of UV–absorption decreases the photo–ionization length [24] and so, decreases the discharge uniformity [25, 26]. Transition of the volumetric diffuse discharge in air in a multichannel discharge structure has been observed for atmospheric pressure at small addition of hydrocarbons corresponding to lean mixtures (CH_4 at ER=0.3 and C_3H_8 at ER=0.8) [25]. This is in correlation with experimental results of [26], where a multichannel discharge structure was observed at C_3H_8 additions on the level of 2% (ER=0.52). This correspond to the following densities of hydrocarbons: $[CH_4] \approx 7 \cdot 10^{17}$ cm^{-3}, and $[C_3H_8] \approx 5 \cdot 10^{17}$ cm^{-3}. For the radiation at the wavelength range $\lambda = 98 - 103$ nm, this gives, taking into account the cross–sections from [27], the absorption coefficient $20 - 30$ cm^{-1}atm^{-1}. Another important issue is a decrease of ionizing UV radiation because of quenching of the emitting states, $N_2(b'^1\Sigma_u^+)$ and $N_2(b^1\Pi_u)$. These factors are very important for the problem of plasma–assisted combustion by nanosecond discharges, as far as densities of hydrocarbons and H_2O molecules, absorbing efficiently UV–radiation, can be high in combustible mixtures.

Transition from uniform to filamentary mode can also be obtained in pure air with pressure increase. Two processes are responsible for this effect with increase of O_2 density: decrease of the photo–ionization length and increase of attachment rate (both three–body and dissociative attachment rates increase with pressure). Figure 5.9 illustrates the fact that with pressure increase the characteristic time of electron attachment is comparable with a duration of a nanosecond pulse. So, higher E/N values are necessary to keep a given electron density when pressure increases.

In surface discharges, the role of the volume photo–ionization can be relatively small.

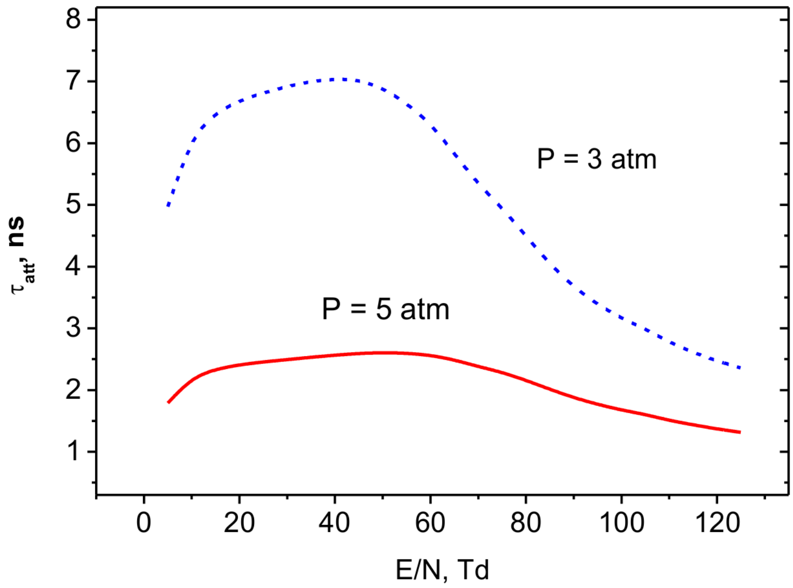

Figure 5.9: Characteristic time of electron attachment to molecular oxygen in air at $T = 300$ K and different pressures as a function of reduced electric field.

Electron emission from the surface of dielectric under the action of UV radiation of streamer head can be an important additional process sustaining the discharge propagation. So, the experimental study of parameters and of a structure of the surface dielectric barrier discharge with a different fraction of hydrocarbons or H_2O molecules in the mixture at fixed high voltage pulse characteristic, pressure and temperature is a topical task in the problem of plasma–assisted combustion.

5.4 Conclusion

The knowledge concerning nanosecond surface dielectric barrier discharge (nSDBD) at elevated pressures is summarized. It is shown that a significant difference between positive and negative polarity discharges is observed already at atmospheric pressure: the length of the maximal propagation of a negative polarity discharge is always smaller. Judging from the propagation length, a drop of potential is higher for the negative polarity streamers. Estimated value of the reduced electric field in the channel of a streamer of negative polarity is about 100 Td. The optical diameters of the streamers at atmospheric pressure comprise parts of millimeter, typical deposited energy per unit length of a streamer is about a few mJ/mm. The temperature increase, measured from optical emission and averaged by a 1 mm of a streamer length, does not exceed a few tens K per ns, and decreases with a distance from the electrode.

At pressure increase from 1 to 6 atm, morphology of streamers practically does not change for positive polarity of the high-voltage electrode: no filamentation is observed for used parameters of the electric pulse. For negative polarity, the streamers slow down at a few mm from the high-voltage electrode and the discharge transforms into the filamentary form. The total current through the discharge does not change, and the total energy is distributed between filaments. The filamentary form can be a tool of energy concentration in plasma-assisted combustion at high pressures. The filaments propagates at longer distances comparing to streamers, so the electric field in the filaments must be lower than in the streamers.

Addition of hydrocarbons or increase of density of molecular oxygen with pressure can cause the discharge branching and filamentation because of decrease of the absorption length for UV radiation and increase of the attachment rate. Presence of a dielectric surface can stabilize the discharge due to electron emission from the surface of dielectric under the action of UV radiation. Study of nanosecond surface dielectric barrier discharges at high pressures in mixtures with small densities of combustible gases can be an efficient tool to study the physics of nSDBD in conditions close to internal combustion engines.

Bibliography

[1] Starikovskiy A and Aleksandrov N. 2013. Plasma–assisted ignition and combustion. *Progress in Energy and Combustion Science* **39** 61—110.

[2] Starikovskaia SM. 2014. Plasma-assisted ignition and combustion: nanosecond discharges and development of kinetic mechanisms. *J. Phys. D: Appl. Phys.* **47** 353001 (34pp).

[3] Ju Y, Sun W. 2015. Plasma assisted combustion: dynamics and chemistry. *Progress in Energy and Combustion Science* **48** 21—83.

[4] Rusterholtz DL, Lacoste DA, Stancu GD, Pai DZ, Laux CO. 2013. Ultrafast heating and oxygen dissociation in atmospheric pressure air by nanosecond repetitively pulsed discharges. *J. Phys. D: Appl. Phys.* **46** 464010 (21pp).

[5] Starikovskiy A, Rakitin A, Correale G, Nikipelov A, Urushihara T and Shiraishi T. 2012. Ignition of hydrocarbonair mixtures with nonequilibrium plasma at elevated pressures *Proc. of 50th AIAA Aerospace Sciences Meeting including the New Horizons Forum and Aerospace Exposition* Nashville, USA, 9-12.

[6] Gundersen MA, Singleton D, Kuthi A, Lin Y and Sanders J. March 2012. Transient plasma for marine diesel GHG abatement *China Maritime Week*, Hong Kong.

[7] Kosarev IN, Khorunzhenko VI, Mintoussov EI, Sagulenko PN, Popov NA and Starikovskaia SM. 2012. A nanosecond surface dielectric barrier discharge at elevated pressures: time-resolved electric field and efficiency of initiation of combustion *Plasma Sources Sci. Technol.* **21** 045012 (15pp).

[8] Stepanyan SA, Boumehdi MA, Vanhove G, Starikovskaia SM. 7-10 January 2013. Timeresolved electric field measurements in nanosecond surface dielectric discharge. Comparison of different polarities. Ignition of combustible mixtures by surface discharge in a rapid compression machine *Proc. of 51st AIAA Aerospace Sciences Meeting*, Grapevine, Texas, AIAA-2013-1053.

[9] Boumehdi MA, Stepanyan S, Desgroux P, Vanhove G and Starikovskaia S. 2014. Ignition of methane- and n–butane–containing mixtures at high pressures by pulsed nanosecond discharge. Accepted for publication.

[10] Shcherbanev SA, Stepanyan SA, Boumehdi MA, Vanhove G, Desgroux P, Starikovskaia SM. 9-15 January 2015. Energy balance in surface nanosecond dielectric barrier discharge. Plasma-assisted ignition of heavy hydrocarbons at high pressures.

Proc. of 53rd AIAA Aerospace Sciences Meeting, Kissimmee, Florida, AIAA-2015-0668.

[11] Starikovskii AYu, Nikipelov AA, Nudnova MM, Roupassov DV. 2009. SDBD plasma actuator with nanosecond pulse-periodic discharge. *Plasma Sources Sci. Technol.* **18** 034015 (17pp).

[12] Nudnova MM, Aleksandrov NA, Starikovskiy AYu. 2010. Influence of polarity on the properties of a nanosecond surface barrier discharge in air. *Plasma Phys. Rep.* **36** 1, p.94-103 (In Russian).

[13] Adamovich IV, Choi I, Jiang N, Kim J-H, Keshav S, Lempert WR, Mintusov EI, Nishihara M, Samimy M, Uddi M. 2009. Plasma assisted ignition and high-speed flow control: non-thermal and thermal effects. *Plasma Sources Sci. Technol.* **18** 034018 (13pp).

[14] Soloviev V, Krivtsov V. 2009. Surface barrier discharge modelling for aerodynamic applications *J. Phys. D: Appl. Phys.* **42** 125208 (13pp).

[15] Gibalov VI, Pietsch GJ. 2012. Dynamics of dielectric barrier discharges in different arrangements *Plasma Sources Sci. Technol.* **21** 024010 (35pp).

[16] Paris P, Aints M, Valk F, Plank T, Haljaste A, Kozlov K V, Wagner H-E. 2005. Intensity ratio of spectral bands of nitrogen as a measure of electric field strength in plasmas *J. Phys. D: Appl. Phys.* **38** 3894-3899.

[17] Paris P, Aints M, Valk F. 2009. Collisional quenching rates of $\mathrm{N}_2^+(\mathrm{B}^2\Sigma_g^+, v = 0)$, *Proceedings of* 17th Symposium on Application of Plasma Processes and Visegrad Workshop on Research of Plasma Physics. Slovakia, 17–22 January 2009, pp. 227—228.

[18] Stepanyan SA, Soloviev VR, Starikovskaia SM, 2014. An electric field in nanosecond surface dielectric barrier discharge at different polarities of the high voltage pulse: spectroscopy measurements and numerical modeling. *J. Phys. D: Appl. Phys.* **47** 485201 (13pp).

[19] Laux CO. 2002. *Radiation and nonequilibrium collisional-radiative models. Physico-Chemical Modeling of High Enthalpy and Plasma Flows.* (von Karman Institute Lecture Series 2002-07) ed. D Fletcher et al (Rhode-Saint-Genese, Belgium: Von Karman Institute).

[20] Stepanyan SA, Starikovskiy AYu, Popov NA, Starikovskaia SM. 2014. A nanosecond surface dielectric barrier discharge in air at high pressures and different polarities of applied pulses: transition to filamentary mode. *Plasma Sources Sci. Technol.* **23** 045003 (14pp).

[21] Popov NA. 2011. Fast gas heating in a nitrogenoxygen discharge plasma: I. Kinetic mechanism. *J. Phys. D: Appl. Phys. 44* 285201 (16pp)

[22] Leonov SB, Petrishchev V, Adamovich IV. 2014. Dynamics of energy coupling and thermalization in barrier discharges over dielectric and weakly conducting surfaces on μs to ms time scales. *J. Phys. D: Appl. Phys* **47** 465201 (18pp).

[23] Luque A, Ratushnaya V, Ebert U. 2008. Positive and negative streamers in ambient air: modeling evolution and velocities. *J. Phys. D: Appl. Phys.* **41** 234005.

[24] Naidis GV. 2007. Modelling of transient plasma discharges in atmospheric-pressure methaneair mixtures *J. Phys. D: Appl. Phys.* **40** 4525-4531.

[25] Pendleton SJ, Montello A, Carter C, Lempert W and Gundersen MA. 2012. Vibrational and rotational CARS measurements of nitrogen in afterglow of streamer discharge in atmospheric pressure fuel/air mixtures. *J. Phys. D: Appl. Phys.* **45** 1-8.

[26] Bentaleb S, Tardiveau P, Moreau N, Jeanney P, Jorand F, Pasquiers S. 2011. Filamentation of a nanosecond pulse corona discharge in air-propane mixtures at atmospheric pressure *IEEE Trans. Plasma Sci.* **39** 2236-2237.

[27] Hudson RD. 1971. Critical review of ultraviolet photoabsorption cross sections for molecules of astrophysical and aeronomic interest. *Rev. Geophys. Space Phys.* **9** 305-406.

Chapter 6

Possibility of ignition by nanosecond surface dielectric barrier discharge at high pressures

.

6.1 Kinetics for n–butane containing mixture at initial parameters corresponding to experimental conditions

6.1.1 Experimental setup: Rapid Compression Machine

High-Pressure experiments on plasma–assisted combustion in Rapid Compression Machine (RCM), cited in this chapter, were performed in collaboration with Dr. Pascale Desgroux and Dr. Guillaume Vanhove partially in the frame of National Research Agency of France (ANR) PLASMAFLAME project. The rapid compression machine (RCM) was designed at PC2A laboratory, University of Lille [1]. The combustion chamber of RCM is a cylinder 50 mm in diameter and 16 mm in height at top dead center (TDC). The reaction chamber can be heated uniformly to selected temperatures, and is equipped with a Kistler 601 A piezoelectric pressure transducer, a sampling port and two optical windows. The analog signals are acquired with a National Instruments card linked to a computer, with a time step of 40 μs.

The electrode system developed and tested in LPP Ecole Polytechnique was mounted instead of the end plate of the RCM (see Fig. 6.1). A coaxial electrode system [2] has been developed to obtain a quasi-uniform discharge that propagates along the surface within a radially symmetrical geometry. The central coaxial high voltage (HV) electrode is connected to segment of a sphere, its height did not exceed 1 mm and diameter was equal to d=20 mm. The inner diameter of the low voltage electrode is equal to the outer diameter of the HV electrode, and the outer diameter of grounded electrode is equal to the inner diameter of combustion chamber, D=50 mm. A dielectric layer 0.3 mm in thickness made of PVC covers the low–voltage electrode. The discharge is initiated from the edge of the high–voltage electrode and propagates above the surface of PVC layer.

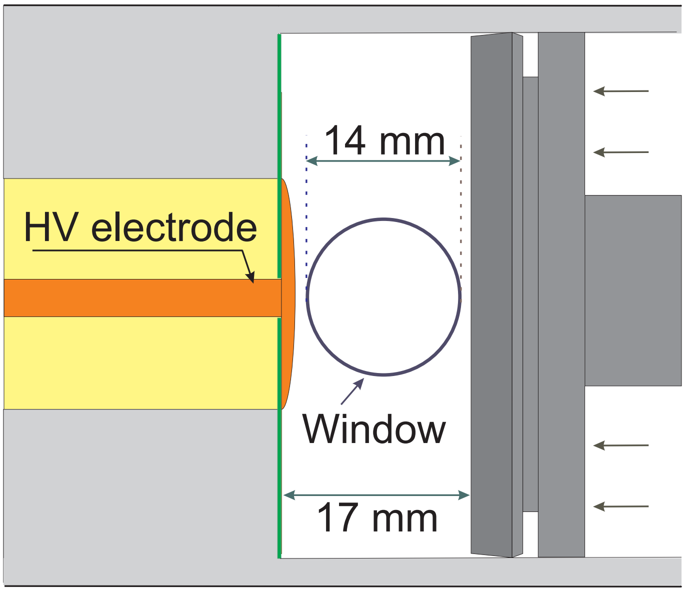

Figure 6.1: Combustion chamber of rapid compression machine with mounted electrode system of surface dielectric barrier discharge. Orange color represents HV electrode, grey color — grounded electrode, green color — dielectric PVC layer, yellow color — dielectric material.

6.1.2 Description of ignition by the discharge and approach to numerical modeling

The peculiarity of the described experiments is that the discharge is not uniform in space; so the task is not 0–dimensional. As it was mentioned, the discharge develops in the form of streamers which start synchronously within 0.5 ns from the high–voltage electrode and propagate in radial direction. Under these conditions, the ignition starts in the vicinity of the high–voltage electrode, near the end plate of a combustion chamber, and then the combustion wave propagates in the chamber. There are two possibilities for the mixture ignition at the conditions of a nanosecond surface dielectric barrier discharge: ignition can take place in very narrow zone near the high voltage electrode, and no intensification of combustion is observed along the streamer channels. This model was suggested in [2], where a good coincidence between the experimentally observed ignition delay time and calculated values for ethane:oxygen mixture has been obtained. A second possible scenario is when the direction along the streamers is considered as a special zone where an intensification of ignition process is observed due to production of radicals and excited species. With a high probability, the main energy release takes place near the high-voltage electrode, but the role of a streamer zone is a still a question under study. The first experiments revealing the role of the energy distribution will be reported at the end of the present chapter.

For the conditions considered the discharge processes occurred on a nanosecond scale, whereas the ignition processes occurred on a milisecond scale. Therefore, the temporal evolution of the densities of particles important for plasma-assisted ignition can be traced separately in the discharge phase and in the ignition phase.

Preliminary calculations are performed in 0–D approximation. Two actions of the

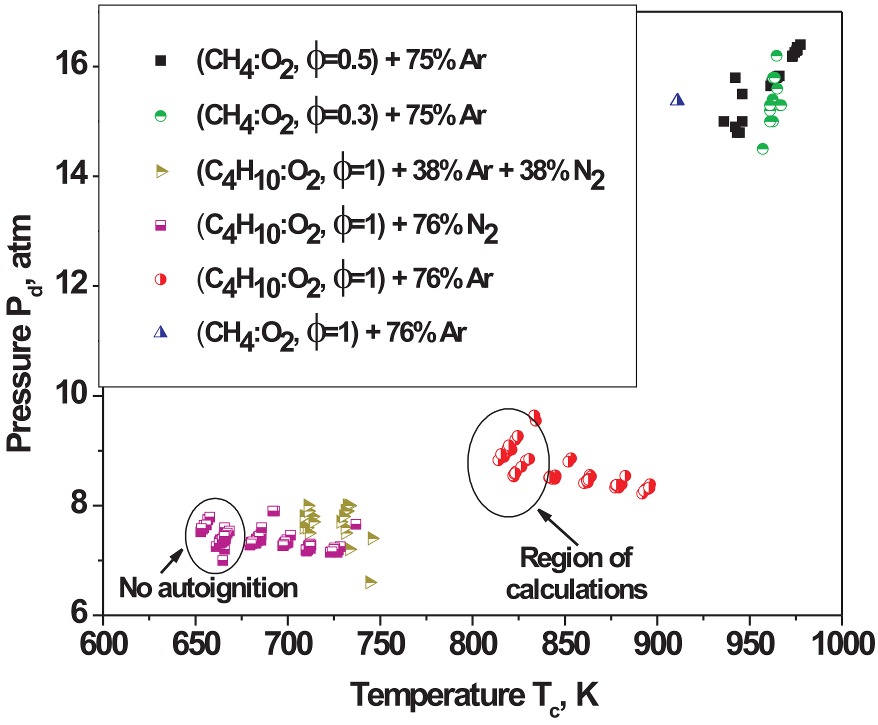

Figure 6.2: Range of investigated conditions for different mixtures.

discharge on the chemically active mixtures are the most important for initiation of combustion chemistry: production of active species and fast relaxation of energy deposited into internal degrees of freedom (so–called fast gas heating). The parametric study, corresponding to different amount of atomic oxygen added at initial time moment, is performed for conditions close to the experimental results at rapid compression machine [3].

Calculations were carried out in the zero-dimensional approximation at a fixed gas volume using the code CHEMKIN [4]. In calculations, we determined the ignition delay time as the interval between the instant at which active particles were injected and the onset of the efficient increase of pressure in the ignition phase. The ignition process in the n–C_4H_{10}:O_2:Ar mixture was numerically simulated using the kinetic mechanism suggested in [5] and verified based on the autoignition delay time measured in RCM for the considered mixture (see the detailed description below). It is important to note that this ignition scheme was developed for modeling of autoignition of RCM experiments and tested on autoignition experiments for a wide range of parameters.

The review of the experimental parameters, tested with nanosecond SDBD discharge at RCM of Lille University within a joint ANR PLASMAFLAME Project is given in Fig. 6.2 ([3]). Two fuels were chosen for the experimental program: methane and n–butane. The reason to use methane for the experiments were that: (i) it is complicated to dissociate methane, and the ignition delay time is much longer for methane–containing mixture comparing to the other hydrocarbons, while plasma–assisted ignition of methane is efficient [6, 7]; (ii) cross-sections of methane collisions with electrons are relatively well–

known which allows a detailed modeling of the discharge stage. N–butane was chosen because of well–pronounced cool flames and zone of a negative temperature coefficient (NTC). In the future, detailed discharge action on kinetics in the cool flame zone and on the NTC region is planned within a joint experimental program. Fig 6.2 summarizes all the experiments were plasma assisted ignition was successful. They are the experiments in methane–containing mixtures of a different stoichiometry at initial temperatures 900 − 1000 K and pressures about 15 bar, and the experiments in n–butane–containing mixtures at initial temperatures 650 − 900 K ant initial pressures 7 − 9 bar. Region where no autoignition was observed (ignition with plasma was successful) is marked in the figure. In the preliminary calculations, we will use gas mixture corresponding to the minimum energy losses, to avoid the calculation of the energy losses in the real RCM. The corresponding region is also marked in the Figure.

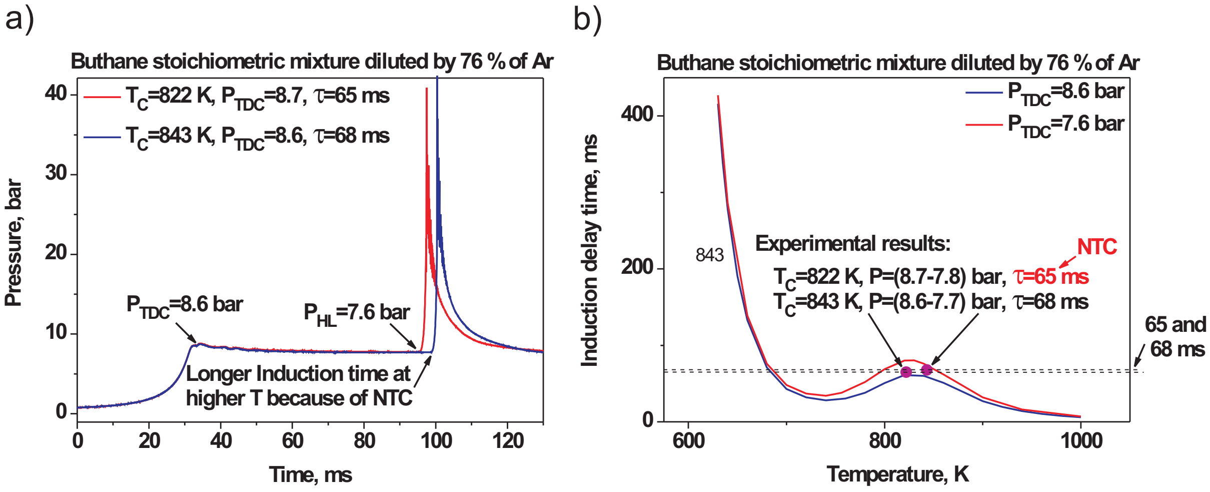

Figure 6.3: Results of experiments and numerical calculations in negative temperature coefficient region.

6.1.3 Results of numerical modeling: recombination of radicals and initiation of the cool flame

Figure 6.3a) demonstrates the typical results of experiments in NTC region for butane/oxygen stoichiometric mixture diluted by 76 percent of argon. First 30 ms in Fig. 6.3a) correspond to the process of gas compression when the pressure and temperature reach the values when the combustible mixture can be ignited. Than after the ignition delay period the process of ignition occurs. It is seen from Fig. 6.3a) that for higher temperature the induction delay time is longer than for lower temperature. It is caused by that the experimental conditions correspond to the region where occurs NTC phenomena. It is also necessary to note that during the induction period pressure decreases due to the heat exchange of the gas and chamber walls. The heat losses at these particular experiments are about 10%. That means that right before the ignition pressure is P_{HL}=7.6 bar instead of pressure in top dead center P_{TDC}=8.6 bar. The influence of heat losses on induction time strongly depends on temperature at the moment of maximal

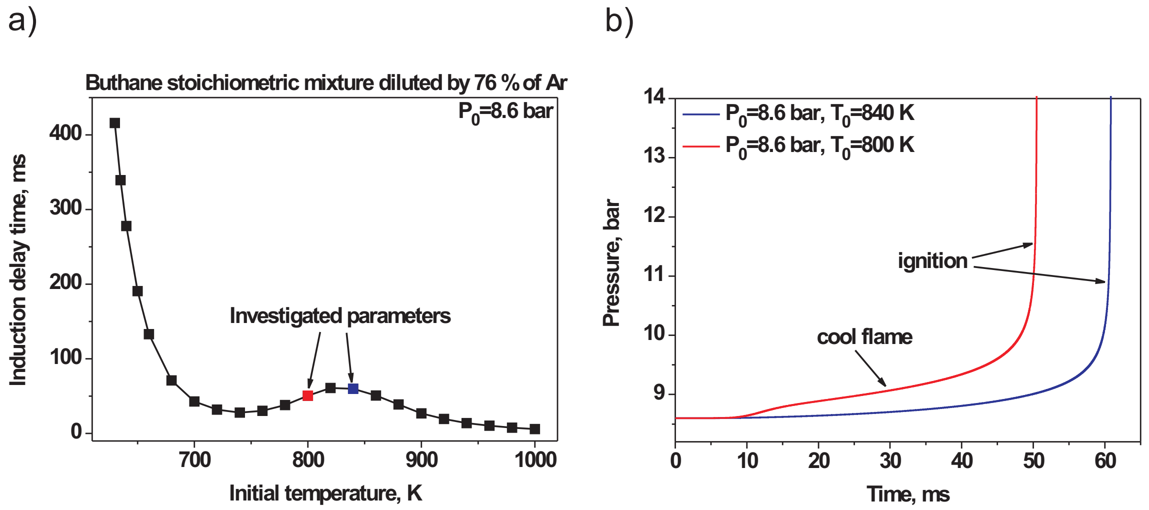

Figure 6.4: The results of calculation for butane/oxygen stoichiometric mixture: a) Dependence of the induction time *vs* temperature at initial pressure P=8.6 bar; b) comparison of the pressure profiles for T˙0=800 K (NTC) and T˙0=800 K (no NTC).

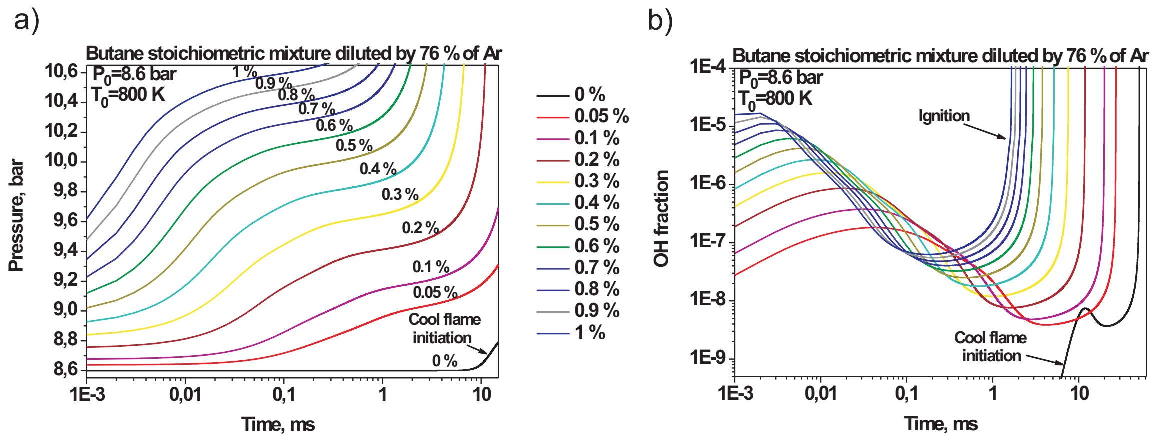

Figure 6.5: Influence of the initially dissociated percent of oxygen to the beginning of ignition process: a) dependence of pressure *vs* time; b) OH fraction*vs* time.

compression. Figure Fig. 6.3b) demonstrates the results of numerical calculations of the induction delay time vs initial temperature for two different initial pressures P=8.6 bar and P=7.6 bar. It is clearly seen that the influence of initial pressure on induction time is more significant near the region of NTC. It is reasonable to assume that in case of heat losses in system the induction time must take a value higher than for minimal pressure (right before ignition) but lower than for maximal pressure (pressure in top dead center). That is confirmed by comparison of the experimental results and the results of the modeling presented in Fig. 6.3b). It is seen from Fig. 6.3b) that the experimentally obtained values of the induction time are lower than the induction times calculated for pressure in TDC but higher that those calculated for minimal pressure right before ignition. The accuracy of the induction time modeling is satisfactory: the lowest accuracy $\delta\tau/\tau$=10%

correspond to the temperature T=850 K. In case the dilutant is nitrogen instead of argon the heat losses will be significantly higher and the modeling process has to take into account the heat exchange between the gas and walls.

One of the peculiarities of NTC region is the cool flame phenomena. Typical increase of temperature in cool flames is a few hundreds K and typical increase of pressure is about 5-10%. Figure 6.4 compares the results of calculation for two different initial temperatures: T_0=800 K and T_0=840 K at initial pressure P_0=8.6 K. Temperature T_0=800 K corresponds to NTC region instead of T_0=840 K (see Fig. 6.4a)). Pressure profiles for T_0=800 K and T_0=840 K are presented in Fig 6.4b). For T_0=840 K, the pressure rise till 60 ms is very slow and at 60 ms the ignition and sharp pressure increase is observed. The situation is different for T_0=800 K: after 10 ms pressure starts to increase slowly with time what is the evidence of the cool flame initiation and then, 40 ms later, the ignition occurs and leads to the sharp increase of pressure.

To estimate the action of the discharge, a given amount of oxygen atoms is added at the initial time instant, similar to calculations performed in [8]. Atomic oxygen is selected because it is one of the most active components for ignition process and as one of the radicals intensively produced by nanosecond discharges in the process of O˙2 dissociation. When a certain number of O–atoms was added, the appropriate number of O_2 molecules was taken out from the mixture, $\Delta[O]_2=2[O]$. Figure 6.5 represents the dependencies of pressure and OH concentration *vs* time for different fractions of initially dissociated O_2, from 0.05% to 1%, which is, actually, low concentrations for nanosecond discharges at atmospheric pressure. The significant modification of pressure and [OH] is observed under the action of the discharge. It should be noted that significant decrease of atomic oxygen density is observed at the very beginning of the modeling, in sub–microsecond time. This must correlate with a fast energy release and following reaction acceleration. In this version of the code, fast gas heating from the discharge is not taken into account, so the shift of the ignition delay time corresponds to the lower possible limit. Decrease of O generated at the initial time moment correlates with increase of OH density. Then OH decay is observed, and it is is important to note that OH density, for all the investigate regimes, does not decay lower than the density of OH in the corresponding cool flame at aoutoignition conditions (see Fig.6.5b)).

So, the preliminary numerical modeling demonstrates significant change of the kinetics of autoignition under the addition of O–radicals. Even small addition of oxygen (0.05%) causes developed radical kinetics, which is, by a physical nature, is similar to the cool flame. The future plans in the field of PAI/PAC numerical modeling are to make the next step and to consider detailed discharge chemistry; and finally to check how important is the discharge chemistry at high pressures. The coupling of the discharge and combustion chemistry will be checked.

6.2 Plasma assisted ignition of n–heptane containing mixtures

Experiments on h–heptane were performed in collaboration with Lille University using Rapid Compression Machine to prepare gas mixture at given initial pressure and temperature. As it was reported above, nanosecond multi–streamer discharge, providing moderate

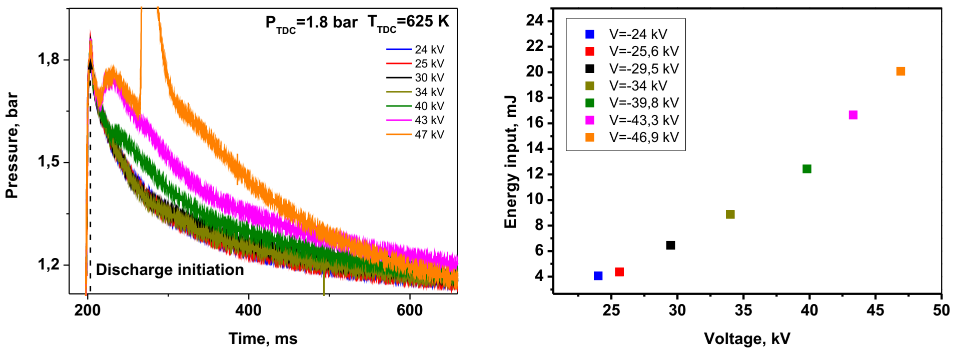

a) b)

Figure 6.6: (a) Modification of pressure traces under the action of nanosecond surface dielectric barrier discharge, n–C_7H_{16}:O_2:N_2=1.8:19.6:78.6 mixture, P_{TDC} = 1.8 bar, T_C = 626 K. Two nanosecond pulses, at time instance 210 ms and 270 ms, are applied to the system. Negative polarity pulses, voltage amplitude is between 24 and 46.9 kV. (b) deposited energy in the first pulse as a function of voltage amplitude on the high–voltage electrode in n–heptane–containing mixture.

temperature increase and elevated densities of atoms and radicals, can be used as initiator of combustion at high pressures. Action of nanosecond DBD in this case leads to multi–spot ignition in the vicinity of the high–voltage electrode with a following propagation of the combustion wave in the combustion chamber of a rapid compression machine [9]. A

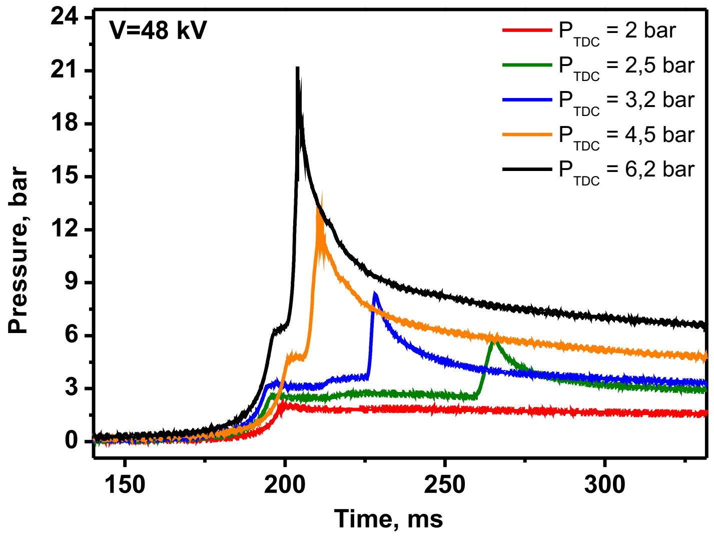

Figure 6.7: Modification of pressure traces under the action of nanosecond surface dielectric barrier discharge, n–C_7H_{16}:O_2:N_2=1.8:19.6:78.6 mixture, different initial pressures. Negative polarity pulses, voltage amplitude is 46.9 kV.

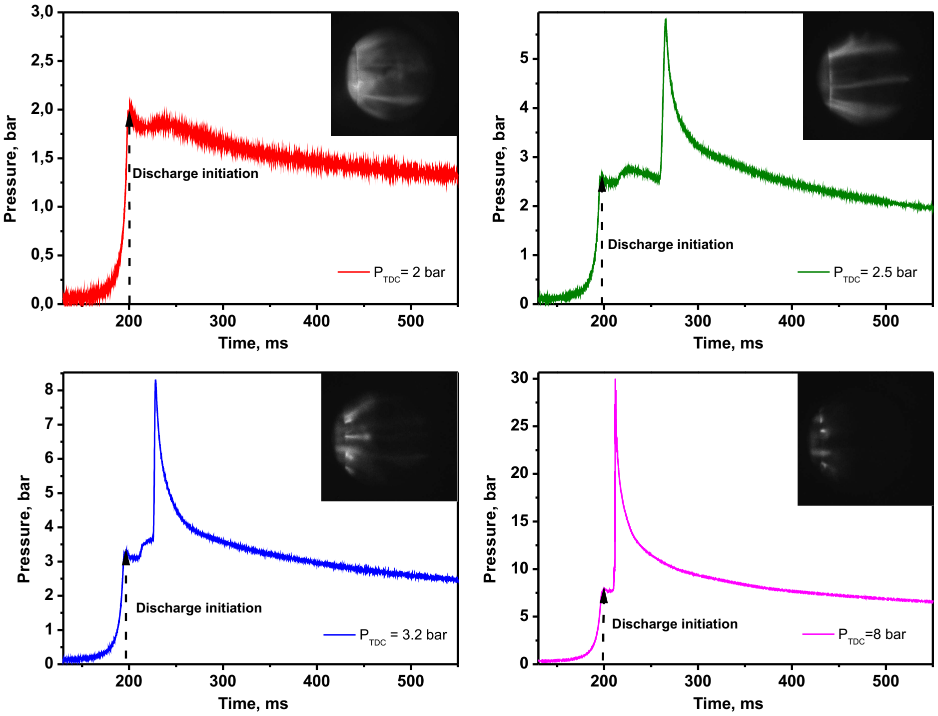

Figure 6.8: Pressure profiles in n–C_7H_{16}:O_2:N_2=1.8:19.6:78.6 mixture at $U = -46.9$ kV and corresponding ICCD images of the discharge. ICCD gate is 100 ns.

capability of a nanosecond discharge to produce a volumetric excitation and to trigger a cool flame was tested on example of a stoichiometric n–heptane/air mixture.

To get a volumetric initiation of combustion, relatively low pressures were used in the RCM. It was possible to get a discharge–triggered cool flame with further transition to a regular heptane–air flame by two different experimental ways: increasing deposited energy (when increasing applied voltage) or increasing initial pressure of the gas mixture. These two ways are demonstrated by figures 6.6–6.8.

Pressure profiles in RCM combustion chamber at initial pressure 1.8 bar and initial temperature 626 K are given by figure 6.6. In this particular regime, two successive discharge pulses were used, the first pulse at the point of maximum compression (corresponds to $t = 200$ ms in the figure), and the second pulse 60 ms later. Slight changes of gas pressure become visible at 19–34 kV of high voltage amplitude on the electrode. At 40 kV, well pronounced pressure increase 25 ms after the point of maximum compression is clearly seen. At 43 kV pressure increase starts earlier, 10 ms after the first discharge. Second discharge slightly increases the pressure. Finally, at 47 kV, the second pulse triggers a regular flame, providing significant, more than twice, pressure increase in the combustion chamber. Voltage increase from 24 to 47 kV corresponds to deposited energy increase from 4 to 20 mJ. At $P = 1.8$ bar and $T = 626$ K, two–phase ignition was possible only when triggered by a sequence of pulses.

Single pulse experiments at different pressures and at maximum voltage, $U = 48$ kV, have been carried out. When pressure rises from 2.0 to 6.2 bar, the pressure trace modifies from a trace corresponding to a cool flame triggered by the discharge (at 1.8 bar) to a trace corresponding to ignition near the electrode and following combustion wave propagation, similar to regimes observed in methane– and n–butane–containing mixtures [9]. The sequence of pressure profiles is given by figure 7.15, and pressure profiles with corresponding ICCD images taken during the discharge are presented in figure 6.8. The camera gate was 100 ns so that all the light emitted during the discharge pulse was recorded. The wavelength range was determined by combination of transmission of the optical window and of the broad band filter, and was equal to $300 - 400$ nm. It was found that at high pressure (8 bar) the discharge develops mainly in the plane of the electrode system. At low pressure (2 bar) the discharge is volumetric: bright longitudinal structures developing from the electrode situated at the left hand side of the frame are clearly seen at $P = 2$ bar. For intermediate pressures (2.5–5 bar) the discharge is still volumetric; two–phase ignition, with delay time changing as a function of pressure, is observed in the system.

6.3 Conclusions

Experiments at high initial pressures have shown that nanosecond surface dielectric barrier discharge is an efficient tool for initiation of combustion. The experiments in the framework of ANR PLASMAFLAME Project in collaboration with Lille University demonstrated efficient multi-point ignition of methane–, n–butane–, and n–heptane–containing mixtures. Numerical analysis of the ignition by a nanosecond discharge has been performed. for the strongly diluted (76% of Ar) stoichiometric n–butane:oxygen mixture. It was shown that significant modification of a cool flame can be achieved under the action of the discharge due to initiation of reactions with atomic oxygen; even small additions of O–atoms, $< 1\%$ shift the ignition delay time by a few order of magnitude. To understand physics of ignition by multi-streamer or multi-filament discharge, it was necessary to build an experimental setup with broad optical access allowing controllable preliminary heating at high pressure environment. The next chapter is devoted to the high pressure high temperature (HPHT) discharge cell developed at LPP and to high pressure discharge/combustion experiments.

Bibliography

[1] Crochet M, Minetti R, Ribaucour M, Vanhove G, 2010 A detailed experimental study of n-propylcyclohexane autoignition in lean conditions *Combustion and Flame* **157(11)** 2078—2085

[2] Kosarev I N, Khorunzhenko V I, Mintoussov E I, Sagulenko P N, Popov N A, Starikovskaia S M, 2012 A nanosecond surface dielectric barrier discharge at elevated pressures: time-resolved electric field and efficiency of initiation of combustion *Plasma Sources Sci. Technol.* **21** 045012 (15pp)

[3] Boumehdi M A, Stepanyan S, Desgroux P, Vanhove G and Starikovskaia S 2014 Ignition of methane- and n–butane–containing mixtures at high pressures by pulsed nanosecond discharge. Submitted; under revision, 2014

[4] M.K. Alkam, V.M. Pai, P.B. Butler, N.B. French, University of Iowa, 1993, Report No. SAND89-8009

[5] Healy D, Kalitan D M, Aul C J, Petersen E L, Bourque G, and Curran H J, Oxidation of C_1–C_5 Alkane Quinternary Natural Gas Mixtures at High Pressures, 2010 *Energy Fuels* **24** 1521—1528

[6] Kosarev I N, Aleksandrov N L, Kindysheva S V, Starikovskaia S M, Starikovskii A Yu, Kinetics of ignition of saturated hydrocarbons by nonequilibrium plasma: CH_4–containing mixtures, 2009 *Combustion and Flame* **154** 569–586.

[7] Kosarev I N, Aleksandrov N L, Kindysheva S V, Starikovskaia S M, Starikovskii A Yu, Kinetics of ignition of saturated hydrocarbons by nonequilibrium plasma: C_2H_6-to C_5H_{12}-containing mixtures, 2009 *Combustion and Flame* **156** 221–233.

[8] Boumehdi M A, Stepanyan S, Starikovskaia S, Desgroux P and Vanhove G 2013 Plasma assisted ignition inside a rapid compression machine *Proc. of European Combustion Meeting*, 25–28 June 2013, Lund, Sweden

[9] Boumehdi M A, Stepanyan S, Starikovskaia S, Desgroux P and Vanhove G, Ignition of methane- and n-butane-containing mixtures at high pressures by pulsed nanosecond discharge, 2015 *Combustion and Flame* **162** 1336–1349

Chapter 7

Ignition of high pressure lean H_2:air mixture along the multiple channels of nanosecond surface discharge: HPHT chamber

.

Initiation and sustaining of combustion in lean mixtures is a challenge for the combustion community. One suggested solution is ignition/combustion assisted by low temperature nonequilibrium plasma, or plasma assisted ignition/combustion (PAI/PAC) [1]. The mechanisms of plasma assisted ignition and combustion [2, 3, 4] include dissociation of molecular species by electron impact, energy transfer from electronically excited species, like $N_2(B^3\Pi_g)$, $N_2(C^3\Pi_u)$, $O(^1D)$ and others to dissociation or to the fast increase of gas temperature (so–called fast gas heating [5, 6]) and partial reforming of fuel [7, 8].

These mentioned non–elastic processes require relatively high energy of electrons, $5-15$ eV, that is high reduced electric fields [9], $E/N \approx 100$ Td, where E is the electric field, N is the gas density, and 1 Td=10^{-17} V$\cdot$ cm^2. Nanosecond discharges [10, 11, 12] provide high reduced electric fields even at high pressures.

A recent review of ignition of combustible mixtures by nanosecond discharges [13] points out that the advantages of plasma assisted ignition are demonstrated and proved quantitatively for moderate gas densities, $N \leq N_{atm}$, where N_{atm} is a normal gas density at $T = 300$ K and atmospheric pressure. A very limited number of scientific groups [14, 15, 16, 17] work on initiation of combustion by nanosecond discharges at high gas densities. Real combustion devices operate at $P \geq 10-20$ bar. Little is known about the development of discharges in combustible mixtures at high pressures. With gas temperature, discharge parameters change only slightly, while the rates of combustion reactions increase exponentially. At the same time with gas density increase, discharge spatial structure rearranges itself to keep the E/N value high enough for efficient ionization.

Sustaining homogeneous plasmas at high gas density is a complex technical problem. A lot of conditions should be fulfilled: it is necessary to provide significant pre-ionization of gas mixture by UV or fast electrons [18, 19], to keep the voltage rise time short enough and so to provide the conditions when the local field is higher than the critical ionization field [20] etc.

In most cases of practical interest, as gas density increases, the discharge loses its uniformity and must be considered as a set of separate channels. For a fixed gas composition, voltage pulse shape and amplitude, three different scenarios are possible for the high pressure nanosecond discharges: (i) nanosecond spark if the distance between the electrode is small and the discharge bridges a gap [21]; (ii) transient streamer discharge when the distance between the electrode is longer, typically on the order of centimeters, and the pulse duration is not enough to close the discharge gap [16]; and (iii) nanosecond dielectric barrier discharges (DBD) when the electrodes are separated by dielectric and so the discharge gap can not be closed by conductivity current. Two form of DBDs are usually considered: volume DBD, when discharge develops in a few millimeters gas gap between the electrodes for the conditions that are at least one of the electrodes is covered with dielectric; and surface dielectric barrier discharge (SDBD), when the discharge develops along the surface of dielectric dividing two electrodes, one of the "classical" examples of a discharge in so called air–flow configuration [22].

In nanosecond surface dielectric barrier discharge (nSDBD) the deposited energy is equally distributed over the set of 100–200 streamers [23, 24, 25]. The streamers start from the high-voltage electrode synchronously within at least 0.2 ns. The nanosecond surface dielectric barrier discharge was suggested for PAI/PAC [24, 26] due to the fact that a quasi-uniform plasma pattern is produced at elevated pressures in the plane of high voltage electrode for a typical time much shorter than the ignition delay for combustible mixtures; the produced plasma is a non-equilibrium plasma acting on the gas *via* the production of atoms/radicals/excited species and temperature increase due to their recombination and relaxation, and *via* possible hydrodynamic effects.

The paper [27] reports efficient multi–point ignition by nSDBD for stoichiometric and lean methane- and n–butane containing mixtures [27]. The rapid compression machine (RCM) of the University of Lille 1 RCMs simulated a single compression stroke and was used as a tool to get, after compression, pressures ranging from 6 to 16 bar and temperatures from 600 to 1000 K. The end plate of the combustion chamber was replaced by the system of electrodes; plasma assisted ignition was compared to autoignition in a cylindrical combustion chamber which was 50 mm in diameter and 17 mm in height at top dead center (TDC).

Although the advantages of nSDBD for the initiation of combustion were clearly demonstrated, the discharge in high–pressure combustible mixtures is practically not studied and the mechanism of ignition of gas mixtures by nSDBD plasma is not clear yet. The majority of papers [27, 28] combines results on the discharge in air or non–combustible mixtures with experiments or modeling of plasma assisted ignition. There exists a set of scattered and sometimes contradictory experimental data. For example, it was found that the ignition threshold is lower for a negative polarity discharge [27, 28]. The authors [28] concluded, on the basis of 2D numerical modeling, that energy release in negative polarity surface streamers at atmospheric pressure is concentrated near the high–voltage electrode, while in positive polarity discharge the deposited energy is spread along the entire streamer. At the same time, we were not able to find any significant difference in Schlieren images for positive and negative polarity nSDBDs at a time instant 1 μs after the discharge. It was found [27] that small changes of hydrocarbon concentration in a gas mixture changes substantially the deposited energy. It was suggested, in analogy with [29, 30] that this observed effect is due to changes in the spatial struc-

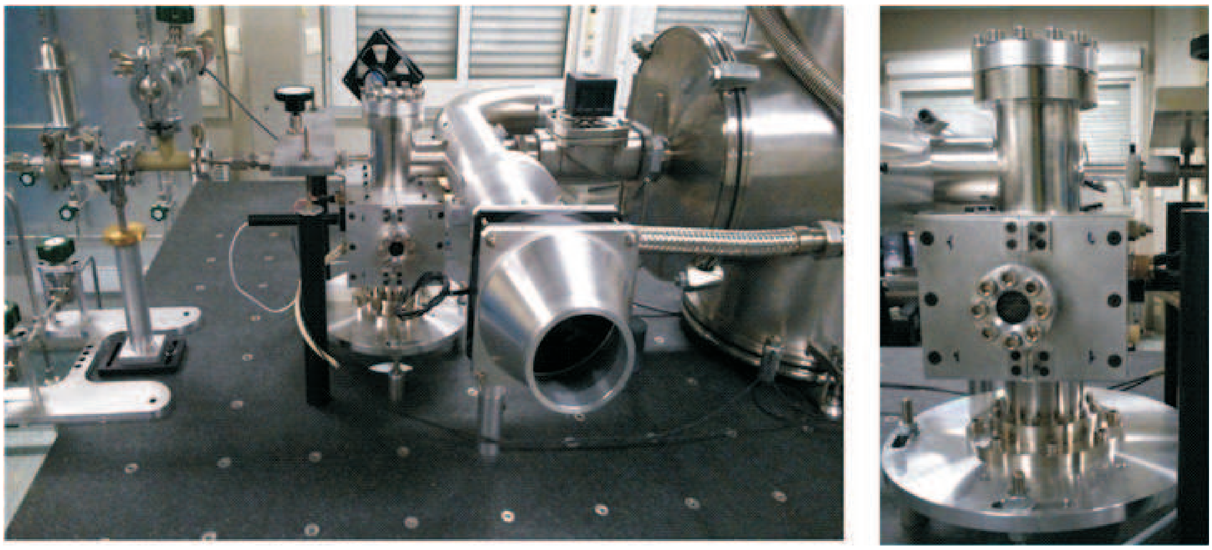

Figure 7.1: Photo of the High Pressure High temperature (HPHT) discharge cell. An example of the ICCD image of the discharge through the upper window is given by the frame in the left lower corner of the photo.

ture of the discharge, but this assumption has not been yet confirmed experimentally. Finally, transformation of streamer surface DBD to filamentary mode in a single–shot regime during a few nanoseconds was recently demonstrated [25, 31] in air for the pressure range $P < 6$ atm and negative polarity of the high–voltage pulse. To understand the physics of discharge in fuel–containing mixtures and following combustion, the discharge and combustion experiments should be carried out in the same experimental setup.

The aims of the present work are (i) to develop a high pressure high temperature (HPHT) discharge cell providing a broad optical access to the discharge and combustion experiments; (ii) to study the nSDBD morphology and the conditions of streamer–to–filament transition at pressures up to 12 bar; (iii) to demonstrate, on the example of lean hydrogen/air mixtures, a correlation between the discharge appearance and the behavior of the ignition pattern; (iv) to check if the ignition along the multiple channels, over the maximum possible surface, can be achieved at elevated pressures.

7.1 Experimental setup

7.1.1 High-pressure high-temperature plasma/combustion setup

To study ignition of combustible mixtures by nanosecond surface dielectric barrier discharge (SDBD) under controlled initial parameters, the High Pressure High Temperature (HPHT) chamber was developed. The range of initial pressures and temperatures is close to the lowest P and T from experimental range of RCMs. The design of the chamber allows, in the same experiment, observation of optical emission from the discharge and from the initial stage of combustion. A photo of the designed and assembled HPHT reactor is presented in Fig. 7.1.

A general scheme of the HPHT setup is shown in Figure 8.4. The walls of the chamber are made of stainless steel. The chamber is surrounded with a heating jacket to keep the initial gas temperature between 300 and 700 K.

The temperature is controlled with three thermocouples: two thermocouples of type K (0-1100 C^o chromel-alumel) are installed directly into the heating jacket to follow the dynamics of heating, and the third one, mounted into the chamber wall, is used to measure gas temperature before the experiment (thermocouple type J 0-750 C^o iron-constantan).

The chamber is pumped down to 10^{-2} Torr before filling with gas mixture under study. The pressure of the gas mixture can be up to 15 bar in stationary regime. Pressure in the chamber is controlled with three pressure gauges: (1) low pressure detector Pfeiffer Vacuum D-35614 Asslar to control a residual pressure between the experiments; (2) stationary membrane gauge SMC ISE300-01-65 to measure initial pressure before the experiment and (3) KULITE high temperature IS pressure piezo-transducer (XTEH-10L-190 series) to measure pressure profile during ignition. The piezo-transducer is mounted in the discharge chamber wall at the distance 7 mm from the electrode plane. To prepare a gas mixture, four booster cylinders 500 cm^3 in volume each, connected to four membrane manometers was used.

Ignition is initiated in the volume in the center of HPHT chamber indicated as "discharge cell" in figure 8.1. The volume represents a disk 50 mm in diameter and 15 mm in height. Side view is provided by two quartz optical windows, 10 mm in diameter each. A top view through the 50 mm in diameter top quartz window is partially closed by the upper flange of the discharge cell (see figure 8.1). When the HPHT chamber is filled with a gas mixture under study, combustion is initiated by the nanosecond discharge near the lower flange of the discharge cell.

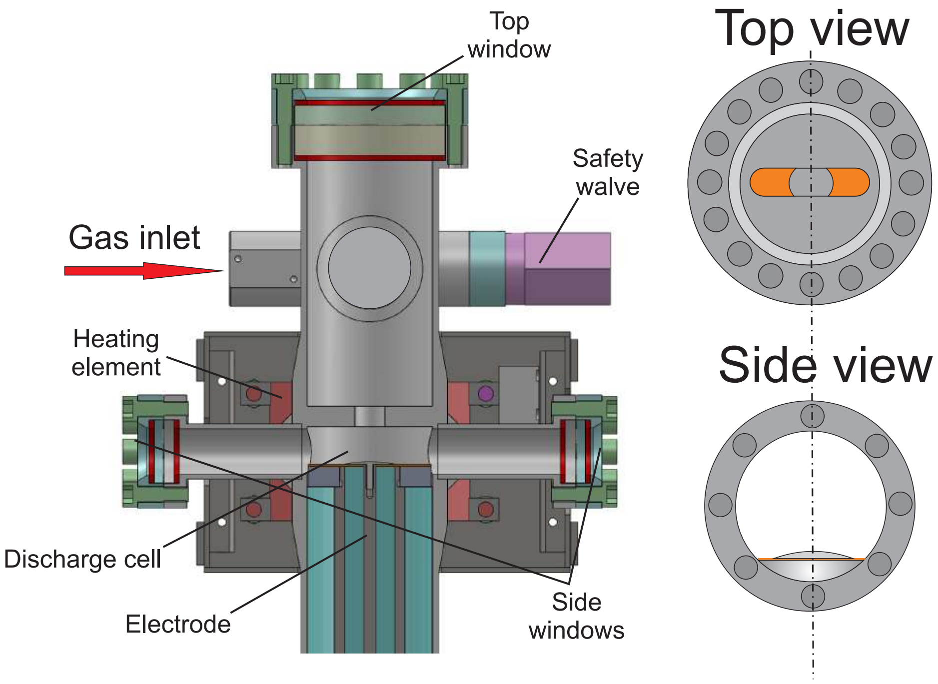

Figure 7.2: The schematic representation of High-Pressure High-Temperature (HPHT) reactor and the views of the flanges (top, side).

7.1.2 Electrode system; measurements of electrical current and delivered energy

The coaxial electrode system, similar to the system used in experiments in a rapid compression machine [25, 27] is mounted into HPHT chamber. The details of the electrode system are given in Figure 8.2. The high-voltage electrode is a segment of sphere 2 cm in diameter and 5 cm of a curvature radius, made of stainless steel. The inner diameter of the low-voltage electrode is equal to the outer diameter of the HV electrode, and the outer diameter of the low-voltage electrode is equal to 48 mm. PVC film 0.3 mm in thickness is used as a dielectric separating the high-voltage and grounded electrode.

The high-voltage pulse of positive polarity, 20 ns duration at FWHM, 2 ns rise time and 10-30 kV amplitude (see figure 8.3) is generated by a commercial pulser FID Technology, FPG20-03PM. General scheme of the experimental setup is shown in figure 8.4. The pulse is submitted to the electrode system via 50 Ohm high voltage coaxial cable. Two calibrated custom made back current shunts (BCS) are soldered in the shield of the cable: one, BCS1 in the middle of the cable, and another, BCS2 1 m apart from the FID generator. The length of the cable, 30 m, is selected to separate the incident pulse and the pulse, reflected from the discharge cell, on the BCS1 shunt (see figure 8.3b). The BCS1 is used to measure pulse shape and absolute values of electrical current. The energy deposited into plasma is calculated as a difference between the energies stored in the incident and in the reflected pulses taking into account energy losses in the cable and the losses to charge the electrode system. The details of the technique can be found elsewhere [32]. The BCS2 is used to synchronize optical diagnostics with the discharge.

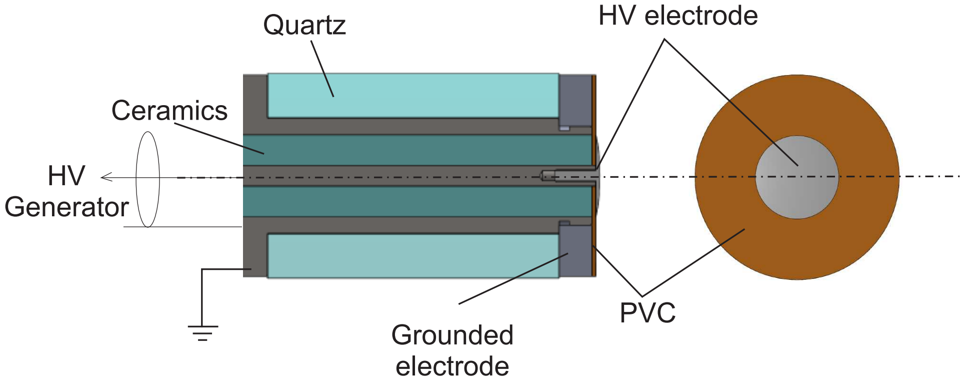

Figure 7.3: SDBD electrode in cylindrical configuration

7.1.3 Optical emission measurements

To study the spatial structure and the development of the discharge and of the following combustion, the images of the discharge/combustion integrated over the wavelength range $300 - 800$ nm were recorded by an Pi-Max4 Princeton Instruments ICCD camera with Edmund Optics 50 mm FL objective. To identify the nature of the optical emission, spectra in the range 300-600 nm where recorded with the help of ACTON spectrometer (SP-7500i) and Pi-Max4 Princeton Instruments ICCD camera. To study the temporal

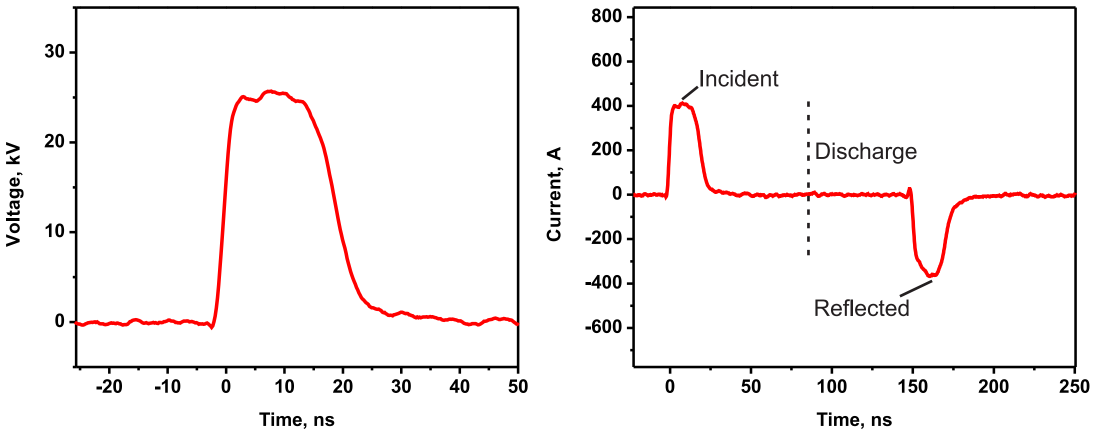

a) b)

Figure 7.4: Applied and reflected HV pulses. The oscillogram is obtained with BCS1 installed in the middle of 30 m coaxial cable.

behavior of selected molecular bands, monochromator ANDOR SR-300i with 600 l/mm grating combined with H6610 photomultiplier tube (Hamamatsu) was used. All electrical and optical signals were registered by two LeCroy WaveRunner 600MHz oscilloscopes, separately for nanosecond and for millisecond time scale.

Discharge experiments in non–combustible mixtures were carried out in N_2, air, N_2:CH_4 $= 99 : 1$ and N_2:CH_4 $= 94 : 6$ in the pressure range $1 - 12$ bar. Discharge and following initiation of combustion were studied in H_2:air mixture at $P = 6$ bar, $ER = 0.5$. Minimum ignition energy was studied in H_2:air mixture at $P = 3$ bar and $P = 6$ bar for $ER = 0.6$. H_2, N_2 and O_2 (Air Liquide) with <100 ppm of impurities and CH_4 with <600 ppm (Air Liquide) of impurities where used. All the experiments where carried out in a single shot regime.

7.2 Discharge morphology at high pressures

7.2.1 Streamer-to-filament transition of nSDBD discharge in non–combustible mixtures

For nanosecond discharges in air and fuel–air mixtures, the main emission in the wavelength range $200 - 400$ nm during the discharge stage is the emission of the second positive system of molecular nitrogen, $N_2(C^3\Pi_u) \rightarrow N_2(B^3\Pi_g)$. The emission of the 2^+ system of molecular nitrogen was used to describe the discharge morphology. The density of $N_2(C^3\Pi_u)$ can be described as

$$\frac{d[N_2(C)]}{dt} = k_e n_e [N_2] - [N_2(C)] \cdot (\frac{1}{\o} + \Sigma k_q^M [M]), \tag{7.1}$$

where τ is a radiation lifetime of the upper state, k_q is a quenching rate constant, M is a density of quencher, n_e is the electron density, and the rate of excitation by electron impact, k_e, is a function of reduced electric field, E/N [9]. At high pressures the quenching

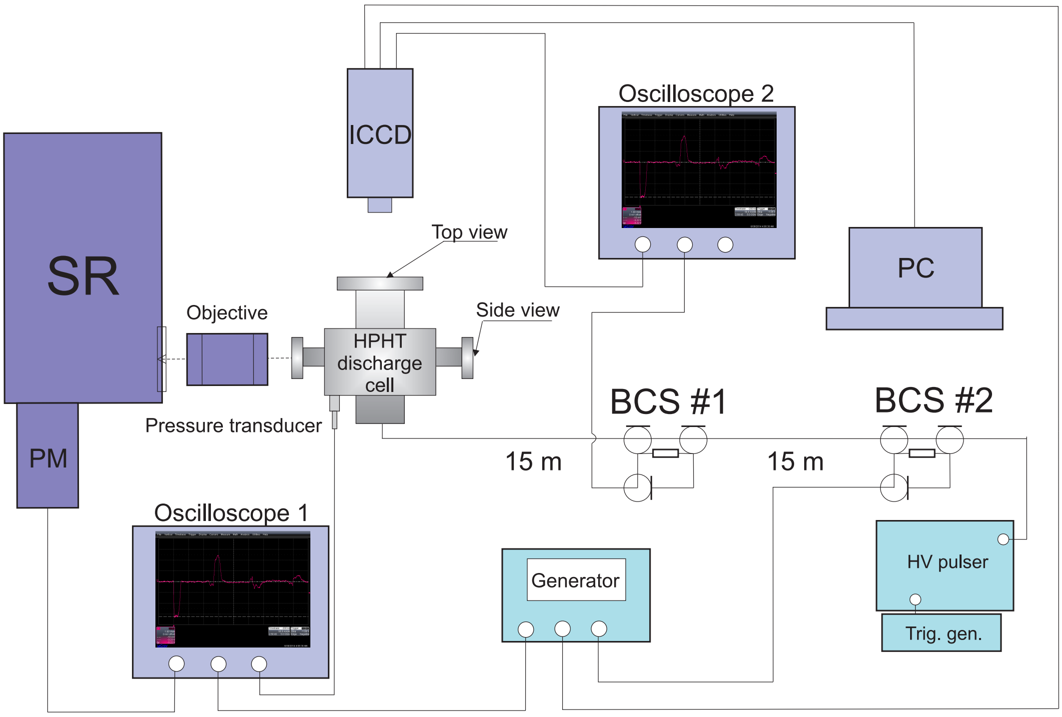

Figure 7.5: General scheme of experimental setup. SR - spectrograph, ICCD - PiMax 4 ICCD camera, PM - Photomultiplier tube.

is fast, a typical time of quenching of $N_2(C^3\Pi_u)$ state by N_2 and O_2 molecules in air is less that 1 ns [33]. This means that a pattern of $N_2(C)$ emission represents adequately the discharge behavior in time and space, giving the idea about $(k_e \cdot n_e)$ distribution.

Four ICCD images of nanosecond surface dielectric barrier discharge in air at different pressures and voltage amplitudes are given by figure 7.6a–d. At relatively low pressures, $1-3$ bar, the nSDBD discharge starts from HV electrode as a set of synchronous plasma channels (streamers) covering quasi–uniformly the dielectric and propagating rapidly almost up to the end of the dielectric layer, 15 mm from the HV electrode (see figure 7.6a, for $P = 2$ bar and $U_0 = +30$ kV).

In assumption that after charging the dielectric the influence of the surface on the processes in the bulk of plasma is low, the potential on the high voltage electrode is divided between the potential of the near–electrode layer U_{el}, potential drop along the streamer channel, ΔU_s, and potential of the streamer head, U_h. Under given conditions, $U_{el} << \Delta U_s$ ($U_{el} = 0.3 - 0.5$ kV) [9]. When streamer stops, $U_h << \Delta U_s$, and the E/N value can be estimated as:

$$\frac{E}{N} \approx \frac{U_0}{L_{max} \cdot N} = const, \tag{7.2}$$

where U_0 is a voltage on the HV electrode, L_{max} is a maximal distance of streamer propagation. It should be noted that in 2D calculations [34] and experiments [25] in air at $P \geq 1$ bar, the calculated and estimated values of the electric field were equal to $E/N = 80 - 100$ Td. The length of the streamer propagation decreases with pressure to keep the reduced electric field in the channel constant. The decrease of maximal length of nSDBD streamers in air at $P = 8$ bar is clearly seen in figure 7.6b for somewhat lower voltage, $U_0 = +22$ kV.

One of the aims of the present work is to check if the ignition along the multiple channels, over maximum possible surface, can be achieved at elevated pressures. This kind of ignition can be obtained if combustion starts not in the near-electrode zone but along the channels at the condition that the length of the channels is significant.

According to (8.2), the only visible possibility to increase the length of streamer channels with pressure is to use higher amplitude of voltage pulse. Physics of nanosecond surface DBDs is so that increase of voltage at relatively high pressures triggers an abrupt transformation of the spatial structure of the discharge. A filamentary mode of nSDBD was observed for the first time in [25] for high voltage pulses of negative polarity in synthetic air at $P = 1-6$ bar. The filamentation threshold, $\{P_f, U_f\}$ comprised, for example, $U = -47$ kV at $P = 3$ bar. At voltage higher than the filamentation threshold, streamers propagate at the distance L_{max} determined by expression (8.2), then slow down practically to zero velocity, and regular structure of filaments starts from the high voltage electrode, the brightness of a filament being $20-40$ times higher than a brightness of a streamer. The space between the filaments corresponds to a few streamers; the filaments propagate with a high velocity for a distances $3-4$ times longer that L_{max}. The difference of the present work is that, at pressures higher than in [25] the filamentation is observed not only at negative but also at positive polarity of the high–voltage pulse. Examples of filamentary nSDBD in air at 6 bar and 12 bar for voltage +50 kV on the high voltage electrode are given by figure 7.6c and figure 7.6d respectively. Filamentation happens in a single-shot mode, abruptly, within a few nanoseconds. No electrical closing of the gap is observed: the current closes, similar to streamer mode of SDBD discharge, by displacement current [9].

The $x-t$ diagrams for the experimental conditions corresponding to figures 7.6a–d are given in figure 7.6e. It is clearly seen that increase of gas pressure causes significant, a few times, decrease of the propagation length L_{max} of the streamers and so, plasma action of streamers–mode DBD at high pressures is limited by a narrow zone near the high voltage electrode. Filamentary mode of the discharge produces, at high pressure, a "grid" of long channels - filaments with a regular structure of chemical and hydrodynamic perturbations. The most remarkable fact is that, at constant voltage, $U = +50$ kV, filamentation allows (6 and 12 bar) approximately the same maximal length of the discharge L_{max} that the length of a streamer discharge at 2 bar.

On the basis of results [25, 31] and of the results of the present work, a very important conclusion about a general nature of filamentation of a single-shot nSDBD in molecular gases can be done. Figure 7.7 presents review of parameters of transition for air, N_2 and N_2:CH_4 mixtures at $1-12$ bar and $20-55$ kV for negative and positive polarities of high-voltage pulse. The data were taken for the conditions when filamentation happens during first 15 ns of the pulse. The data from [25] are in good agreement with the curve for air (figure 7.7a) but give slightly higher values of U_f. This can be explained by the fact that (i) in [25] the data were taken for the conditions when filamentation happens during first 7 ns of the discharge; (ii) rise time of the pulse was 4 times shorter than in the present work. The parameters of transition to filamentary mode, P_f and U_f, depend upon voltage rise time, polarity and gas mixture. In particular, it can be seen that discharge filamentation in air occurs easier for negative polarity, whereas in pure molecular nitrogen it is easier for positive polarity of applied pulses. Although a physical

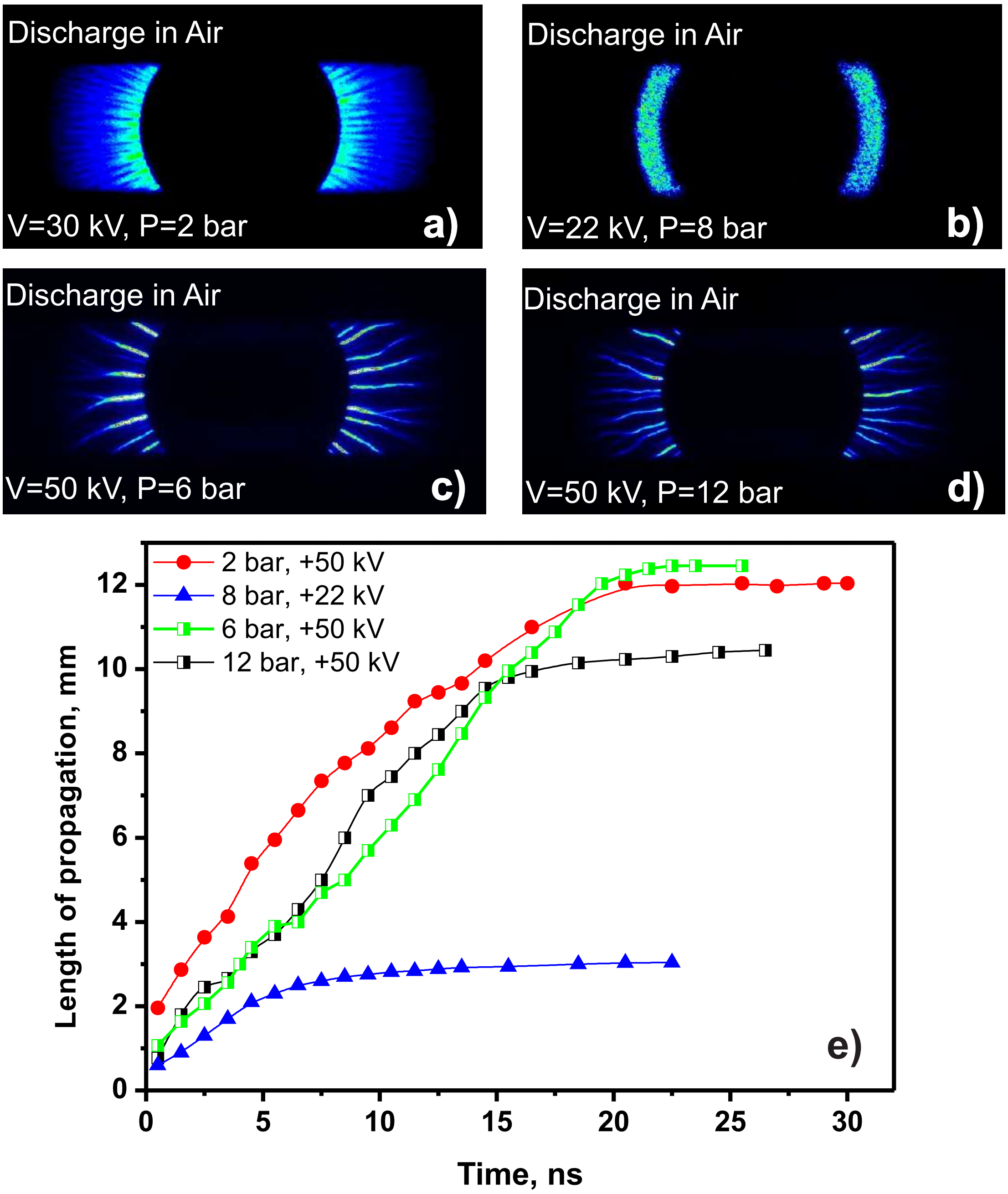

Figure 7.6: Integral ICCD images of positive polarity nanosecond surface barrier discharge (nSDBD) in air for different voltage of applied pulses and pressures: (a) $U = +30$ kV, $P = 2$ bar, (b) $U = +22$ kV, $P = 8$ bar, (c) $U = +50$ kV, $P = 6$ bar, (d) $U = +50$ kV, $P = 12$ bar. ICCD camera gate is 100 ns, pressure and voltage are indicated at each frame. (e) Selected x-t diagrams. ICCD gate is 0.5 ns.

nature of filamentation is not clear yet, it is extremely interesting to study if filamentation exists in combustible mixtures and if the length of filaments in important for initiation of combustion.

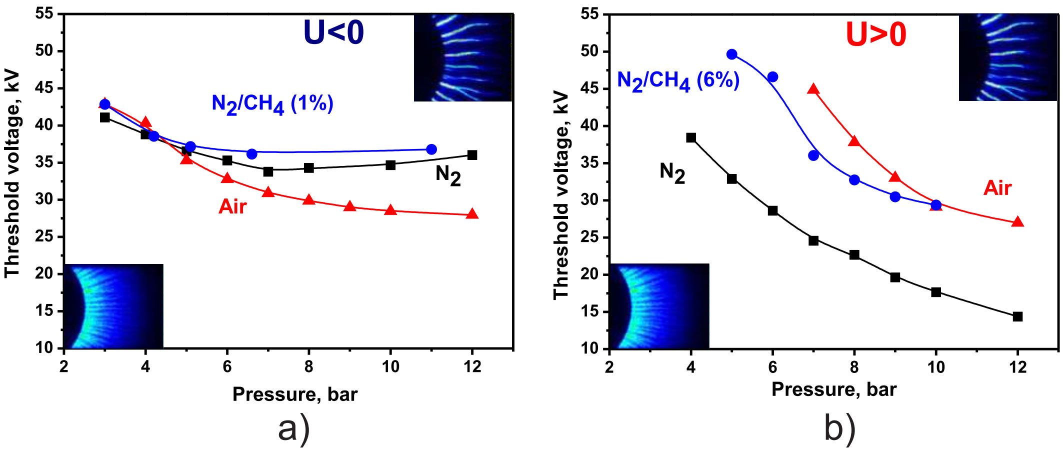

Figure 7.7: Threshold pressure and voltage for streamer–to–filament transition in different gases: (a) negative polarity of applied voltage; (b) positive polarity. Typical ICCD images of streamer and filamentary nSDBD (camera gate is 20 ns) are presented below and above the transition curve. The criterion for streamer–to–filament transition was that the transition happens within first 15 ns of the discharge.

7.2.2 Streamer-to-filament transition of nSDBD discharge in H_2:air mixture

The difference in maximal propagation length of streamers and filaments in H_2:air ($P = 6$ bar, $ER = 0.5$) mixture is not so well pronounced like for air or nitrogen, the transition between streamer and filamentary modes is smooth. This is illustrated by figure 7.8a representing L_{max} as a function of applied voltage. The ICCD images for selected conditions, $U = +20$, $+33$ and $+52$ kV, are given in the same plot. A streamer discharge is observed for +20 and +33 kV. At high voltage (+52 kV), a filamentary mode is clearly seen. The difference between streamer and filamentary mode is the most clearly seen form the angular (transversal) distribution of emission, see figure 7.8b . Filamentary mode provides a regular structure of bright emitting channels, with emission intensity $20 - 30$ times higher than emission of a streamer mode at relatively close voltage amplitudes, +33 and +40 kV. Another possibility to distinct between a streamer and a filamentary mode in lean H_2:air mixture is illustrated by figure 7.8a: maximal length of propagation, L_{max} in streamer mode are situated on the line $E/N = const \approx 70$ Td, while L_{max} for filaments is significantly higher. To understand a correlation between the discharge appearance and the behavior of the ignition pattern, a set of experiments was carried out with the only varying parameter, the amplitude of the high voltage pulse. A broad optical access provided by HPHT discharge cell and so a possibility to study discharge and following combustion under the same experimental condition is an important feature of the present work.

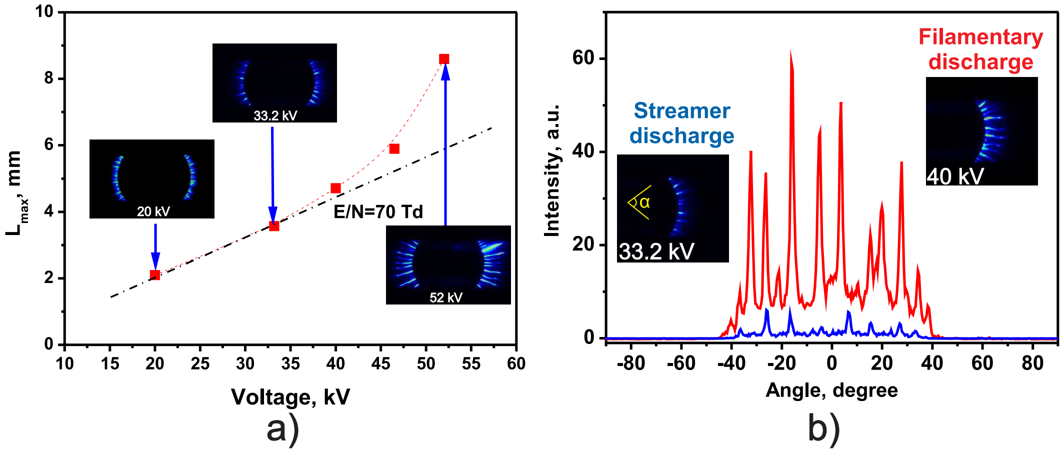

Figure 7.8: (a) Maximal length of discharge propagation in H_2:air mixture as a function of applied voltage. $P = 6$ bar, $T = 300$ K, $ER = 0.5$; (b) comparison of angular distribution of emission intensity for streamers, $U = +33$ kV and filaments, $U = +40$ kV on the high–voltage electrode.

7.3 Initiation of combustion in the afterglow of nS-DBD discharge in H_2:air mixture

7.3.1 OH emission pattern and temperature after the discharge ignition of H_2:air mixture

Spectral analysis shows that after the discharge, the dominating emission is the emission of OH radical ($\lambda = 306.4$ nm, $A^2\Sigma(v' = 0) \rightarrow X^2\Pi(v'' = 0)$ transition). This molecular band was chosen to study initiation of combustion after the discharge action.

ICCD images of OH emission for H2:air ($ER = 0.5$) mixture at $P = 6$ bar are presented in figure 7.9a. Voltage pulse $U = +53$ kV in amplitude is applied to the high–voltage electrode at time instant $t = 0$. Frontal and side ICCD images are synchronized in time, the time instant is marked in the left upper corner of each pair of frames. It is seen that the emission front starts after the discharge action from the near-electrode zone, propagates gradually and reaches the upper flange of the discharge chamber in a few milliseconds. OH–emission pattern at $t = 100$ μs (the first frame) is similar in shape to the discharge.

Figure 7.9b represents synchronized oscillograms of pressure in HPHT chamber and OH emission taken with the PMT connected to the Acton spectrometer. Joint analysis of the OH behavior and ICCD images proves that sharp increase of pressure between 2 and 4 ms is accompanied by a sharp increase of intensity of OH emission. So, between 2 and 4 ms the initiation of combustion in the entire volume of HPHT chamber takes place, and the combustion front expands out of the discharge chamber through the rectangular slit in the upper flange.

To study the process of development of combustion at time interval $0 - 3$ ms, when pressure rise is small but already clearly seen, the spectra of two different molecular transitions were analyzed. The rotational temperatures of hydroxyl radicals and molecular

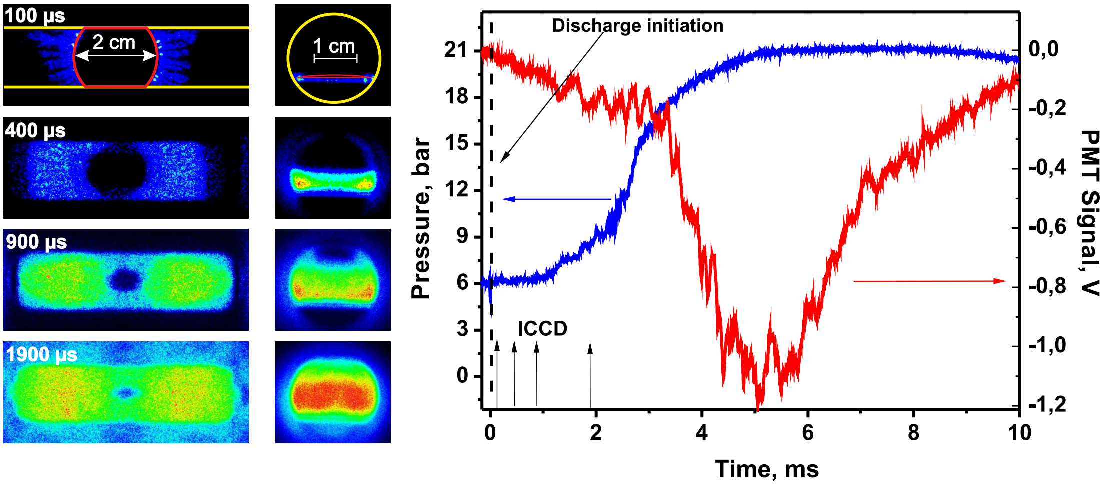

a) b)

Figure 7.9: (a) ICCD images of frontal and side views of ignition of H_2:air mixture with nSDBD: $U = +53$ kV. $P = 6$ bar, $T = 300$ K, $ER = 0.5$. Camera gate is equal to 50 μs, delay between the discharge and ICCD gate is indicated in each frame; (b) pressure and OH emission as a function of time. Vertical arrows indicate the time instants where the ICCD images were taken.

nitrogen were recorded at 306.4 nm and 337.1 nm respectively. OH-emission was available all the time in the discharge afterglow, so the emission spectra of excited hydroxyl radical corresponding to $A^2\Sigma^+$, v'=0 → $X^2\Pi$, v"=0 transition were recorded at different time instances: $100, 400, 900$ and 1900 μs after the discharge. To get $N_2(C^3\Pi_u \rightarrow B^3\Pi_g)$ emission, molecular nitrogen was excited by the discharge. The spectra were taken during the main discharge and in the additional probe pulse, initiated only for this kind of measurements 1.9 ms after the main pulse. All theoretical spectra were simulated with SpecAir code [35, 36] with the known slit function of the spectrometer calculated from the broadening of Hg line of a calibration source.

The OH spectrum taken at 1.9 ms and corresponding simulated spectrum are represented in figure 7.10a. The rotational temperature, calculated from OH emission, is approximately equal to T_{rot}=3500 K. It should be noted that the T_{rot} was approximately constant for all the OH spectra measured at different time instants.

The main reaction responsible for production of $OH(A^2\Sigma^+)$ in the discharge afterglow or in flame is $O+H+M=OH(A^2\Sigma^+)+M$. In this reaction the radical is formed with high rotational energy. The rate constants of quenching of $OH(A^2\Sigma^+)$ radicals by H_2,O_2,H_2O molecules are high, on the order of $(2-5)\cdot 10^{-10}$ cm^3/s (see table 7.1), so the quenching of $OH(A^2\Sigma^+)$ is faster than thermalization of the rotational distribution. The fact that during $0-3$ ms, the OH rotational temperature stay unchanged means that a chemical way to get the $OH(A^2\Sigma^+)$ does not change during this period. The intensity of emission and therefore the concentration of radicals increase, the rotational temperature remains the same, and so, does not allow calculating the gas temperature.

Figure 7.10b demonstrates the experimental and theoretical emission spectra of N_2

Table 7.1: Reactions of production and quenching of excited OH radicals

No	Reaction	Rate constant	Reference
R1	$H + O + M \rightarrow OH^* + M$	$3.3 \cdot 10^{-35} exp(\frac{-3500}{T})$ cm^6/s	[37]
R2	$OH^* + H_2 \rightarrow OH + H_2$	$(4.6\pm0.2) \cdot 10^{-10}$ cm^3/s	[38]
R3	$OH^* + O_2 \rightarrow OH + O_2$	$(1.5\pm0.5) \cdot 10^{-10}$ cm^3/s	[38]
R4	$OH^* + N_2 \rightarrow OH + N_2$	$(1.0\pm0.2) \cdot 10^{-11}$ cm^3/s	[38]
R5	$OH^* + H_2O \rightarrow OH + H_2O$	$(4.4\pm0.3) \cdot 10^{-10}$ cm^3/s	[38]

emission in the discharge and 1.9 ms after the discharge. Acquired spectra of molecular nitrogen correspond to rotational temperatures $T^C_{rot} = 330$ K in the discharge and 1300 K at the time instant 1.9 ms.

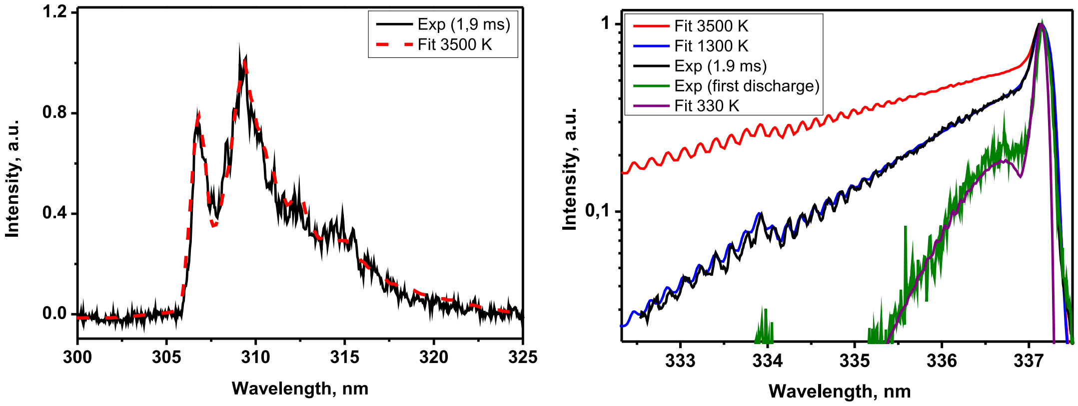

a) b)

Figure 7.10: Spectra of emission of (a) OH–radical, ICCD gate is 50 μs, delay 1.9 ms after the discharge; and (b) molecular nitrogen, ICCD gate is 1 μs, delays 0 ns and 1.9 ms after the discharge. Fits are calculated in SpecAir software [35, 36].

Excitation of molecular nitrogen in nanosecond discharge takes place mainly due to direct electron impact. In this case the distribution of the rotational levels remains the same as for ground state of N_2, and so the recorded rotational temperature of excited nitrogen T^C_{rot} and translational temperature T are linked by the following equation: $T = T^X_{rot} = (B^X_e/B^C_e)T^C_{rot} = 1.1T^C_{rot}$. So, the temperature recorded in H_2:air mixture in the vicinity of the discharge (camera gate was 1 μs) is equal to $T = 363$ K, and 1.9 ms after the discharge (camera gate was 50 μs) is equal to $T = 1430$ K, what is close to adiabatic flame temperature for considered experimental conditions, about 1550 K [39].

So, the conclusion from analysis of pressure waveform, ICCD images and emission behavior is that (a) observed emission patterns correspond to initiation of combustion; (b) before the main pressure increase, a system of combustion waves develops and propagates in the discharge chamber, the temperature in the flame zone being close to adiabatic combustion temperature.

7.3.2 Discharge modes and three regimes of flame initiation

To analyze a correlation between the discharge appearance and the behavior of the ignition pattern, imaging of combustion was made for the initial period of flame development in the discharge cell for three different amplitudes of the high–voltage pulse. Figure 7.11a presents ICCD images of ignition at 20 kV on the high voltage electrode, the total deposited energy being equal to $W = 3$ mJ. These parameters correspond to developed streamer mode of SDBD discharge. The flame starts 300 μs after the discharge as a few ignition kernels developing at the edge of the high-voltage electrode. The kernels expand as spherical combustion waves and interacting, form an irregular structure at $1 - 3$ ms. Despite the fact that discharge energy is distributed equally between the streamers, the ignition starts only from one or several kernels. The number of ignition kernels increases with voltage. This regime of ignition is unstable and extremely sensitive to applied voltage. Even with a slight voltage deviation, the number of kernels and the time of ignition in each kernel change significantly the time of initiation of combustion in entire volume.

When the voltage reaches the value of $U = +33$ kV (deposited energy is $W = 5$ mJ), the combustion kernels are distributed evenly along the edge of the high–voltage electrode, and ignition starts from a quasiuniform structure near the electrode (see figure 7.11b). In this case, maximal energy release is presumably concentrated near the high-voltage electrode, whatever polarity is, and synchronous structure of combustion waves propagates with a high visible velocity. Emission from excited OH appears approximately 50 μs after the discharge initiation. The repeatability of the experiments in this mode is high enough: the scattering of ignition delay time did not exceed 10%. This mode of ignition has already been mentioned in [24] and later in [28], where ignition of stoichiometric C_2H_6:O_2 and C_2H_2:air mixtures respectively was studied at atmospheric pressure.

The third mode of flame initiation is demonstrated in figure 7.11c. This regime has not been observed before and corresponds to the ignition by filamentary discharge. The applied voltage was equal to $U = +53$ kV, and total energy deposition was $W = 10$ mJ. In this mode, similarly to streamer mode of the discharge, the initial distribution of energy is inhomogeneous along the discharge channel: a few bright spots in the near–electrode region can be easily seen in the frame corresponding to time period $t < 150$ μs. The bright spots do not expand and decay in $150 - 250$ μs (see figure 7.11c) not influencing the morphology of the ignition. Combustion starts along entire length of each filament. We believe that quenching of the bright spots near the electrode can be explained by heat removal to the electrode or by non–sufficient size of the ignition kernel [40]. The ignited channels expand in three directions: (i) in radial direction, that is elongation of the ignition channels; (ii) in azimuthal direction; (iii) in direction perpendicular to the electrode, in the volume of the discharge chamber.

7.3.3 Propagation of combustion wave

Velocities of flame propagation in different directions are summarized in figure 7.12b-d for two different modes: streamer discharge at $U = +33$ kV (conditions as in the figure 7.11b) and filamentary discharge at $U = +53$ kV (conditions as in the figure 7.11c). The details of the geometry are explained by figure 7.12a. The formation of combustion pattern in the plane of the electrode is quite complex. Figures 7.12b,c present velocity in radial and azimuthal direction respectively. They differ significantly for streamer and filamentary

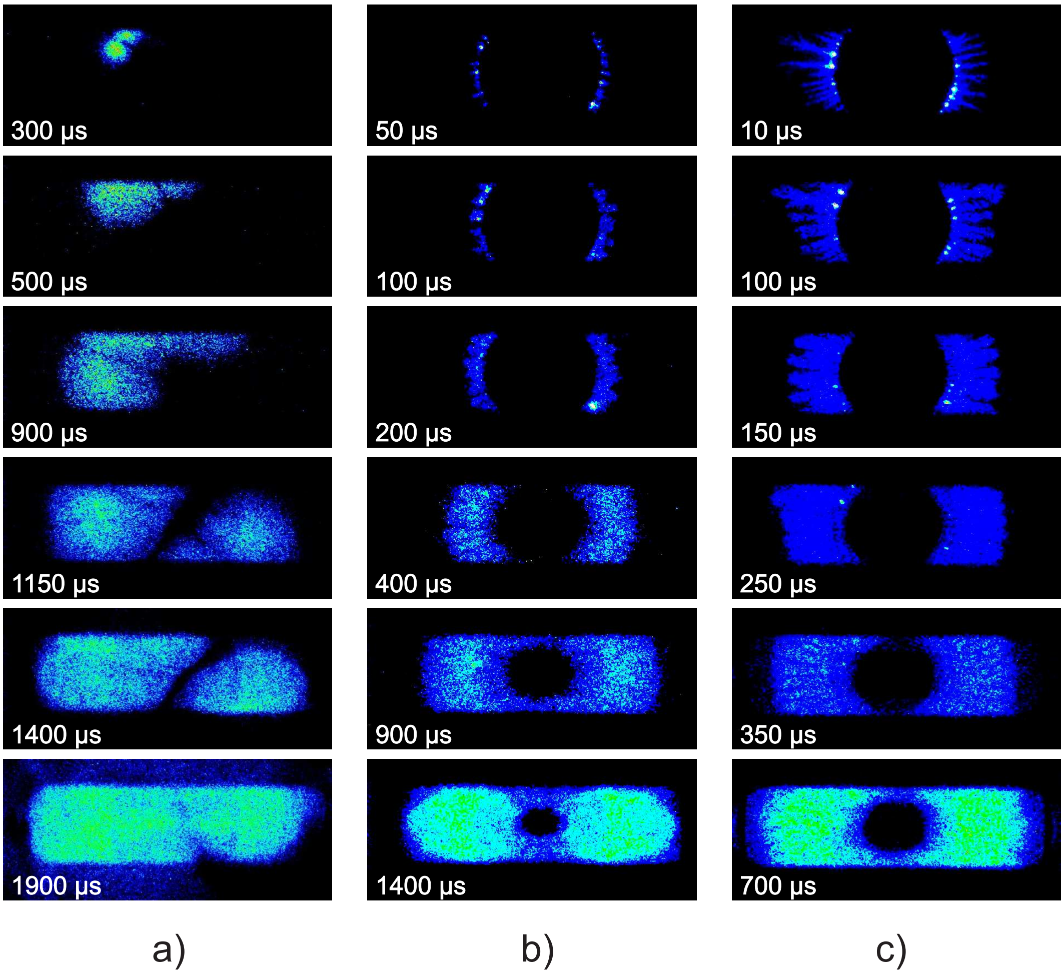

Figure 7.11: Three regimes of ignition of H_2:air mixture with nSDBD: (a,b) streamer discharge; (c) filamentary discharge. Voltage on the electrode is equal to (a) $U = +20$ kV; (b) $U = +33.2$ kV; (c) $U = +53$ kV. $P = 6$ bar, $T = 300$ K, $ER = 0.5$. Camera gate is equal to 50 μs, delay between the discharge and ICCD gate is indicated in each frame.

mode. When the 2D pattern of combustion is formed near the electrode, the flame front propagates from the lower end plate of the discharge chamber with velocity 10.3 m/s both for streamer and filamentary discharge modes (figure 7.12d). High velocity of propagation corresponds to the fact presented recently in [41] that nanosecond SDBD discharge with high specific delivered energy can produce significant hydrodynamic perturbations. The highest obtained velocity, 14 m/s in radial direction was obtained for filamentary mode of the discharge.

Measured velocities are comparable or higher than the velocity of flame propagation for the given conditions. Velocities of flame propagation in the H_2:air mixture (ER=0.5, that is the fraction of hydrogen in the mixture is about 17%, P=6 bar, T_0=300 K), can be estimated in the following way. The normal propagation velocity of the flame under the considered conditions is V_n=50 cm/s [42]. The coefficient of expansion is $\rho/\rho_0 \approx T_{max}/T_0 = 5$. Thus, the observed speed of the combustion wave, measured in the experiment, is equal to

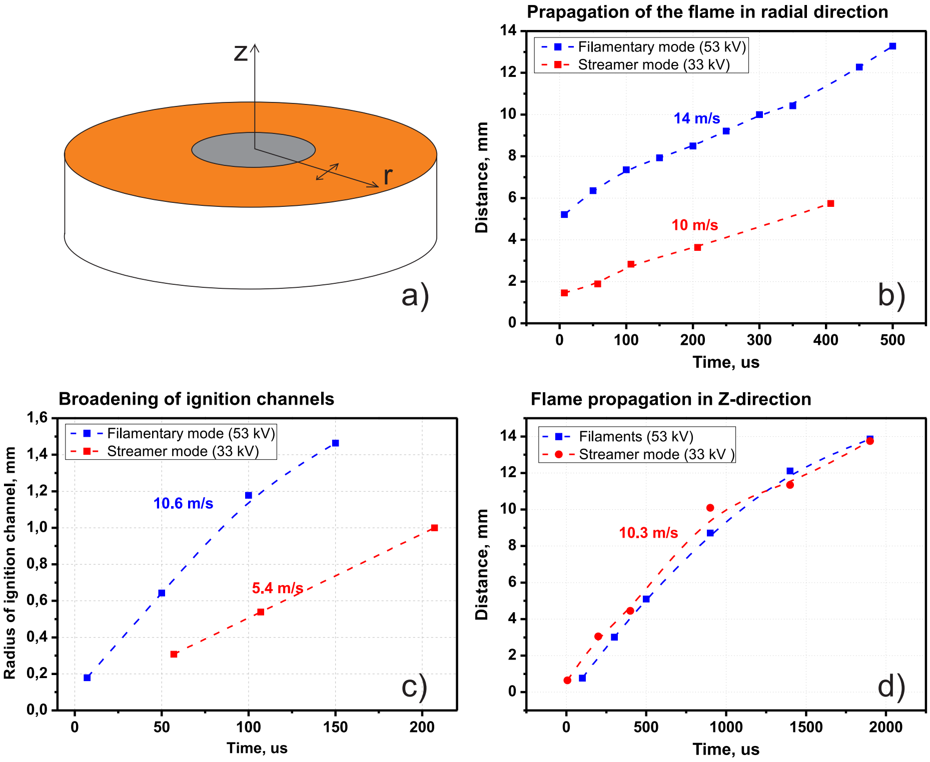

Figure 7.12: Flame velocities. (a) scheme of electrode system and the representation of direction of flame propagation; (b) propagation in radial direction; (c) expansion of ignition channels; (d) flame propagation in the volume of the chamber.

$$V^* = V_n \cdot \rho/\rho_0 = 2.5 \text{ m/s}. \tag{7.3}$$

The measured velocity of the combustion wave in the experiments of the present work is $10-14$ m/s (see figure 7.12), that is $4-5$ times higher than V^* value (7.3). It should be noted that high flame velocities achieved in lean mixtures (ER=0.5 in our experimental case) can be an interesting issue for industrial applications.

One of the possible reasons of increasing of combustion wave speed is the turbulization of the flow field in the vicinity of the front of the combustion wave. This may be the result of interactions of weak gas-dynamic perturbations initiated by discharge channels, with the flame front. According to [43], $4-5$ times increase of the velocity of the combustion wave is observed when the rate of turbulent fluctuations in the flame front exceeds 3 m/s.

7.4 Discharge energy needed for ignition. Measurements of MIE

Nanosecond surface dielectric barrier discharge is a 3D structure with a complex distribution of energy over the discharge volume. Nevertheless, observed symmetry and regular structure of the discharge allow calculation of minimal ignition energy (MIE) on the basis of experimentally measured energy delivered to the discharge. Kinetic modeling is used to estimate the specific energy in discharge filaments needed for ignition and the corresponding spatial characteristics of the plasma channels.

7.4.1 Deposited energy as a function of applied voltage

At $P = 6$ bar and $ER = 0.5$ the mixture ignited at the lowest possible voltage of the generator. To study minimum ignition energy, the experiments were carried out at $P =$ 3 bar, $ER = 0.6$ and $P = 5$ bar, $ER = 0.6$. Figure 7.13a presents the total energy deposited into plasma as a function of applied voltagae at $P = 3$ bar, $ER = 0.6$ and voltages $U = 20 - 55$ kV on the electrode. An example of the integral ICCD image of the discharge (camera gate is equal to 100 ns, wavelength range is equal to $300 - 800$ nm) for $U = +53$ kV is shown at the left upper corner of the figure. It is clearly seen that at $P = 3$ bar, even at the highest voltage amplitude, the discharge is a streamer discharge, no filaments is observed. It is interesting to compare deposited energies at $P = 3$ bar, $ER = 0.6$ to those at $P = 6$ bar, $ER = 0.5$: the energies are higher for 3 bar, the difference increases progressively with voltage, and the ratio of delivered energies at 3 bar and 6 bar is approximately equal to 2/3/6 for 20/30/50 kV of voltage amplitude.

ICCD images of OH emission after the discharge, integrated over 500 μs, are presented in figure 7.13b. To eliminate any emission corresponding to the discharge, the images were taken with $\tau = 5$ μs delay after the discharge initiation. It is clearly seen that the structure of ignition kernels is similar to the structure obtained at higher pressure in the streamer mode of the discharge: (compare with Figure 7.11 a,b): a few kernel are observed at low voltages; with voltage increase, a regular structure appears around the high–voltage electrode. Ignition always appears at the edge of the high–voltage electrode, and the length of the propagation at given time instant is a function of high voltage amplitude. It should be noted that at $P = 3$ bar and $ER = 0.4$ the ignition was unstable, a probability to ignite the mixture at highest used amplitude was not higher than 50%.

7.4.2 Measurements of MIE

Time of initiation of combustion in entire volume, τ_{comb}, was determined as a beginning of a sharp rise of OH emission, corresponding to pressure increase in HPHT chamber (see figure 7.9b). The τ_{comb} progressively decreases with deposited energy. This fact is illustrated by figure 7.14, where the time τ_{comb} for $P = 3$ bar and $P = 5$ bar is presented. It is clearly seen from the figure that, when ignition starts in a few points around the electrode, the τ_{comb} is high. With increased energy deposition, τ_{comb} decreases drastically. This part of curve, marked as “1” in figure 7.14, corresponds to increase of number of ignition kernels around the electrode and to beginning of the interaction between separate combustion waves. Ignition of entire volume depends upon the initiation of combustion in each of kernels and by the velocity of the flame propagation. Starting from some value of deposited energy, 13 mJ for 3 bar and 5 mJ for 5 bar, ignition delay time practically does not change with deposited energy. This part, marked as “2”, corresponds to a “saturated” chain of ignition kernels along all the perimeter of the high-voltage electrode. In this case, the time τ_{comb} is determined mainly by a flame propagation velocity. Ignition presented in figure 7.14 corresponds to streamer mode of nSDBD discharge.

The ICCD images of combustion pattern on the right hand side of figure 7.14 illustrate

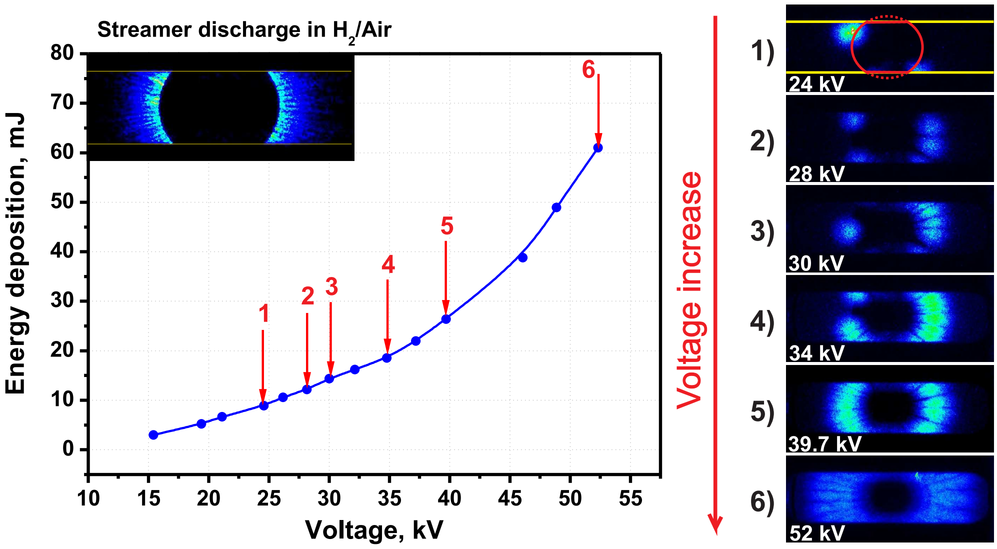

a) b)

Figure 7.13: H_2:air mixture, $ER = 0.6$, $P = 3$ bar, $T = 300$ K. (a) Total energy deposited in plasma as a function of voltage on the electrodes and the discharge image for $U = +53$ kV on the electrode. Red arrows at the plot show the experimental conditions where ICCD images in the afterglow were taken; (b) Integral ICCD images of emission in the afterglow for different voltages. Camera gate is 500 μs, time delay from the discharge initiation is 5 μs.

the approach used to calculate a minimal ignition energy (MIE). The voltage amplitude was decreased to the threshold U_{min} when combustion appears statistically in a regular way not more than in $1-3$ kernels and the flame propagation, followed by combustion in the whole volume, is observed. We believed that the threshold is reached when combustion appeared with 90% probability. The delivered to the discharge energy corresponding to this voltage, W_{min}, was divided by a number of streamers, Z_s at these experimental conditions. Minimum ignition energy for H_2:air mixture at ER=0.6 was estimated as 50 μJ at $P = 3$ bar ($W_{min} = 2.8\ mJ$, $Z_s \approx 120$) and 20 μJ at $P = 5$ bar ($W_{min} = 1.6\ mJ$, $Z_s \approx 80$). Difference of MIE for $P = 3$ bar and 5 bar can be explained by increase of reactivity of combustible mixture at higher pressure. On the other hand, this difference would be not so significant if more realistic energy parameter, namely specific delivered energy, was compared. It should be noted that the MIE for H_2:O_2 mixture ignited by spark discharge at $ER = 0.6$ at atmospheric pressure is reported to be 50 μJ [39]. A few experiments on MIE measurements for plasma assisted combustion is known. In particular, MIE was measured for transient plasma of nanosecond discharge in point–to–plane geometry for propane- and n–heptane containing mixtures [30]. They reported a value of MIE equal to 17 mJ for stoichiometric mixtures of both hydrocarbons under study. Although experimentally obtained MIE is in reasonable correlation with the data of other authors, it should be noted that, for plasma assisted ignition, MIE is more complicated parameter than for spark ignition. Indeed, in addition to ideas of critical flame radius and quenching distance, processes of relaxation of nonequilibrium energy must be considered.

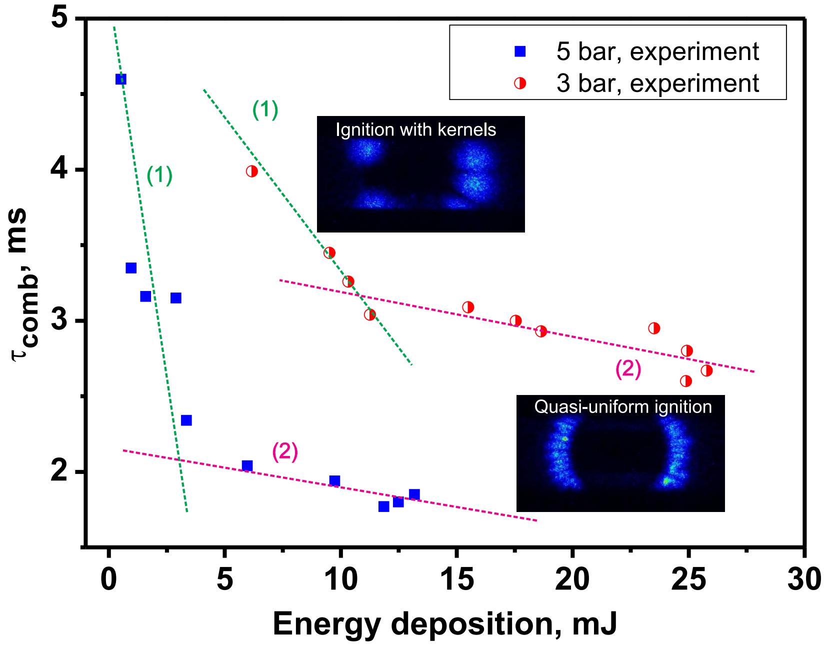

Figure 7.14: Time of initiation of combustion in entire volume as a function of delivered energy for different pressures. H_2:air mixture, $ER = 0.6$.

7.4.3 Numerical calculations and analysis of specific deposited energy

The aim of numerical modeling was (i) to analyze kinetics of ignition initiated by nSDBD for conditions close to the experimental conditions of the present work; (ii) to provide, on the basis of calculations, minimum specific energy giving experimentally observed ignition delay time.

The kinetic model used to study plasma–assisted ignition of H_2:air mixtures is described in detail in the previous work [43]. The model includes “plasma” reactions, such as electron impact ionization, dissociation and excitation of mixture molecules, ion-molecular reactions, reactions between electronically excited atoms and molecules, as well as “combustion” processes describing ignition of hydrogen/air mixture.

Figure 7.15 presents the results of calculations of gas temperature, densities of atomic species and of excited $OH(A^2\Sigma^+)$ molecules in H_2:air mixture ($ER = 0.5$) in the afterglow of the discharge with reduced electric field $E/N = 200$ Td at specific deposited energy $w = 0.2$ eV/molecule. The calculation were made using model [43], in isobaric approximation.

The decay of O- and H-atoms in the near afterglow is relatively fast. The reactions (R6)-(R7) are responsible for decrease of O atoms density:

$$O(^3P) + HO_2 \rightarrow OH + O_2 \qquad (R6)$$
$$O(^3P) + OH \rightarrow H + O_2 \qquad (R7)$$

Decay of atomic hydrogen is mainly due to reactions

$$\begin{aligned}&\mathrm{H + O_2 + M \rightarrow HO_2 + M} && \text{(R8)}\\ &\mathrm{H + HO_2 \rightarrow OH + OH} && \text{(R9)}\\ &\mathrm{H + HO_2 \rightarrow H_2 + O_2} && \text{(R10)}\end{aligned}$$

In the afterglow of the discharge, the production of electronically excited $OH(A^2\Sigma^+)$ molecules is due to the reaction (R1):

$$\mathrm{H + O + M \rightarrow OH(A^2\Sigma^+) + M}$$

so the kinetic curve of $OH(A^2\Sigma^+)$ "follows" the density of the atomic species. Increase of gas temperature in the afterglow is due to (i) recombination of atoms (R6)-(R10) and (ii) VT - relaxation of molecular nitrogen, $N_2(v)$. At $w = 0.2$ eV/mol and $E/N = 200$ Td, maximal possible vibrational temperature is $T_v(N_2) = 2120$ K. Relaxation takes place mainly in collisions with H_2 and produced H_2O molecules. Typical time of VT-relaxation under the conditions of figure 7.15 is $7-8$ μs.

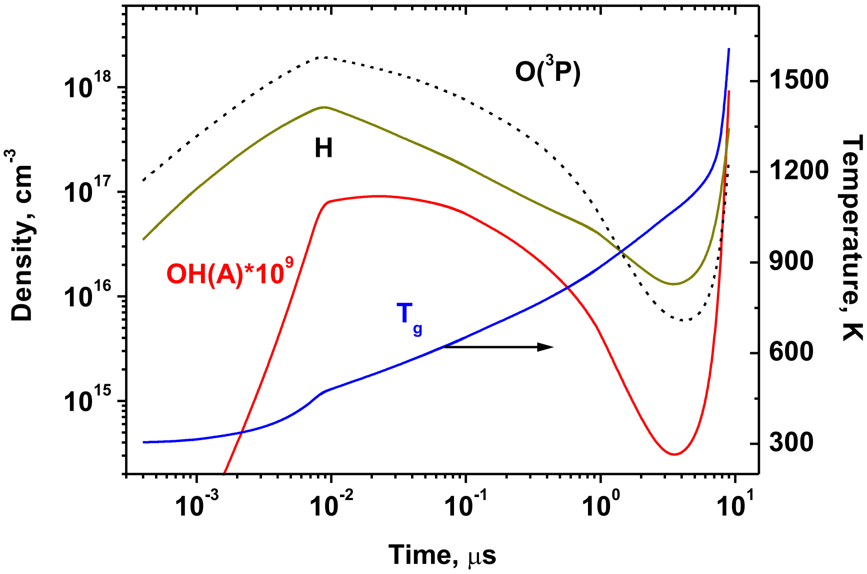

Figure 7.15: Gas temperature, densities of atomic species and of excited $OH(A^2\Sigma^+)$ molecules in the afterglow of the discharge in H_2:air ($ER = 0.5$) at $= 6$ bar and $T_0 = 300$ K. Specific deposited energy is $w = 0.2$ eV/mol, reduced electric field is $E/N = 200$ Td.

To compare the efficiency of equilibrium and non-equilibrium ignition of H_2:air mixtures, the numerical calculations were performed for both autoignition (given as "equilibrium" energy release corresponding to gas heating by the shock wave in the experiments [44]) and ignition by pulsed discharge. For the equilibrium case it was suggested that total deposited energy goes directly to heating of the mixture and initial energy distribution corresponds to the Boltzmann distribution. In nonequilibrium regime the energy is distributed over internal degrees of freedom depending upon E/N. To calculate energy branching, a two-term approximation of Boltzmann equation for EEDF has been solved with *BOLSIG+* code [45, 46].

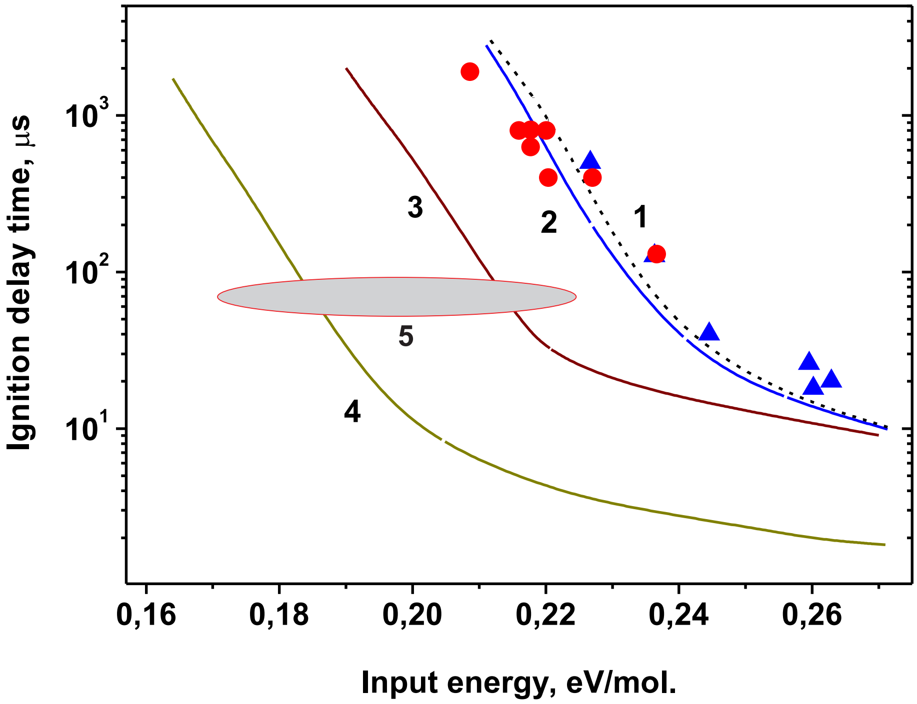

Figure 7.16: The induction delay time as a function of specific energy. H_2/air mixture, P=4-6 bar, T_0=300 K, ER=0.44-0.5. Results of simulation (curves 1,2) and experimental data (dots) [44], for the conditions when the total energy of the discharge instantly goes to the gas heating; ER = 0.44, P = 4 bar (curve 1), P = 6 bar (curve 2). Curves 3 and 4 correspond to the simulation with real energy distribution over the degrees of freedom at $E/N = 100$ Td (3) and $E/N = 200$ Td (4), ER=0.5, P=6 bar. The shaded area 5 is the experimental data on the induction delay time τ_{ind}=50-70 μs, obtained in given work.

To compare the simulation results with the measurement data in autoignition mode, the calculations were carried out for the experimental conditions of [44]. The experimental results of [44] represent the ignition delay measured in the shock tube for lean H_2:air mixture in the pressure range between 3 and 5 bar. The results of numerical simulation of ignition delay time as a function of specific energy w for H_2:air mixture with $ER = 0.44$, $P = 4$ bar (curve 1) and $P = 6$ *bar* (curve 2) are presented in figure 7.16;

$$W = (T - T_0)\gamma/(\gamma - 1), \tag{7.4}$$

where T is gas temperature behind the shock wave, T_0=300 K is initial temperature of the mixture, γ is an adiabatic index. Similar calculations, but taking into account nonequilibrium distribution of the discharge energy over degrees of freedom, are also presented in the figure 7.16 for $E/N = 100$ Td (curve 3) and $E/N = 200$ Td (curve 4). In the case of nonequilibrium distribution the part of energy goes to the dissociation of mixture molecules, to vibrational excitation as well as to the gas heating [43]).

At $E/N = 100$ Td almost half of the discharge energy is spent for the excitation of vibrational degrees of freedom of molecular nitrogen $N_2(\nu)$. The characteristic time of VT-relaxation of $N_2(\nu)$ molecules under the following conditions is about hundreds of microseconds [47]), therefore the gas temperature remains relatively low on a timescale less than a characteristic time of VT relaxation. The calculation results underline the fact that in the case of non-equilibrium plasma-assisted ignition the rate of gas heating has a significant impact on the ignition delay.

According to figure 7.16, at $E/N = 100 - 200$ Td the ignition delays τ_{ind}=50-70 μs correspond to specific energies (0.2±0.01) eV/mol. The possibility of achieving such values of specific deposited energy can be estimated in the following way. The average maximum length of the filaments calculated from the ICCD images is equal to $< L_m >= 4.5$ mm. If the total energy deposition into the volume occupied by the discharge is about $W = 10$ mJ, and the number of channels (filaments) is N_{ch}=50, then the energy per unit length in the channel can be estimated as W_d=0.4 mJ/cm. It was assumed, according to the distribution of emission intensity, that the energy is distributed homogenously along the filaments.

Volume occupied by the discharge can be estimated on the basis of ICCD images. The average maximum length of a filament and the average radius were estimated from the images of the discharge in H_2:air; the thickness of the plasma layer was taken from the experimental data for air [25].

If the discharge channel can be presented as a half–cylinder, extended on the dielectric surface, then at $P = 6$ bar, $T = 300$ K and $W_d = 0.4$ mJ/cm to achieve the specific energy of $w = 0.2$ eV/mol, the radius of the cylinder must be around 70 μm ($S_{ch} = 8{\cdot}10^{-5}$ cm^2), which seems to be quite reasonable value. It should be noted that optical radius obtained directly from ICCD images is about 130 μm, that is approximately two times higher. The possible reason of this distinction is that generally the optical radius of the discharge channels is significantly larger than “current” radius [48] corresponding to the distribution of the electron density.

ICCD data can be used for the estimate of the discharge current assuming that the current density in cathode layer is normal. Normal density of electrical current in cathode layer at $P = 6$ bar and $T = 300$ K is equal to j_n=6 kA/cm2 [9]. Taking the section of the discharge channel equal to S_{ch}=8·10^{-5} cm^2 and the number of channels equal to N_{ch}=50, will obtain for the total current $I = 25$ A, which is in a reasonable correlation with the experimentally measured value.

7.5 Conclusions

Development of nanosecond surface dielectric barrier discharge (nSDBD) in air, N_2, N_2:CH_4 mixtures at high pressures ($P = 1 - 12$ bar) and $U = 20 - 55$ kV has been studied. It was found that filamentation reported recently in [25] is a general feature of nSDBDs when pressure and/or voltage increases. The filamentation threshold is a function of numerous parameters, including gas mixture composition and polarity of the high–voltage electrode. A benefit for combustion applications is that filamentation mode of discharge represents a uniform “grid” of equidistant parallel channels separated by a few millimeters and propagating at a typical distances about 1 cm from the high-voltage electrode at pressures around 10 bar.

Discharge and following initiation of combustion were studied in H_2:air mixture at $P = 6$ bar, $ER = 0.5$ and ambient initial temperature. It was shown that there is a strong correlation between the discharge appearance and the behavior of the ignition pattern. At lowest voltage, a few ignition kernels appear on the edge of the high-voltage electrode.

When voltage increases, the number of ignition kernels increases, and at relatively high applied voltage, combustion starts from a continuous chain of ignition kernels around the high-voltage electrode. At high pressures and/or voltages the flame is initiated by the filamentary discharge. The most distinctive feature of ignition by filamentary nSDBD is that the combustion starts simultaneously from the entire length of each filament. The interaction of combustion waves initiated by separate filaments results in high visible speeds of flame propagation, about 10 m/s, which is a few times higher than the observed speed of combustion wave should be.

Minimum ignition energy, MIE, was measured at low voltages, when combustion starts from a few ignition kernels near the high-voltage electrode. The obtained values are MIE= 50 μJ for 3 bar and ER= 0.6; and MIE= 20 μJ for 5 bar and ER= 0.6. An important role of the spatial distribution of energy release for MIE definition for the case of non-equilibrium plasma discharges is underlined. Kinetic modeling of plasma assisted ignition for the electric fields typical for nSDBD, $E/N = 100 - 200$ Td, showed that to get the experimentally observed values of the ignition delay, the specific deposited energy in the discharge must be higher than 0.2 eV/mol. This is possible only if the radius of the filaments is less than 70 μm. The conclusion for such a small radius of filaments in nSDBD is new; it seems that high-pressure non-equilibrium surface discharges suggest an opportunity of “self-concentration” of energy in distributed channels. This, in particular, can produce effective hydrodynamic perturbations, both from the discharge and from the interaction of combustion waves. Although hydrodynamic effects need additional investigation, it can be concluded that the obtained system of regular channels of a filamentary nanosecond surface dielectric barrier discharge is an efficient tool for ignition of lean mixtures at elevated pressures.

Bibliography

[1] Starikovskaia S M 2006 Plasma assisted ignition and combustion *Journal of Physics D: Applied Physics* **39** R265

[2] Starikovskiy A and Aleksandrov N 2013 Plasma-assisted ignition and combustion *Progress in Energy and Combustion Science* **39** 61—110

[3] Adamovich I V, Li T and Lempert W R 2015 Kinetic mechanism of molecular energy transfer and chemical reactions in low-temperature air-fuel plasmas *Philosophical Transactions of the Royal Society of London A: Mathematical, Physical and Engineering Sciences* **373** 20140336

[4] Ju Y and Sun W 2015 Plasma assisted combustion: Dynamics and chemistry *Progress in Energy and Combustion Science* **48** 21—83

[5] Aleksandrov N L, Kindysheva S V, Nudnova M M and Starikovskiy A Y 2010 Mechanism of ultra-fast heating in a non-equilibrium weakly ionized air discharge plasma in high electric fields *Journal of Physics D: Applied Physics* **43** 255201

[6] Popov N A 2011 Fast gas heating in a nitrogen-oxygen discharge plasma: I. Kinetic mechanism *Journal of Physics D: Applied Physics* **44** 285201

[7] Kim W, Mungal M G and Cappelli M A 2010 The role of in situ reforming in plasma enhanced ultra lean premixed methane/air flames *Combustion and Flame* **157** 374--383

[8] Nagaraja S, Sun W and Yang V 2015 Effect of non-equilibrium plasma on two-stage ignition of n-heptane *Proceedings of the Combustion Institute* **35** 3497–3504

[9] Raizer Y P 1991 Gas Discharge Physics (New York: Springer)

[10] Vasilyak L M, Kostyuchenko S V, Kudryavtsev N N and Filyugin I V 1994 Fast ionisation waves under electrical breakdown conditions *Physics-Uspekhi* **37** 247

[11] Starikovskaia S M, Anikin N B, Pancheshnyi S V, Zatsepin D V and Starikovskii A Y 2001 Pulsed breakdown at high overvoltage: development, propagation and energy branching *Plasma Sources Science and Technology* **10** 344

[12] Pai D Z, Lacoste D A and Laux C O 2010 Nanosecond repetitively pulsed discharges in air at atmospheric pressure - the spark regime *Plasma Sources Science and Technology* **19** 065015

[13] Starikovskaia S M 2014 Plasma-assisted ignition and combustion: nanosecond discharges and development of kinetic mechanisms *Journal of Physics D: Applied Physics* **47** 353001

[14] Pancheshnyi S V, Lacoste D A, Bourdon A and Laux C O 2006 Ignition of propane–air mixtures by a repetitively pulsed nanosecond discharge *IEEE Transactions on Plasma Science* **34** 2478–2487

[15] Wang F, Liu J B, Sinibaldi J, Brophy C, Kuthi A, Jiang C, Ronney P and Gundersen M A 2005 Transient plasma ignition of quiescent and flowing air/fuel mixtures *IEEE Transactions on Plasma Science* **33** 844–849

[16] Singleton D, Pendleton S J and Gundersen M A 2011 The role of non-thermal transient plasma for enhanced flame ignition in C_2H_4-air *Journal of Physics D: Applied Physics* **44** 022001

[17] Starikovskiy A, Rakitin A, Correale G, Nikipelov A, Urushihara T and Shiraishi T 2012 Ignition of hydrocarbon-air mixtures with non-equilibrium plasma at elevated pressures *Proc. 50th AIAA Aerospace Sciences Meeting* (Nashville, TN, 912 January 2012) AIAA2012–0828

[18] Shao T, Zhang C, Niu Z, Yan P, Tarasenko V F, Baksht E K, Burahenko A G and Shutko Y V 2011 Diffuse discharge, runaway electron, and x-ray in atmospheric pressure air in an inhomogeneous electrical field in repetitive pulsed modes *Applied Physics Letters* **98** 021503

[19] Chen S, Heijmans L C J, Zeng R, Nijdam S and Ebert U 2015 Nanosecond repetitively pulsed discharges in N_2:O_2 mixtures: inception cloud and streamer emergence *Journal of Physics D: Applied Physics* **48** 175201

[20] Tardiveau P, Moreau N, Bentaleb S, Postel C and Pasquiers S 2009 Diffuse mode and diffuse-to-filamentary transition in a high pressure nanosecond scale corona discharge under high voltage *Journal of Physics D: Applied Physics* **42** 175202

[21] Rusterholtz D L, Lacoste D A, Stancu G D, Pai D Z and Laux C O 2013 720 Ultrafast heating and oxygen dissociation in atmospheric pressure air by nanosecond repetitively pulsed discharges *Journal of Physics D: Applied Physics* **46** 464010

[22] Bletzinger P, Ganguly B N, Wie D V and Garscadden A 2005 Plasmas in high speed aerodynamics *Journal of Physics D: Applied Physics* **38** R33

[23] Roupassov D V, Nikipelov A A, Nudnova M M and Starikovskii A Y 2009 Flow separation control by plasma actuator with nanosecond pulsed-periodic discharge *AIAA Journal* **47** 168185

[24] Kosarev I N, Khorunzhenko V I, Mintoussov E I, Sagulenko P N, Popov N A and Starikovskaia S M 2012 A nanosecond surface dielectric barrier discharge at elevated pressures: time-resolved electric field and efficiency of initiation of combustion *Plasma Sources Science and Technology* **21** 045012

[25] Stepanyan S A, Starikovskiy A Y, Popov N A and Starikovskaia S M 2014 A nanosecond surface dielectric barrier discharge in air at high pressures and different polarities of applied pulses: transition to filamentary mode *Plasma Sources Science and Technology* bf 23 045003

[26] Starikovskaia S M, Allegraud K, Guaitella O, Kosarev I, Mintusov E, Pendleton S, Popov N, Sagulenko P and Rousseau A Surface discharges: possible applications for plasma-assisted ignition and electric field measurements *Proc. of 48th AIAA Aerospace Sciences Meeting* (4 - 7 Jan 2010, Orlando, Florida) AIAA20101587

[27] Boumehdi M A, Stepanyan S A, Desgroux P, Vanhove G and Starikovskaia S M 2015 Ignition of methane- and n-butane-containing mixtures at high pressures by pulsed nanosecond discharge *Combustion and Flame* **162** 1336— 1349

[28] Anokhin E M, Kuzmenko D N, Kindysheva S V, Soloviev V R and Aleksandrov N L 2015 Ignition of hydrocarbon:air mixtures by a nanosecond surface dielectric barrier discharge *Plasma Sources Science and Technology* **24** 045014

[29] Pendleton S J, Montello A, Carter C, Lempert Wand Gundersen M A 2012 Vibrational and rotational CARS measurements of nitrogen in afterglow of streamer discharge in atmospheric pressure fuel/air mixtures *Journal of Physics D: Applied Physics* **45** 495401

[30] Tardiveau P, Bentaleb S, Jeanney P, Jorand F and Pasquiers S 2012 Comparative study of air-propane and air-heptane mixtures ignition by nanosecond pulsed discharges *International Journal of Plasma Environmental Science & Technology* **6** 130–134

[31] Shcherbanev S A, Stepanyan S A, Popov N A and Starikovskaia S M 2015 Dielectric barrier discharge for multi-point plasma-assisted ignition at high pressures *Philosophical Transactions of the Royal Society of London A: Mathematical, Physical and Engineering Sciences* **373** 20140342

[32] Anikin N, Starikovskaia S and Starikovskii A 2004 Study of the oxidation of alkanes in their mixtures with oxygen and air under the action of a pulsed volume nanosecond discharge *Plasma Physics Reports* **30** 1028–1042

[33] Pancheshnyi S, Starikovskaia S and Starikovskii A 2000 Collisional deactivation of $N_2(C^3\Pi_u, v = 0, 1, 2, 3)$ states by N_2, O_2, H_2 and H_2O molecules *Chemical Physics* **262** 349–357

[34] Gibalov V I and Pietsch G J 2012 Dynamics of dielectric barrier discharges in different arrangements *Plasma Sources Science and Technology* **21** 024010

[35] Laux C O 2002 Radiation and nonequilibrium collisional-radiative models, in: Physico-Chemical Modeling of High Enthalpy and Plasma Flows (von Karman Institute Lecture Series 2002-07) ed D Fletcher et al (Rhode-Saint-Genese, Belgium: Von Karman Institute)

[36] Laux C O, Spence T G, Kruger C H and Zare R N 2003 Optical diagnostics of atmospheric pressure air plasmas *Plasma Sources Science and Technology* **12** 125

[37] Hidaka Y, Takuma H and Suga M 1985 Shock-tube study of the rate constant for excited hydroxyl ($OH^*(A_2\Sigma^+)$) formation in the nitrous oxide-molecular hydrogen reaction *The Journal of Physical Chemistry* **89** 4903–4905

[38] Fairchild P W, Smith G P and Crosley D R 1983 Collisional quenching of $OH^*(A_2\Sigma^+)$ at elevated temperatures *The Journal of Chemical Physics* **79** 1795–1807

[39] Lewis B and Von Elbe G 1987 Combustion, flames and explosions of gases. *Third edition (Academic Press, Inc.,Orlando, FL)*

[40] Ombrello T 2016 Pulse-to-Pulse Coupling for Ignition in Cross-Flow Using Nanosecond-Pulsed High-Frequency Discharge *Proc. 54th AIAA Aerospace Sciences Meeting (San Diego, California, CA, 48 January 2016)* AIAA20161210

[41] Leonov S B, Petrishchev V and Adamovich I V 2014 Dynamics of energy coupling and thermalization in barrier discharges over dielectric and weakly conducting surfaces on s to ms time scales *Journal of Physics D: Applied Physics* **47** 465201

[42] Gelfand B, Popov O and Chayvanov B 2008 Hydrogen. Parameters of combustion and explosion *(PhysMatLit (in russian))*

[43] Popov N A 2008 Effect of a pulsed high-current discharge on hydrogen-air mixtures *Plasma Physics Reports* **34** 414430

[44] Wang B, Olivier H and Grnig H 2003 Ignition of shock–heated H_2–air–steam mixtures *Combustion and Flame* **133** 93–106

[45] Hagelaar G J M and Pitchford L C 2005 Solving the Boltzmann equation to obtain electron transport coefficients and rate coefficients for fluid models *Plasma Sources Science and Technology* **14** 722

[46] http://www.bolsig.laplace.univ-tlse.fr/

[47] Popov N A 2016 Kinetics of plasma-assisted combustion. Effect of non-equilibrium excitation on the ignition and oxidation of combustible mixtures *Plasma Sources Science and Technology* **25**

[48] Babaeva N Y and Naidis G V 1996 Two–dimensional modelling of positive streamer dynamics in non–uniform electric fields in air *Journal of Physics D: Applied Physics* **29** 2423

Chapter 8

Optical emission spectrum of filamentary nanosecond surface dielectric barrier discharge

.

Nanosecond surface dielectric barrier discharges (nSDBD) are developed for flow control applications [1, 2], laser pumping [3], plasma-assisted combustion [4, 5, 6]. It was found recently [7] that at pressure and/or voltage increase, a single-shot nSDBD transforms into a filamentary form. Streamers start from the high voltage (HV) electrode, slow down and stop. At this instant, a few nanosecond after the discharge start, a set of bright filaments starts from the HV electrode. The number of filaments is $4-5$ times less that the initial number of streamers.

Streamer–to–filament transition is a general feature of nanosecond surface discharges at high pressures [8]: filamentation was observed for both polarities of voltage, different dielectrics, and in different gases. Critical pressure P_c and voltage V_c when the filamentation happens are the functions of polarity and gas mixture. Filamentary discharges ignite combustible mixtures at initial gas pressures up to 15 bar [8, 9]; very specific regimes, when the mixture ignites simultaneously along multiply discharge channels, were observed at high pressures. The fact of simultaneous uniform ignition along the filaments proves, although indirectly, that the specific deposited energy in the filaments is high. At the same time, the information about parameters of plasma in the filaments is practically absent. The aim of the present chapter is to study the behavior of the filamentary nSDBD using time- and space-resolved emission spectroscopy.

8.1 Experimental setup

Two electrode systems in coaxial configuration are described elsewhere [7, 8]. A metal disk 20 mm in diameter served as a HV electrode. The internal diameter of the low-voltage (LV) ground electrode was equal to the diameter of the HV electrode, and the external diameter of the LV electrode was 50 mm. To change the surface of the dielectric without changing the capacitance of the electrode system, PVC ($\varepsilon = 3-3.5$) of a thickness $d = 0.3$ mm or ceramics (MACOR, $d = 0.5$ mm, $\varepsilon = 5-6$) were glued to the grounded electrode by Geocel FIXER Mate silicon glue ($\varepsilon \approx 3$). The electrode system was installed

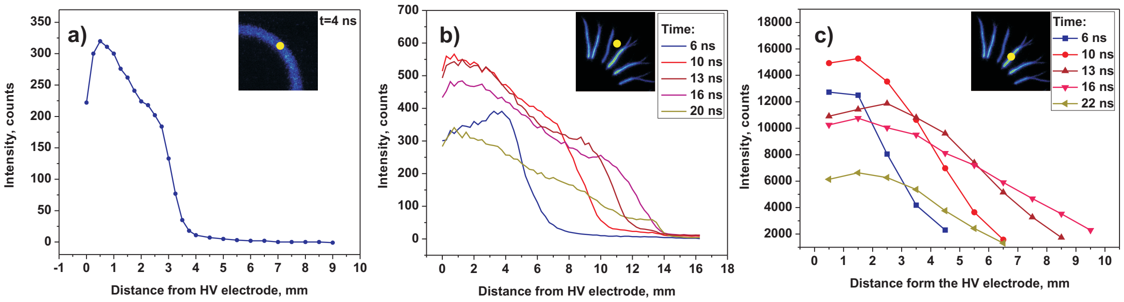

Figure 8.1: Relative intensity of $\lambda = 300 - 800$ nm emission in (a) streamer mode; (b) between the filaments and (c) in the filaments *vs* distance from the edge of the HV electrode at different time instants. Synthetic air, $U = -47$ kV, $P = 3$ bar. ICCD images, gate 2 ns, are given as inserts.

in constant volume chamber [7] allowing work at pressures 100 $Torr < P < 8$ bar or in high–pressure high–temperature (HPHT) chamber [8], 10 $Torr < P < 15$ bar.

High–voltage pulses, 20 ns in duration and 2 ns rise time, positive or negative polarity, $20 - 60$ kV in amplitude on the HV electrode were delivered by the coaxial 30 m long 50–Ohm cable from the FPG20-03PM or FPG20-03PN pulser (FID Technology). Calibrated custom–made back current shunt (BCS) installed in the center of the cable allowed measurements of current and voltage waveforms.

ICCD images ($\lambda = 300 - 800$ nm) were taken by Pi-Max4 Princeton Instruments ICCD camera. Narrow–band optical filters (ThorLabs), FWHM=10 nm were used for discharge ICCD imaging at selected wavelength. Optical spectra, $\lambda = 250 - 500$ nm, where recorded by ACTON spectrometer (SP7500i, 600 I/mm grating) coupled with the ICCD camera.

Before the experiment, the discharge cell was pumped down to 10^{-2} Torr. H_2, N_2, O_2 and Ar (Air Liquide) with <100 ppm of impurities were used to prepare the mixtures. The experiments were carried out in a single shot regime at ambient initial temperature in air, N_2, H_2:N_2=1:4, H_2:N_2=1:59 and O_2:Ar=2:3 mixtures.

8.2 Results

For any studied conditions the emission intensity in filaments I_f is tens of times higher than the emission between the filaments I_f^0 or in streamers I_s, two last values are comparable. From figure 8.1 for synthetic air

$$I_f/I_f^0/I_s \approx 50/1.8/1. \tag{8.1}$$

Preliminary experiments revealed two most important components in nitrogen–containing mixtures: bands of molecular nitrogen and broadband continuum. To understand a spectral distribution of emission in space, a series of ICCD images with narrow band filters has been taken. The central wavelengths of the filter were selected to transmit “only nitrogen emission” or “only continuum emission”. Figure 8.2 presents typical images taken without and with described filtering.

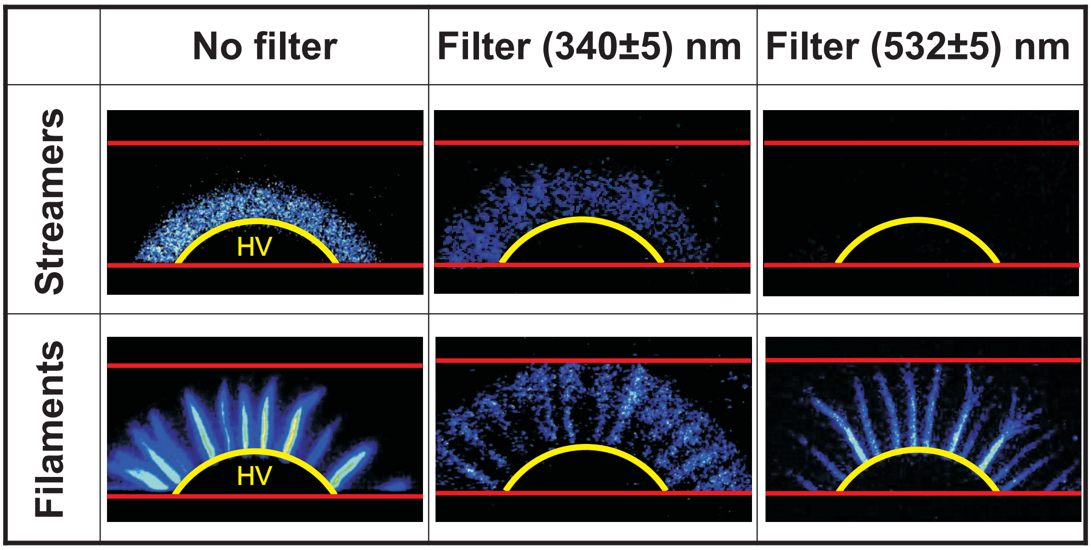

Figure 8.2: ICCD images of streamer and filamentary mode with bandwidth filters. Streamers: time delay is 0 ns, camera gate is 5 ns; filaments: time delay is 5 ns, camera gate is 20 ns. Synthetic air, $U = -52$ kV, $P = 4$ bar.

To distinguish streamers from filaments, we used the fact that a few first nanoseconds the nSDBD develops in a streamer mode. The discharge starts and develops during a few first nanoseconds with a typical velocity a few mm/ns from the edge of the highvoltage electrode. At this period, the optical emission from the discharge consists mainly of the bands of the second positive (2^+) system of molecular nitrogen. In the filament mode two separate zones are clearly seen: the emission of the 2^+ system corresponds to the zone "around and ahead of" each filament, while continuous wavelength (cw) emission comes from the filament core, or from the filament "channel". It should be noted that we do not analyze the discharge spectra in the direction perpendicular to the dielectric as far as a typical scale of changes in this direction is small comparing to resolution of the system.

Detailed spectral analysis demanded to fix the position of the filament, so the discharge was stabilized in space using the technique suggested in [6]: the HV electrode have been replaced by a toothed wheel. A filament was selected and the discharge chamber rotated so that the filament was aligned with the spectrometer slit. The system provided temporal resolution of 0.5 ns and spatial — of 0.3 mm. To our knowledge, this is a first available data on time- and space-resolved emission of the filaments in nSDBD.

Figure 8.3 presents typical spectra of nSDBD as a function of wavelength and of distance from the high–voltage electrode. First three images (figure 8.3 (a–c)) show spectra taken for positive polarity discharge. The inserts in the right upper corners provide the position of the ICCD gate relative to the voltage waveform. The emission of the 2^+ band of N_2 is clearly seen in the propagating front (figure 8.3 (a)). At $t \approx 2$ ns a streamer–to–filament transition occurs. The filaments propagate from the HV electrode as a wave of the cw emission. The start of the filaments corresponds to the regions $0-2$ and $2-4$ mm where the cw spectrum is already seen. Emission of the first negative system of N_2^+ at the regions $0-2$ and $4-6$ mm at 391.4 nm indicates high electric fields in the front of the discharge. When the filament is formed, the N_2 emission is replaced by cw emission, and the intensity of N_2 emission drops dramatically (figure 8.3 (b)). High voltage is keeping on the electrode, and the discharge propagates, leaving behind the front a bright channel – a filament.

No well–defined atomic lines or molecular bands can be distinguished in the spectra for $\lambda = 250 - 500$ nm; slight decrease of emission is observed after 400 nm. It should be noted that absence of NO(γ) emission, $\mathrm{NO}(\mathrm{A}^2\Sigma^+, v) \rightarrow \mathrm{NO}(\mathrm{X}^2\Pi, v') + h\nu$, at $\lambda <$ 300 nm means absence of high specific deposited energy. Electronically excited NO state is produced by electron impact and in the reaction $\mathrm{N}_2(\mathrm{A}^3\Sigma_u^+) + \mathrm{NO}(\mathrm{X}^2\Pi) \rightarrow \mathrm{N}_2(\mathrm{X}^1\Sigma_g^+, v)$ $+ \mathrm{NO}(\mathrm{A}^2\Sigma^+, v)$. At low dissociation degree, the $\mathrm{NO}(\mathrm{X}^2\Pi)$ density is small, so no strong NO(γ) emission is observed [10].

When the trailing edge of the pulse comes to the electrode, the second ionization wave starts and propagates on the trace of the filament. The second ionization wave contains emission of the 2^+ system of molecular nitrogen (see figure 8.3 (c)) indicating on the electric field comparable to the fields in the discharge front. This emission was used to measure the rotational temperature on the trailing edge of the pulse.

An example of emission of the negative polarity nSDBD is presented in figure 8.3 (d). The intensity of emission is systematically $3 - 4$ times higher, and the shape is different comparing to positive polarity discharge.

It should be noted that the integration of emission obtained as presented in figure 8.3 over the distance from the high–voltage electrode gives a picture similar to figure 8.1 c: the front of the signal is mainly due to 2^+ emission of molecular nitrogen, and the "body" of the function, where the maximum of emission is observed, is due to cw radiation.

The width of selected spectral lines can answer the question about the electron density in the filaments. The experiments were carried out in 5 bar H_2:N_2=1:4 ($U > 0$), 6 bar H_2:N_2=1:59 ($U < 0$) and 5 bar O_2:Ar=2:3 mixtures; lines of atomic hydrogen (656.3 nm, H_α) and atomic oxygen (777.3 nm, 3^5P–3^5S) have been analyzed. Continuous spectra similar to measured in air were observed in both mixtures. Similar cw spectra in so different mixtures prove that the spectra are not due to a particular molecular continuum or molecular bands, like continuum of molecular hydrogen or NO_2^* emission [11]. The time instant of appearance of the lines coincided with the appearance of the cw spectra.

Dynamics of the FWHM for H_α calculated from Lorenz function is given by figure 8.4 (a) for both polarities of the pulse, together with the waveforms of voltage on the high voltage electrode and electrical current for negative polarity discharge. The FWHM is enormously large in the discharge, $20 - 30$ nm. Two decays are observed: the first one is in a good correlation with the decay of electrical current; the second is longer: already in the "current-free" zone, when the electron temperature is low, a typical time of 50% decrease of the FWHM is equal to $10 - 20$ ns. Figure 8.4 (b), presenting the FWHM for 777 nm oxygen line, provides 15 ns decay, in correlation with H_α. The FWHM itself is narrower for oxygen, 6 nm in the discharge, according to the idea that hydrogen is more sensitive to the reason of broadening. Figure 8.4 (b) shows also cw emission in the vicinity of 777 nm, and the integral of O-atom emission over the wavelength, proportional to O*–atoms density in 3^5P state. The FWHM of O–atoms practically does not change along the filament.

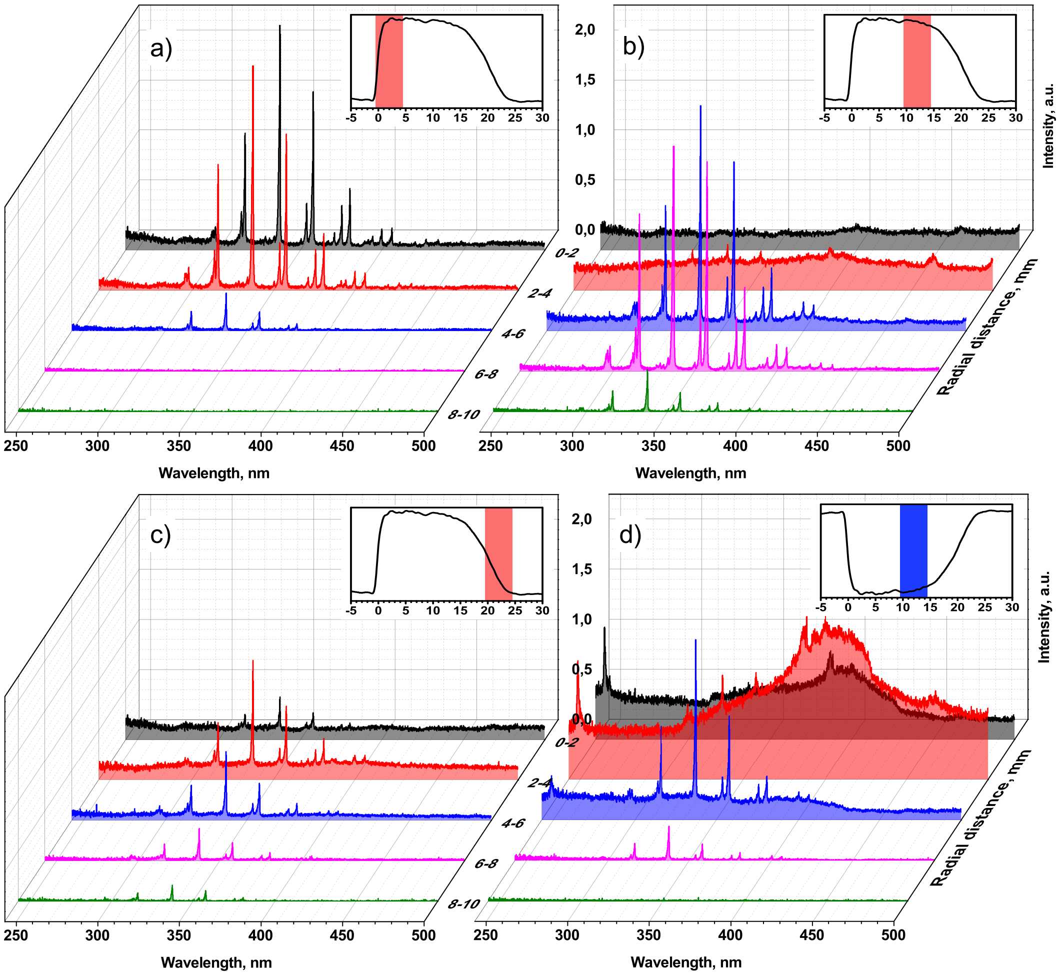

Figure 8.3: Time– and space–resolved spectra of (a)-(c) positive polarity and (d) negative polarity filamentary discharges. Synthetic air, $U = \pm 50$ kV, $P = 6$ bar. Inserts show the ICCD gate relative to the voltage waveform.

8.3 Discussion

No lines corresponding to the material of electrode were detected in the spectra. No difference was found between the spectra for different dielectrics. PVC is produced by polymerization of C_2H_3Cl; ceramics consists of non-organic materials (for MACOR: SiO_2 (46%), Al_2O_3 (16%), MgO (17%), KO_2 (10%), B_2O_3 (7%), F (4%)). Similar cw spectra prove that the emission does not originate from damaging the dielectric.

The spectrum is not a Planck emission. Indeed, the gas temperatures calculated from the rotational temperature at the rise front and trailing edge of the pulse, do not differ significantly: for both instants, gas temperature is $T_g = 300 - 500$ K. The analysis of the radial distribution of the emission proves that the light comes from the central part of the channel, not from the surface. Finally, the most important evidence is a temporal behavior of the emission: if this was Planck radiation, it would increase with time corresponding to fast energy relaxation in the afterglow [12, 13]. This is not a case: the cw emission

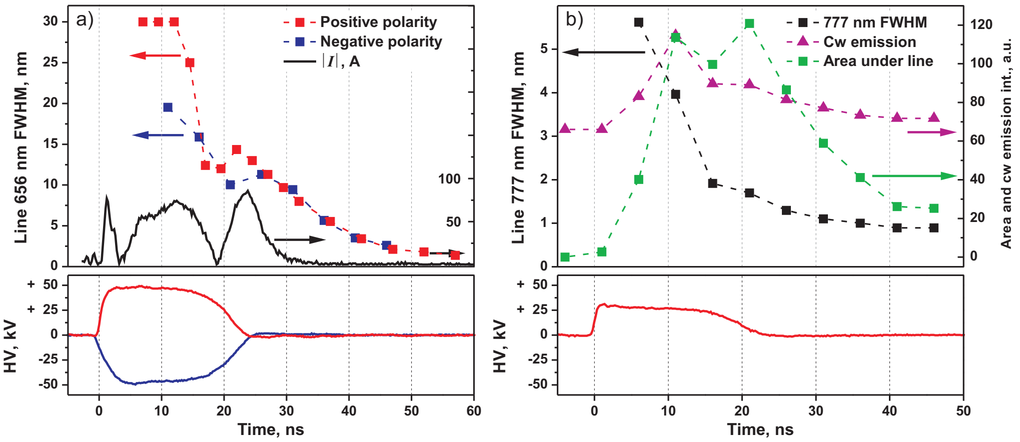

Figure 8.4: FWHMs *vs* time: (a) H_α superimposed with the voltage coming to the electrode and current through the discharge; (b) 777 nm of atomic oxygen superimposed with the voltage waveform, the area under the line and cw emission near 777 nm.

goes down within a few tens of nanoseconds, and hydrodynamic expansion on the time scale 50 ns is small to provide significant cooling: for the filament radius $r_f \approx 70$ μm [8] and $T_g = 500$ K, a gas–dynamic time is about 200 ns.

Continuum emission in visible and UV was recorded [14, 15, 16, 17] in pulsed discharges in atmospheric pressure air. Atomic lines of materials of electrodes were observed [14]. More "soft" spectra were obtained [16] in air at $P = 1$ atm and $U = 90$ kV: no materials of electrodes but the lines of ionized nitrogen atoms were clearly seen. Similar spectra, with atomic N-ions lines dominated over the cw emission, were observed in emission of constricted SDBD [17] powered by a burst of unipolar 400 μs pulses at $U = 20$ kV.

Nanosecond discharges excited in open atmosphere at high voltages, $U = 150-250$ kV, generate [14, 15] high energy runaway electrons and secondary X-ray bremsstrahlung. The nSDBD studied in the present work seems to be a discharge with significantly smaller specific deposited energy, and the question about the physics of the cw emission remains open. Experimental observations can be summarized in the following way: cw emission does not exists at the rising front of the pulse (figure 8.3 a); the cw emission in the filaments and emission of broad atomic lines appear at the same time and come from the same space region. Temporal behavior of the cw emission and of FWHM of the O-atom and H-atom lines is similar: typical decay comprises a few tens of nanoseconds (figure 8.4). Density of excited O-atoms estimated from the integral of emission at 777 nm, has a similar shape but somewhat broader maximum, and slightly delayed relative to the maximum of the FWHM.

Two types of emission due to high electron density can be considered here: bremsstrahlung and recombination radiation [18]. Bremsstrahlung originates from acceleration of an electron in Coulomb collisions with ions. Energy per 1 cm^3 per second in SGC system in assumption of Maxwellian EEDF is written as

$$P_b = 1.5 \cdot 10^{-27} Z^2 n_e n_i \sqrt{T_e[\mathrm{K}]}. \tag{8.2}$$

Recombination radiation is a process of emitting of the photon in recombination of ion and electron, and can be expressed as

$$P_r = 5 \cdot 10^{-22} Z^4 n_e n_i \sqrt{1/T_e[\mathrm{K}]}. \tag{8.3}$$

Here Z is a charge of ion, n_e, n_i are electron and ion densities respectively, T_e is electron temperature. The fact that $P_b = P_r$ at $T_e \approx 30$ eV means that in our case recombination radiation should dominate.

To get recombination radiation at the experimental conditions of nSDBD, the electron density in the filaments should be extremely high. If to suggest that the broadening is due to electron density, a maximum value of $n_e^{max} \sim 10^{19}$ cm^{-3} can be obtained from FWHM of H_α following the procedure described in [19].

High values of n_e from H$_\alpha$ and N–atoms broadening were obtained earlier in $P = 1$ atm discharge in N_2:H_2O mixture for 9 kV/170 ns pulses [19]. Values up to $n_e = 4 \cdot 10^{18}$ cm^{-3} ($n_e/N > 10\%$) with a long decay rate, $8.6 \cdot 10^6$ s^{-1}, were obtained. The authors explain a long decay by additional production of electrons in the afterglow *via* Penning and associative ionization and remark that the density of excited species should be comparable to n_e. At the same time, our estimates of energy release at so high ionization degree gives too high values of gas heating: $\Delta E = 2.25$ eV in electron–ion recombination of N_2^+ [20] and $\Delta E \approx 2$ eV in quenching of N(^2D) [21] results in $T_g = 1500 - 1900$ K at 100 ns, while measured temperature is $T_g \leq 800$ K [19].

Although our case is similar and extra–high n_e values need additional verification, it is evident that the cw spectra correlate in time with high electron density. Filamentation is a reason for n_e increase. Highly conductive channels originates near the HV electrode; the velocity of filaments is $V = 5 \cdot 10^7 - 10^8$ cm/s [22]. Contraction and appearance of a bright channel was observed before in high–power discharges [23, 24]. Formation of current spot on the electrode was a reason of constriction of a stable homogeneous plasma column and development of a bright channel propagating with $V = 10^4 - 10^6$ cm/s [23]. High–current nanosecond discharge ($j \geq 100$ A/cm^2) constricted at moderate pressures, $P = 76$ Torr, produced high electron densities, $n_e \sim 10^{17}$ cm^{-3}, provided $V \sim 10^6 - 10^7$ cm/s [24].

In our case, the filamentation can be triggered by formation of at least one current spot on the HV electrode. Both field emission and explosive emission can be important on this time scale [25]. Produced filament propagates from the electrode due to local enhancement of the electric field in the head, suppresses adjacent streamers because of high carried electric charge and define, by the value of the change, a minimal possible distance between the filaments. Neighboring filaments follow the same rules, and in a few nanoseconds or less, a regular structure of filaments is formed around the HV electrode.

8.4 Conclusions

Streamer–to–filament transition is a characteristic feature of nanosecond surface dielectric barrier discharges (nSDBDs) at high pressures and voltages. Bright optical emission from filamentary nSDBD, 50 times more intense that the emission from the streamer nSDBD, is due to continuous wavelength radiation, intense in the UV and decreasing in visible and IR regions. Space- and time-resolved emission from the surface filament has been measured for the first time. Continuum spectrum emits from the “body” of the filament, mainly from the central part of the filament channel. The filaments are enveloped in streamer–like emission (the second positive system of molecular nitrogen for nitrogen–containing mixtures).

It is suggested that the streamer–to–filament transition can be considered as the instability caused by current spots on the high-voltage electrode. As a result, a regular structure of plasma channels with high electron density (filaments) is formed instead of streamers and propagates from the high–voltage electrode as a second ionization wave. High electron densities are confirmed experimentally by space-and time-resolved measurements of the FWHMs of the selected atomic lines. The distance between the filaments is regulated by electrical charge of the individual filaments. Observed cw spectrum is presumably caused by high density of electrons.

Bibliography

[1] Roupassov D V, Zavyalov I N, Starikovskii A Yu, Saddoughi S G 2006 Boundary layer separation plasma control using low-temperature non-equilibrium plasma of gas discharge" *44th AIAA Aerospace Sciences Meeting and Exhibit*, 9 - 12 January 2006, Reno, Nevada. AIAA 2006—373

[2] Leonov S B, Adamovich I V and Soloviev V R 2016 Dynamics of near-surface electric discharges and mechanisms of their interaction with the airflow, *Plasma Sources Sci. Technol.*, accepted

[3] Treschalov A B, Lisovskiy A A 2012 Source of the VUV radiation on the basis of surface discharge *Optics Journal* **79(8)** (In Russian) 15—23

[4] Allegraud K, Guaitella O, Kosarev I N, Mintusov E I, Pendleton S J, Popov N A, Sagulenko P N, Rousseau A and Starikovskaia S M 2010 Surface discharges: possible applications for plasma–assisted ignition and electric field measurements *Proc. of 48th AIAA Aerospace Sciences Meeting Including The New Horizons Forum and Aerospace Exposition*, 4—7 Jan 2010, Orlando, Florida, USA, AIAA–2010–1587

[5] Kosarev I N, Khorunzhenko V I, Mintoussov E I, Sagulenko P N, Popov N A and Starikovskaia S M 2012 A nanosecond surface dielectric barrier discharge at elevated pressures: time-resolved electric field and efficiency of initiation of combustion *Plasma Sources Sci. and Techn.* **21** 045012

[6] Anokhin E M , Kuzmenko D N, Kindysheva S V, Soloviev V R, and Aleksandrov N L 2015 Ignition of hydrocarbon:air mixtures by a nanosecond surface dielectric barrier discharge *Plasma Sources Sci. Technol.* **24** 045014

[7] Stepanyan S A, Starikovskiy A Yu, Popov N A and Starikovskaia S M 2014 A nanosecond surface dielectric barrier discharge in air at high pressures and different polarities of applied pulses: transition to filamentary mode *Plasma Sources Sci. and Technol.* **23** 045003

[8] Shcherbanev S A, Popov N A, Starikovskaia S M 2016 Ignition of high pressure lean H_2:air mixture along the multiple channels of nanosecond surface discharge *Combustion and Flame*, accepted for publication

[9] Boumehdi M A, Stepanyan S A, Desgroux P, Vanhove G and Starikovskaia S M 2015 Ignition of methane- and n-butane-containing mixtures at high pressures by pulsed nanosecond discharge *Combustion and Flame* **162** 1336—1349

[10] Popov N A 2016 Pulsed nanosecond discharge in air at high specific deposited energy: fast gas heating and active particles production *Plasma Sources Sci. Technol.* **25** 044003

[11] Okabe H 1978 Photochemistry of small molecules *John Wiley & Sons, Inc.*

[12] Rusterholtz D L, Lacoste D A, Stancu G D, Pai D Z and Laux C O 2013 Ultrafast heating and oxygen dissociation in atmospheric pressure air by nanosecond repetitively pulsed discharges *J. Phys. D: Appl. Phys* **46** 464010 (21pp)

[13] Klochko A V, Lemainque J, Booth J–P and Starikovskaia S M 2015 TALIF measurements of oxygen atom density in the afterglow of a capillary nanosecond discharge, *Plasma Sources Sci. Technol.* **24** 025010

[14] Babich L P, Loiko T V, Tsukerman V A 1990 High-voltage nanosecond discharge in a dense gas at a high overvoltage with runaway electrons *Sov. Phys. Usp.* **33**(7) 521—540

[15] Babich L P and Loiko T V 2010 Peculiarities of detecting pulses of runaway electrons and X-rays generated by high-voltage nanosecond discharges in open atmosphere *Plasma Physics Reports* **36**(3) 263–270

[16] Shao T, Tarasenko V F, Zhang Ch, Lomaev M I, Sorokin D A, Yan P, Kozyrev A V and Baksht E Kh 2012 Spark discharge formation in an inhomogeneous elec-tric field under conditions of runaway electron generation *Journal of Applied Physics* **111** 023304

[17] Houpt A W and Leonov S B 2016 Charge transfer in constricted form of surface barrier discharge at atmospheric pressure *Journal of Thermophysycs and Heat Transfer* Article in advance

[18] Artsimovich L A, Sagdeev R Z 1979 Physics of plasmas for physicists *Moscow: Atomizdat*

[19] Van der Horst R M, Verreycken T, Van Veldhuizen E M and Bruggeman P J 2012 Time–resolved optical emission spectroscopy of nanosecond pulsed discharges in atmospheric-pressure N_2 and N_2/H_2O mixtures *J. Phys. D: Appl. Phys.* **45** 345201

[20] Mintoussov E I, Pendleton S J, Gerbault F G, Popov N A and Starikovskaia S M 2011 Fast gas heating in nitrogen-oxygen discharge plasma: II. Energy exchange in the afterglow of a volume nanosecond discharge at moderate pressures *J. Phys. D: Appl. Phys.* **44** 285202

[21] Galvao B R L, Braga J P, Belchior J C., and Varandas A. J. C. 2014 Electronic quenching in $N(^2D) + N_2$ collisions: a state–specific analysis via surface hopping dynamics *J. Chem. Theory Comput.* **10** 1872—1877

[22] Shcherbanev S A, Stepanyan S A, Popov N A and Starikovskaia S M 2015 Dielectric barrier discharge for multi–point plasma–assisted ignition at high pressures *Phil. Trans. A* **373**(2048) 20140342

[23] Akishev Yu, Karalnik V, Kochetov I, Napartovich A, Trushkin N 2014 High-current cathode and anode spots in gas discharges at moderate and elevated pressures *Plasma Sources Sci. Technol.* **23** 054013

[24] Genkin S A, Kozurev A V, Korolev Yu D, Tipchurin K A 1985 it Zurnal Techn. Phys. **55**(6) 1216 (in Russian)

[25] Levko D, Yatom S, Vekselman V and Krasik Ya E 2012 Electron emission mechanism during the nanosecond high-voltage pulsed discharge in pressurized air *Appl. Phys. Lett.* **100** 084105

Chapter 9

Analysis of the main processes of atomic particles production in fuel-air mixtures

Problem of plasma-assisted ignition at elevated pressures is a multidisciplinary problem. In addition to physics and chemistry of discharge considered earlier, chemistry of combustion modified by the discharge chemistry should be considered. Dissociation of mixture molecules by electron impact and quenching of electronically excited states of nitrogen $N_2(A^3\Sigma_u^+,v)$, $N_2(B^3\Pi_g,v)$, $N_2(C^3\Pi_u,v)$ by fuel and O_2 molecules are the main reactions of atomic particles production in fuel–air mixtures. The cross sections for the electron impact dissociation of hydrocarbons and O_2 molecules are analyzed in [1] and [2],[3], respectively. In this chapter, we discuss quenching of electronically excited states of nitrogen by O_2 molecules and hydrocarbons.

9.1 Quenching of excited nitrogen molecules

Figure 9.1 shows the experimental data [4]—[8] on the rate constants for quenching of electronically excited states $N_2(A^3\Sigma_u^+,v)$, $N_2(B^3\Pi_g,v)$, $N_2(C^3\Pi_u,v)$ by O_2, CH_4, C_2H_4, and C_2H_6 molecules. Curves (1—7) correspond to the reactions (R1-R7):

(R1)	$N_2(A^3\Sigma_u^+,v) + CH_4 \rightarrow$ products	[4, 5]
(R2)	$N_2(A^3\Sigma_u^+,v) + O_2 \rightarrow$ products	[4, 5]
(R3)	$N_2(A^3\Sigma_u^+,v) + C_2H_6 \rightarrow$ products	[5, 6]
(R4)	$N_2(A^3\Sigma_u^+,v) + C_2H_4 \rightarrow$ products	[5, 6]
(R5)	$N_2(B^3\Pi_g,v) + O_2 \rightarrow$ products	[7]
(R6)	$N_2(B^3\Pi_g,v) + CH_4 \rightarrow$ products	[7]
(R7)	$N_2(C^3\Pi_u,v) + CH_4 \rightarrow$ products	[8]

It is clear that the quenching rate constants for $N_2(B^3\Pi_g,v)$ and $N_2(C^3\Pi_u,v)$ states by O_2 and CH_4 molecules (curves 5—7) are close to the gas kinetic values [7, 8]. Furthermore, these rates are almost independent on the vibrational level number. So, we can assume that the quenching of electronically excited states of $N_2(B^3\Pi_g)$, and $N_2(C^3\Pi_u)$ leads to the

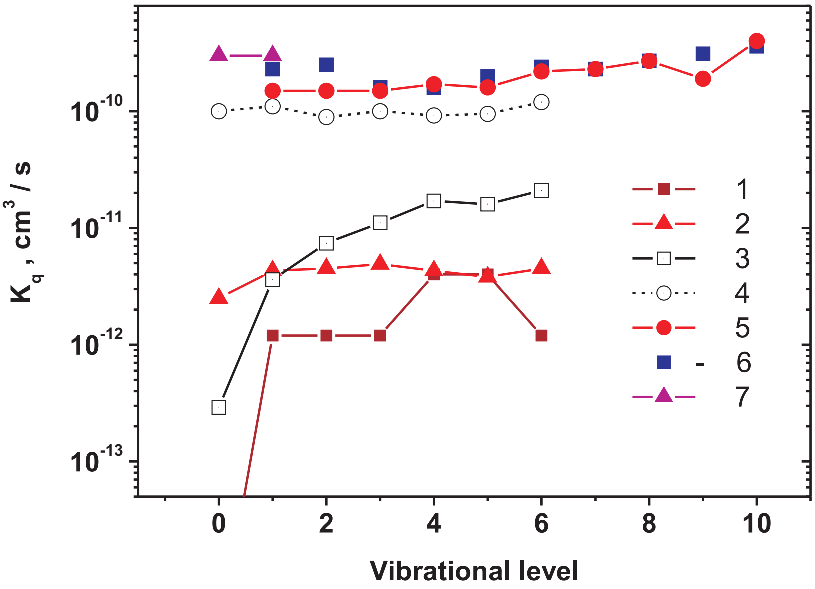

Figure 9.1: Dependence of the rate constants for quenching of electronically excited states $N_2(A^3\Sigma_u^+)$, $N_2(B^3\Pi_g)$, $N_2(C^3\Pi_u)$ on the vibrational levels number according to the experimental data [4]–[8] (see text)

dissociation of quenchers. Quenching rate constants of $N_2(A^3,v)$ molecules by unsaturated hydrocarbons C_2H_2, C_2H_4 et al. are also high and close to the gas-kinetic [5, 6]. Therefore it is also necessary to assume that the most likely result of $N_2(A^3,v)$ quenching is the dissociation C_2H_2, C_2H_4 molecules, which is confirmed by the results of measurements [9].

The rate constants for quenching of $N_2(A^3,v)$ by saturated hydrocarbons CH_4, C_2H_6, C_3H_8 etc. are considerably less than unsaturated, and, most importantly, there is a rather strong dependence on the vibrational level number. In particular, quenching rate constant of $N_2(A^3,v)$ is significantly reduced in the transition from $v = 1$ to $v = 0$ vibrational level. All this suggests that in this case there may be a relaxation of the vibrational excitation of $N_2(A^3,v)$ on the hydrocarbon molecules, for example,

$$N_2(A^3\Sigma_u^+, v > 0) + CH_4 \rightarrow N_2(A^3\Sigma_u^+, v - \Delta v) + CH_4(v').$$

In lean and stoichiometric hydrocarbon-air mixtures the role of quenching of electronically excited states $N_2(A^3\Sigma_u^+, B^3\Pi_g, C^3\Pi_u)$ in active particles production strongly depends on the fraction of dissociation channel in the process of deactivation of these states by O_2 molecules.

Calculations for the quenching rates of $N_2(A^3,v)$ molecules by oxygen are given in [10] It is shown that for vibrational levels $N_2(A^3, v > 0)$ the main result of the reaction with O_2 molecules is the dissociation of oxygen (reaction (R8)). For $N_2(A^3,v{=}0)$ level there are two main channels of quenching by oxygen molecules: due to dissociation (R9) and production of electronically excited $O_2(^3\Sigma_u^+, C^3\Delta_u, ^1\Sigma_u^-)$ molecules (R10). The rate constants of these processes are $k_9 = 1.0{\cdot}10^{-12}$ and $k_{10} = 1.5{\cdot}10^{-12}$ cm^3/s respectively [10].

(R8) $N_2(A^3\Sigma_u^+,v > 0) + O_2(^3\Sigma_g^-) \rightarrow N_2(^1\Sigma_g^+,v') + 2O(^3P)$
(R9) $N_2(A^3\Sigma_u^+,v = 0) + O_2(^3\Sigma_g^-) \rightarrow N_2(^1\Sigma_g^+,v') + 2O(^3P)$
(R10) $N_2(A^3\Sigma_u^+,v = 0) + O_2(^3\Sigma_g^-) \rightarrow N_2(^1\Sigma_g^+,v') + 2O(^3P) + O_2(c^1,A'^3,A^3)$

Thus, for an adequate description of the atomic particles production in reactions of electronically excited $N_2(A^3)$ molecules, the calculations of vibrational distribution function of $N_2(A^3,v)$ are necessary [11].

In the modern kinetic models (see [12]-[15], etc.) it is typically assumed that quenching of the electronically excited states $N_2(B^3\Pi_g,C^3\Pi_u, a'^1\Sigma_u^-)$ by oxygen leads to O_2 dissociation (reactions (R12)-(R14)). To test the validity of this assumption, the calculations of the dynamics of O atoms in the afterglow of a pulsed nanosecond discharge in air at atmospheric pressure under the experimental conditions of [16, 17] were carried out [18].

In [16, 17], the time evolution of $O(^3P)$ atoms density was measured by the TALIF technique. The absolute $O(^3P)$ density was determined by calibrating the measured results against the test TALIF spectrum of Xe atoms. The results of measurements [16] are plotted by symbols in Figure 9.2, together with the results of calculations of atomic oxygen production [18].

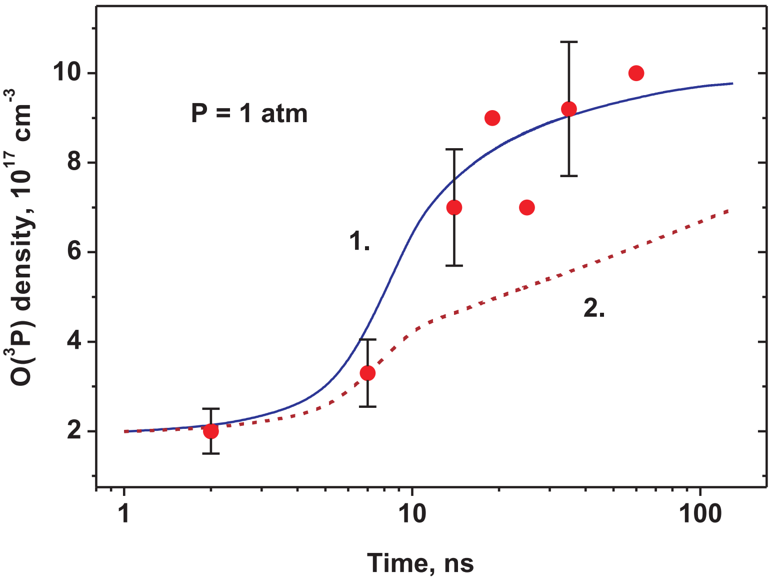

Figure 9.2: Time evolution of the density of $O(^3P)$ atoms under the conditions of [16, 17]. The dots are for the experimental data from [16], and the curves 1 and 2 are for the numerical results [18] at the discharge axis (see text).

Two stages of production of oxygen atoms can be clearly distinguished:
(i) The electron impact dissociation of oxygen during the discharge pulse,

$$\text{(R11)} \quad e + O_2 \rightarrow O(^3P) + O(^3P),\ e + O_2 \rightarrow O(^3P) + O(^1D)$$

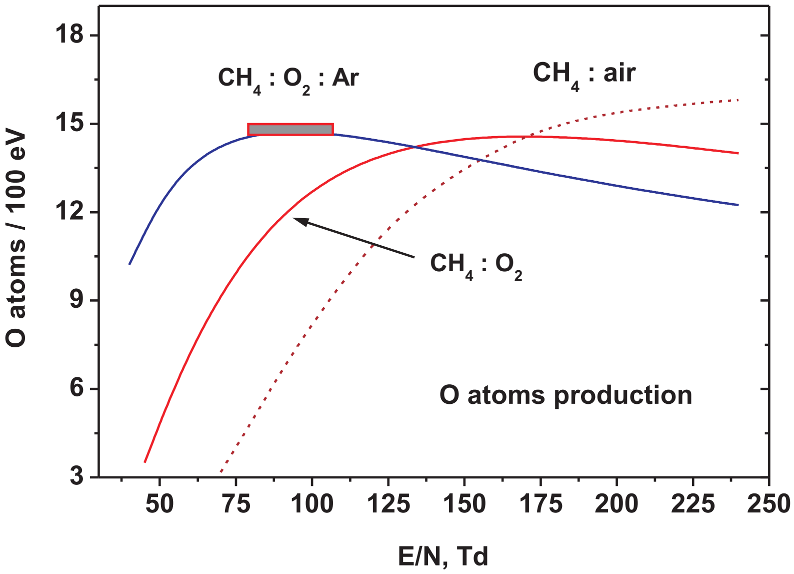

Figure 9.3: Dependence of the energy efficiency of atomic oxygen production (G is a number of atoms per 100 eV of deposited energy) on the reduced electric field, E/N, in stoichiometric CH_4 : O_2 : 90% Ar, CH_4 : O_2 and CH_4 : air mixtures. The shaded area is for the experimental data reviewed in [33].

and the production of oxygen atoms *via* quenching of electronically excited $N_2(B^3\Pi_g)$ and $N_2(C^3\Pi_u)$ molecules,

$$\begin{array}{ll} \text{(R12)} & N_2(B^3\Pi_g) + O_2 \rightarrow N_2(v) + 2\ O(^3P) \\ \text{(R13)} & N_2(^3\Pi_u) + O_2 \rightarrow N_2(v) + 2\ O(^3P,^1D) \end{array}$$

The characteristic time of this stage does not exceed $3-4$ ns (see Figure 9.2).

(ii) The dissociation of oxygen during the quenching of $N_2(a'^1\Sigma_u^-)$ and $N_2(A^3\Sigma_u^+)$ molecules,

$$\begin{array}{ll} \text{(R14)} & N_2(a'^1\Sigma_u^-) + O_2 \rightarrow N_2(v) + 2\ O(^3P,^1D) \\ \text{(R8–R9)} & N_2(A^3\Sigma_u^+,v) + O_2 \rightarrow N_2(v) + 2\ O(^3P) \end{array}$$

on the time scale of tens of nanoseconds.

In Figure 9.2 the curves 1 and 2 are the numerical results according to models 1 and 2, correspondingly. In model 1 it was assumed that quenching of the electronically excited states $N_2(B^3\Pi_g)$, $N_2(C^3\Pi_u)$ and $N_2(a'^1\Sigma_u^-)$ by oxygen leads to O_2 dissociation (reactions (R12)-(R14)), and in model 2 that the quenching of $N_2(B^3\Pi_g)$, $N_2(C^3\Pi_u)$ and $N_2(a'^1\Sigma_u^-)$ states results in $N_2(A^3\Sigma_u^+)$ molecules formation, and that the main atomic oxygen production occurs finally in reaction (R8)–(R9). It is clear that model 1 describes experimental data [16] rather well whereas the results of calculations with model 2 contradict to those

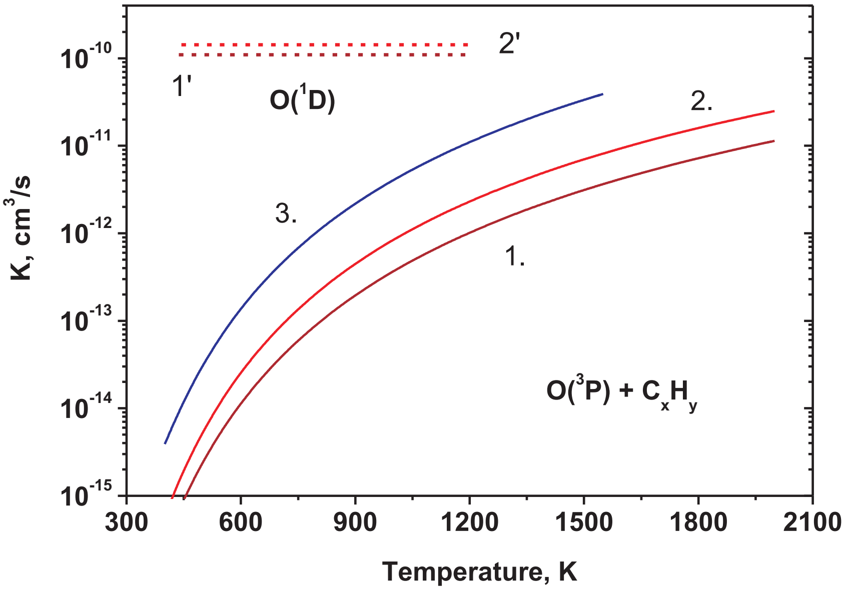

Figure 9.4: The rate constants of the reactions of O(^{3}P) and O(^{1}D) atoms with H_2 (curves 1,1'), CH_4 (curves 2,2'), and C_2H_6 (curve 3) molecules *vs* gas temperature [26],[23]-[25].

measurements.

This suggests that the quenching of electronically excited states of $N_2(B^3\Pi_g)$, $N_2(C^3\Pi_u)$ and $N_2(a'^1\Sigma_u^-)$ by oxygen molecules leads mainly to the dissociation of O_2. Thus, in gas-discharge plasma of a lean and stoichiometric hydrocarbon-air combustible mixtures, the main active particles are oxygen atoms in ground O(^{3}P) and electronically excited O(^{1}D) states, as well as the products of dissociation of hydrocarbons by electron impact and by the quenching of electronically excited states of nitrogen.

Figure 9.3 shows the comparison of energy efficiency of atomic oxygen production in a gas-discharge plasma of different combustible mixtures: stoichiometric mixtures of $CH_4 : O_2$, CH_4 : air, and $CH_4 : O_2 : Ar$ with 90% argon dilution. The shaded area corresponds to the experimental data reviewed in [33], curves correspond to the calculations. The electron impact rate constants and drift velocities were calculated by solving the Boltzmann equation in the two-term approximation with the use of the BOLSIG+ code [20]. The cross sections for electron scattering from O_2 and CH_4 molecules were taken from [2] and [21], respectively. The calculations were carried out taking into account the production of atomic particles in the reactions of quenching of electronically excited argon atoms (2.2) and $N_2(B^3\Pi_g)$, $N_2(C^3\Pi_u)$, $N_2(a'^1\Sigma_u^-)$ molecules (R12–R14).

It is clear that the maximum values of energy efficiency of atomic oxygen production in these mixtures changed only slightly, $G_O = 14 - 16$ atoms/100 eV. In these cases the fraction of deposited energy spent on the production of chemically active particles reaches 50% with consideration for the reactions of CH_4 dissociation by electron impact and the quenching of electronically excited O(^{1}D) atoms. The rest of the energy is spent on the excitation of $O_2(a^1\Delta_g$, $b^1\Sigma_g^+)$ electronic states, vibrational excitation of nitrogen molecules and gas heating.

9.2 Reactions of O(^{1}D) atoms with fuel molecules

Electronically excited atoms O(^{1}D) (excitation energy 1.967 eV [22]) even at $T = 300$ K quickly react with fuel molecules, resulting in production of chemically active particles [23]—[25]:

(r1) $O(^1D) + H_2 \rightarrow H + OH$
(r2) $O(^1D) + CH_4 \rightarrow CH_3 + OH$, $O(^1D) + CH_4 \rightarrow CH_3O + H$
(r3) $O(^1D) + C_2H_6 \rightarrow C_2H_5 + OH$, $O(^1D) + C_2H_6 \rightarrow CH_2OH + CH_3$
(r4) $O(^1D) + C_3H_8 \rightarrow C_3H_7 + OH$, $O(^1D) + C_3H_8 \rightarrow CH_2OH + C_2H_5$

The rate constants of reactions of ground state O(^{3}P) atoms [26] and electronically excited O$^($1D) atoms [23]—[25] with H_2, CH_4 and C_2H_6 molecules as a function of gas temperature presented in Figure 9.4. Quenching rate constants of excited O(^{1}D) atoms are weakly dependent on the gas temperature [27, 28]. It is clear that at relatively low temperatures reactions of ground state O(^{3}P) atoms occur much more slowly than the reaction of the excited atoms. Thus, at low temperatures the effect of excited O(^{1}D) atoms on the oxidation kinetics of combustible mixtures shall be particularly significant. Addition of electronically excited O(^{1}D) atoms leads to the chemically active particles production (r.1–r.4), and also to the additional gas heating during their quenching. It should be noted that, according to [24, 25], the probability of C-C bonds cleavage in the reaction of O(^{1}D) atoms with C_2H_6 , C_3H_8 is large enough. Although, in general, the question about the products distribution in these reactions remains open.

In air, the main channels of O(^{1}D) atoms production are the reactions ([12]–[14]):

(r5) $e + O_2 \rightarrow e + O(^3P) + O(^1D)$
(r6) $N(^2D) + O^2 \rightarrow O(^3P,^1D) + NO$
(r7) $N_2(a'^1\Sigma_u^-, C^3\Pi_u) + O_2 \rightarrow N_2 + O(^3P) + O(^1D)$

In fuel-air mixtures, in addition to the reactions (r.1-r.4), quenching of excited O(^{1}D) atoms by N_2 and O_2 molecules should be considered.

Table 9.1: Quenching rate constants of excited O(^{1}D) atoms [cm^3/s] by N_2, O_2, H_2, CH_4, C_2H_6, and C_3H_8 molecules at $T = 300$ K

	N_2	O_2	H_2	CH_4	C_2H_6	C_3H_8
k_f, cm^3/s [23]	-	-	$1.1 \cdot 10^{-10}$	$1.3 \cdot 10^{-10}$	$4.4 \cdot 10^{-10}$	$5.8 \cdot 10^{-10}$
k_f, cm^3/s [24]	-	-	$1.03 \cdot 10^{-10}$	$2.2 \cdot 10^{-10}$	$6.3 \cdot 10^{-10}$	$7.9 \cdot 10^{-10}$
k, cm^3/s [12]	$2.57 \cdot 10^{-11}$	$4.0 \cdot 10^{-11}$	-	-	-	-
ν_{fuel}/ν_{air}	-	-	$1.44 - 1.54$	$0.46 - 0.77$	$0.88 - 1.26$	$0.58 - 0.79$

Quenching rates of O(^{1}D) atoms by N_2, O_2, H_2, CH_4, C_2H_6, and C_3H_8 molecules, as well as the ratio of quenching frequencies of these atoms by air and fuel molecules

$$\nu_{fuel}/\nu_{air} = k_f \cdot [\mathrm{M_f}]/(k_{\mathrm{N_2}} \cdot [\mathrm{N_2}] + k_{\mathrm{O_2}} \cdot [\mathrm{O_2}]),$$

are presented in Table 9.1 for stoichiometric fuel-air mixtures. It is clear that for all mixtures,

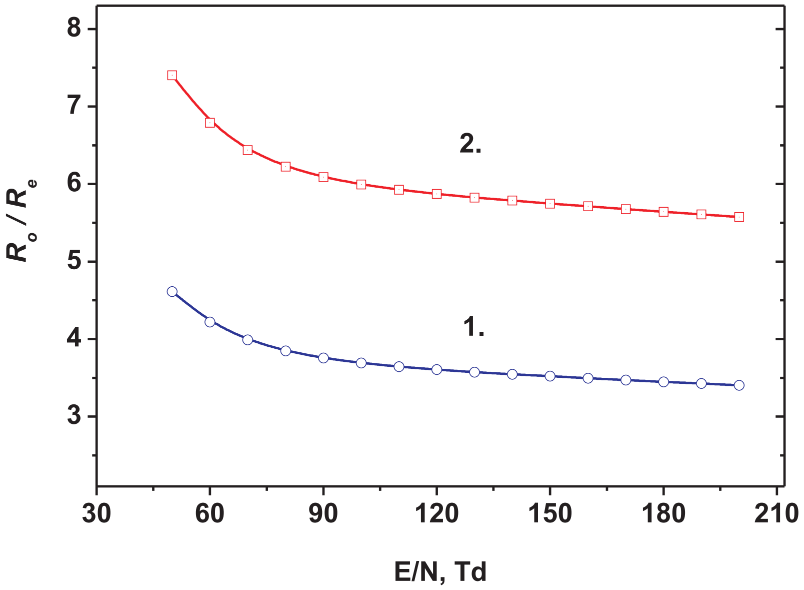

Figure 9.5: The ratio of rates of methane dissociation reactions (4.8) and (4.9), R_o/R_e, in CH_4-air mixtures as a function of reduced electric field E/N. The curve 1 correspond to the equivalent ratio $ER = 1$, the curve 2 - $ER = 0.1$.

a substantial fraction of $O(^1D)$ atoms reacts with fuel molecules. The most significant ratio is observed in hydrogen–air mixture.

Significant dilution of combustible mixtures by noble gases, commonly used in shock tubes [29]—[30], [31]—[33], and rapid compression machines (RCM) [34]—[36] experiments, leads to the additional channels of excited $O(^1D)$ atoms production, such as [37]:

$$Ar(^3P_{0,2}) + O_2 \rightarrow Ar + O(^3P) + O(^1D,^1S).$$

Quenching rate of $O(^1D)$ by noble atoms essentially depends on the type of atoms. Table 9.2 shows the experimental and calculated rate constants of $O(^1D)$ deactivation by He, Ne, Ar, Kr, Xe atoms. It is clear that the difference between the rate constants of these reactions may exceed a factor of 106, and this difference is observed in the measurements [38, 39], and in the calculation [40]. Adding of He and Ne atoms to the mixture has almost no effect on the frequency of $O(^1D)$ deactivation, while quenching by Kr and Xe atoms can be very significant.

Table 9.2: Quenching rate constants of excited $O(^1D)$ atoms [cm^3/s] by He, Ne, Ar, Kr and Xe atoms at $T = 300$ K

	He	Ne	Ar	Kr	Xe
k_{exp}, cm^3/s [38]	$< 7.0 \cdot 10^{-16}$	$(1.1 \pm 0.1) \cdot 10^{-14}$	$(7.1 \pm 0.6) \cdot 10^{-13}$	$(1.55 \pm 0.1) \cdot 10^{-11}$	$(1.0 \pm 0.1) \cdot 10^{-10}$
k_{exp}, cm^3/s [39]	$< 3.2 \cdot 10^{-16}$	$(5 \pm 1.4) \cdot 10^{-15}$	$(7.1 \pm 0.6) \cdot 10^{-13}$	$(7 \pm 1.87) \cdot 10^{-11}$	$(4.55 \pm 1.3) \cdot 10^{-10}$
k_{cal}, cm^3/s [40]	10^{-24}	$4.98 \cdot 10^{-19}$	$5.19 \cdot 10^{-13}$	$1.58 \cdot 10^{-11}$	$1.66 \cdot 10^{-11}$

The calculated ratio of rates of methane dissociation in reactions (4.8) and (4.9), R_o/R_e:

$$\begin{array}{ll} (r8) & O(^1D) + CH_4 \rightarrow \text{products}, \\ (r9) & e + CH_4 \rightarrow e + CH_3 + H, \end{array}$$

is shown in Figure 9.5. In these calculations $O(^1D)$ atom production in reactions (4.5-4.7) was taken into account together with the loss during quenching by N_2, O_2, and CH_4 molecules (with rate constants k_{N_2}, k_{O_2}, k_{CH_4} respectively, see Table 9.1). The ratio R_o/R_e is given by:

9.3 Conclusions

So, the analysis of role of O(^{1}D) in plasma–assisted combustion including gas mixtures with hydrocarbons is presented. At relatively low initial temperatures, the effect of electronically excited O(^{1}D) atoms on the oxidation and reforming of combustible mixtures is crucial due to the high rates of reactions of O(^{1}D) atoms with hydrogen and hydrocarbon molecules and low rates of the reactions of atomic particles in the ground electronic state. Efficient dissociation of hydrocarbons in collisions with O(^{1}D) atoms allows to neglect the uncertainty of the cross sections of electron impact dissociation of hydrocarbons when calculating plasma–assisted ignition of hydrocarbon–containing mixtures.

Bibliography

[1] Aleksandrov N.L., Kindysheva S.V. and Kochetov I.V. Kinetics of low-temperature plasmas for plasma-assisted combustion and aerodynamics *Plasma Sources Sci. Technol.* 2014. V. 23. P. 015017 (13pp)

[2] Braginskiy O.V., Vasilieva A.N., Klopovskiy K.S., Kovalev A.S., Lopaev D.V., Proshina O.V., Rakhimova T.V., Rakhimov A.T. Singlet oxygen generation in O_2 flow excited by RF discharge: I. Homogeneous discharge mode: α-mode *J. Phys. D Appl. Phys.* 2005. V. 38. P. 3609-3625.

[3] Kovalev A.S., Lopaev D.V., Mankelevich Yu.A., Popov N.A., Rakhimova T.V., Poroykov A.Yu., Carroll D.L. // Kinetics of $O_2(b^1\Sigma_g^+)$ in oxygen RF discharges *J. Phys. D: Appl. Phys.* 2005. V. 38. P. 2360-2370.

[4] Thomas J.M., Kaufman F., Golde M.F. Rate constants for electronic quenching of $N_2(A^3\Sigma_u^+$, v=0-6) by O_2, NO, CO, N_2O and C_2H_4 *J. Chem. Phys.* 1987. V. 86. P. 6885-6892.

[5] Herron J.T. Evaluated chemical kinetics data for reactions on $N(^2D)$, $N(^2P)$, and $N_2(A^3\Sigma_u^+)$ in the gas phase *J. Phys. Chem. Ref. Data.* 1999. V. 28. P. 1453.

[6] Dreyer J.W., Perner D. Deactivation of $N_2(A^3\Sigma_u^+)$,v=0-7) by ground state nitrogen, ethane and ethylene measured by kinetic absorption spectroscopy *J. Chem. Phys.* 1973. V. 58. P. 1195-1201.

[7] Piper L.G. Energy transfer studies on $N_2(^1\Sigma_g^+$,v) and $N_2(B^3\Pi_g)$ *J. Chem. Phys.* 1992. V. 97. P. 270-275.

[8] Albugues F., Birot A., Blanc D., Brunet H., Galy J., Millet P., Teyssier J. L. Destruction of the levels $C^3\Pi_u$ (v' =0, v'= 1) of nitrogen by O_2, CO_2, CH_4 and H_2O *J. Chem. Phys.* 1974. V. 61. P. 2695-2699.

[9] Umemoto H. Production yields of H(D) atoms in the reactions of $N_2(A^3\Sigma_u^+$,v=0-6) with C_2H_2, C_2H_4, and their deuterated variants *J. Chem. Phys.* 2007. V. 127. P. 014304.

[10] Kirillov A.S. The study of intermolecular energy transfers in electronic energy quenching for molecular collisions N_2-N_2, N_2-O_2, O_2-O_2 *Ann. Geophys.* 2008. V. 26. P. 1149-1157.

[11] Popov N.A. Vibrational kinetics of electronically-excited $N_2(A^3\Sigma_u^+$,v) molecules in nitrogen discharge plasma *J. Phys. D: Appl. Phys.* 2013. V. 46. P. 355204 (11pp)

[12] Kossyi I.A., Kostinsky A.Y., Matveev A.A., Silakov V.P. Kinetic scheme of the non-equilibrium discharge in nitrogen-oxygen mixtures *Plasma Sources Sci. Technol.* 1992. V. 1. 3. P. 207.

[13] Capitelli M., Ferreira C.M., Gordiets B.F., Osipov A.I. Plasma kinetics in atmospheric gases. Springer. 2000. 297 c.

[14] Popov N.A. Fast gas heating in a nitrogen-oxygen discharge plasma: I. Kinetic mechanism *J. Phys. D: Appl. Phys.* 2011. V. 44. 285201 (16 pp).

[15] Aleksandrov N.L., Kindusheva S.V., Nudnova M.M., Starikovskii A.Yu. Mechanism of ultra-fast heating in a non-equilibrium weakly ionized air discharge plasma in high electric fields *J. Phys. D: Appl. Phys.* 2010. V. 43. P. 255201 (19 pp).

[16] Rusterholtz D. L., Pai D. Z., Stancu G. D., Lacoste D. A., Laux C. O. Ultrafast heating in nanosecond discharges in atmospheric pressure air *50th AIAA Aerospace Sciences Meeting* (9-12 January, 2012, Nashville, Tennessee). AIAA 2012-0509. (11 pp).

[17] Rusterholtz D. L., Lacoste D. A., Stancu G. D., Pai D. Z., Laux C. O. Ultrafast heating and oxygen dissociation in atmospheric pressure air by nanosecond repetitively pulsed discharges *J. Phys. D: Appl. Phys.* 46 (2013) 464010 (21pp)

[18] Popov N. A. Active particles production by pulsed nanosecond discharge in ambient air. Quenching of electronically excited states of nitrogen by O_2 molecules and $O(^3P)$ atoms *53nd AIAA Aerospace Sciences Meeting* (5-9 January, 2015, Kissimmee, Florida). AIAA-2015

[19] Starikovskaia S.M., Aleksandrov N.L., Kosarev I.N., Kindysheva S.V., Starikovskii A.Yu. Ignition with low-temperature plasma: kinetic mechanism and experimental verification *High Energy Chem.* 2009. V. 43. P. 213-218.

[20] Hagelaar G.J., Pitchford L.C. Solving the Boltzmann equation to obtain electron transport coefficients and rate coefficients for fluid models *Plasma Sources Sci. Technol.* 2005. V. 14. P. 722-733.

[21] Morgan W.L. A critical evaluation of low-energy electron impact cross sections for plasma processing modeling *Plasma Chemistry and Plasma Processing.* 1992. V. 12. P. 477.

[22] Radzig A.A., Smirnov B.M. Reference data on atoms, molecules and ions (Berlin, Springer). 1980.

[23] Fletcher I.S., Husain D. The collisional quenching of electronically excited oxygen atoms, $O(^1D)$, by the gases NH_3, H_2O_2, C_2H_6, C_3H_8, and $C(CH_3)_3$, using time-resolved attenuation of atomic resonance radiation *Can. J. Chem.* 1976. V. 54. P. 1765-1770.

[24] Matsumi Y, Tnokura K, Inagaki Y and Kawasaki M Isotopic branching ratios and translational energy release of H and D atoms in reaction of $O(^1D)$ atoms with alkanes and alkyl chlorides *J. Phys. Chem.* 1993. V. 97. P. 6816-6821.

[25] Shu J., Lin J.J., Lee Yu.T., Yang X. Multiple pathway dynamics of the $O(^1D) + C_2H_6$ reaction: A crossed beam study *J. Chem. Phys.* 2001. V. 115. P. 849.

[26] Baulch D.L., Cobos C.J., Cox R.A. et al Summary table of evaluated kinetic data for combustion modelling *Combust. Flame.* 1994. V. 98. No 1. P. 59-79.

[27] Starikovskiy A., Rakitin A., Correale G., Nikipelov A., Urushihara T., Shiraishi T. Ignition of hydrocarbon-air mixtures with non-equilibrium plasma at elevated pressures *50th AIAA Aerospace Sciences Meeting*, Nashville, TN, USA, 9-12 January 2012, AIAA-2012-0828.

[28] Stepanyan S.A., Boumehdi M.A., Vanhove G., Starikovskaia S.M. Time-resolved electric field measurements in nanosecond surface dielectric discharge. Comparison of different polarities. Ignition of combustible mixtures by surface discharge in a rapid compression machine *51st AIAA Aerospace Sciences Meeting.* 07 - 10 January 2013, Grapevine (Dallas/Ft. Worth Region), Texas AIAA 2013-1053

[29] Starikovskiy A., Aleksandrov N. Plasma-assisted ignition and combustion *Progress in Energy and Combustion Science.* 2013. V. 39. 1. P. 61-110.

[30] Starikovskaia S.M. Plasma assisted ignition and combustion. Nanosecond discharges and development of kinetic mechanisms *J. Phys. D: Appl. Phys.* 2014. V. 47. P. 353001 (34pp)

[31] Bozhenkov S.A., Starikovskaia S.M., Starikovskii A.Yu. Nanosecond gas discharge ignition of H2 and CH4 - containing mixtures *Combust. Flame.* 2003. V. 133. No 1-2. P. 133-146.

[32] Kosarev I.N., Aleksandrov N.L., Kindysheva S.V., Starikovskaia S.M., Starikovskii A.Yu. Kinetics of ignition of saturated hydrocarbons by nonequilibrium plasma: C_2H_6 to C_5H_{12} containing mixtures *Combust. Flame.* 2009 V.156. P. 221-233.

[33] Starikovskaia S.M., Aleksandrov N.L., Kosarev I.N., Kindysheva S.V., Starikovskii A.Yu. Ignition with low-temperature plasma: kinetic mechanism and experimental verification *High Energy Chem.* 2009. V. 43. P. 213-218.

[34] Boumehdi M.A., Stepanyan S.A., Desgroux P., Vanhove G., Starikovskaia S.M. Ignition of methane- and n-butane-containing mixtures at high pressures by pulsed nanosecond discharge *Comb. Flame.* 2015. V. 162. P. 1336-1349.

[35] Heidner R. F. and Husain D. A study of the collisional quenching of $O(^1D)$ by the noble gases employing time-resolved attenuation of atomic resonance radiation in the vacuum ultraviolet *Int. J. Chem. Kinetics.* 1974. V. 6. P. 77-87.

[36] Phillips L. F. Theoretical curves of growth for $O(^1D)$ absorption at 115.2 nm *Chem. Phys. Letters.* 1976. V. 37. P. 421-424.

[37] Balamuta J., Golde M.F. Formation of electronically excited oxygen atoms in the reactions of $Ar(^3P_{0,2})$ and $Xe(^3P_2)$ atoms with O_2 *J. Phys. Chem.* 1982. V. 86. P. 2765-2771.

[38] Kinnersly S.R., Murrell J.N., Rodwell W.R. Collisional quenching of $O(^1D)$ by rare gas atoms *J. Chem. Soc., Faraday Trans.* 2, 1978. V.74. P. 600-606.

[39] Popov N.A. Dissociation of nitrogen in a pulse-periodic dielectric barrier discharge at atmospheric pressure *Plasma Physics Reports.* 2013. V. 39. P. 420-424.

[40] Cosby P.C. Electron-impact dissociation of nitrogen *J. Chem. Phys.* 1993. V. 98. P. 9544-9552.

[41] Popov N.A. Effect of a pulsed high-current discharge on hydrogen-air mixtures *Plasma Physics Reports.* 2008. V. 34. P. 376-391.

[42] Starikovskaia S.M., Starikovskii A.Yu., Zatsepin D.V. Hydrogen oxidation in a stoichiometric hydrogen-air mixture in the fast ionization wave *Comb ust. Theory and Modelling.* 2001. V. 5. P. 97.

Chapter 10

Review on the state–of–art in plasma assisted combustion/ignition

This chapter summarizes available information in the field of plasma assisted ignition/combustion, giving review of available papers in the field for the period since 2006 to the time of the present Porject, summarizing initial thermodynamic conditions for available experiments with nanosecond discharges and discussing the conditions of kinetic experiment in the field.

10.1 Available review papers and the aim of the present review

A few review papers are available in the field of plasma assisted ignition. The first review [1] summarizing non–numerical, at that time, studies of applications of nonequilibrium plasma for ignition/combustion enhancement and comparing the efficiency of thermal initiation of ignition and ignition by nonequilibrium plasma was published in 2006. The main principles of plasma assisted combustion are discussed in [1], together with analysis of different gas discharges used for PAI/PAC. Three experimental approaches are considered: ignition by microwave discharge in supersonic flows; ignition by different discharges in low–speed flows in laboratory facilities; and ignition by a nanosecond discharge in shock tube (ShT) experiments. It is concluded that the experimental data on gas temperature and densities of intermediate species during the induction period will provide a basis for kinetic models of PAI/PAC. It was suggested to study the class–by–class impact of different kinds of particles produced in the discharge on the subsequent chemistry.

Nanosecond discharge was suggested as a tool for plasma–assisted ignition in 1996 [2] by the Physics of Nonequilibrium Systems Laboratory in Moscow Institute of Physics and Technology. The review of the experimental work of this group in the period between 1996 and 2009 is presented in [3]. Starting from the numerical modeling of the kinetics of combustible mixture in shock tubes, the authors suggested using a ShT as a means for getting a given pressure and temperature of the gas mixture. The nanosecond discharge was initiated behind the reflected shock wave, allowing direct comparison of autoignition (or thermal) delay time with the delay time caused by the impact of the highly nonequilibrium plasma of a nanosecond discharge. More than 10 gas mixtures with different combustible agents, from hydrogen to pentane, have been studied at initial temperatures close to the autoignition threshold. A corresponding kinetic mechanism was suggested, and it was confirmed by numerical modeling that, at high initial temperatures, a decrease of ignition delay time by a few orders of magnitude is explained by efficient dissociation in the discharge and early afterglow, mainly caused by the production of atomic oxygen.

Review [4], published in 2009, analyzes non–thermal and thermal effects in plasma–asssited ignition and high speed flow control. This is mainly a review of experimental and numerical work of the Michael A. Chaszeyka Nonequilibrium Thermodynamics Laboratories, Gas Dynamics and Turbulence Laboratory of Ohio State University, for the period 2005—2009. The authors suggested experiments in a low pressure, $P = 60$ Torr, test section with a slow (a few m/s) flow of an air–fuel mixture. The discharge initiated as a barrier electrodeless discharge, and the ignition length has been measured for different parameters of the discharge and gas flow. The pulse generator was operated in a burst mode, producing sequences of up to 1000 pulses 20 kV in amplitude at repetition rates varying from 20 to 50 kHz. Comparing the ignition delay time predicted by the model for plasma assisted ignition and for ignition by equilibrium heating, the authors concluded that chain reactions of radicals generated by the plasma reduce ignition time by up to two orders of magnitude and the ignition temperature by up to 300 K.

A few original papers [5, 6, 7] should also be noted here. Presenting kinetic models of discharge action on different gases, the papers give a detailed analysis of kinetic data available in the literature and the results of numerical modeling of the experimental work of other authors. For these reasons, they can be considered as review papers of a kind. A model describing the influence of a nanosecond discharge on H_2–air mixtures is developed in [5]. The model includes processes of: ionization, dissociation, and excitation by electron impact; ion-molecular reactions and processes with electronically excited atoms and molecules; reactions of neutral species, describing the ignition of hydrogen-oxygen mixtures. The calculations are done for a wide range of reduced electric fields, E/N, here E is an electric field and N is a gas number density. The model is tested on autoignition experiments and used finally to analyze the ignition of H_2–air mixture by a pulsed discharge. The author concludes that, for discharges at high E/N values and at high temperatures, the ignition delay can be significantly reduced by the artificial addition of atoms produced by the discharge, while at low initial temperatures the dominating process responsible for the decrease of the ignition delay time, is a gas self–heating due to the recombination of atoms.

The paper [6] studies the effect of singlet oxygen $O_2(a^1\Delta_g)$ molecules produced in a gas discharge on the ignition of H_2:O_2 mixtures. The excitation energy of singlet oxygen is 0.98 eV [8]. Analysis of available information and numerical modeling corresponding to the conditions of a few experimental papers allowed the author to conclude that quenching of molecular singlet oxygen is more efficient than chain initiation or branching with $O_2(a^1\Delta_g)$. The author claims that even small initial densities of atomic oxygen, about 10^{-4} at relatively high pressure, lead to dominant role of O–atoms in comparison with singlet oxygen, and so discharges at high electric fields optimal for dissociation are more efficient for PAC than the discharges at low electric fields.

Although the paper [7] describes the kinetics in N_2:O_2 mixtures, the presented results are crucial for plasma–assisted combustion. Fast relaxation, at a time scale less than that of VT–relaxation, of the discharge energy in a wide range of reduced electric fields, $E/N < 1000$ Td, is considered. According to the model, the dissociation of O_2 by electron impact, quenching of N_2 ($B^3\Pi_g$, $C^3\Pi_u$, $a'^1\Sigma_u^-$) by oxygen, and quenching of excited $O(^1D)$ atoms by nitrogen provide the main input to a fast gas heating. At $E/N > 400$ Td, the dominant reactions are the quenching of excited molecular nitrogen by O_2 and the processes involving charged particles. The author suggests a simple estimate of the energy η_E converted to fast gas heating: in a wide range of parameters η_E can be estimated, for air, as 30% of the energy expended on the excitation of electronic degrees of freedom, ionization and dissociation of molecules. Finally, a review of experimental and theoretical papers concerning the effect of atoms and electronically excited $O_2(a_g^\Delta)$ molecules on the ignition delay time and on the shift of the ignition temperature threshold of hydrogen–oxygen and hydrogen–air mixtures is presented in [9].

The Handbook of Combustion, published in 2010, contains two chapters devoted to the interaction of low temperature plasma with the combustion process. One of them gives a brief review of — available in 2010 — experimental data and theoretical approaches [10] and the second chapter [11] reviews available diagnostic tools in the field of combustion enhancement and flame stabilization by nonequilibrium plasmas.

The paper [12] presents an invited review written around 15 different "key topics" in the physics of plasmas. One of the conclusions is that further understanding of PAI/PAC physics and chemistry at low gas temperatures, low equivalent ratios and/or high pressures needs detailed chemical mechanisms to be developed taking into account joint discharge and combustion chemistry.

A series of review papers [13, 14] provide the most complete observation of the state of the art in the field of plasma assisted ignition and combustion. In particular, the review [14] presents experimental results obtained recently in different conditions — going from supersonic flows to quiescent gases. Detailed analysis of the action of plasma on combustible mixtures is given. The authors discuss the formation of an electron energy distribution function (EEDF) and energy branching in different discharges. A hierarchy of energy relaxation is traced with examples taken from the literature. Rotational, vibrational relaxation, quenching of low–energy electronic states, like $O_2(a^1\Delta_g)$ are considered. Special attention is given to the analysis of the dissociative quenching of high energy electronic levels, in particular – to dissociation of O_2 via excitation of $N_2(C^3\Pi_u)$ state of molecular nitrogen. The model of fast gas heating, suggested in [14], is different from the model of [7], providing more heating at high electric fields. The role of VUV emission, ionization and recombination processes is analyzed. Plasma action on combustible mixtures for different initial temperatures (room temperature, and temperatures below and above the self–ignition threshold) is discussed. Different aspects on plasma action on flames, like chemo–ionization, flow turbulization and radical generation ahead of the flame front are reviewed.

An idea of the complexity of the air flow, plasma and combustion interaction can be obtained from papers where the ignition of supersonic and fast subsonic gas flows by plasma is studied [15, 16, 17]. Hydrodynamic effects are also extremely important for high voltage pulsed discharges in quiescent gas mixtures, when the energy is released during a short time scale [18].

Advanced numerical modeling, such as the 2D–modeling of discharge [19], with plasma chemical kinetics, and plasma–initiated combustion [20], linked or not with the discharge, has recently become available in the literature. This approach with multiple scales in time and space, although neglecting the detailed analysis of chemical pathways, allows the most general analysis of PAC as a complex physical phenomenon including the physics of gas discharge, hydrodynamics and chemical kinetics. Although the interaction of these fields can be very important, in the present paper we will, when possible, restrict the description to the consideration of the chemistry initiated by nonequilibrium plasma in combustible systems.

In spite of the fact that different discharges, as RF ones [21] or gliding arcs [22], are used for plasma–assisted ignition/combustion, high–voltage nanosecond discharge, at low and at elevated pressures, has been the most popular tool, during a last decade, for studying kinetic effects connected to PAI/PAC problem. Specific reasons for this are that the nanosecond discharges: (i) are uniform at low and moderate gas densities; (ii) are naturally synchronized in time in the case of a multi–streamer configuration at high gas densities; (iii) provide efficient excitation and dissociation of the gas at a time scale shorter than the typical time scale of combustion kinetics. Another important issue is the recent progress of solid–state high power electronics: modern companies suggest high–voltage nanosecond generators (see, for example, [23]) for a broad range of parameters of the pulse, allowing operation both in laboratories and in the

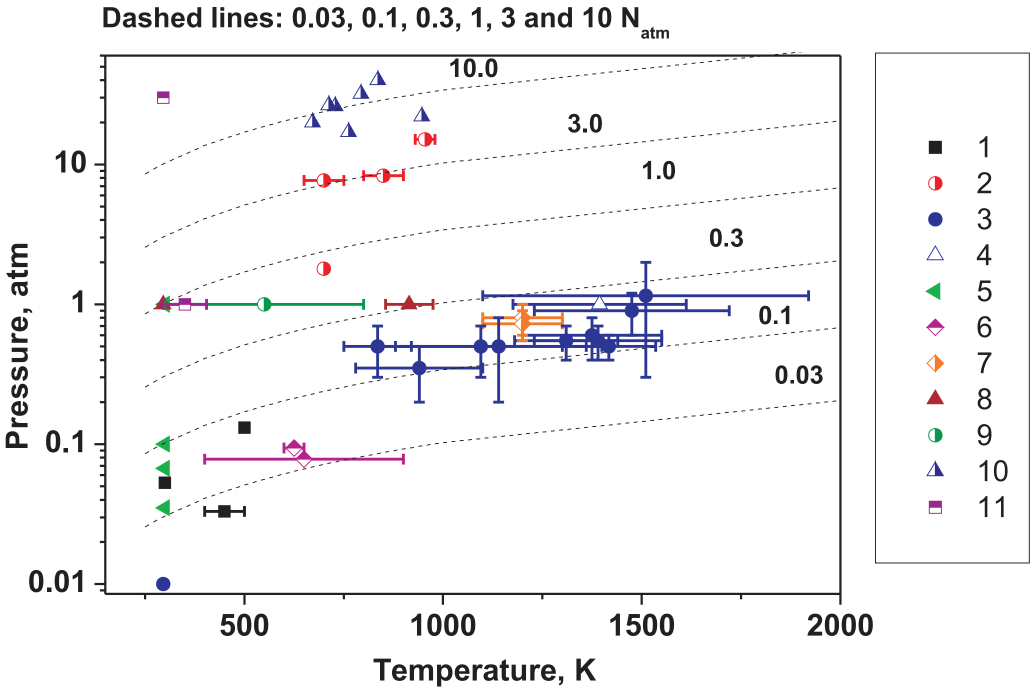

Figure 10.1: $P - T$ diagram of available in the literature experiments on combustion initiated or assisted by nanosecond discharges. The details of symbols in the legend are given by the table 10.1. Dashed lines represent the isolines of gas density, N, normalized to atmospheric gas density N_{atm} at normal conditions.

extreme conditions of industrial applications. Here, we will indicate the second restriction of the present review: the analysis will be limited by mainly experimental works on PAI/PAC triggered by short pulsed discharges.

10.2 Review of available experiments. General remarks and conclusions

To summarize the knowledge relating to the experimental conditions studied by different scientific groups, the initial experimental pressures and temperatures from papers of different authors have been plotted as a "pressure—temperature" diagram (figure 10.1). As the initial pressure and initial temperature are the parameters typically used to unify combustion experiments, it seems reasonable to plot the same diagram for PAI/PAC experiments. Showing explicitly the gas number density and temperature for each of the experiments, the diagram allows comparison of data relating to discharge development and combustion kinetics respectively.

The symbols, numbered on right–hand side of the plot, relate to the appropriate papers in Table 10.1. The mixtures investigated are schematized in the same table in the form $F_i/O_i/D_i$, where F_i is a fuel, O_i is an oxidizer, and D_i is diluent. Each set of experiments is represented in the figure 10.1 as a single symbol with an error bar, where the symbol designate the center of the investigated domain, and error bar covers all the intervals of temperatures or pressures under study. Dashed lines represent the isolines of the gas density, N, normalized with respect to the atmospheric gas density under normal conditions.

It is seen from the figure, that experiments at ambient initial temperature cover a wide range of pressures: from combustible mixture oxidation in fast ionization waves at $P = 1 - 10$ Torr [24, 25, 26] to transient plasma ignition at 30 atm [27]. Stationary reactors with the possibility of preliminary gas heating are used for pressures of $25 - 100$ Torr [28, 29]. High–temperature experiments, $700 - 2000$ K, at atmospheric pressure and lower correspond to shock tube facilities [3, 30, 31]. High pressure ($2 - 50$ atm) and moderate temperature ($700 - 100$ K) conditions are covered by the experiments using rapid compression machines [32, 33, 34, 35]. Finally, low pressure or atmospheric pressure burners are used for the intermediate range of temperatures, $500 - 1000$ K [36, 37, 38]. Isolines of the gas number density, plotted with dash lines in the figure, clearly demonstrate that the main parts of PAI/PAC experiments have been carried out at gas densities lower than normal atmospheric gas density: $N < N_{atm}$. This means that a discharge can be produced uniformly in space in the majority of aforementioned experiments, except the high–pressure RCM experiments.

Table 10.1: References and mixtures under study for the data presented on the $P - T$ diagram in figure 10.1.

N of symbol	Reference	Mixture composition, $F_i/O_i/D_i$
1	[28, 29, 39]	H_2,CH_4,C_2H_4,C_3H_8/O_2/N_2,Ar
2	[33, 34, 35]	CH_4,C_4H_{10},C_7H_{16}/O_2/N_2,Ar
3	[25, 26, 24, 3]	H_2,$C_nH_{(2n+2)}$, n=(1-6), $C_{10}H_{22}$/O_2,N_2O/N_2,Ar,He
4	[31]	C_2H_6/O_2/N_2,Ar
5	[40, 41]	CH_4,C_2H_4,C_3H_8/O_2/N_2,Ar
6	[36]	CH_4,DME/O_2/He,Ar
7	[30]	C_2H_2/O_2/Ar
8	[37, 38]	CH_4/O_2/N_2
9	[42]	$C_nH_{(2n+2)}$, n=(1-5)/O_2/N_2
10	[32]	C_3H_8/O_2/N_2
11	[43, 44, 27]	C_2H_2,CH_4/O_2/N_2

The detailed kinetics of fuel–air mixtures under the action of pulsed nonequilibrium plasmas remains far from understood, in spite of considerable experimental advances achieved over the past two decades. High–temperature conditions, close to the ignition threshold, can de described fairly well with existing kinetic mechanisms taking into account the integral production of radicals by the discharge. In this case the non–thermal character of ignition can easily be demonstrated, the ignition delay can be predicted within at least an order of magnitude accuracy, and the care must be taken mainly about making correct measurements of the energy release in the discharge and calculations of the energy branching in the fuel–containing mixture.

With decrease of the initial temperature, the combustion chemistry becomes more sensitive to the details of the plasma action. Modification of S–curve, suppression of NTC region and changes of cool flame chemistry are the convincing examples of plasma–combustion interaction demanding to develop the links between plasma and combustion kinetics. We consider these conditions to be the most challenging for studying chemical mechanisms of plasma–assisted ignition/combustion.

Another important issue concerns a practical result which has to be derived from numerical modeling. For most practical conditions, the recombination of charged species and relaxation of the greater part of the electronically excited atoms and molecules take times shorter than the

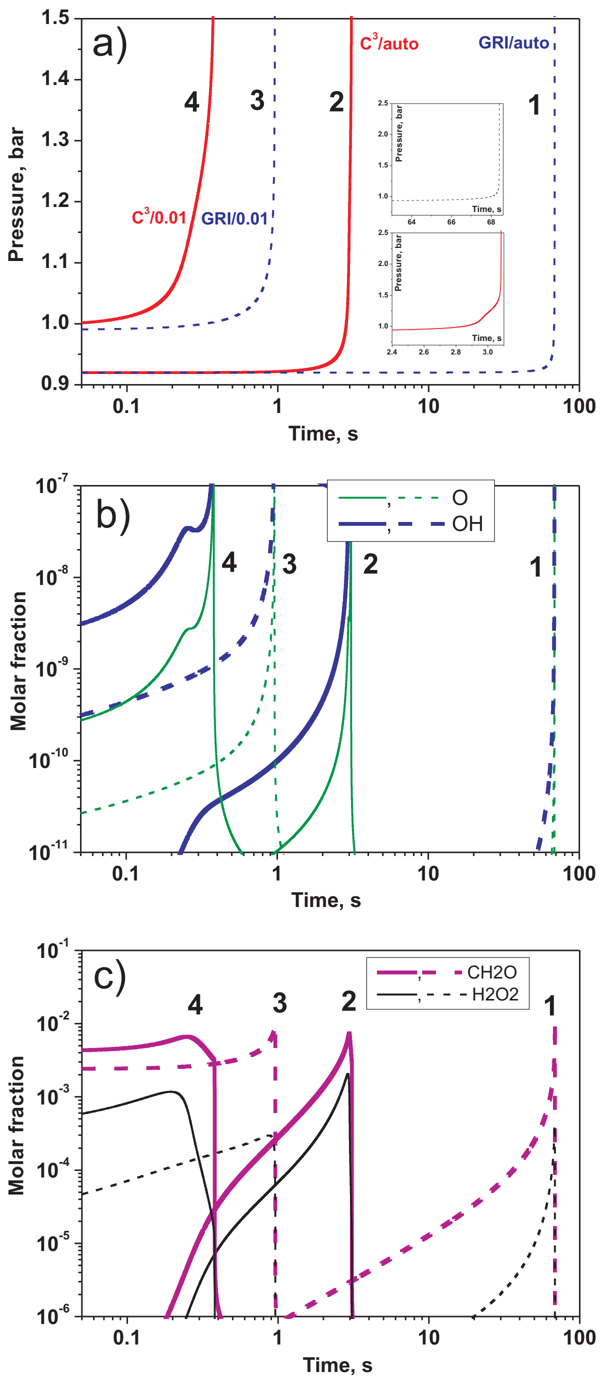

Figure 10.2: Calculated autoignition (1,2) and ignition at artificial injection of 1% of atomic oxygen (3,4) of a CH_4:O_2=2:1 mixture at $P_0 = 700$ Torr and $T_0 = 800$ K. GRI–Mech 3.0 (1,3) [46] and Combustion Chemistry Center (2,4) [47] mechanisms were taken as test mechanisms. (a) — pressure traces, (b) — mole fractions of O and OH, (c) — mole fractions of CH_2O and H_2O_2.

ignition delay time. If the aim of the calculations is to estimate the plasma–triggered ignition delay time, and if the action of plasma — that is, the deposited energy, electric field and electron density distribution in time and in space, cross–sections of electron impact with the molecules of the mixture under study and kinetics in the near afterglow — are known, any reasonable combustion kinetic mechanism can be considered as a predictive mechanism: the shortening of the ignition delay time will be obtained with an accuracy within about an order of magnitude. But if the aim of the study is to reveal the details of the kinetics, or to trace the absolute values and time–dependent behavior of the minor components, then no predictive mechanism exist at the moment.

To illustrate the ideas stated above, calculations of the ignition delay time and molar fractions of O, OH, CH_2O and H_2O_2 were carried out for a CH_4:O_2=2:1 mixture at the initial pressure and temperature of 700 Torr and 800 K respectively. The choice of the mixture and of the initial parameters was dictated by three reasons: (i) the majority of PAI/PAC papers use the GRI–Mech mechanism, developed for the high–temperature range, to model methane combustion, even if ignition by plasma starts at the initial room temperature; (ii) mechanisms including the low temperature kinetics for higher hydrocarbons are developed and available in the literature; (iii) a cool flame in a methane–containing mixture has been obtained experimentally [45] under the aforementioned conditions. Calculations were performed at constant volume. The autoignition delay time derived from the pressure traces (figure 10.2 a) calculated on the basis of the GRI–Mech 3.0 [46] mechanism is equal to 70 s. The autoignition delay time for the Combustion Chemistry Center (C^3) [47] mechanism is shorter: 3 s. No cool flame is observed in GRI kinetics, and a well–pronounced cool flame is seen when modelling with the C^3 scheme (see the inserts in figure 10.2 a). It should be mentioned here that there is a principal difference between the autoignition kinetics and the kinetics of plasma–assisted ignition: for autoignition, one of the most important first elementary steps is a reaction of hydrogen abstraction from hydrocarbon; for PAI, the first step is a reaction of hydrocarbon with O–atoms produced by the discharge. Addition of 1% of atomic oxygen, with simultaneous removal of 0.5% of O_2, smoothes over the contradictions between the kinetic schemes: for GRI and C^3 the ignition delay becomes equal 1 s and 0.4 s, respectively. Although the ignition delays do not differ dramatically for the O atom activated kinetics for the two mechanisms, the difference in density of the intermediate species is evident from figures 10.2 b–c: the difference in formaldehyde density is limited by a coefficient of 2–3, and the differences in H_2O_2, O and OH densities are 1–2 orders of magnitude. It can be concluded that, in order to build a kinetic mechanism of plasma–assisted ignition and combustion, special attention should be paid to the organization of experiments in order to obtain reliable unambiguous data.

A special set of conditions must be fulfilled to consider an experiment on combustion triggered by plasma as a kinetic experiment. We suggest to formulate them in the following way:

(i) The discharge action and the combustion chemistry should be separated in time or in space; if not, their mutual influence has to be studied.

(ii) The spatial homogeneity of the discharge must be analyzed.

(iii) The plasma parameters (shapes and amplitudes of the voltage and current, deposited energy, electric field, electron density) are the primary parameters of interest. As the detailed discharge–combustion mechanism for heavy hydrocarbons is a challenge, special attention must be given to discharge experiments on mixtures containing hydrocarbons, starting from the energy distribution and finishing with cross–section data sets for electron interaction with higher hydrocarbons;

(iv) The action of plasma on the gas mixture at early afterglow, namely the formation of a "pool" of active species, their dependence upon the E/N value and the gas mixture composition, and the increase of the gas temperature due to relaxation of the energy stored in the electronic degrees of freedom (in a PAI/PAC field, historically, this relaxation is called fast gas heating) must be studied. It is important to note that, to trace the chemical transformation caused by plasma, the smallest possible energy release in the discharge is needed, to avoid the shift of the equilibrium to higher temperatures. The importance of the analysis of the spatial distribution of the energy release in the discharge and the following spatial distribution of the gas heating and related hydrodynamic phenomena must not be underestimated.

(v) Reliable data on ignition/combustion modification in plasma/combustion facilities must be obtained; special analysis is needed to clearly distinguish phenomena linked to discharge–induced hydrodynamics or flame propagation from plasma–triggered kinetic phenomena.

(vi) It is necessary to record the kinetic curves of the main components, including products/reagents/the most important intermediates within the time scale of their changes.

(vii) Sensitivity analysis must be considered as an integral part of PAI/PAC kinetic analysis, to reveal the most important conditions and sub–mechanisms and to suggest ways in which their experimental verification can be achieved.

A few new reviews on plasma–assisted combustion published recently are the results of active work of a few strong scientific groups in the field of plasma assisted combustion [48, 49, 50]. The authors of the present Report do believe that the field of plasma assisted ignition and combustion is a modern scientific field combining a lot of experimental and theoretical efforts in the fields of physics of gas discharge, hydrodynamics, combustion and detailed plasma and combustion kinetics and providing high level internationally competitive fundamental scientific results for any of mentioned fields.

Bibliography

[1] Starikovskaia S M 2006 Plasma assisted ignition and combustion *J. Phys.D.: Appl. Phys.* **39** R265—R299

[2] Kof L M and Starikovskii A Yu 1996 Oxygen–hydrogen mixtures ignition under the high–voltage ionization wave conditions at high temperatures *26th Int. Symposium on Combustion. Abstracts of Work–in–Progress Papers* (Napoli, 1996, the Combustion Institute Publ.) P.406

[3] Starikovskaia S M, Aleksandrov N L, Kosarev I N, Kindysheva S V, and Starikovskii A Yu 2009 Ignition with low–temperature plasma: kinetic mechanism and experimental verification, *High Energy Chemistry* **43/3**, 213–218

[4] Adamovich I V, Choi I, Jiang N, Kim J–H, Keshav S, Lempert W R, Mintusov E I, Nishihara M, Samimy M and Uddi M 2009 Plasma assisted ignition and high-speed flow control: non-thermal and thermal effects *Plasma Sources Sci. Technol.* **18** 034018 (13pp)

[5] Popov N A 2008 Effect of a pulsed high–current discharge on hydrogen-air mixtures, *Plasma Physics Reports* **34/5** 376–391

[6] Popov N A 2011 Effect of singlet oxygen $O_2(a^1\Delta_g)$ molecules produced in a gas discharge plasma on the ignition of hydrogen-oxygen mixtures. *Plasma Sources Sci. Technol.* **20** 045002 (11pp)

[7] Popov N A 2011 Fast gas heating in a nitrogen-oxygen discharge plasma: I. Kinetic mechanism *J. Phys. D: Appl. Phys.* **44** 285201 (16pp)

[8] Radsig A A, Smirnov B M 1980 *Handbook on Atomic and Molecular Physics.* (Moscow: Atomizdat publ.), (*In Russian*)

[9] Popov N A 2012 Effect of nonequilibrium excitation on the ignition of combustible mixtures Proc. of 43rd AIAA Plasmadynamics and Laser Conference, 25–28 June 2012, New Orleans, Louisiana, AIAA–2012–2989

[10] Starikovskaia S M, Starikovskii A Yu 2010 Plasma assisted ignition and combustion, *In: Handbook of Combustion, by M. Lackner (Ed.), F. Winter (Ed.), A.K. Agarwal (Ed.)*, Wiley-VCH, ISBN; 978-3527324491, pp.71—93

[11] Vincent–Randonner A 2010 Combustion Ecnhancement and stabilization: principles of plasma assitance and diagnostic tools, *In: Handbook of Combustion, by M. Lackner (Ed.), F. Winter (Ed.), A.K. Agarwal (Ed.)*, Wiley-VCH, ISBN; 978-3527324491, pp.125—160

[12] Samukawa S, Hori M, Rauf Sh, Tachibana K, Bruggeman P, Kroesen G, Whitehead J Ch, Murphy A B, Gutsol A F, Starikovskaia S, Kortshagen U, Boeuf J–P, Sommerer T J,

Kushner M J, Czarnetzki U, and Mason N 2012 The 2012 Plasma Roadmap, *J. Phys. D: Appl. Phys.* **45** 253001 (37pp)

[13] Starikovskiy A and Aleksandrov N 2011 Plasma–assisted ignition and combustion, *In: Aeronautics and Astronautics. Ed by: Max Mulder. ISBN 978–953–307–473–3*

[14] Starikovskiy A and Aleksandrov N 2013 Plasma–assisted ignition and combustion *Progress in Energy and Combustion Science* **39** 61—110

[15] Leonov S, Napartovich A, Kochetov I and Yarantsev D 2014 Multi–pulse operation at plasma-assistance in high–speed combustion, Proc. of 52nd AIAA Aerospace Sciences Meeting, 13–17 January 2014, National Harbor, Maryland, AIAA–2014–0662

[16] Leonov S, Adamovich I, Lempert W 2014 Transient injection of supercritical fuel, Proc. of 52nd AIAA Aerospace Sciences Meeting, 13–17 January 2014, National Harbor, Maryland, AIAA–2014–0815

[17] Leonov S, Vincent A, Sabelnikov V, Firsov A, Yarantsev D 2014 Plasma-assisted combustion in supersonic airflow: optimization of electrical discharge geometry, Proc. of 52nd AIAA Aerospace Sciences Meeting, 13–17 January 2014, National Harbor, Maryland, AIAA–2014–0988

[18] Xu D A, Lacoste D A, Rusterholtz D L, Elias P–Q, Stancu G D and Laux C O 2011 Experimental study of the hydrodynamic expansion following a nanosecond repetitively pulsed discharge in air *Appl. Phys. Lett.* **99** 121502, 3 pp

[19] Tholin F, Lacoste D A, Bourdon A 2014 Influence of fast–heating processes and O atom production by a nanosecond spark discharge on the ignition of a lean H_2-air premixed flame *Combustion and Flame* **161** 1235–1246

[20] Breden D, Raja L L, Idicheria Ch A, Najt P M and Mahadevan Sh 2013 A numerical study of high-pressure non–equilibrium streamers for combustion ignition application *J. Appl. Phys.* **114** 083302

[21] Chintala N, Bao A, Lou G and Adamovich I V 2006 Measurements of combustion efficiency in nonequilibrium RF plasma–ignited flows *Combust. Flame* **144** 744–756

[22] Ombrello T, Qin X, Ju Y, Gutsol A, Fridman A, Carter C 2006 Combustion enhancement via stabilized piecewise nonequilibrium gliding arc plasma discharge *AIAA Journal* **44**(1) 142—150

[23] http://www.fidtechnology.com

[24] Anikin N B, Starikovskaia S M and Starikovskii A Yu 2006 Oxidation of saturated hydrocarbons under the effect of nanosecond pulsed space discharge *J. Phys. D: Appl. Phys.* **39** 3244–3252

[25] Starikovskaia S M, Starikovskii A Yu and Zatsepin D V 2001 Hydrogen oxidation in a stoichiometric hydrogenair mixture in the fast ionization wave *Combust. Theory Modelling* **5** 97–129

[26] Anikin N B, Starikovskaia S M and Starikovskii A Yu 2004 Study of the oxidation of alkanes in their mixtures with oxygen and air under the action of a pulsed volume nanosecond discharge *Plasma Physics Reports* **30**(12) 1028–1042

[27] Gundersen M A, Singleton D, Kuthi A, Lin Y and Sanders J 2012 Transient plasma for marine diesel GHG abatement *China Maritime Week*, March 2012, Hong Kong

[28] Yin Z, Montello A, Carter C D, Lempert W R and Adamovich I V 2013 Measurements of temperature and hydroxyl radical generation/decay in lean fuel–air mixtures excited by a repetitively pulsed nanosecond discharge *Combustion and Flame* **160** 1594—1608

[29] Li T, Adamovich I V and Sutton J A 2013 A burner platform for examining the effects of non–equilibrium plasmas on oxidation and combustion chemistry *Combustion Sci. Technol.* **185** 990—998

[30] Kosarev I N, Pakhomov A I, Kindysheva S V, Anokhin E M and Aleksandrov N L 2013 Nanosecond discharge ignition in acetylene–containing mixtures *Plasma Sources Sci. Technol.* **22** 045018 (9 pp)

[31] Belaia V, Starikovskiy A Yu 2014 Nanosecond discharge ignition of lean C_2H_6–containing mixtures at elevated temperatures *Proc. of AIAA SciTech, 52nd Aerospace Sciences Meeting* 13–17 January 2014, National Harbor, Maryland, AIAA 2014-1181

[32] Starikovskiy A, Rakitin A, Correale G, Nikipelov A, Urushihara T and Shiraishi T 2012 Ignition of hydrocarbon-air mixtures with non-equilibrium plasma at elevated pressures *Proc. of 50th AIAA Aerospace Sciences Meeting including the New Horizons Forum and Aerospace Exposition* Nashville, USA, 9—12 January 2012.

[33] Stepanyan S A, Boumehdi M A, Vanhove G, Desgroux P and Starikovskaia S M 2013 Time–resolved electric field measurements in nanosecond surface dielectric discharge. Comparison of different polarities. Ignition of combustible mixtures by surface discharge in rapid compression machine *Proc. of 51st AIAA Aerospace Sciences Meeting* 7-10 January 2013, Grapevine, Texas, AIAA–2013–1053

[34] Boumehdi M A, Stepanyan S, Starikovskaia S, Desgroux P and Vanhove G 2013 Plasma assisted ignition inside a rapid compression machine *Proc. of European Combustion Meeting*, 25-28 June 2013, Lund, Sweden

[35] Boumehdi M A, Stepanyan S, Desgroux P, Vanhove G and Starikovskaia S 2014 Ignition of methane- and n–butane–containing mixtures at high pressures by pulsed nanosecond discharge. Submitted; under revision, 2014

[36] Sun W, Won S H and Ju Y 2014 In situ plasma activated low temperature chemistry and the S-curve transition in DME/oxygen/helium mixture *Combust. Flame*, in Press, available online 17 February 2014

[37] Bak M S, Do H, Mungal M G, Cappelli M A 2012 Plasma–assisted stabilization of laminar premixed methane/air flames around the lean flammability limit *Combust. Flame* **159** 3128–3137

[38] Bak M S, Im S–K, Mungal M G and Cappelli M A 2013 Studies on the stability limit extension of premixed and jet diffusion flames of methane, ethane, and propane using nanosecond repetitive pulsed discharge plasmas *Combust. Flame* **160** 2396–2403

[39] Yin Z, Eckert Z, Adamovich I V, and Lempert W R 2014 Time–resolved measurements of temperature and species concentrations distributions in Ar–based mixtures excited by a nanosecond pulse discharge *Proc. of AIAA SciTech, 52nd Aerospace Sciences Meeting* 13–17 January 2014, National Harbor, Maryland, AIAA 2014—1361

[40] Ombrello T, Won S H, Ju Y and Williams S 2010 Flame propagation enhancement by plasma excitation of oxygen. Part II: Effects of $O_2(a^1\delta_g)$ *Combust. Flame* **157** 1916–1928

[41] Ombrello T, Won S H, Ju Y and Williams S 2010 Flame propagation enhancement by plasma excitation of oxygen. Part I: Effects of O_3 *Combust. Flame* **157** 1906–1915

[42] Wu L, Lane J, Cernansky N P, Miller D L, Fridman A A and Starikovskiy A Yu 2011 Plasma–assisted ignition below self–ignition threshold in methane, ethane, propane and butane–air mixtures *Proc. of the Combustion Institute* **33** 3219–3224

[43] Singleton D, Pendleton S J and Gundersen M A 2011 The role of non–thermal transient plasma for enhanced flame ignition in C_2H_4-air *J. Phys. D: Appl. Phys.* **44** 022001 (6pp)

[44] Pendleton S J, Bowman S, Carter C, Gundersen M A and Lempert W 2013 The production and evolution of atomic oxygen in the afterglow of streamer discharge in atmospheric pressure fuel/air mixtures *J. Phys. D: Appl. Phys.* **46** 305202 (7pp)

[45] Sokolov O V, Parfenov Yu V, Arutyunov V S, Basevich V Ya and Vedeneev V I Study of cool flame phenomena during self–ignition of methane–oxygen mixtures 1996 *Russian Chemical Bulletin* **45**(10) 2316—2320

[46] Smith G P, Golden D M, Frenklach M, Moriarty N W, Eiteneer B, Goldenberg M, Bowman C T, Hanson R K, Song S, Gardiner W C, Jr., Lissianski V V, Qin Z, http://www.me.berkeley.edu/gri_mech

[47] http://c3.nuigalway.ie

[48] Starikovskiy A and Aleksandrov N 2013 Plasma-assisted ignition and combustion *Progress in Energy and Combustion Science* **39** 61—110

[49] Adamovich I V, Li T and Lempert W R 2015 Kinetic mechanism of molecular energy transfer and chemical reactions in low-temperature air-fuel plasmas *Philosophical Transactions of the Royal Society of London A: Mathematical, Physical and Engineering Sciences* **373** 20140336

[50] Ju Y and Sun W 2015 Plasma assisted combustion: Dynamics and chemistry *Progress in Energy and Combustion Science* **48** 21—83

Acknowledgements

The authors are grateful to US AFOSR for permanent support of their scientific work during a long period; personally to Dr. Julian Tishkoff for his continuous interest in plasma assisted combustion and to Prof. Chiping Li for his leading role as AFOSR Manager at present in the field of Energy Conversion and Combustion Science. The work was partially supported by French National Agency, ANR (PLASMAFLAME Project, 2011 BS09 025 01), PICS–RFBR grant (5745–11.02.91063–a/5745), by LabEx Plas@Par, Associated International Laboratory LIA KaPPA (CNRS) and by PUF (Partner University Foundation).

List of Figures